Dissertation zur Erlangung des Doktorgrades
der Fakultät für Chemie und Pharmazie
der Ludwig-Maximilians-Universität München

Narrow-band Emitting Phosphors for Solid-State Lighting

Philipp Jean Strobel

aus

München, Deutschland

2018

Erklärung

Diese Dissertation wurde im Sinne der von § 7 der Promotionsordnung vom 28. November 2011 von Herrn Prof. Dr. Wolfgang Schnick betreut.

Eidesstattliche Versicherung

Diese Dissertation wurde eigenständig und ohne unerlaubte Hilfe erarbeitet.

München, den 07. Mai 2018

…….

(Philipp Jean Strobel)

Dissertation eingereicht am 08. Mai 2018

1. Gutachter: Prof. Dr. W. Schnick

2. Gutachter: Prof. Dr. A. Moewes

Mündliche Prüfung am 14. Juni 2018

Für meine Familie

Danksagung

Ganz besonderer Dank geht an Herrn Prof. Dr. Wolfgang Schnick für die Möglichkeit meine Doktorarbeit über ein äußerst innovatives Thema in seiner Arbeitsgruppe anzufertigen. Die große Freiheit bei der Themenwahl sowie der Umsetzung neuer Ideen in einem so interessanten Forschungsgebiet sowie die hervorragenden Arbeitsbedingungen waren die beste Voraussetzung für den Erfolg dieser Arbeit. Auch für die Möglichkeit, Ergebnisse in wissenschaftlichen Fachzeitschriften und auf (inter)nationalen Tagungen darzustellen sowie der Möglichkeit zur aktiven Teilnahme an Projekten wie der sehr inspirierenden Kooperation mit Philips/Lumileds möchte ich mich herzlich bedanken.

Herzlich danken möchte ich Herrn Prof. Dr. Alexander Moewes für die Übernahme des Koreferats sowie für die intensive und persönliche Betreuung während meiner Zeit in Kanada. Das offene Ohr für Fragen aller Art zu den Besonderheiten von Synchrotronstrahlung und deren Anwendung auf die Untersuchung von Festkörperverbindungen möchte ich hier besonders erwähnen. Zahlreiche Besprechungen und Diskussionen waren eine große Hilfe bei meinem komplexen physikalischen Exkurs sowie beim Ausarbeiten der Forschungsinhalte und Vorbereitung der Publikationen.

Den Herren Prof. em. Dr. Wolfgang Beck, Prof. Dr. Hans-Christian Böttcher, Prof. Dr. Dirk Johrendt und Prof. em. Dr. med. habil. Dr.-Ing. Wolfgang Plitz danke ich für die Bereitschaft, als weitere Prüfer zur Verfügung zu stehen.

Großer Dank für viele Diskussionen um kristallographische Probleme und Gespräche um Lumineszenz geht insbesondere an meine Kollegen und Freunde, die Herren Christian Maak und Peter Wagatha.

Herzlichst danken möchte ich meinen kanadischen Kollegen Thomas Tolhurst, Tristan de Boer und Josha Ho für die Durchführung von Synchrotron-Untersuchungen, die intensive Betreuung sowie die schöne und kurzweilige Zeit in Saskatoon.

Auch möchte ich mich ganz herzlich bei allen Beteiligten der Kooperation mit Lumileds bedanken. Hierbei möchte ich besonders Dr. Peter J. Schmidt, Volker Weiler, Cora Hecht, Detlef Wichert, Petra Huppertz und Andreas Tücks hervorheben, die mir durch zahlreiche Synthesen und vor allem mit intensiver Charakterisierung der Lumineszenzeigenschaften den Weg durch die Doktorarbeit erleichtert haben. Die enge Zusammenarbeit hat mir einen tiefen Einblick in die Anwendung unterschiedlichster Leuchtstoffe in der modernen Beleuchtungstechnologie vermittelt. Insbesondere konnten durch unsere gemeinsame Forschung nachhaltige Ergebnisse geschaffen werden.

Frau Olga Lorenz, Herrn Thomas Miller und Herrn Wolfgang Wünschheim danke ich für die Hilfe bei allerlei technischen, organisatorischen, computertechnischen und sicherheitsrelevanten Fragen. Dadurch war es mir möglich, mich ganz meinen Ideen und meiner Forschung hinzugeben und auch trotz IT-Sanierung nahezu lückenlos weiterzuarbeiten.

Ferner danken möchte ich auch Dr. Constantin Hoch, Dr. Thomas Bräuniger und Dr. Peter Mayer für die zahlreichen Einkristall- oder NMR-Untersuchungen und auch für den intensiven Beistand bei diversen Problemdatensätzen.

Vielen Dank auch an Herrn Christian Minke für die zahlreichen Stunden am REM, die unzähligen EDX-Messungen, die aufgenommenen Bilder sowie die NMR-Messungen. Auch denke ich gerne an den ein oder anderen Nachmittag auf der Wiesn, der Weinmesse oder unserem Dorffest.

Ganz besonderer Dank gilt auch meinen übrigen Laborkollegen aus D2.100 und D2.107 für die schöne Zeit. Vielen Dank an Niklas Cordes, Lucien Eisenburger, Eugenia Elzer, Jonas Häusler, Lukas Neudert und Christine Pösl sowie an die Mitglieder des AK Lotsch, Kerstin Gottschling und Claudia Lermer, die es mit uns im Labor aushalten mussten. Vielen Dank besonders an Herrn Robin Niklaus für die theoretischen Ratschläge und Rechnungen.

Natürlich gilt auch größter Dank meinen Praktikanten Veit Giegold, Maximilian Schuster, Andrea Stegner, Alexander Beck und Yao Xuanyu. Ohne den ständigen Ehrgeiz zur Forschung und die tatkräftige Unterstützung beim Synthetisieren und Auswerten wäre all das kaum möglich gewesen.

Ich möchte mich auch bei allen weiteren Kollegen der Arbeitkreise Schnick, Hoch, Bräuniger, Johrendt und Lotsch ganz herzlich für die vielen lustigen Film- und Schafkopf-Abende und die tolle Zeit bedanken.

Ein herzlicher Dank geht auch an meine Freunde, Leo Diehl, Stephan Reuther, Hendrik Schlomberg und Henry Schurkus, die sich mit mir durch das Studium und die anschließende Promotion gekämpft und dabei für die nötige Abwechslung gesorgt haben.

Großer Dank gilt den beiden Doktoren Sebastian Schmiechen und Philipp Pust, die bei mir schon während meiner Praktikantenzeit die Begeisterung für Festkörperchemie und die Welt der Leuchtstoffe geweckt und den Grundstein für meine Forschung gelegt haben.

Allergrößter Dank gilt aber meinen Eltern sowie meiner Freundin Jane. Ohne eure Hilfe und Unterstützung wäre all dies nicht möglich gewesen.

οἶδα οὐκ εἰδώς

(Platon)

Table of Contents

1 Introduction

Electrical energy consumed by lighting represents a significant share of global energy use. Concerns about climate change and desire for energy independence are causing the global lighting market to develop more energy-efficient light sources.[1] As a result, white light emitting diodes (LEDs) have been introduced to replace conventional incandescent light bulbs as well as fluorescent lamps. Recently, solid-state lighting (SSL) has emerged with improved energy efficiency, light quality and long-term durability, but there is still room for improvement in packaging, engineering and phosphor development.[2] New materials and applications for phosphor-converted (pc-)LEDs are expected to support this technological revolution.

The SSL development stands for a radical transformation in how we consider and implement lighting, and represents a huge chance to significantly reduce energy consumption. LED lighting in the US is forecasted to represent 88% of the lumen-hours produced by general illumination in the year 2030, while a 40–60% reduction of electricity consumption is expected in comparison to a "no-LED" scenario.[1] From an economic point of view, the LED market is growing rapidly. The revenue of the worldwide LED lighting industry is predicted to raise from US$20 billion in 2014 to US$45.5 billion in 2022.[3] LEDs are increasingly important in general lighting applications that were dominated by light bulbs since the end of the 19th century. Further application of white LEDs is established by integration, e.g., in flat, backlit liquid crystal displays (LCDs).[4] In future, challenges, such as the interdependence of efficient lighting and everyday's life, are quested, such as the enhancement of intelligent street lighting as well as innovative lighting solutions in the automotive sector and in medical devices.[5,6]

So far, general lighting is still the largest market for pc-LEDs as the rapid development of LEDs with high quality illumination grade light allows catching up with classic light bulbs. The greatest advantage of the incandescent lamps is their yet unmatched color rendering with a CRI (color rendering index) value ≤100 corresponding to the sun's spectral coverage.[7] Nevertheless, production and sale of light bulbs was banned by law in the EU in 2009 because in incandescent lamps only 5–10% of the electric energy is converted into visible emission. The remaining 90–95% are radiated as heat, therefore representing a huge energy waste.[8] Prior to the conquest of the lighting marked by LEDs, fluorescent lamps were the only energy efficient alternative to incandescent light bulbs. But due to containing toxic mercury and the insufficient light quality with CRI values of only 60–80, fluorescent lamps are only an interim solution.[7] The most promising alternative for covering the total general lighting market are state of the art LEDs achieving CRI values >90 combined with excellent energy efficiency.

The decisive value in the discussion of energy efficiency of a light source is the overall luminous efficacy that is determined by the ratio of produced luminous flux and consumed energy. Luminous efficacy can be used to compare the energy efficiency of a light source, and gives a comparable value

for the total quantity of visible light, emitted by a light source, divided by the total consumed power of an LED package. While classical light bulbs reach values of only 15 lm/W, fluorescent lamps have values up to 100 lm/W. These values are already significantly exceeded by LEDs with values of 100–140 lm/W. A goal defined by the US Department of Energy (DOE) is the development of a LED package with a luminous efficacy exceeding 240 lm/W in 2025.[1] This goal applies for both, warm white and cool white pc-LED packages for specific applications. The terms warm white and cool white refer to the correlated color temperature (CCT), i.e. the temperature of a black body radiator emitting white light. With a CCT of 2700–4000 K light is considered warm white while a CCT of 5000–6000 K corresponds to cool white light.

Due to the luminous flux being weighted with the human eye's sensitivity to different wavelengths, a maximum in luminous efficacy of 683 lm/W is attainable with green light (λ = 555 nm). The human eye's sensitivity is given by the luminosity function reaching from 400 to 700 nm with its maximum in the green spectral area. Emission profiles of light sources need to be adapted to this curve for gaining optimum efficiency, and additionally they have to contain all colors of the visible spectrum for sufficiently large CRI values. The future challenge is to develop a LED with both, high efficiency and excellent color rendering.[9]

In LED packages several methods to obtain white light that comprises the whole visible spectrum are used. In general, white light is generated by additive color mixing. The simplest method is the use of three individual monochromatic blue, yellow-green and red diodes. This solution provides only insufficient color rendition as well as poor long-time stability and intensity. In contrast, the combination of a monochromatic, large band gap semiconductor LED and light converting phosphor materials promises high illumination grade quality and energy efficiency. Figure 1 demonstrates the schematic setup of a phosphor converted LED. A high energy nUV (near ultraviolet) to blue emitting LED is the foundation in color-converted LEDs; three standard methods can be distinguished:[9]

1. Blue LED with a yellow-green phosphor (1pc-LED)
2. Blue LED with yellow-green and orange-red phosphors (2pc-LED)
3. nUV LED with blue, yellow-green and orange-red phosphors (RGB pc-LED)

The accessible maximum CRI values increase from methods 1–3, as more regions of the visible spectrum are represented. Multi-phosphor pc-LEDs using a blue LED to excite yellow-green and orange-red phosphors give the best results in color rendering combined with high luminous efficacy. The excellent color rendition of a full-conversion LED is accompanied by the loss of energy efficiency due to the use of a high-energy UV-LED, and the repeated conversion of energy by the sequence towards green-yellow and finally orange-red emission.

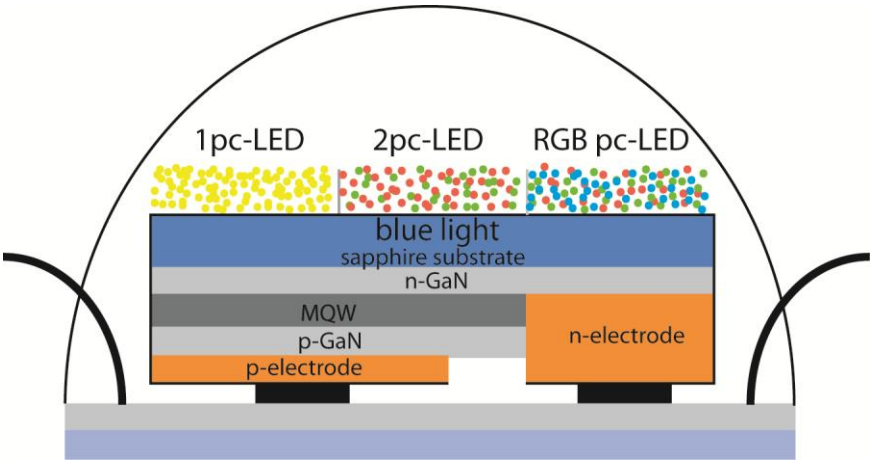

Figure 1. Schematic setup of a flip-chip pc-LED. Yellow-green, orange-red and/or blue phosphors cover a nUV or blue emitting primary LED and white light is obtained by energy down-conversion.[9,10]

A prerequisite for the development of white pc-LEDs was the development of highly efficient UV-blue semiconductor LEDs. This challenging invention was mainly accomplished by the work of *Isamu Akasaki*, *Hiroshi Amano* and *Shuji Nakamura*. In 2014, they were rewarded with the Nobel Prize in Physics for "*the invention of efficient blue light-emitting diodes which has enabled bright and energy-saving white light sources*".[11] The emission color of a semiconductor LED is directly dependent on the material's band gap size. For high-energy blue emission a direct band gap of ≈ 3.4 eV is required.[12] A large band gap material was found with the development of p- and n-doped GaN. Light is emitted upon applying a voltage on p- and n-doped semiconductor layers. As a result of the applied voltage, electron-hole pairs are formed that emit photons during recombination. For the efficient generation of blue light with GaN, three major challenges had to be solved: growth of high quality GaN single crystals, identifying a suitable dopant for the acceptor material, and increasing the emission intensity.[12] In 1986, *Isamu Akasaki* and *Hiroshi Amano* succeeded in synthesizing high quality GaN crystals by Metal-organic Vapor Phase Epitaxy (MOVPE).[12] Suitable p-doped acceptor materials have been developed by doping of GaN with Mg or Zn. The first step to successfully optimizing efficiency was accomplished by *Nakamura*, who observed that the annealing of Mg-doped GaN leads to the reduction of hydrogen complexes and therefore activation of the material lowering the defect concentration.[12] With the development of a blue-emitting InGaN/AlGaN double heterojunction exhibiting a quantum efficiency of 2.7%, the technological breakthrough was achieved by *Nakamura*. This allowed for development of white pc-LEDs, applying energy-converting phosphors on the surface of blue semiconductor primary LEDs to generate light covering the entire visible spectrum.[13]

A number of different solid-state compound groups are available as phosphor materials, each with specific advantages and drawbacks. But all compounds share the same physical principle. For obtaining luminescence it is necessary to introduce point defects into an optical transparent material, the host. These defects are obtained by the precise incorporation of an activator into the host material. As a result, a phosphor allows conversion of photon energy. Four different steps are necessary to gain

visible emission by a phosphor, and are visualized in the configurational coordinate diagram in Figure 2:[14]

1. Absorption of a high energy photon
2. Excitation of an electron within the activator center to form an excited state
3. Vibrational relaxation of the excited state
4. Relaxation to the ground state by emission of a lower energy photon

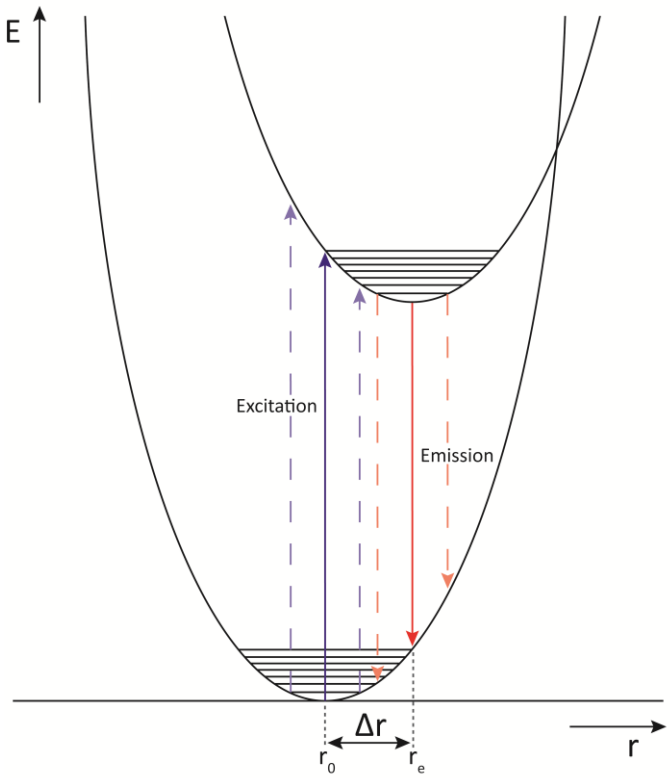

Figure 2. Configurational coordinate diagram of an activator with broadband emission. Excitation of an electron upon absorption of a photon (blue line), vibrational relaxation of the excited state, emission of a photon (red line) with lower energy due the Stokes-shift, and relaxation to the ground state. r is the activator–ligand distance.[15]

In pc-LEDs, the energy absorbed by the phosphor is provided by high energy photons of a blue InGaN LED. This absorption and emission process is called photoluminescence. Only few activators allow absorption of UV or blue light accompanied by subsequent emission in the visible spectrum. Important activator elements are transition metals, such as Mn^{4+} and rare earth (*RE*) elements, e.g., Ce^{3+}, Eu^{2+} or Eu^{3+}.[7,16] The emission color of a phosphor is strongly dependent on the type of the incorporated activator as well as the host material. Activators can be classified in two groups, exhibiting either line emission or broadband emission. Mn^{4+} and Eu^{3+} are assigned to the first group, as emission is observed by transitions of parity-forbidden *d–d* or *f–f* transitions, respectively. Eu^{3+}-doped phosphors' emission is only found in the orange to red spectral region as strong shielding effects of unoccupied 5*d* levels reduce the influence of the ligand field on the *f*-states. Consequently,

the emission is largely unaffected by the host material. Mn^{4+}-emission is influenced by the crystal field splitting, and several emission lines are observed, often in the red spectral region.[9,16]

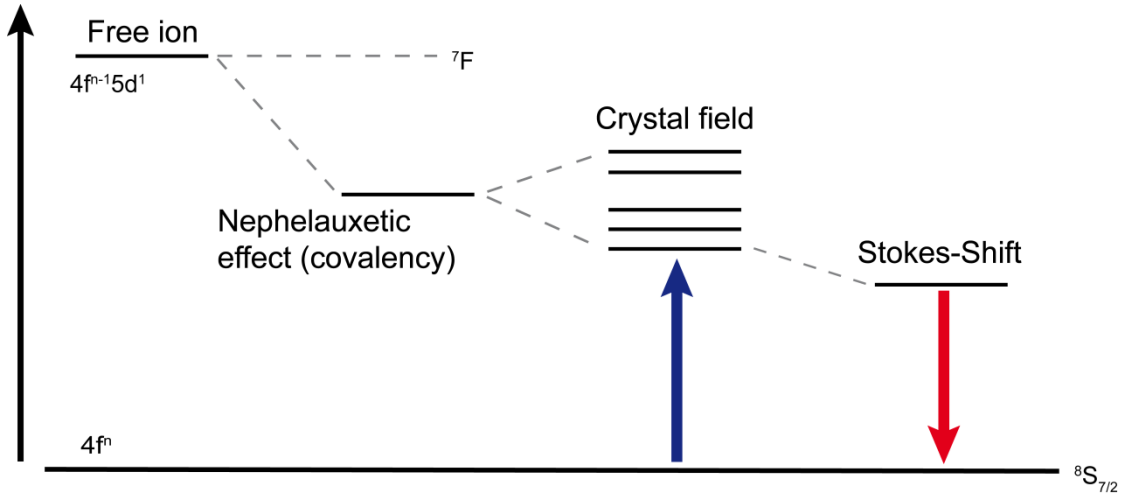

Figure 3. Excitation and emission process in Eu^{2+}- and Ce^{3+}-doped band-emitting phosphors. Major influences of the activator coordination are displayed. Excitation is indicated by a blue arrow, emission by a red arrow.[10]

Ce^{3+} and Eu^{2+} cause broadband emission due to overlapping energy levels, a large number of allowed transitions and the direct influence of the vibrating activator coordination. At the same time, Ce^{3+}- and Eu^{2+}-doped phosphors show strong absorption in the blue spectral area and therefore are highly excitable by blue light. A photon emitted by the blue LED is used to excite an electron from the 4*f* ground state to an excited 5*d* state. The subsequent relaxation, e.g., in Eu^{2+}-doped phosphors is a parity allowed $4f^6(^7F)5d^1 \rightarrow 4f^7(^8S_{7/2})$ transition with intense emission. While Eu^{2+}-doped phosphors with a single activator site usually show one emission maximum, Ce^{3+}-doped materials have two emission maxima due to a split ground state. The energetic distance between the excited 5*d* state and the ground state determines the emitted color and is directly dependent on the host material. Three major influences on the energetic level of the 5*d* state can be distinguished and are displayed in Figure 3. The first effect strongly depends on the bonding character of the activator ion and its ligands. This nephelauxetic effect is the foundation for the energetic decrease with increasing covalent character of the bond. A more ionic bonding character results in an energetically increased 5*d* level. Consequently the replacement of O by N leads to red-shifted emission. While oxides usually emit in the blue to yellow range, red emission is accessible in nitride compounds. The second effect is the influence of the crystal field on the splitting of the 5*d* energy states that is directly dependent on the ligand field strength around the activator site and the activator's coordination geometry. Thirdly, the Stokes-shift is the energetic difference between absorption and emission maximum and strongly depends on the host materials vibrational rigidity. Hence, the use of broadband emitters allows the adaption of the emission color by choosing a suitable host material to any point of the visible spectrum. Therefore, dopants such as Ce^{3+} and Eu^{2+} are often introduced in highly condensed solid-

state host materials that are of high importance for the development of highly efficient, illumination grade white pc-LEDs.[2]

The most commonly used material in pc-LEDs with a single phosphor (1pc-LED) is YAG:Ce ($Y_3Al_5O_{12}:Ce^{3+}$), a broad-band emitting yellow phosphor. As red spectral parts are not contained in the emission of YAG:Ce, a 1pc-LED has a rather high CCT and only a CRI <80 is obtained.[9] To gain increased CRI values, red emission needs to be added by complementary phosphors, leading to the development of 2pc-LEDs. First red phosphor materials were based on Eu^{2+}-doped metal sulfides that show only poor chemical stability against hydrolysis. More stable red emitting materials are highly condensed Eu^{2+}-doped nitrides. Two of the most important nitride red emitters are $(Ba,Sr)_2Si_5N_8:Eu^{2+}$ (BSSNE) and $(Sr,Ca)AlSiN_3:Eu^{2+}$ (SCASN).[2,10] Both show excellent chemical and thermal stability, a large band gap and high quantum efficiency (QE). With these phosphors color rendering exceeding CRI values of 80–90 is possible. A drawback of such broadband red-emitting materials with a full width at half maximum (*fwhm*) of the emission band >80 nm (>2000 cm^{-1}) is decreased luminous efficacy, as significant shares of the light are emitted in the non-visible infra-red. Another interesting red-emitting phosphor is $K_2SiF_6:Mn^{4+}$ (KSF), but poor stability, strong concentration quenching, and a long decay time limit possible applications.[9]

The next step in phosphor development is the investigation of new host materials that allow emission with limited emission band width for increased luminous efficacy. Optimum emission of an orange-red phosphor is found in a spectral area around 630 nm with *fwhm* of approximately 50 nm (<1200 cm^{-1}). This would reduce the emission in the IR to a minimum and increase the overall luminous efficacy of the LED by up to 30%. Promising materials have been developed by *Schmiechen* and *Pust* on the field of nitridosilicates and -aluminates. Several compounds, crystallizing in the highly symmetric UCr_4C_4-type or derived structure types, $Na[Li_3SiO_4]$ or $Cs[Na_3PbO_4]$, have been investigated. These novel compounds are $AE[Mg_3SiN_4]$ (*AE* = Ca–Ba), $AE[Mg_2Al_2N_4]$ (*AE* = Ca–Ba) and $AE[LiAl_3N_4]$ (*AE* = Ca,Sr).[17-21] So far, $Sr[Mg_3SiN_4]:Eu^{2+}$ (SMS) is the overall most narrow-band emitting red phosphor with maximum emission at 615 nm with *fwhm* of only 43 nm (1170 cm^{-1}). Nevertheless, due to a small band gap and therefore strong thermal quenching at room temperature, application is not intended. The most promising phosphor for application is narrow-band red emitting $Sr[LiAl_3N_4]:Eu^{2+}$ (SLA) with an emission maximum at 650 nm with *fwhm* of 1180 cm^{-1} It was shown that an increase of 4–12% of luminous efficacy compared to commercial high CRI LEDs can be expected by application of SLA.[2,21] Therefore, the development and addition of excellent narrow-band red emitting phosphors has a significant influence on the improvement of LED light quality gaining CRI values >90.

For further increasing the CRI of blue excited pc-LEDs an additional challenge is the development of cyan emitting phosphors in the area around 490–500 nm. Missing emission between the blue primary LED and the broadband green-yellow phosphor, the so-called cyan gap, limits the color rendition due to poor rendering of cyan shades. The most promising phosphor with cyan emission is

$BaSi_2O_2N_2:Eu^{2+}$ (Ba222, λ_{em} = 495 nm, *fwhm* = 35 nm), but due to their layered structure, $MSi_2O_2N_2:Eu^{2+}$ (*M* = Ca–Ba) phosphors exhibit only poor thermal and chemical stability.[22,23]

LEDs with improved color point stability, excellent color rendition and high color rendering can be obtained by development of RGB pc-LEDs. Efficiency and light quality is limited in 2pc-LEDs due blue overshoot i.e. wasted energy of the intense blue primary and insufficient color point stability. These challenges can be addressed by the combination of a nUV emitting primary LED with highly efficient narrow-band emitting phosphors in the blue–cyan and orange–red spectral regions and a broad-emitting yellow–green phosphor. Nevertheless, several issues need to be solved for the development of an efficient RGB pc-LED. Since the emission of nUV primary LEDs is very close to the emission of a required blue phosphor, restrictions are imposed on the development of a suitable highly efficient blue phosphor. Additionally, when exciting with a high energy primary, the Stokes loss from down-conversion reduces the overall efficiency of the RGB pc-LED.[24] The optimum emission wavelength of a nUV primary for gaining maximum efficacy with a standard current density of 35 A/cm^2 is 425 nm, compared to a standard 440 nm blue LED. In the optimum case, excitation peaks of all phosphors should match the LED emission peak, with no absorption of longer wavelengths (re-absorption).[24]

Four of the most interesting narrow-band blue emitting phosphors for application with nUV LEDs are $Ba_3MgSi_2O_8:Eu^{2+}$ (BMSO), $(Ca,Sr,Ba)_{10}(PO_4)_6Cl_2:Eu^{2+}$ (SCAP), $BaMgAl_{10}O_{17}:Eu^{2+}$ (BAM) and $LiCaPO_4:Eu^{2+}$ (LCP), emitting between 438 nm to 475 nm, with emission *fwhm* of 30–60 nm.[24,25] For covering the yellow-green spectral range in RGB pc-LEDs, phosphors with improved absorption in the nUV range compared to YAG:Ce are required. Interesting materials are oxonitridosilicates, such as $BaSi_2O_2N_2:Eu^{2+}$ and $Sr_{0.25}Ba_{0.75}Si_2O_2N_2:Eu^{2+}$ with tunable emission from 495 nm to 565 nm, as well as orthosilicates ($(Ca,Sr,Ba)Si_2O_4:Eu^{2+}$).[22] The optimum choice of a red emitter is the same for 2pc- and RGB pc-LEDs. BSSNE and SCASN as well as SLA are adequate red emitters, while better options with efficient narrow-band emission around 630 nm still need to be developed. The biggest challenge of future phosphor research is the elimination of self- and re-absorption effects in such broadband emitting phosphors with Eu^{2+} and Ce^{3+}. Currently, there are also no efficient, suitable red emitting phosphors based on trivalent *RE* activators, such as Eu^{3+}.[24] An appropriate phosphor choice in conversion solutions might be KSF, as less lumen loss compared to broadband red phosphors is obtained, but one big disadvantage of Mn^{4+}-doped phosphors is their long radiative lifetime.[24]

As stated above, various solutions of phosphor-converted LEDs can be applied to improve light quality and energy efficiency in general lighting. Similar methods can also be deployed in other lighting applications: 2pc-LEDs based on YAG:Ce and a red phosphors (SCASN or KSF) are applied, e.g., in background lit LCDs. These displays can cover all colors contained in a color gamut determined by the position of the blue, red and green shares in a CIE (Commission Internationale de l'Éclairage) diagram.[26] For display technology the gamut needs to be adapted to specific standards (for instance the National Television Standard Committee (NTSC), CIE 1931). For increasing the color

gamut especially in the green spectral region where the human eye is most sensitive, and allow the perception of more color shades, green phosphors with narrow-band emission are required. A widely used material in such LEDs is β-SiAlON:Eu^{2+}, emitting at 525 nm with *fwhm* of 50 nm but low absorption in the blue spectral region.[2] Requirements for novel narrow-band green phosphors are emission between 530–535 nm and *fwhm* of about 50 nm.[27,28]

Summarizing, narrow-band emitting phosphors of all colors are subject of worldwide research because they are required for the improvement of pc-LEDs for diverse applications. Many promising compounds have been developed on the base of doped oxo- and nitridosilicate structures. Recent results suggest that specific structural properties of these compounds have a large influence on electronic and emission properties. This allows the straightforward investigation of novel Eu^{2+} doped compounds to improve luminescence properties and obtain efficient narrow-band emission.

Several requirements are derived for efficient narrow-band emission: A large band gap, as the excited Eu 5*d* state should have a sufficient distance to the conduction band (CB); High thermal stability, as strong thermal quenching due to thermally excited electrons to the CB; Superior chemical stability i.e. against hydrolysis or thermal degradation, to provide long-time stability. Emission characteristics of a phosphor directly depend on its characteristic absorption bands, as the absorbed photon is re-emitted with lower energy due to the Stokes-shift. For narrow-band emission it is of uttermost importance to minimize the Stokes-shift that is directly dependent on lattice vibrations.[29] A large Stokes-shift again increases the emission band width.[15] Direct influence is given by activator-ligand distances, symmetry of the activator coordination, change of the size of the excited activator, and network rigidity.

Novel materials with a chemically and thermally stable, rigid crystal structure with a high degree of condensation and a highly symmetrically coordinated activator site are of strong interest in phosphor research. Oxo- and nitridosilicates as well as substitutional variants are highly interesting phosphor materials due to their chemical, thermal and electronic properties.[30]

The compound class of silicates offers tremendous diversity of crystal structures due to the variability of SiO_4-tetrahedra linking. The tetrahedra are connected by common oxygen atoms to manifold anionic building units. Depending on their building unit, silicates can be divided in categories: structures consisting of non-condensed SiO_4-tetrahedra or rings, chains or layers of condensed SiO_4-tetrahedra as well as three-dimensional networks can be distinguished. The degree of condensation κ is a value for the molar ratio of Si:O.[30,31] The lowest value of $\kappa = 0.25$ corresponds to non-condensed tetrahedra, the highest value is obtained in the binary compound SiO_2 ($\kappa = 0.5$). Nevertheless, the structural variety in silicates is limited. In oxosilicates O can only be bound terminally to Si ($O^{[1]}$) or simply bridge two Si atoms ($O^{[2]}$). Additionally, the connectivity of SiO_4-tetrahedra is limited to bridging vertices. Connection of SiO_4 tetrahedra by common edges or even faces is usually not observed due to the strong repulsion of the highly charged Si^{4+} cations. One possibility to overcome these structural limits is the complete or partial exchange of O by N, leading to

the materials class of (oxo)nitridosilicates. The tetrahedral coordination of Si by the more electronegative N increases the covalence of the Si-ligand bond and therefore the Si–N distance. This allows threefold $N^{[3]}$ and even fourfold ammonium-type $N^{[4]}$ coordination, and the connection of tetrahedra by common edges. A well known example displayed in Figure 4 is $Ba_2Si_5N_8$, consisting of a network with $N^{[2]}$ and $N^{[3]}$ atoms.[32] An additionally increased structural variety is accessible by exchange of Si by various cations. The most prominent example is the substitution of Si^{4+} by Al^{3+}, leading to the class of (nitrido)alumosilicates, the SiAlONs. Recent experiments demonstrated that substitution of Si by, e.g., Li^+, Mg^{2+}, Ga^{3+}, Ge^{4+} and P^{5+} gives access to novel crystal structures, such as above described SLA (Figure 4) and SMS, as well as $Li_2Ca_2[Mg_2Si_2N_6]$, Mg_3GaN_3, $Ba[Mg_3GeN_4]$, or $Ba_3P_5N_{10}Br$.[17,19,21,30,33-40] This also allows to increase the maximum degree of condensation, when extending the atomic ratio to $T^{[4]}$:(O,N) (T = Li,Mg,Al,Si,etc.). In nitridosilicates, the maximum value is $\kappa = 0.75$ for Si_3N_4, while the substitution of Si allows even larger values, e.g., in $Sr[Mg_3SiN_4]$ and $Sr[LiAl_3N_4]$ with $\kappa = 1$.

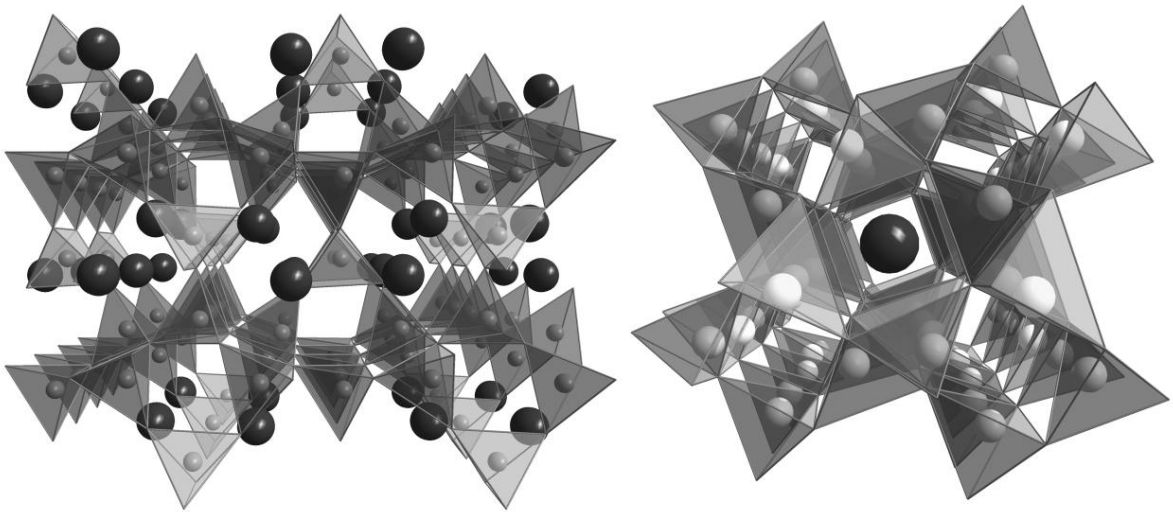

Figure 4. Highly condensed networks of nitridometallates. Left: $Ba_2Si_5N_8$ along [010]; Ba atoms: black; SiN_4 tetrahedra: dark and light gray. Right: $Sr[LiAl_3N_4]$ along [011]; Sr atoms: black; AlN_4 tetrahedra dark gray; LiN_4 tetrahedra light gray.[21,32]

Another interesting element for substitution of tetrahedrally coordinated Si is the lightest alkaline earth element Be. A similar ionic radius ≈ 0.3 Å like Si^{4+}, and compared to Mg increased electronegativity opens up possibilities for the formation of stable, rigid network structures with large band gaps suitable for development of narrow-band emitting phosphors.

For example, the mineral *beryl* $Be_3Al_2[Si_6O_{18}]$ usually described as hexacyclosilicate, contains Be in a distorted tetrahedral coordination.[41] Further substitutional variants were already described by *Liebau*.[31] Yet, only few artificial oxo- and nitridoberyllates have been investigated as Be dusts are toxic and accumulate in the human body causing cancer and berylliosis. Nowadays, hazards are minimized by working in closed containers, such as glove-boxes, allowing the safe characterization of beryllate compounds. In contrast to other alkaline earth oxides, BeO crystallizes in the *wurtzite*

structure type and is therefore isotypic to AlN.[42] At very high pressures, a transition of *wurtzite*-type BeO to the *zinc blende*-type is predicted.[43] α-Be_3N_2 is isotypic to Mg_3N_2 and crystallizes in the cubic *anti-bixbyite* structure type. It transforms to a hexagonal high temperature β-modification above 1400 °C.[44-46] Only few ternary beryllates and nitridoberyllates containing either a second alkaline earth metal or another network element such as Si or Al, have been investigated. *Chrysoberyl*, Al_2BeO_4, with Be in tetrahedral and Al in octahedral coordination, is an aluminum oxoberyllate. In *phenakite*, Be_2SiO_4, BeO_4 and SiO_4 tetrahedra form a highly condensed network.[47,48] The only known alkaline earth beryllates are $Ca_{12}Be_{17}O_{29}$ with a Zeolithe-like structure, $SrBe_3O_4$ with a 3D network structure, and $Ba_3Be_5O_8$ with a chain structure.[49-51] Particularly notable are the two different coordination spheres of Be in these compounds. In addition to tetrahedrally coordinated Be trigonal planarly coordinated Be is observed as well. Further known nitride compounds are $BeSiN_2$ and LiBeN. While $BeSiN_2$ crystallizes as a substitutional variant of the *wurtzite* structure type,[52] LiBeN consists of a network of LiN_4-tetrahedra and trigonal planar BeN_3-units.[53] The compounds $AE[Be_2N_2]$ (*AE* = Mg–Ba) are the only known nitridoberyllates.[51,54] The beryllium nitridophosphate BeP_2N_4 with *phenakite* structure was observed by *Karau*.[55]

Luminescent oxo- and nitridoberyllates could be of high interest for application in pc-LEDs. Extremely rigid networks with a degree of condensation $\kappa \geq 1$ are accessible, promising ultra narrow-band emission. κ is expected to reach values up to 1, e.g., in binary BeO and 1.5 in Be_3N_2. This is possible due to the low formal charge of Be^{2+}, and the small ion radius comparable to Si^{4+}. At the same time, large band gap materials with high chemical and thermal stability are expected, similar to silicates.

This thesis focuses on the development of novel narrow-band emitting phosphors throughout the entire visible spectrum. Next to fundamental technology barriers, such as current efficiency droop, and the efficiency gap of green LEDs, a major goal is the development of highly efficient, narrow-band emitting phosphors as down-conversion materials.[1] Narrow-band red to orange as well as blue to cyan phosphors with a small Stokes-shift are required for increasing energy efficiency and further improving light quality and long-time stability of pc-LEDs. Novel compounds based on nitrido(alumo)silicate structures as well as oxo- and nitridoberyllates have been synthesized and their luminescence properties characterized. Additionally, soft-X-ray synchrotron investigations have been applied for a detailed electronic examination of narrow-band emitting phosphors. Analytic and synthetic results help to understand the relation of a phosphor host lattice and its characteristic, narrow-band luminescence for more efficient pc-LEDs.

References

[1] U.S. Department of Energy, Solid-State Lighting - R&D Plan, **2016**

[2] Pust, P.; Schmidt, P. J.; Schnick, W. A revolution in lighting. *Nat. Mater.* **2015**, *14*, 454-458.

[3] https://de.statista.com/statistik/daten/studie/316119/umfrage/umsatz-auf-dem-led-markt-weltweit/, visited on January 09th, **2018**

[4] Xie, R.-J.; Hirosaki, N.; Takeda, T. Wide Color Gamut Backlight for Liquid Crystal Displays Using Three-Band Phosphor-Converted White Light-Emitting Diodes. *Appl. Phys. Express* **2008**, *2*, 022401-022403.

[5] http://www.lighting.philips.de/systeme/vernetzte-beleuchtung/city-touch, visited on January 9th, **2018**

[6] http://www.all-electronics.de/osram-continental-automotive-licht-joint-venture/, visited on January 9th, **2018**

[7] George, N. C.; Denault, K. A.; Seshadri, R. Phosphors for Solid-State White Lighting. *Annu. Rev. Mater. Res.* **2013**, *43*, 481-501.

[8] Feldmann, C. Technical Revolution underway: Nitride-based Phosphors for LED Application. *Z. Anorg. Allg. Chem.* **2012**, *638*, 2169-2171.

[9] Kitai, A., *Materials for Solid State Lighting and Displays*, John Wiley and Sons: West Sussex, U.K., **2017**.

[10] Schmiechen, S.; Pust, P.; Schmidt Peter, J.; Schnick, W. Weißes Licht aus Nitriden. *Nachr. Chem.* **2014**, *62*, 847-851.

[11] https://www.nobelprize.org/nobel_prizes/physics/laureates/2014/, visited on January 31th, **2018**

[12] Aldridge, S.; Downs, A. J., *The Group 13 Metals Aluminium, Gallium, Indium and Thallium: Chemical Patterns and Peculiarities.*, John Wiley & Sons, Ltd: West Sussex, UK, **2011**.

[13] S. Nakamura, T. M., M. Senoh Candela-class high-brightness InGaN/AlGaN double-heterostructure blue-light-emitting diodes. *Appl. Phys. Lett.* **1994**, *64*, 1687-1689.

[14] Ropp, R. C., *Luminescence and the Solid State*, 2 ed., Elsevier: Warren, USA, **2004**.

[15] Blasse, G.; Bril, A. Characteristic luminescence. *Philips Tech. Rev.* **1970**, *31*, 304-314.

[16] Xia, Z.; Liu, Q. Progress in discovery and structural design of color conversion phosphors for LEDs. *Prog. Mater. Sci.* **2016**, *84*, 59-117.

[17] Schmiechen, S.; Schneider, H.; Wagatha, P.; Hecht, C.; Schmidt, P. J.; Schnick, W. Toward New Phosphors for Application in Illumination-Grade White pc-LEDs: The Nitridomagnesosilicates $Ca[Mg_3SiN_4]:Ce^{3+}$, $Sr[Mg_3SiN_4]:Eu^{2+}$, and $Eu[Mg_3SiN_4]$. *Chem. Mater.* **2014**, *26*, 2712-2719.

[18] Schmiechen, S.; Strobel, P.; Hecht, C.; Reith, T.; Siegert, M.; Schmidt, P. J.; Huppertz, P.; Wiechert, D.; Schnick, W. Nitridomagnesosilicate $Ba[Mg_3SiN_4]:Eu^{2+}$ and Structure–Property Relations of Similar Narrow-Band Red Nitride Phosphors. *Chem. Mater.* **2015**, *27*, 1780-1785.

[19] Pust, P.; Hintze, F.; Hecht, C.; Weiler, V.; Locher, A.; Zitnanska, D.; Harm, S.; Wiechert, D.; Schmidt, P. J.; Schnick, W. Group (III) Nitrides $M[Mg_2Al_2N_4]$ (*M* = Ca, Sr, Ba, Eu) and $Ba[Mg_2Ga_2N_4]$ – Structural Relation and Nontypical Luminescence Properties of Eu^{2+} Doped Samples. *Chem. Mater.* **2014**, *26*, 6113-6119.

[20] Pust, P.; Wochnik, A. S.; Baumann, E.; Schmidt, P. J.; Wiechert, D.; Scheu, C.; Schnick, W. $Ca[LiAl_3N_4]:Eu^{2+}$ - A Narrow-Band Red-Emitting Nitridolithoaluminate. *Chem. Mater.* **2014**, *26*, 3544-3549.

[21] Pust, P.; Weiler, V.; Hecht, C.; Tücks, A.; Wochnik, A. S.; Henß, A. K.; Wiechert, D.; Scheu, C.; Schmidt, P. J.; Schnick, W. Narrow-band red-emitting $Sr[LiAl_3N_4]:Eu^{2+}$ as a next-generation LED-phosphor material. *Nat. Mater.* **2014**, *13*, 891-896.

[22] Bachmann, V.; Ronda, C.; Oeckler, O.; Schnick, W.; Meijerink, A. Color Point Tuning for (Sr,Ca,Ba)$Si_2O_2N_2$:Eu^{2+} for White Light LEDs. *Chem. Mater.* **2009**, *21*, 316-325.

[23] Wang, C.-Y.; Xie, R.-J.; Li, F.; Xu, X. Thermal degradation of the green-emitting $SrSi_2O_2N_2$:Eu^{2+} phosphor for solid state lighting. *J. Mater. Chem. C* **2014**, *2*, 2735-2742.

[24] Piquette, A.; Bergbauer, W.; Galler, B.; Mishra, K. C. On Choosing Phosphors for Near-UV and Blue LEDs for White Light. *ECS J. Solid State Sci. Technol.* **2016**, *5*, R3146-R3159.

[25] McKittrick, J.; Hannah, M. E.; Piquette, A.; Han, J. K.; Choi, J. I.; Anc, M.; Galvez, M.; Lugauer, H.; Talbot, J. B.; Mishra, K. C. Phosphor Selection Considerations for Near-UV LED Solid State Lighting. *ECS J. Solid State Sci. Technol.* **2013**, *2*, R3119-R3131.

[26] Oleari, C., *Standard Colorimetry: Definitions, Algorithms and Software*, John Wiley & Sons: West Sussex, UK, **2016**.

[27] Hirosaki, N.; Xie, R.-J.; Kimoto, K.; Sekiguchi, T.; Yamamoto, Y.; Suehiro, T.; Mitomo, M. Characterization and properties of green-emitting β-SiAlON:Eu^{2+} powder phosphors for white light-emitting diodes. *Appl. Phys. Lett.* **2005**, *86*, 211905.

[28] Seong, T.-Y.; Han, J.; Amano, H.; Morkoc, H., *III-Nitride Based Light Emitting Diodes and Applications*, Springer: Dordrecht, Germany, **2013**.

[29] de Jong, M.; Seijo, L.; Meijerink, A.; Rabouw, F. T. Resolving the ambiguity in the relation between Stokes shift and Huang-Rhys parameter. *Phys. Chem. Chem. Phys.* **2015**, *17*, 16959-16969.

[30] Zeuner, M.; Pagano, S.; Schnick, W. Nitridosilicates and Oxonitridosilicates: From Ceramic Materials to Structural and Functional Diversity. *Angew. Chem. Int. Ed.* **2011**, *50*, 7754-7775.

[31] Liebau, F., *Structural Chemistry of Silicates*, Springer: Berlin, **1985**.

[32] Schlieper, T.; Schnick, W. Nitrido-silicate. II: Hochtemperatur-Synthesen und Kristallstrukturen von $Sr_2Si_5N_8$ und $Ba_2Si_5N_8$. *Z. Anorg. Allg. Chem.* **1995**, *621*, 1380-1384.

[33] Zeuner, M.; Pagano, S.; Hug, S.; Pust, P.; Schmiechen, S.; Scheu, C.; Schnick, W. $Li_2CaSi_2N_4$ and $Li_2SrSi_2N_4$ – a Synthetic Approach to Three-Dimensional Lithium Nitridosilicates. *Eur. J. Inorg. Chem.* **2010**, 4945-4951.

[34] Pagano, S.; Lupart, S.; Schmiechen, S.; Schnick, W. $Li_4Ca_3Si_2N_6$ and $Li_4Sr_3Si_2N_6$ – Quaternary Lithium Nitridosilicates with Isolated $[Si_2N_6]^{10-}$ Ions. *Z. Anorg. Allg. Chem.* **2010**, *636*, 1907-1909.

[35] Hintze, F.; Johnson, N. W.; Seibald, M.; Muir, D.; Moewes, A.; Schnick, W. Magnesium Double Nitride Mg_3GaN_3 as New Host Lattice for Eu^{2+} Doping: Synthesis, Structural Studies, Luminescence, and Band-Gap Determination. *Chem. Mater.* **2013**, *25*, 4044-4052.

[36] Schmiechen, S.; Nietschke, F.; Schnick, W. Structural Relationship between the Mg-Containing Nitridosilicates $Ca_2Mg[Li_4Si_2N_6]$ and $Li_2Ca_2[Mg_2Si_2N_6]$. *Eur. J. Inorg. Chem.* **2015**, 1592-1597.

[37] Marchuk, A.; Schnick, W. $Ba_3P_5N_{10}Br$:Eu^{2+}: A Natural-White-Light Single Emitter with a Zeolite Structure Type. *Angew. Chem. Int. Ed.* **2015**, *54*, 2383-2387.

[38] Pucher, F. J.; Marchuk, A.; Schmidt, P. J.; Wiechert, D.; Schnick, W. Luminescent Nitridophosphates CaP_2N_4:Eu^{2+}, SrP_2N_4:Eu^{2+}, BaP_2N_4:Eu^{2+}, and $BaSr_2P_6N_{12}$:Eu^{2+}. *Chem. Eur. J.* **2015**, *21*, 6443-6448.

[39] Poesl, C.; Niklaus, R.; Schnick, W. The Crystal Structure of Nitridomagnesogermanate $Ba[Mg_3GeN_4]$:Eu^{2+} and Theoretical Calculations of Its Electronic Properties. *Eur. J. Inorg. Chem.* **2017**, *2017*, 2422-2427.

[40] Poesl, C.; Schnick, W. Crystal Structure and Nontypical Deep-Red Luminescence of $Ca_3Mg[Li_2Si_2N_6]:Eu^{2+}$. *Chem. Mater.* **2017**, *29*, 3778-3784.

[41] Bragg, W. L.; West, J. The Structure of Beryl, $Be_3Al_2Si_6O_{18}$. *Proc. R. Soc. London, Ser. A* **1926**, *111*, 691-714.

[42] Zachariasen, W. Über die Kristallstruktur von BeO. *Norsk. Geol. Tidssk* **1925**, *8*, 189-200.

[43] Duman, S.; Sütlü, A.; Bağcı, S.; Tütüncü, H. M.; Srivastava, G. P. Structural, elastic, electronic, and phonon properties of zinc-blende and wurtzite BeO. *J. Appl. Phys.* **2009**, *105*, 033719.

[44] Stackelberg, M. v.; Paulus, R. Untersuchungen über die Kristallstruktur der Nitride und Phosphide zweiwertiger Metalle. *Z. Phys. Chem.* **1933**, *22B*, 305-322.

[45] Eckerlin, P.; Rabenau, A. Zur Kenntnis des Systems Be_3N_2-Si_3N_4. Die Struktur einer neuen Modifikation von Be_3N_2. *Z. Anorg. Allg. Chem.* **1960**, *304*, 218-229.

[46] Hall, D.; Gurr, G. E.; Jeffrey, G. A. Zur Kenntnis des Systems Be_3N-Si_3N_4. V. A Refinement of the Crystal Structure of *β*-Beryllium Nitride. *Z. Anorg. Allg. Chem.* **1969**, *369*, 108-112.

[47] Bragg, W. L.; Brown, G. B. The Crystalline Structure of Chrysoberyl. *Proc. R. Soc. London, Ser. A* **1926**, *110*, 34-63.

[48] Farrell, E. F.; Fang, J. H.; Newnham, R. E. Refinement of the chrysoberyl structure. *The American Mineralogist* **1963**, *48*, 804-810.

[49] Harris, L. A.; Yakel, H. L. The crystal structure of calcium beryllate, $Ca_{12}Be_{17}O_{29}$. *Acta Crystallogr.* **1966**, *20*, 295-301.

[50] Harris, L. A.; Yakel, H. L. The crystal structure of $SrBe_3O_4$. *Acta Crystallogr. Sect. B* **1969**, *25*, 1647-1651.

[51] Leoni, S.; Niewa, R.; Akselrud, L.; Prots, Y.; Schnelle, W.; Göksuc, T.; Cetinkol, M.; Somer, M.; Kniep, R. Novel Barium Beryllates $Ba[Be_2N_2]$ and $Ba_3[Be_5O_8]$: Syntheses, Crystal Structures and Bonding Properties. *Z. Anorg. Allg. Chem.* **2005**, *631*, 1818-1824.

[52] Eckerlin, P. Zur Kenntnis des Systems Be_3N_2-Si_3N_4, IV. Die Kristallstruktur von $BeSiN_2$. *Z. Anorg. Allg. Chem.* **1967**, *353*, 225-235.

[53] Somer, M.; Carrillo-Cabrera, W.; Peters, E.-M.; Peters, K.; von Schnering, H. G. Crystal structure of lithium beryllium nitride, LiBeN. *Z. Kristallogr.* **1996**, *211*, 635.

[54] Somer, M.; Yarasik, A.; Akselrud, L.; Leoni, S.; Rosner, H.; Schnelle, W.; Kniep, R. $Ae[Be_2N_2]$: Nitridoberyllates of the Heavier Alkaline-Earth Metals. *Angew. Chem. Int. Ed.* **2004**, *43*, 1088-1092.

[55] Pucher, F. J.; Römer, S. R.; Karau, F. W.; Schnick, W. Phenakite-Type BeP_2N_4 – A Possible Precursor for a New Hard Spinel-Type Material. *Chem. Eur. J.* **2010**, *16*, 7208-7214.

2 Nitrido(alumo,litho,magneso)silicates – Host Lattices for Narrow-band Emitting Phosphors

2.1 Narrow-Band Green Emitting Nitridolithoalumosilicate $Ba[Li_2(Al_2Si_2)N_6]:Eu^{2+}$ with Framework Topology whj for LED/LCD-Backlighting Applications

published in: *Chem. Mater.* **2015**, *27*, 6109-6115
authors: Philipp Strobel, Sebastian Schmiechen, Markus Siegert, Andreas Tücks, Peter J. Schmidt and Wolfgang Schnick
DOI: 10.1021/acs.chemmater.5b02702

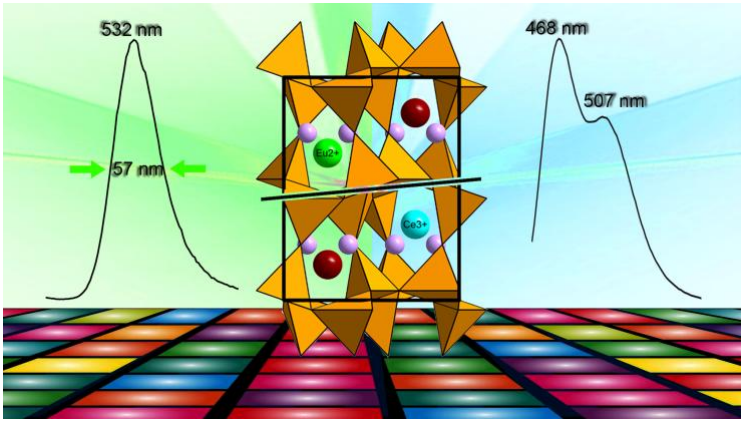

Abstract. Eu^{2+}- as well as Ce^{3+}-doped $Ba[Li_2(Al_2Si_2)N_6]$ and its related Mg-substituted compounds $Ba[(Mg_{2-x}Li_x)(Al_{4-x}Si_x)N_6]:Eu^{2+}$ (x = 0–2) with x = 1.6, 1.8 have been synthesized by metathesis reactions in tantalum ampules. Crystal structures were solved and refined from single-crystal X-ray diffraction data. All three compounds crystallize in tetragonal space group *P*4/*ncc* (no. 130) (Z = 4, $Ba[Li_2(Al_2Si_2)N_6]:Eu^{2+}$: a = 7.8282(4), c = 9.9557(5) Å, $R1$ =0.0144, $wR2$ = 0.0366). Their crystal structures, exhibiting the novel framework topology **whj**, consist of a highly condensed anionic tetrahedra network of disordered $(Li/Mg)N_4$ and $(Al/Si)N_4$ units connected to each other by common edges and corners. The degree of condensation (i.e., atomic ratio (Al,Li,Mg,Si):N) is κ = 1. The Ba^{2+}-position is coordinated eight-fold by N^{3-} in form of a truncated square pyramid. Upon doping with Eu^{2+}, narrow-band emission in the green to yellow spectral range is observed (λ_{em} = 532–562 nm, *fwhm* ≈ 1962 cm^{-1}). Ce^{3+}-doped crystals of $Ba[Li_2(Al_2Si_2)N_6]$ show blue emission (λ_{em} = 468; 507 nm). According to the tunability of the narrow-band green emission, application in LED-backlight liquid crystal displays appears promising.

2.1.1 Introduction

The quest for even thinner and lighter modern high-contrast LCDs (liquid crystal displays) with applications in televisions and portable devices demands replacement of common cold cathode fluorescent lamps (CCFLs) with solid-state LEDs (light-emitting diodes).[1,2] Highly efficient phosphor converted (pc-)LEDs combine very desirable properties such as fast switching time and dimming as well as no turn-on delay. They allow construction of flat displays and are environmentally friendly, showing low energy consumption.[3]

Pc-LEDs currently used in LCDs consist of highly efficient blue-emitting (In,Ga)N-LEDs and the yellow emitting phosphor $Y_{3-x}Gd_xAl_{5-y}Ga_yO_{12}:Ce^{3+}$ (YAG:Ce). To improve emission quality, red and green luminophors are discussed to replace this broad-band yellow phosphor.[4] Exploiting narrow-band emitting luminescent materials reduces LED emission that needs to be excluded by filters. To achieve a brilliant image with high color saturation, narrow-band emission especially in the green spectral region is mandatory.[5] This leads to a huge demand for innovative narrow-band green and red emitting luminescent materials. Recently, we have reported on next generation Eu^{2+}-doped narrow-band red-emitting phosphors, the nitridolithoaluminate $Sr[LiAl_3N_4]:Eu^{2+}$ (SLA) and the nitridomagnesosilicate $Sr[Mg_3SiN_4]:Eu^{2+}$ (SMS). SLA shows narrow-band emission at 650 nm with *fwhm* (full width at half-maximum) of ~1180 cm^{-1} (~50 nm); SMS exhibits even narrower emission with *fwhm* of only 1170 cm^{-1} (~43 nm, λ_{em} = 615 nm).[6-8] Examples for green Eu^{2+} phosphors are $(Ba,Sr)_2SiO_4:Eu^{2+}$ and the oxonitridosilicate $SrSi_2O_2N_2:Eu^{2+}$. The latter exhibits an emission maximum of 535 nm with *fwhm* ~2600 cm^{-1}.[9,10] β-SiAlON:Eu^{2+} is currently the most promising green phosphor for backlighting applications in high-gamut displays. It shows emission at 528–550 nm (*fwhm* ~1760 cm^{-1}). However, its external quantum efficiency is limited (EQE < 70%) due to relatively low absorption in the blue spectral region compared to other phosphors (e.g., $(Ba,Sr)_2SiO_4:Eu^{2+}$ EQE ≈ 80%).[11,12] Yet, there is a lack of Eu^{2+}-doped nitrides with sufficient green emission peaking at 530–535 nm with *fwhm* ~50 nm and high EQE > 80%. To improve color saturation, the discovery of green phosphors that meet the requirements mentioned is of high relevance.

In this contribution, we describe syntheses and characterization of the nitridolitho(magneso)alumosilicates $Ba[(Mg_{2-x}Li_x)(Al_{4-x}Si_x)N_6]$ (x = 0–2) with x = 1.6, 1.8, and 2.0. The respective Eu^{2+}-doped materials show promising luminescence properties in the green to yellow region of the visible spectrum under blue light irradiation, which makes them promising candidates for implementation in white pc-LEDs for LCD backlighting applications.[11]

2.1.2 Experimental Section

2.1.2.1 Synthesis

All experiments were carried out in argon-filled glove boxes (Unilab, MBraun, Garching, O_2 <1 ppm, H_2O <1 ppm) and in dried Schlenk-type glassware connected to a vacuum line (10^{-3} mbar). Argon (5.0, Air Liquide) was cleaned by streaming through columns filled with silica gel (Merck), molecular sieve (Fluka, 4 Å), KOH (Merck, ≥85%), P_4O_{10} (Roth, ≥99%), and titanium sponge (Johnsen Matthey, 99.5%, at 700 °C). The synthesis of single crystals was achieved by solid-state metathesis in sealed tantalum ampules. Eu^{2+}-doped $Ba[Li_2(Al_2Si_2)N_6]$ ([**1**]) was synthesized using BaF_2 (0.10 mmol, 17.5 mg; Sigma-Aldrich, 99.99%), AlF_3 (0.20 mmol, 16.8 mg; Sigma-Aldrich, 99.99%), "$Si(NH)_2$" (0.20 mmol, 11.6 mg; synthesized according to the method by Lange et al.),[13] and LiN_3 (0.20 mmol, 9.8 mg; synthesized according to the method by Fair et al.).[14] For the synthesis of $Ba[(Mg_{0.2}Li_{1.8})(Al_{2.2}Si_{1.8})N_6]:Eu^{2+}$ ([**2**]) and $Ba[(Mg_{0.4}Li_{1.6})(Al_{2.4}Si_{1.6})N_6]:Eu^{2+}$ ([**3**]), the precursors "$Ba_3Mg_3N_2F_6$" (0.08 mmol, 50.1 mg, synthesized by reaction of three equivalents of BaF_2 (Sigma-Aldrich, 99.99%) and one equivalent of Mg_3N_2 (Sigma-Aldrich, 99.5%) at 950 °C for 12 h), "$Si(NH)_2$" (0.16 mmol, 9.6 mg), AlF_3 (0.08 mmol, 6.7 mg; Sigma-Aldrich, 99.99%), and LiN_3 (0.16 mmol, 7.8 mg) were selected as starting materials. For Eu^{2+}-doping, EuF_3 (1–2 mol %) (Sigma-Aldrich, 99.99%) was employed. The reactants were ground in an agate mortar and filled into the reaction vessel. Li pieces (1.00 mmol, 6.9 mg; Alfa Aesar, 99.9%) were added as fluxing agent. The Ta-crucible was welded shut by the TIG (Tungsten Inert Gas Welding) method.[15] The ampule was water-cooled during welding to avoid uncontrolled reaction of the reactants. The vessel was placed in a silica tube and heated in a tube furnace after evacuation. The following temperature program was carried out: heating to 950 °C within 3 h, maintaining temperature for 24 h, and cooling to 500 °C in 60 h. The crucible was finally cooled down to room temperature.

2.1.2.2 X-ray Spectroscopy

Eu^{2+}-doped samples of [**1**–**3**] were investigated by energy-dispersive X-ray spectroscopy (EDX) to identify the chemical composition. With a JSM-6500 scanning electron microscope (SEM, JEOL), containing a Si/Li EDX detector (Oxford Instruments, model 7418), a number of crystallites and bulk samples were probed.

2.1.2.3 Single-Crystal Diffraction

Eu^{2+}-doped crystals of [**1**–**3**] were selected and sealed in glass capillaries. The crystal quality was examined on a Buerger precession camera. X-ray diffraction data were collected on a Bruker D8 Quest diffractometer with microfocus and a Bruker D8 Venture diffractometer with rotating anode, respectively. Both devices operate with graphite monochromator and Mo–Kα radiation (λ = 0.071073 Å). An absorption correction was executed with SADABS,[16] and the crystal structures were solved by Direct Methods (SHELXS)[17] and refined by full-matrix least-squares methods

(SHELXL).[18,19] Eu^{2+} was disregarded for structure determination. Because of its low content, the contribution to the scattering density is insignificant. The (Al,Si) network was further investigated with TOPOS, which is a program package for topological analysis of crystal structures.[20]

Further details of the crystal structure investigations may be obtained from the Fachinformationszentrum Karlsruhe, 76344 Eggenstein-Leopoldshafen, Germany (Fax, (+49)7247–808–666; e-mail, crysdata@fiz-karlsruhe.de) upon quoting the depository numbers CSD-429872 ($Ba[Li_2(Al_2Si_2)N_6]$), CSD-429873 ($Ba[(Mg_{0.2}Li_{1.8})(Al_{2.2}Si_{1.8})N_6]$, and CSD-429874 ($Ba[(Mg_{0.4}Li_{1.6})(Al_{2.4}Si_{1.6})N_6]$).

2.1.2.4 Powder X-ray Diffraction

The structural model obtained from single-crystal data was verified from powder X-ray data with the TOPAS Academic 4.1 package.[21] A sample of Eu^{2+}-doped [**1**] was measured in a sealed capillary on a STOE STADI P diffractometer (Cu–$K\alpha_1$ radiation, Ge(111) monochromator, Mythen1K detector) in Debye–Scherrer geometry. Refinement was carried out with the Rietveld method by applying the fundamental parameters approach (direct convolution of source emission profiles, axial instrument contributions, crystallite size, and microstrain effects). Capillary absorption correction (inner diameter 0.08 mm) was carried out using the calculated absorption coefficient.[22,23]

2.1.2.5 H_2O-Sorption

Water vapor sorption measurements on [**1**] were performed with a Quantachrome Intrument Autosorb IQ with vapor option at 288 K. Water in Millipore quality was degassed for 5 min *in vacuo* before use. The temperature was controlled by a thermostat using water as coolant.

2.1.2.6 UV/vis Spectroscopy

A reflectance spectrum of Eu^{2+}-doped [**1**] was recorded on an Edinburgh Photonics FLS920-s spectrometer using a Xe900 450 W arclamp (single photon-photomultiplier detector, Czerny-Turner monochromator with triple grating turret). The spectrum was obtained between 230 and 780 nm with 5 nm step size. A reflectance spectrum of $BaSO_4$ was used as reference to calculate the sample absorption from the difference in the reflectance of sample and reference. The QE is given as the quotient of sample emission and absorption. The band gap of Eu^{2+}-doped [**1**] was derived from UV/vis-reflectance data by drawing two line tangents to the slope of the reflectance curve. The point of intersection of the tangents is the value of the band gap.

2.1.2.7 Luminescence

Eu^{2+}-doped samples of [**1**–**3**] as well as Ce^{3+}-doped [**1**] were investigated. A HORIBA Fluoromax4 spectrofluorimeter system, attached via optical fibers to an Olympus BX51 microscope, was used. The samples were measured inside glass capillaries. The spectral width of the excitation wavelength at 420 or 450 nm, respectively, was 10 nm. Emission spectra were captured with 2 nm step size in a wavelength range between 450 and 800 nm. Excitation spectra were obtained with a monitoring

wavelength of 480 nm ([**1**]:Ce^{3+}), 540 nm ([**1**]:Eu^{2+}), or 550 nm ([**2**]:Eu^{2+}, [**3**]:Eu^{2+}). The thermal quenching performance of [**1**]:Eu^{2+} was investigated with an AvaSpec-2048 Spectrometer. For excitation, a LED light source (450 nm) was used. Samples were measured in a temperature range from RT–330 °C with a step size of ~24 °C, heated with an IR lamp.

2.1.3 Results and Discussion

2.1.3.1 Synthesis and Chemical Analysis

Greenish crystallites of [**1**]:Eu^{2+} with strong green luminescence under blue irradiation were obtained. By adding Mg to the reaction mixture, green to yellowish crystallites of [**2**]:Eu^{2+} and yellowish crystallites of [**3**]:Eu^{2+} were synthesized. A Ce^{3+}-doped sample of [**1**] showed blue emission. Crystallites of each compound were isolated and investigated by single-crystal X-ray diffraction. Elemental analysis on single crystals using EDX spectroscopy gave an atomic ratio Ba:Al:Si:N of 1:2:2.2:7.9 for [**1**], a ratio Ba:Mg:Al:Si:N of 1:0.2:2.3:2.1:11 for [**2**], and of 1:0.3:2:1.8:7.9 for [**3**]. No further elements were detected.

2.1.3.2 Crystal Structure Determination

Crystallites of [**1**–**3**] were investigated by single-crystal X-ray diffraction. All three compounds crystallize in tetragonal space group *P*4/*ncc* (no. 130). Details of the structure solution and refinement are given in Table 1. Atomic coordinates and isotropic displacement parameters for [**1**] are shown in Table 2. Atomic coordinates and isotropic displacement parameters for [**2**] and [**3**] as well as anisotropic displacement parameters and selected bond lengths for all three compounds are listed in the Supporting Information (Tables S1–S3). Figure S1 illustrates the anisotropic refinement of each crystallographic atom position.

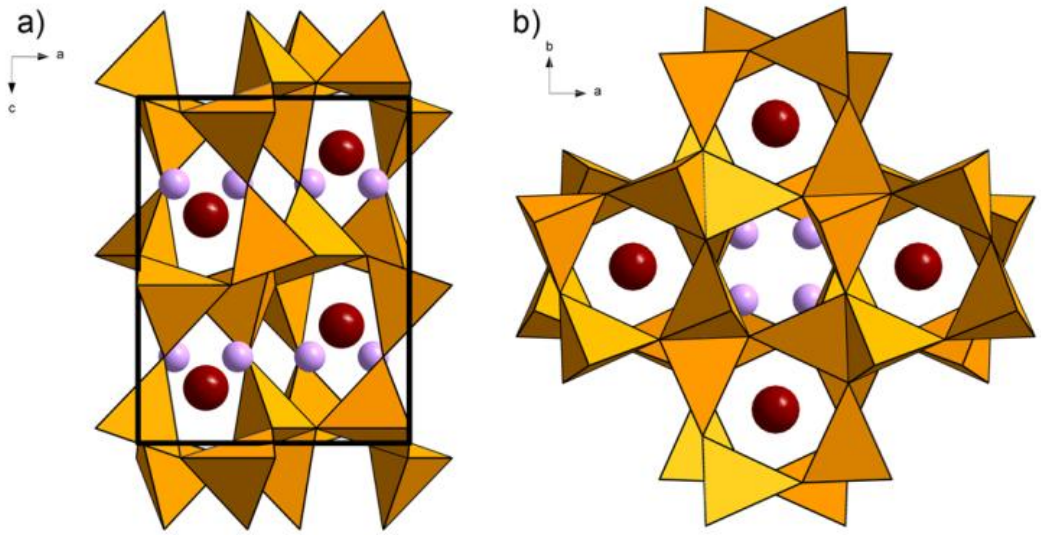

Figure 1. Crystal structure of $Ba[Li_2(Al_2Si_2)N_6]$, $(Al,Si)N_4$-tetrahedra (orange), Li (violet), Ba (red); (a) viewing direction [010]; (b) viewing direction [001].

2.1.3.3 Crystal Structure Description

As a member of the solid-solution series $Ba[(Mg_{2-x}Li_x)(Al_{4-x}Si_x)N_6]$ (x = 0–2), the structure of the end member $Ba[Li_2(Al_2Si_2)N_6]$ is described representatively. The crystal structure is built up from corner- and edge-sharing $(Al,Si)N_4$-tetrahedra with a statistical distribution of Al^{3+} and Si^{4+}. The tetrahedra form two *vierer* ring layers, which are opposed to each other in [100] direction and are connected by common corners (Figure 1).[24,25] Two types of *vierer* ring channels are built running along [001]. Smaller *vierer* ring channels of $(Al,Si)N_4$ tetrahedra are connected to each other by common corners in an up–down sequence. Larger *vierer* ring channels consist of equally aligned $(Al,Si)N_4$ tetrahedra. (Al,Si)-N bond lengths range from 1.75(6)–1.83(2) Å at an average of 1.79 Å. The averaged sum of the ionic radii according to Baur is found to be 1.82 Å.[26] Further nitridoalumosilicates with a mixed occupation of TN_4 tetrahedra (T = Al,Si) show comparable bond lengths T–N of 1.81 Å ($CaAlSiN_3$).[27,28] For $Ba_2AlSi_5N_9$, a value of 1.80 Å was found.[29]

TOPOS analysis of the (Al,Si) network revealed the first representative of an only theoretically calculated tetragonal Fischer-Koch sphere packing (symbol: **whj**) that has not been observed yet.[30] In this framework, the tetrahedral centers of the network build tetrahedra on their own (Figure 2).

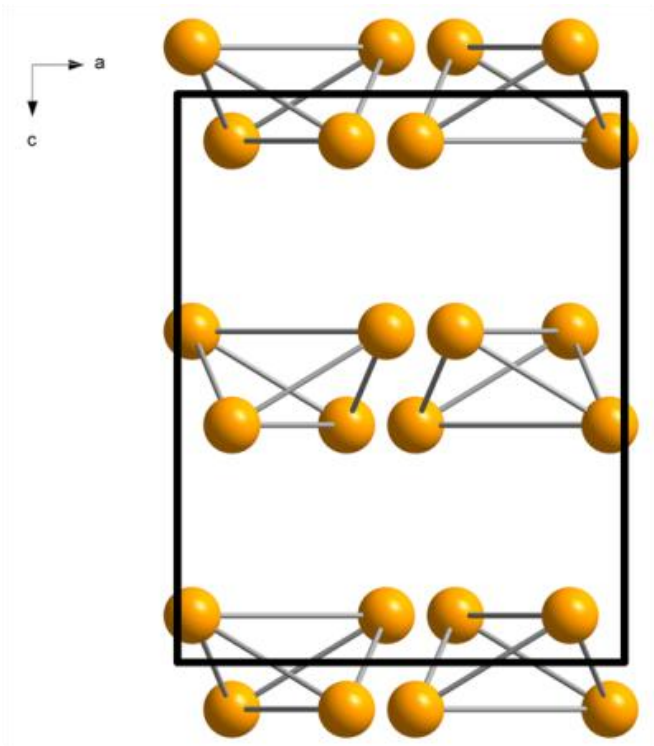

Figure 2. Network typology **whj**, built of $(Al,Si)N_4$-tetrahedra (tetrahedra centers orange), viewing direction [010].

The smaller *vierer* ring channels are centered by LiN_4-tetrahedra. It was found that Li can partially be substituted by Mg, while because of electroneutrality, the Al-content is increased, and Si-content is decreased. Since the Li-position is also in a tetrahedral coordination, it can be considered being part of the network. Resulting [**1**] can thus be classified as a nitridolithoalumosilicate.[6] The degree of

condensation (i.e., atomic ratio (Si,Al,Li,Mg):N) of this network is found to be $\kappa = 1$. This high value is comparable to recently reported nitridoaluminates and -silicates crystallizing in the UCr_4C_4-structure-type and their variants. The LiN_4 tetrahedra are linked to each other by common edges forming bow-tie units of Li_2N_6, which have not been observed as yet in nitridosilicates. These units are connected to form a tetragonal Li_4N_{12}-bisphenoid inside the smaller *vierer* ring channels (Figure 3).

The bond lengths Li–N are in a range of 2.14(4)–2.30(2) Å and slightly extended compared to the averaged sum of the ionic radii (2.08 Å).[26] In general, the Li bond lengths are in the same range as found for other Li-containing nitridosilicates.[6,31-35] Because of the edge-sharing of the bow-tie units, the corresponding Li–Li distances are comparatively short (2.59(1) Å). A similar observation was reported for Si_2N_6 bow-tie units.[31-33,36] The larger *vierer* ring channels are exclusively centered by Ba^{2+}, which is eight-fold coordinated by N^{3-}. A truncated square pyramid results as coordination polyhedron, where base and deck areas are rotated by ~5°. The polyhedra are staggered along [001] and connected to each other by common corners in [100] direction. Every second truncated square pyramid is rotated by 40° against its neighbor pyramid to fit between the layers of opposed $(Al,Si)N_4$-tetrahedra. The Ba–N bond lengths are in an order of 2.93(2)–3.10(9) Å. The medium range matches well with the sum of the ionic radii of 3.05 Å.[26] $Ba[Mg_3SiN_4]$ and $Ba_2AlSi_5N_9$, also containing Ba^{2+} in eight-fold coordination by N^{3-}, show Ba–N bond lengths comparable to this nitridolithoalumosilicate.[37] Increasing Mg-content in the solid-solution series $Ba[(Mg_{2-x}Li_x)(Al_{4-x}Si_x)N_6]$ (x = 0–2) causes increasing lattice parameters.

However, nitridosilicates with a mixed occupation of tetrahedrally coordinated Li^+ and Mg^{2+} have not been reported in the literature. Accordingly, bond lengths in the Mg-containing compounds are compared with bonds in $(Li_{0.51}Mg_{2.49})N_{1.83}$. $(Li_{0.51}Mg_{2.49})N_{1.83}$ has (Li,Mg)–N bond lengths ranging from 2.04–2.27 Å[38] that fit well with the observed distances found in [**3**] (2.18(3) Å and 2.27(2) Å). Selected bond lenghts are displayed in Table S3.

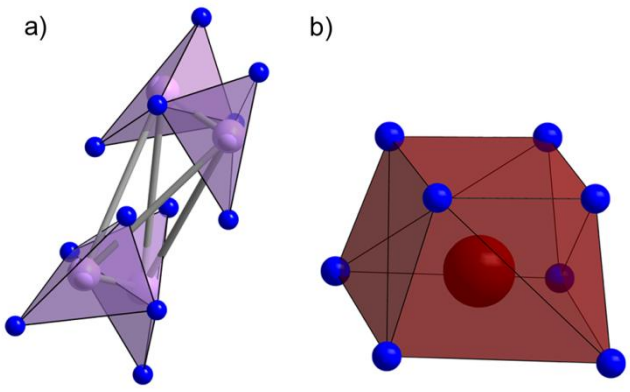

Figure 3. (a) Bisphenoidal arranged tetrahedra of Li_2N_6-units; (b) truncated square pyramid of BaN_8.

Table 1. Crystallographic data of $Ba[Li_2(Al_2Si_2)N_6]$, $Ba[(Mg_{0.2}Li_{1.8})(Al_{2.2}Si_{1.8})N_6]$, and $Ba[(Mg_{0.4}Li_{1.6})(Al_{2.4}Si_{1.6})N_6]$[a]

	$Ba[Li_2(Al_2Si_2)N_6]$ ([1])	**$Ba[(Mg_{0.2}Li_{1.8})(Al_{2.2}Si_{1.8})N_6]$ ([2])**	**$Ba[(Mg_{0.4}Li_{1.6})(Al_{2.4}Si_{1.6})N_6]$ ([3])**
formula mass [g mol^{-1}]	345.42	348.67	351.93
cryst syst		tetragonal	
space group		*P*4/*ncc* (no. 130)	
cell params [Å]	a = 7.8282(4)	a = 7.8785(3)	a = 7.8921(3)
	c = 9.9557(5)	c = 9.9833(4)	c = 9.9948(4)
vol [Å^3]	610.09(7)	619.67(4)	622.53(4)
formula units/cell		4	
X-ray density [g cm^{-3}]	3.761	3.737	3.755
abs coeff [μ/mm^{-1}]	7.114	7.014	6.993
F(000)	632	638	645
cryst dimensions [mm^3]	0.050 × 0.040 × 0.020	0.137 × 0.081 × 0.051	0.205 × 0.147 × 0.115
diffractometer	Bruker D8 Quest	Bruker D8 Venture	
radiation		Mo–Kα (λ = 0.71073 Å)	
temp [K]	297	293(2)	293(2)
abs correction		Multi-scan	
Θ range [°]	3.68–27.48	3.66–27.95	3.65–27.97
measured reflns	7512	11696	11776
independent reflns	357 [$R_{(int)}$ = 0.0424]	382 [$R_{(int)}$ = 0.0262]	384 [$R_{(int)}$ = 0.0259]
observed reflns	333	366	381
min./max. transmission	0.2825/0.7461	0.5169/0.8210	0.5505/0.7492
refined params	32	32	33
GOF	1.091	1.057	1.070
R indices ($F_o^2 \geq 2\sigma(F_o^2)$)	R1 = 0.0126, wR2 = 0.0363	R1 = 0.0181, wR2 = 0.0488	R1 = 0.0169, wR2 = 0.0456
R indices (all data)	R1 = 0.0144, wR2 = 0.0366	R1 = 0.0186, wR2 = 0.0494	R1 = 0.0170, wR2 = 0.0456
min./max. residual electron density [eÅ^{-3}]	–0.28/0.53	–1.20/0.55	–0.49/0.71

[a] The e.s.d. values are in parentheses

2.1.3.4 Powder X-ray Diffraction

A bulk sample was further investigated by powder X-ray diffraction. Rietveld refinement on this data strongly support the structural model obtained by single-crystal analysis; details are shown in Figure 4.

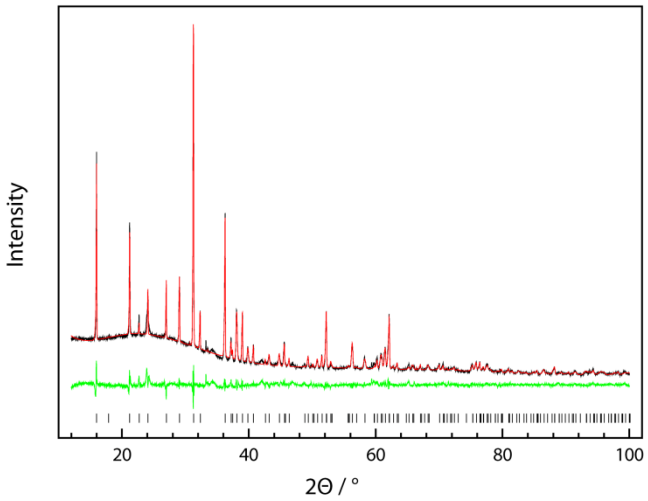

Figure 4. Rietveld refinement of the structural model of $Ba[Li_2(Al_2Si_2)N_6]:Eu^{2+}$ (Cu-Kα_1 radiation). Experimental data (black line), calculated pattern (red line), and difference curve (green line); tickmarks: black, positions of Bragg reflections of $Ba[Li_2(Al_2Si_2)N_6]$ (unidentified reflections marked with an asterisk).

Table 2. Atomic Coordinates and Isotropic Displacement Parameters of $Ba[Li_2(Al_2Si_2)N_6]$[a]

atom (Wyck.)	*x*	*y*	*z*	U_{eq} (Å^3)	*sof*
Ba (4*c*)	1/4	1/4	0.34015(2)	0.0136(11)	1
Li (8*f*)	0.3670(5)	0.6330(5)	1/4	0.0134(10)	1
Al (16*g*)	0.1218(8)	0.5329(8)	0.0825(5)	0.0053(8)	0.5
Si (16*g*)	0.1218(8)	0.5329(8)	0.0825(5)	0.0053(8)	0.5
N1 (8*f*)	0.5056(3)	0.1569(2)	0.0429(17)	0.0107(4)	1
N2 (16*g*)	0.5963(2)	0.4037(2)	1/4	0.0123(5)	1

[a] The e.s.d. values are in parentheses.

2.1.3.5 H_2O-Sorption

H_2O-sorption experiments on [**1**] and application of the Brunauer–Emmett–Teller (BET) theory show no absorption of water by the compound (Figure S2). Water molecules are adsorbed at higher relative pressure between single particles on their surface. The process of absorption is almost completely reversible; just 1 wt % of water is bound irreversible when the relative H_2O-pressure is lowered at ambient temperature. These experiments demonstrate that the novel nitridolithoalumosilicate is stable against hydrolysis.

2.1.3.6 UV/vis Spectroscopy

A Eu^{2+}-doped sample of [**1**] was further investigated by UV/vis reflectance spectroscopy to determine the band gap. The reflectance spectrum of Eu^{2+}-doped [**1**] (Figure 5) shows a broad absorption band around 280 nm with an estimated band gap of ~4.6 eV, and therefore the excited 5*d*-

state of Eu^{2+} should have a large distance to the conduction band edge to allow high quantum efficiency.[39] A large absorption band is detected in the blue to yellow region of the visible spectrum. This band is attributed to the $4f^7$ to $4f^{7-N}5d^N$ absorptions in Eu^{2+}. First measurements for morphologically nonoptimized samples of the title compound as well as the Mg-containing ones shows a proficient QE of ~70%, comparable to that of β-SiAlON:Eu.[11]

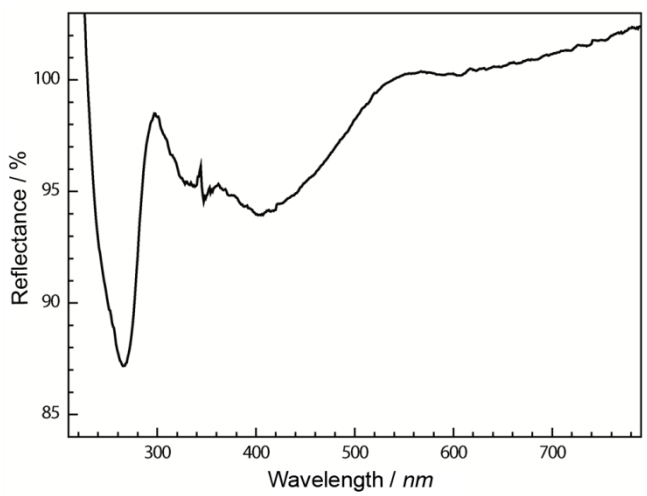

Figure 5. UV/vis reflection spectrum of Eu^{2+}-doped $Ba[Li_2(Al_2Si_2)N_6]$ (1 mol % Eu^{2+}, nominal composition); the artifact around 340 nm corresponds to the lamp switch.

2.1.3.7 Luminescence

Compounds [**1–3**] only differ slightly in chemical composition of the tetrahedral centers, while luminescence properties of their respective Eu^{2+}-doped compounds are strikingly different. It is assumed that the dopants Eu^{2+} and Ce^{3+} occupy the eight-fold coordinated atom position of Ba^{2+}.

In Figure 6, panel a, excitation and emission spectra of [**1**]:Eu^{2+} are depicted. The excitation spectrum ($\lambda_{monitor}$ = 540 nm) shows absorption in the blue spectral range of the visible spectrum with a maximum at 395 nm and a strong decrease toward longer wavelengths. Therefore, the nitridolithoalumosilicate is effectively excitable with UV to blue light as provided, for example, by (In,Ga)N-LEDs. Excited in this spectral region, [**1**]:Eu^{2+} shows luminescence in the green spectral range at 532 nm with *fwhm* = 1962 cm^{-1} (~57 nm, nominal Eu-content 1%). The color coordinates (CIE) are x = 0.30 and y = 0.64. Furthermore, the sample shows a relatively low thermal quenching at 200 °C with a relative emission intensity of ~70% (Figure S3).

With the introduction of Mg into the solid-solution series, excitation and emission maxima are shifted toward longer wavelengths: the excitation spectra of Eu^{2+}-doped [**2**] and [**3**] show broad absorption bands ranging from 400–500 nm (Figure S4). Although the visible luminescences of the characterized Mg-containing compounds differ in color, green (x = 1.8) versus yellow (x = 1.6), the emission spectra match with only a small difference of the maxima. The emission spectrum (λ_{exc} = 400 nm) of the compound with lower Mg-content, [**2**]:Eu^{2+}, shows typical Eu^{2+}-broad-band emission in the green spectral range. It is centered at 560 nm with *fwhm* of ~2654 cm^{-1} (nominal Eu-content ~3%). The emission maximum of the sample with x = 1.6 is shifted to 562 nm (λ_{exc} = 400 nm, *fwhm*

~2739 cm^{-1}). As the maximum emission of [**3**] is slightly shifted to the less energetic spectral range, crystals with yellow body color and luminescence are obtained. To summarize, decreasing Mg- and Al-content shifts the emission toward shorter wavelengths. This effect is potentially influenced by the lower inductive effect of Al^{3+} in comparison with Si^{4+}. Therefore, a higher Al ratio is accompanied by a less distinct nephelauxetic effect.

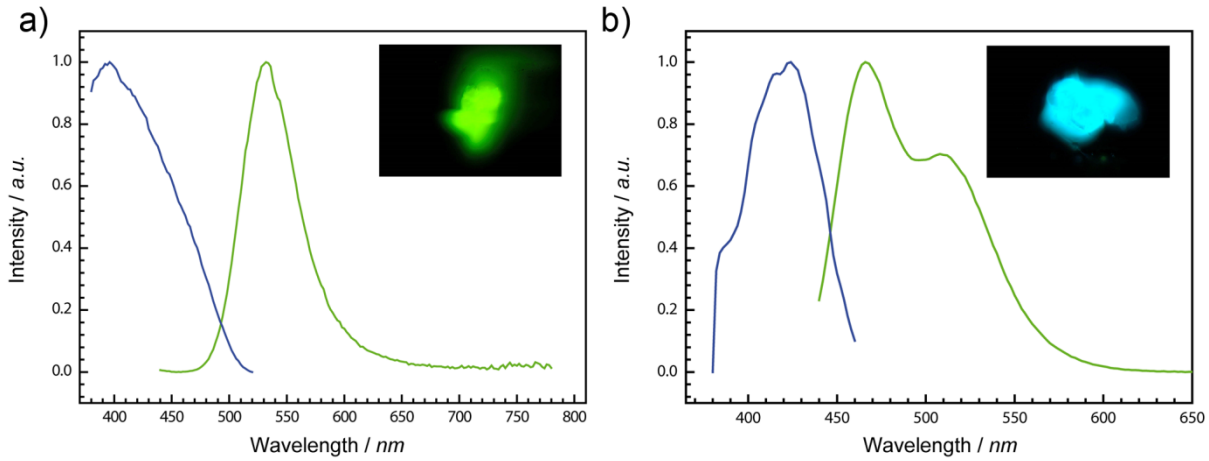

Figure 6. Luminescence characteristics of (a) Eu^{2+}-doped and (b) Ce^{3+}-doped $Ba[Li_2(Al_2Si_2)N_6]$; excitation (blue line) and emission (green line) spectra.

On the opposite, the emission maximum of the characterized compounds is shifted to longer wavelengths toward yellow emission by an increasing Eu-content. There are numerous findings on green-emitting Eu^{2+}-doped (oxo)nitride phosphors (see Introduction). In contrast, there are only few reports on (oxo)nitridosilicate phosphors with yellow emission of the respective Eu^{2+}-doped compounds. One example is $Sr_{0.5}Ba_{0.5}Si_2O_2N_2:Eu^{2+}$ that shows an emission band centered at 565 nm with *fwhm* of ~2744 cm^{-1}.[9]

$CaSi_9Al_3ON_{15}:Eu^{2+}$ (Ca-*α*-SiAlON) is another prominent yellow-emitting compound. It shows a typical broad emission band for Eu^{2+}-doped compounds with *fwhm* of ~2890 cm^{-1}, centered at 581 nm.[29,40]

Additionally, a Ce^{3+}-doped sample of the title compound was investigated. Emission was found in the blue spectral region with two maxima at 468 and 507 nm (Figure 6b) due to the spin–orbit coupling of the ground states of Ce^{3+} ($^2F_{5/2}$ and $^2F_{7/2}$). The excitation spectrum shows a maximum at 420 nm. The blue emitting (oxo)nitridosilicate phosphors $LaSi_3N_5:Ce^{3+}$ (λ_{em} = 424; 458 nm) and $LaSiO_2N:Ce^{3+}$ (λ_{em} = 416; 456 nm) have been reported in the literature.[41,42] In contrast to $Ba[Li_2(Al_2Si_2)N_6]:Ce^{3+}$, their emission maxima are shifted to shorter wavelengths close to the UV-range.

2.1.4 Conclusion

The nitridolitho(magneso)alumosilicates [**1**–**3**] belong to the solid-solution series $Ba[(Mg_{2-x}Li_x)(Al_{4-x}Si_x)N_6]$ (x = 0–2). The new materials contain a hitherto unknown tetrahedra network built-up from $(Al,Si)N_4$-units evolving a new framework topology (symbol: **whj**). The structure shows striking parallels to the UCr_4C_4-type luminescent materials and its closely related structures of $Na[Li_3SiO_4]$ and $Cs[Na_3PbO_4]$. Some recently described nitrides with very interesting luminescence properties in the red spectral region such as $M[Mg_3SiN_4]:Eu^{2+}$ (M = Sr,Ba) and the above-mentioned $AE[LiAl_3N_4]:Eu^{2+}$ (AE = Ca,Sr) crystallize in these structure types.[6,7,37,43] Similarly with [**1**], their highly condensed tetrahedra networks contain two different types of *vierer* ring channels. In $Ba[Li_2(Al_2Si_2)N_6]$, both types of the channels are filled with atoms: Ba^{2+} occupying the larger channels and the smaller ones filled by Li^+ so that bisphenoids of Li_4N_{12} are built. In the UCr_4C_4-type related structures, only one type of channel is centered by a heavy atom, while the other one is empty. By introducing a second filled channel, the new crystal structure of $Ba[Li_2(Al_2Si_2)N_6]$ leads to an additional degree of freedom in the substitution of elements and therefore in luminescence tuning. The host lattice is suitable for various substitutional variants. Besides control of the doping level, the color of the described new phosphor materials can be adjusted by the atomic ratio Li/Mg and Al/Si. A comparable possibility of luminescence tuning including a large range of the visible spectrum is only known from narrow-band emitting QDs.[5]

Compounds of the solid-solution series still need to be synthesized with values of x <1.6 to gain luminescence in the yellow spectral region. The extraordinary tunability gives this material an edge for the usage in pc-LEDs for various applications ranging from display backlighting to illumination or signaling applications.

2.1.5 References

[1] Xie, R.-J.; Hirosaki, N.; Takeda, T. Wide Color Gamut Backlight for Liquid Crystal Displays Using Three-Band Phosphor-Converted White Light-Emitting Diodes. *Appl. Phys. Express* **2008**, *2*, 022401-022403.

[2] Schubert, E. F.; Kim, J. K. Solid-State Light Sources Getting Smart. *Science* **2005**, *308*, 1274-1278.

[3] Lu, R.; Gauza, S.; Wu, S.-T. LED-Lit LCD TVs. *Mol. Cryst. Liq. Cryst.* **2008**, *488*, 246-259.

[4] Lin, C. C.; Liu, R.-S. Advances in Phosphors for Light-emitting Diodes. *J. Phys. Chem. Lett.* **2011**, *2*, 1268-1277.

[5] Steckel, J. S.; Ho, J.; Coe-Sullivan, S. QDs Generate Light for Next-Generation Displays. *Photonic Spectra* **2014**, *9*, 55-61.

[6] Schmiechen, S.; Schneider, H.; Wagatha, P.; Hecht, C.; Schmidt, P. J.; Schnick, W. Toward New Phosphors for Application in Illumination-Grade White pc-LEDs: The Nitridomagnesosilicates $Ca[Mg_3SiN_4]:Ce^{3+}$, $Sr[Mg_3SiN_4]:Eu^{2+}$, and $Eu[Mg_3SiN_4]$. *Chem. Mater.* **2014**, *26*, 2712-2719.

[7] Pust, P.; Weiler, V.; Hecht, C.; Tücks, A.; Wochnik, A. S.; Henß, A. K.; Wiechert, D.; Scheu, C.; Schmidt, P. J.; Schnick, W. Narrow-band red-emitting $Sr[LiAl_3N_4]:Eu^{2+}$ as a next-generation LED-phosphor material. *Nat. Mater.* **2014**, *13*, 891-896.

[8] Pust, P.; Schmidt, P. J.; Schnick, W. A revolution in lighting. *Nat. Mater.* **2015**, *14*, 454-458.

[9] Seibald, M.; Rosenthal, T.; Oeckler, O.; Schnick, W. Highly Efficient pc-LED Phosphors $Sr_{1-x}Ba_xSi_2O_2N_2:Eu^{2+}$ (0<x<1) - Crystal Structures and Luminescence Properties Revisited. *Crit. Rev. Solid State Mater. Sci.* **2014**, *39*, 215-229.

[10] Zhang, M.; Wang, J.; Zhang, Q.; Ding, W.; Su, Q. Optical properties of $Ba_2SiO_4:Eu^{2+}$ phosphor for green light-emitting diode (LED). *Mater. Res. Bull.* **2007**, *42*, 33-39.

[11] Hirosaki, N.; Xie, R.-J.; Kimoto, K.; Sekiguchi, T.; Yamamoto, Y.; Suehiro, T.; Mitomo, M. Characterization and properties of green-emitting β-SiAlON:Eu^{2+} powder phosphors for white light-emitting diodes. *Appl. Phys. Lett.* **2005**, *86*, 211905.

[12] Seong, T.-Y.; Han, J.; Amano, H.; Morkoc, H., *III-Nitride Based Light Emitting Diodes and Applications*, Springer: Dordrecht, Germany, **2013**.

[13] Lange, H.; Wötting, G.; Winter, G. Silicon Nitride – From Powder Synthesis to Ceramic Materials. *Angew. Chem. Int. Ed. Engl.* **1991**, *30*, 1579-1597.

[14] Fair, H. D.; Walker, R. F., *Energetic Materials 1: Physics and Chemistry of the Inorganic Azides*, 1st ed., Plenum Press: New York, London, **1997**.

[15] Grill, A. Effect of current pulses on the temperature distribution and microstructure in TIG tantalum welds. *Metall. Trans. B* **1981**, *12*, 187-192.

[16] Sheldrick, G. M., *SADABS, v. 2: Multi-Scan Absorption Correction*, Bruker-AXS, **2012**.

[17] Sheldrick, G. M., *SHELXS-97: A program for crystal structure solution*, University of Göttingen, **1997**.

[18] Sheldrick, G. M., *SHELXL-97: A program for crystal structure refinement*, University of Göttingen, **1997**.

[19] Sheldrick, G. M. A short history of SHELX. *Acta Crystallogr. Sect. A* **2008**, *64*, 112-122.

[20] Blatov, V. A.; Shevchenko, A. P.; Proserpio, D. M. Applied Topological Analysis of Crystal Structures with the Program Package ToposPro. *Cryst. Growth Des.* **2014**, *14*, 3576-3586.

[21] Coelho, A. A., *TOPAS-Academic*, Version 4.1: A program for Rietveld refinement: Brisbane, Australia, **2007**.

[22] Bergmann, J.; Kleeberg, R.; Haase, A.; Breidenstein, B. Advanced fundamental parameter model for improved profile analysis. *Mater. Sci. Forum* **2000**, *347-349*, 303-308.

[23] Cheary, R. W.; Coelho, A. A.; Cline, J. P. Fundamental Parameters Line Profile Fitting in Laboratory Diffractometers. *J. Res. Natl. Inst. Stand. Technol.* **2004**, *109*, 1-25.

[24] Liebau, F., *Structural Chemistry of Silicates*, Springer: Berlin, **1985**.

[25] The term *vierer* ring was coined by Liebau and is derived from the german word “vierer” ; a *vierer* ring comprises four tetrahedra centers and is not a four-membered ring.

[26] Baur, W. H. Effective ionic radii in nitrides. *Crystallogr. Rev.* **1987**, *1*, 59-83.

[27] Uheda, K.; Hirosaki, N.; Yamamoto, H. Host lattice materials in the system Ca_3N_2–AlN–Si_3N_4 for white light emitting diode. *Phys. Status Solidi A* **2006**, *203*, 2712-2717.

[28] Uheda, K.; Hirosaki, N.; Yamamoto, Y.; Naita, A.; Nakajima, T.; Yamamoto, H. Luminescence Properties of a Red Phosphor, $CaAlSiN_3:Eu^{2+}$, for White Light-Emitting Diodes *Electrochem. Solid State Lett.* **2006**, *9*, H22-H25.

[29] Kechele, J. A.; Hecht, C.; Oeckler, O.; Schmedt auf der Günne, J.; Schmidt, P. J.; Schnick, W. $Ba_2AlSi_5N_9$ - A New Host Lattice for Eu^{2+}-Doped Luminescent Materials Comprising a Nitridoalumosilicate Framework with Corner- and Edge-Sharing Tetrahedra. *Chem. Mater.* **2009**, *21*, 1288-1295.

[30] Fischer, W. Tetragonal sphere packings: minimal densities and subunits. *Acta Crystallogr. Sect. A* **2005**, *61*, 435-444.

[31] Schmiechen, S.; Nietschke, F.; Schnick, W. Structural Relationship between the Mg-Containing Nitridosilicates $Ca_2Mg[Li_4Si_2N_6]$ and $Li_2Ca_2[Mg_2Si_2N_6]$. *Eur. J. Inorg. Chem.* **2015**, 1592-1597.

[32] Yamane, H.; Morito, H. $Ba_4Mg[Si_2N_6]$, $Ba_3Ca_2[Si_2N_6]$ and $Ba_{1.6}Sr_{3.4}[Si_2N_6]$ – Quaternary barium alkaline-earth silicon nitrides containing isolated nitridosilicate anions of $[Si_2N_6]^{10-}$. *J. Alloys Compd.* **2013**, *555*, 320-324.

[33] Pagano, S.; Lupart, S.; Schmiechen, S.; Schnick, W. $Li_4Ca_3Si_2N_6$ and $Li_4Sr_3Si_2N_6$ – Quaternary Lithium Nitridosilicates with Isolated $[Si_2N_6]^{10-}$ Ions. *Z. Anorg. Allg. Chem.* **2010**, *636*, 1907-1909.

[34] Lupart, S.; Schnick, W. $LiCa_3Si_2N_5$ – A Lithium Nitridosilicate with a $[Si_2N_5]^{7-}$ Double-Chain. *Z. Anorg. Allg. Chem.* **2012**, *638*, 2015-2019.

[35] Zeuner, M.; Pagano, S.; Hug, S.; Pust, P.; Schmiechen, S.; Scheu, C.; Schnick, W. $Li_2CaSi_2N_4$ and $Li_2SrSi_2N_4$ – a Synthetic Approach to Three-Dimensional Lithium Nitridosilicates. *Eur. J. Inorg. Chem.* **2010**, 4945-4951.

[36] Ottinger, F.; Nesper, R. Synthesis and Crystal Structure of the Nitridosilicates $Ca_5[Si_2N_6]$ and $Ca_7[NbSi_2N_9]$. *Z. Anorg. Allg. Chem.* **2005**, *631*, 1597-1602.

[37] Schmiechen, S.; Strobel, P.; Hecht, C.; Reith, T.; Siegert, M.; Schmidt, P. J.; Huppertz, P.; Wiechert, D.; Schnick, W. Nitridomagnesosilicate $Ba[Mg_3SiN_4]:Eu^{2+}$ and Structure–Property Relations of Similar Narrow-Band Red Nitride Phosphors. *Chem. Mater.* **2015**, *27*, 1780-1785.

[38] Yamane, H.; Okabe, T. H.; Ishiyama, O.; Waseda, Y.; Shimada, M. Ternary nitrides prepared in the Li_3N–Mg_3N_2 system at 900–1000 K. *J. Alloys Compd.* **2001**, *319*, 124-130.

[39] Zhang, Z.-J.; ten Kate, O. M.; Delsing, A.; Dorenbos, P.; Zhao, J.-T.; Hintzen, H. T. Photoluminescence properties of Pr^{3+}, Sm^{3+} and Tb^3+ doped $SrAlSi_4N_7$ and energy level locations of rare-earth ions in $SrAlSi_4N_7$. *J. Mater. Chem. C* **2014**, *2*, 7952-7959.

[40] Xie, R. J.; Hirosaki, N.; Takeda, T.; Suehiro, T. On the performance enhancement of nitride phosphors as spectral conversion materials in solid state lighting. *ECS J. Solid State Sci. Technol.* **2013**, *2*, R3031-R3040.

[41] Cai, L. Y.; Wei, X. D.; Li, H.; Liu, Q. L. Synthesis, structure and luminescence of LaSi3N5:Ce3+ phosphor. *J. Lumin.* **2009**, *129*, 165-168.

[42] Dierre, B.; Xie, R.-J.; Hirosaki, N.; Sekiguchi, T. Blue emission of Ce3+ in lanthanide silicon oxynitride phosphors. *J. Mater. Res.* **2007**, *22*, 1933-1941.

[43] Pust, P.; Wochnik, A. S.; Baumann, E.; Schmidt, P. J.; Wiechert, D.; Scheu, C.; Schnick, W. $Ca[LiAl_3N_4]:Eu^{2+}$ - A Narrow-Band Red-Emitting Nitridolithoaluminate. *Chem. Mater.* **2014**, *26*, 3544-3549.

2.2 Luminescence of the Narrow-Band Red Emitting Nitridomagnesosilicate $Li_2(Ca_{1-x}Sr_x)_2[Mg_2Si_2N_6]:Eu^{2+}$ (x = 0–0.06)

published in: *Chem. Mater.* **2017**, *29*, 1377−1383

authors: Philipp Strobel, Volker Weiler, Cora Hecht, Peter J. Schmidt and Wolfgang Schnick

DOI: 10.1021/acs.chemmater.6b05196

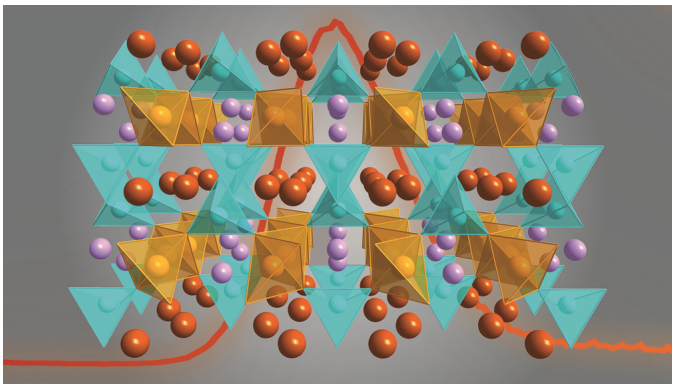

Abstract. The nitridomagnesosilicates $Li_2Ca_2[Mg_2Si_2N_6]:Eu^{2+}$ and $Li_2(Ca_{1.88}Sr_{0.12})[Mg_2Si_2N_6]:Eu^{2+}$ show narrow-band red emission at 638 and 634 nm, respectively, with an emission bandwidth of 62 nm (~1513 cm^{-1}) after excitation in the blue spectral region. Ce^{3+}-doped samples show luminescence in the green spectral range (λ_{em} = 540 nm). The compounds were synthesized via solid-state metathesis reaction in Li melts. Refinement of single-crystal X-ray diffraction data revealed that $Li_2(Ca_{1.88}Sr_{0.12})[Mg_2Si_2N_6]$ crystallizes isomorphic to $Li_2Ca_2[Mg_2Si_2N_6]$: *C*2/*m* [*Z* = 2, *a* = 5.5744(2), *b* = 9.8439(3), *c* = 6.0170(2) Å, β = 97.2520(10)°, *R*1 = 0.021, *wR*2 = 0.047]. Crystal composition was checked by EDS and ICP-OES measurements and luminescence properties are compared to state of the art narrow-band red emitting luminophores. On the basis of its narrow-band emission, application of the novel red luminophore in high CRI white pcLEDs is promising.

2.2.1 Introduction

Narrow-band red emitting phosphors play a key role in development and improvement of white light-emitting high CRI (color rendering index) pcLEDs (phosphor converted LEDs). To enhance luminous efficacy and consequently reduce energy consumption, it is important to find access to red luminophors with minimized emission in the infrared.[1-3] The great energy saving potential of narrow-band red nitride phosphors has been demonstrated with the nitridolithoaluminate $Sr[LiAl_3N_4]:Eu^{2+}$ (SLA) by Pust et al.[4] Due to its emission at 650 nm, further improvement of luminous efficacy could be achieved by a blue shift of the emission from 650 nm to ~630 nm while keeping *fwhm* (full-width at half-maximum) constant.[5]

Besides emission characteristics, luminophors need to possess a number of properties for application in pcLEDs such as chemical and thermal stability as well as optical transparency of the host materials. These requirements are met by compounds in the nitridosilicate class, e.g., $(Ba,Sr)_2Si_5N_8:Eu^{2+}$ and $(Sr,Ca)AlSiN_3:Eu^{2+}$.[6,7] However, both compounds show emission in the orange to red spectral region with *fwhm*s of approximately 90 nm and therefore, loss of energy by emission of light in the infrared.

Explorative syntheses in the system *AE*–Li/Mg–Si–N (*AE* = Ca–Ba) led to the discovery of several novel host materials for LED application.[8-10] Recently found Li- and Mg-containing nitridosilicates and -aluminates show emission with *fwhm* as narrow as 50 nm. To the best of our knowledge, $Sr[Mg_3SiN_4]:Eu^{2+}$ is currently the most narrow red emitting Eu^{2+}-doped compound exhibiting *fwhm* of 43 nm.[8] $Ba[Mg_3SiN_4]$ and SLA also show excellent emission properties when doped with Eu^{2+}.[4,11]

Developing phosphors introducing both elements, Li and Mg, at the same time provides access to novel intriguing host materials. A recently described phosphor containing both elements, Li and Mg, is the solid solution $Ba[(Mg_{2-x}Li_x)(Al_{4-x}Si_x)N_6]:Eu^{2+}$ (x = 0–2) with Li and Mg sharing the same lattice site.[9] Compounds of this materials class are promising candidates, upon doping with Eu^{2+} and Ce^{3+}, for applications that require luminophors with high luminous efficacy, e.g., in illumination grade white pcLEDs.

The results of this contribution are based on the work of Schmiechen et al., describing the nitridomagnesosilicate $Li_2Ca_2[Mg_2Si_2N_6]$.[12] In this article we report on synthesis and structural characterization of compounds in the compositional range $Li_2(Ca_{1-x}Sr_x)_2[Mg_2Si_2N_6]$ (x = 0–0.06). For the first time, optical luminescence properties of the Eu^{2+}-doped nitridomagnesosilicates $Li_2Ca_2[Mg_2Si_2N_6]$ and $Li_2(Ca_{1.88}Sr_{0.12})[Mg_2Si_2N_6]$ are investigated. Both materials show narrow-band red emission under blue light irradiation, which make them attractive for improving color rendition and efficiency of pcLEDs, especially at lower CCTs (correlated color temperature).[1]Substitution on the Ca^{2+} site with the larger Sr^{2+} and its influence on luminescence properties were investigated with the goal of tuning the emission in the red spectral region. Similar investigations proved successful in other luminophors such as green to blue emitting $(Sr,Ca,Ba)Si_2O_2N_2:Eu^{2+}$ and orange to red emitting $(Ba,Sr)_2Si_5N_8:Eu^{2+}$ and $Ca_{1-x}Sr_xAlSiN_3:Eu^{2+}$.[1,7,13] Structure property relations regarding narrow-band emission are investigated and compared to state-of-the-art narrow-band Eu^{2+} luminophors.

When doped with Ce^{3+}, emission of $Li_2Ca_2[Mg_2Si_2N_6]:Ce^{3+}$ is observed in the green to yellow spectral range, similar to the prominent garnet phosphors $YAG:Ce^{3+}$ or $LuAG:Ce^{3+}$.[14]

2.2.1.1 Synthesis

The investigated nitride compounds were synthesized via high-temperature routes in tube furnaces. Solid-state metathesis in sealed tantalum ampules was chosen for single-crystal synthesis. Either Ar-filled glove boxes (Unilab, MBraun, Garching, O_2 <1 ppm, H_2O <1 ppm) or dried Schlenk-type glassware connected to a vacuum line ($\leq 10^{-3}$ mbar) were used for weighing and sample preparation. Argon (5.0, Air Liquide) was purified by streaming through columns filled with KOH (Merck, ≥85%), silica gel (Merck), molecular sieve (Fluka, 3 Å), P_4O_{10} (Roth, ≥99%), and heated titanium sponge (Johnsen Matthey, 99.5%, T = 700 °C).

Starting materials for synthesis of $Li_2Ca_2[Mg_2Si_2N_6]:Eu^{2+}$ and $Li_2Ca_2[Mg_2Si_2N_6]:Ce^{3+}$ were CaF_2 (0.20 mmol, 15.6 mg; Sigma-Aldrich, 99.99%), Mg_3N_2 (0.20 mmol, 20.2 mg; Sigma-Aldrich, 99.5%), "$Si(NH)_2$" (0.40 mmol, 23.3 mg; synthesized according to the method by Lange et al.),[15,16] and LiN_3 (0.45 mmol, 22.0 mg; synthesized according to the method by Fair et al.).[16] For doping (1 mol %) EuF_3 (Sigma-Aldrich, 99.99%) or CeF_3 (Sigma-Aldrich, 99.99%) were added to the reaction mixture. The reactants were ground and mixed thoroughly in agate mortars and filled into Ta ampules. Li metal (1.00 mmol, 6.9 mg; Alfa Aesar, 99.9%) was added as fluxing agent. The reaction vessel was welded shut by the tungsten inert gas welding method.[9,17] The ampule was subsequently inserted into a silica glass tube, evacuated and heated in a tube furnace. The temperature was raised to 950 °C within 3 h, maintained for 24 h and cooled to 500 °C in 60 h. By turning off the furnace the crucible was finally cooled down to room temperature.[12]

Synthesis of single crystals of $Li_2(Ca_{1.88}Sr_{0.12})[Mg_2Si_2N_6]:Eu^{2+}$ was carried out similarly to $Li_2Ca_2[Mg_2Si_2N_6]:Eu^{2+}$. "$Ca_3Mg_3N_2F_6$" (a 3:1 mixture of CaF_2 (Sigma-Aldrich, 99.99%) and Mg_3N_2 (Sigma-Aldrich, 99.5%), reacted at 950 °C for 12 h, 0.10 mmol, 33.5 mg),[18] SrF_2 (0.15 mmol, 18.8 mg; Sigma-Aldrich, 99.99%), Mg_3N_2 (0.05 mmol, 5.0 mg), "$Si(NH)_2$" (0.20 mmol, 11.6 mg), and LiN_3 (0.20 mmol, 9.8 mg) were mixed in an agate mortar. EuF_3 (1 mol %) was added as dopant. Li metal (2.0 mmol, 13.9 mg, Alfa Aesar, 99.9%) was used as fluxing agent.

2.2.1.2 X-ray Spectroscopy

Chemical composition was determined by energy dispersive X-ray spectroscopy (EDS) using a JSM-6500F scanning electron microscope (SEM, JEOL) with Si/Li EDS detector (Oxford Instruments, model 7418). The EDS data were obtained from several particles at an accelerating voltage of 30 kV. The scanning electron microscope was additionally used to collect images of particles for morphology investigation.

2.2.1.3 ICP-OES

The ratio of alkali and alkaline earth metals was determined by inductively coupled plasma optical emission spectrometry (ICP-OES). A Varian Vista RL spectrometer was used for investigations after chemical dissolution.

2.2.1.4 Single-Crystal Diffraction

A red single crystal of $Li_2(Ca_{1.88}Sr_{0.12})[Mg_2Si_2N_6]:Eu^{2+}$ was selected and sealed in a glass capillary in argon atmosphere. Crystal quality was tested with a Buerger precession camera. A Bruker D8 Quest diffractometer with microfocus was used for X-ray diffraction data collection. Goebel mirror optics was used to specifically select Mo–Kα radiation (λ = 0.71073 Å). The program SADABS was chosen for absorption correction.[19] The crystal structure was solved by Direct Methods (SHELXS)[20] and refined by full-matrix least-squares methods (SHELXL).[21,22] Eu^{2+} was disregarded for structure determination due to its low amount and its therefore insignificant contribution to the scattering density. The atomic ratio of the alkaline earth elements in $Li_2(Ca_{1.88}Sr_{0.12})[Mg_2Si_2N_6]$ was determined during the refinement.

Further details on the crystal structure investigations can be obtained from the Fachinformationszentrum Karlsruhe, 76344 Eggenstein-Leopoldshafen, Germany (Fax, (+49)7247–808–666; e-mail, crysdata@fiz-karlsruhe.de) upon quoting the depository numbers CSD-432118.

2.2.1.5 Luminescence

Luminescence spectra of Eu^{2+}-doped samples of both $Li_2Ca_2[Mg_2Si_2N_6]$ and $Li_2(Ca_{1.88}Sr_{0.12})[Mg_2Si_2N_6]$ as well as $Li_2Ca_2[Mg_2Si_2N_6]:Ce^{3+}$ were obtained with a HORIBA Fluoromax4 Spectrofluorimeter system connected to an Olympus BX51 microscope by optical fibers. Samples were sealed inside silica glass capillaries. The spectral width of the excitation wavelength at 440 nm is 10 nm. Emission spectra were recorded in a wavelength range between 460 and 820 nm with 2 nm step size. Excitation spectra were obtained with a monitoring wavelength of 625 nm for Eu^{2+}-doped samples of $Li_2Ca_2[Mg_2Si_2N_6]$ and $Li_2(Ca_{1.88}Sr_{0.12})[Mg_2Si_2N_6]$. For $Li_2Ca_2[Mg_2Si_2N_6]:Ce^{3+}$ a monitoring wavelength of 556 nm was selected.

2.2.1.6 Luminescence Decay

Decay measurements were obtained on a VUV (Vacuum UV) spectrometer assembly consisting of an excitation unit with a pulsed LED (442 nm, 20 kHz, 6 ns pulse width) and collecting optics, a sample chamber and detection unit. The detection unit is arranged in 90° geometry to the excitation unit. The collecting optics features an integrated monochromator (FS9000, Edinburgh Instruments) and photomultiplier tube (Hamatsu R955).

2.2.1.7 UV/vis Spectroscopy

Reflectance spectra of $Li_2Ca_2[Mg_2Si_2N_6]$ and $Li_2Ca_2[Mg_2Si_2N_6]:Eu^{2+}$ were obtained with an Edinburgh Photonics FLS920-s spectrometer equipped with a 450 W Xe900 arc lamp (single photon-

photomultiplier detector, Czerny-Turner monochromator with triple grating turret). The spectra were measured in the wavelength range from 230 to 780 nm (5 nm step size). The band gap of $Li_2Ca_2[Mg_2Si_2N_6]$ was estimated from UV/vis-reflectance data. The intersection of two line tangents to the slope of the reflectance curve yielded the value of the band gap.

2.2.2 Results and Discussion

2.2.2.1 Synthesis

Single crystals of red emitting nitridomagnesosilicates $Li_2Ca_2[Mg_2Si_2N_6]:Eu^{2+}$ and $Li_2(Ca_{1.88}Sr_{0.12})[Mg_2Si_2N_6]:Eu^{2+}$ were synthesized by a modified solid-state metathesis reaction in arc-welded Ta ampules.[12] The formation of LiF as thermodynamic driving force favors the formation of the products. Different impurity phases like $Ca[Mg_3SiN_4]:Eu^{2+}$ and $Ca[Li_2Si_2N_4]$ as well as compounds with a mixed occupation of the alkaline earth position with Ca and Sr, respectively, have been identified.[8,23]

Isolated single crystals of the target compounds show deep red body color and are sensitive to moisture and air. Ce^{3+}-doped crystals of $Li_2Ca_2[Mg_2Si_2N_6]$ were synthesized similarly and show green body color and luminescence. Attempts at increasing the Sr content to more than 7% Sr on the Ca site were not successful. This might be due to size mismatch of the larger ionic radius of Sr^{2+} compared to Ca^{2+}. Ba^{2+} could not be incorporated at any marked concentration.

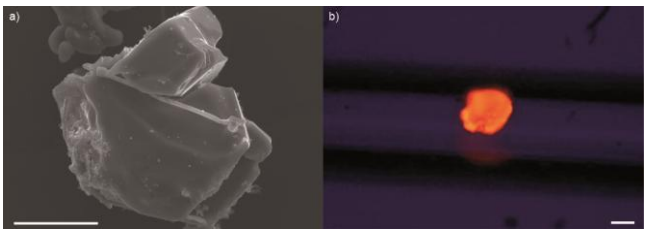

Figure 1. a) SEM image and b) luminescence image of $Li_2(Ca_{1.88}Sr_{0.12})[Mg_2Si_2N_6]:Eu^{2+}$ single crystals. Scale bar, 50 μm.

2.2.2.2 Chemical Analysis

Elemental analysis was performed by EDS analysis and ICP-OES investigations (Table 1). Results from EDS analysis of $Li_2Ca_2[Mg_2Si_2N_6]:Eu^{2+}/Ce^{3+}$ and $Li_2(Ca_{1.88}Sr_{0.12})[Mg_2Si_2N_6]:Eu^{2+}$ single crystals are summarized. The scanning electron microscopy (SEM) image in Figure 1a) shows a single crystal of $Li_2(Ca_{1.88}Sr_{0.12})[Mg_2Si_2N_6]:Eu^{2+}$ with a particle size larger than 100 μm. Oxygen impurities in single crystals as well as in microcrystalline powders were found in all samples due to the compounds' hydrolysis sensitivity. The Li content in a $Li_2(Ca_{1.88}Sr_{0.12})[Mg_2Si_2N_6]:Eu^{2+}$ powder sample was quantified by ICP-OES measurements. The complementary results from elemental analysis agree well with the calculated composition from single-crystal structure refinement within the standard deviations.

Table 1. Summary of EDS and ICP/OES Analysis (Atomic Ratio)

element	$Li_2Ca_2[Mg_2Si_2N_6]:Eu^{2+}$ (EDS)	$Li_2Ca_2[Mg_2Si_2N_6]:Ce^{3+}$ (EDS)	$Li_2(Ca_{1.88}Sr_{0.12})[Mg_2Si_2N_6]:Eu^{2+}$ (EDS)	$Li_2(Ca_{1.88}Sr_{0.12})[Mg_2Si_2N_6]:Eu^{2+}$ (ICP)
Ca	1.0	1.0	0.94	0.89
Sr			0.06	0.11
Li				0.77
Mg	0.8	0.8	1.0	1.04
Si	1.0	1.0	1.0	
N	2.3	2.7	4.2	
O	0.9	1.4	0.4	
Eu/Ce	0.01	0.01	0.01	

Table 2. Crystallographic Data of $Li_2(Ca_{1.88}Sr_{0.12})[Mg_2Si_2N_6]$[a]

formula mass/g mol^{-1}	289.56
crystal system /	monoclinic
space group (no.)	*C*2/*m* (12)
cell parameters (Å, °)	*a* = 5.5744(2)
	b = 9.8439(3)
	c = 6.0170(2)
	β = 97.2520(10)
cell volume (Å^3)	327.54(2)
Z	2
density (X-ray) (g cm^{-3})	2.929
Abs coefficient (mm^{-1})	3.148
F(000)	285
crystal dimensions (mm^3)	0.246 × 0.154 × 0.072
diffractometer	D8 Quest
radiation	Mo–Kα (λ = 0.71073 Å)
temperature (K)	293(2)
Abs correction	multi-scan
θ range (°)	3.413–36.995
measured reflns	5098
independent reflns	882 [R_{int} = 0.0288]
observed reflns	823
min./max. transmission	0.7614/1.000
refined params	37
GOF	1.152
R indices (Fo2 ≥ 2σ(Fo2))	*R*1 = 0.0181, *wR*2 = 0.0449
R indices (all data)	*R*1 = 0.0211, *wR*2 = 0.0467
min./max. residual electron density (eÅ^{-3})	–0.573/0.379

[a] e.s.d.s in parentheses.

2.2.2.3 Single-Crystal Structure Analysis

X-ray diffraction experiments were performed on single crystals of $Li_2(Ca_{1.88}Sr_{0.12})[Mg_2Si_2N_6]$. The compound crystallizes isomorphic to the nitridomagnesosilicate $Li_2Ca_2[Mg_2Si_2N_6]$ in the monoclinic space group *C*2/*m* (no. 12).[12] Crystallographic data of structure solution and refinement are summarized in Table 2. Atomic coordinates and isotropic displacement parameters are given in Table 3. Anisotropic refinement Anisotropic displacement parameters (ADPs) as well as a graphical

presentation of the ADPs of $Li_2(Ca_{1.88}Sr_{0.12})[Mg_2Si_2N_6]$ are given in Table S1 and Figure S1 of the Supporting Information.

2.2.2.4 Crystal Structure Description

The network of $Li_2Ca_2[Mg_2Si_2N_6]$ is made up of edge sharing double tetrahedra with the formula $[Si_2N_6]^{10-}$ that are interconnected by chains of edge sharing MgN_4 tetrahedra (Figure 2).[12] Negative charge of the network is compensated by Ca^{2+}-ions occupying distorted octahedral voids coordinated by N. Octahedrally distorted coordination of two Li atoms by N is shown as well.

Substituting up to 6% Ca by Sr in the crystal structure elongates lattice parameters *a* and *c* by 0.027 and 0.019 Å, respectively. Lattice parameter *b* is not influenced within the standard deviations. The monoclinic angle β is increased slightly by 0.12°. The overall cell volume is increased by 2.54 $Å^3$ or 0.8%.

A comparison of lattice parameters is given in Table 4. The influence of partially introducing a larger cation varies for different coordination polyhedra. In $(Ca,Sr)N_6$ octahedra the (Ca,Sr)-N1 bonds are expanded by 0.014 and 0.008 Å.

Table 3. Atomic Coordinates and Isotropic Displacement Parameters of $Li_2(Ca_{1.88}Sr_{0.12})[Mg_2Si_2N_6]$[a]

atom	Wyckoff position	*x*	*y*	*z*	U_{eq} ($Å^3$)	*site occupancy factor*
Ca	4*g*	0	0.18315(2)	0	0.00862(7)	0.937(2)
Sr	4*g*	0	0.18315(2)	0	0.00862(7)	0.063(2)
Si	4*i*	0.63044(5)	0	0.17903(5)	0.00408(8)	1
Mg	4*h*	0	0.26580(4)	1/2	0.00607(9)	1
Li	4*i*	0.1746(5)	0	0.4060(5)	0.0151(4)	1
N1	8*j*	0.24664(13)	0.35499(8)	0.31046(12)	0.00808(13)	1
N2	4*i*	0.30936(17)	0	0.10946(16)	0.00683(16)	1

[a] e.s.d.s in parentheses.

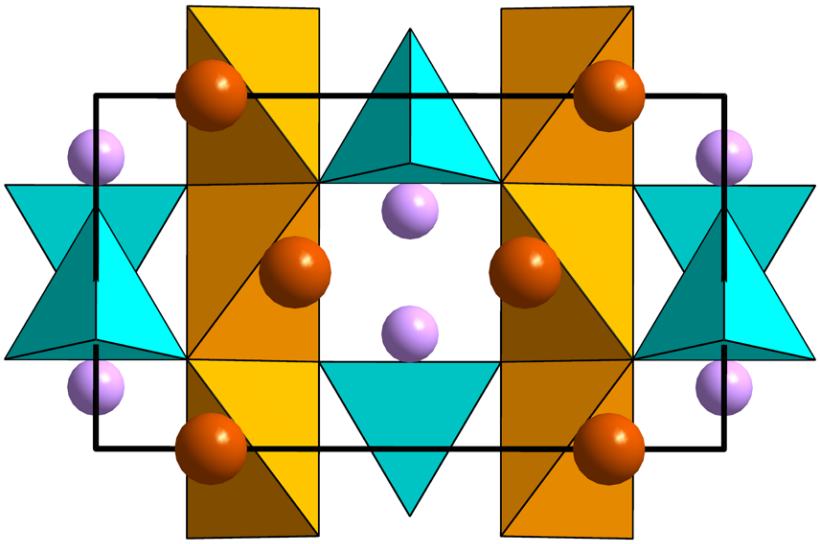

Figure 2. Crystal structure of $Li_2(Ca_{1.88}Sr_{0.12})[Mg_2Si_2N_6]$; SiN_4 tetrahedra (turquoise), MgN_4 tetrahedra (orange), Li (violet), and Ca,Sr (dark orange); viewing direction along (001).

Table 4. Lattice Parameters [Å,°] of $Li_2Ca_2[Mg_2Si_2N_6]$ and $Li_2(Ca_{1.88}Sr_{0.12})[Mg_2Si_2N_6]$[a]

lattice parameter	$Li_2Ca_2[Mg_2Si_2N_6]$	$Li_2(Ca_{1.88}Sr_{0.12})[Mg_2Si_2N_6]$
a	5.5472(11)	5.5744(2)
b	9.844(2)	9.8439(3)
c	5.9978(12)	6.0170(2)
β	97.13(3)	97.252(1)

[a] e.s.d.s in parentheses.

While the SiN_4 tetrahedra remain largely unchanged, Mg–N contacts in MgN_4 tetrahedra are extended by 0.008 and 0.007 Å. The 3-fold coordination of Li by N is compensated by an elongated Li—N2 bond (+0.012 Å) and two contracted Li–N1 bonds (−0.006 Å).

The Li–Li distance is significantly extended by 0.036 Å. Selected bond lengths and angles of $Li_2Ca_2[Mg_2Si_2N_6]$ and $Li_2(Ca_{1.88}Sr_{0.12})[Mg_2Si_2N_6]$ are summarized in Table 5, coordination polyhedra of both compounds are displayed in Figure 3.

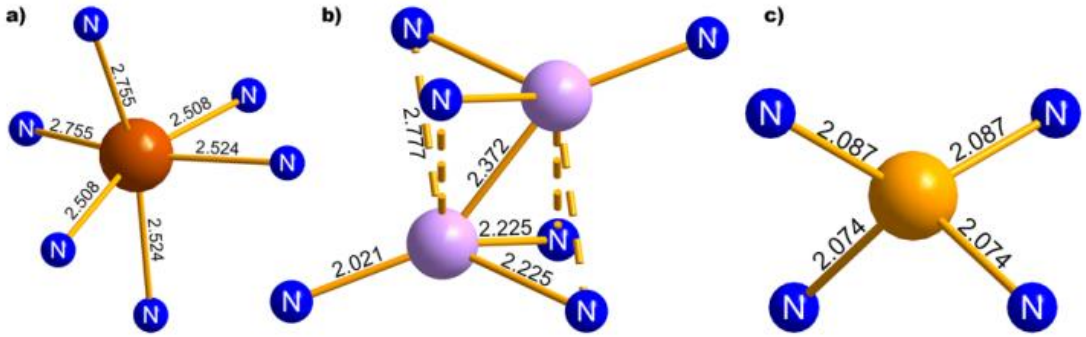

Figure 3. Coordination polyhedra of a) (Ca,Sr), b) Li, and c) Mg; bond lengths given in Å.

Table 5. Selected Bond Lengths [Å] and Angles [°] of $Li_2Ca_2[Mg_2Si_2N_6]$ and $Li_2(Ca_{1.88}Sr_{0.12})[Mg_2Si_2N_6]$[a]

bond/angle name	$Li_2Ca_2[Mg_2Si_2N_6]$	$Li_2(Ca_{1.88}Sr_{0.12})[Mg_2Si_2N_6]$
Ca—N1/(Ca,Sr)—N1 (2x)	2.494(2)	2.508(1)
Ca—N1/(Ca,Sr)—N1 (2x)	2.748(2)	2.756(1)
Ca—N2/(Ca,Sr)—N2 (2x)	2.523(2)	2.524(1)
Si—N1 (2x)	1.721(2)	1.719(1)
Si—N2	1.784(3)	1.786(1)
Si—N2	1.805(3)	1.809(1)
Mg—N1 (2x)	2.066(2)	2.074(1)
Mg—N1 (2x)	2.081(2)	2.088(1)
Li—N1 (2x)	2.231(5)	2.225(2)
Li—N2	2.010(7)	2.022(3)
Li—Li	2.336(13)	2.372(6)
N1—Si—N1	112.38(15)	112.33(5)
N1—Si—N2	109.60(9)	109.68(3)
N1—Si—N2	114.63(9)	114.60(3)
N2—Si—N2	94.44(2)	94.41(4)

[a] e.s.d.s in parentheses.

2.2.2.5 Eu^{2+}-Luminescence

Investigations on luminescence properties of $Li_2Ca_2[Mg_2Si_2N_6]:Eu^{2+}$ and $Li_2(Ca_{1.88}Sr_{0.12})[Mg_2Si_2N_6]:Eu^{2+}$ revealed extraordinary emission characteristics, only exceeded by few red emitting nitride phosphors. Excitation and emission spectra of the Eu^{2+}-doped compounds are compared in Figure 4a. Both compounds can be excited ($\lambda_{monitor}$ = 625 nm) in the blue spectral region of the visible spectrum with maximum absorption between 400 and 460 nm with a second absorption maximum around 530 nm.

Hence, the title compounds are effectively excitable with UV to blue light as supplied by (In,Ga)N-LEDs. When excited, $Li_2Ca_2[Mg_2Si_2N_6]:Eu^{2+}$ and $Li_2(Ca_{1.88}Sr_{0.12})[Mg_2Si_2N_6]:Eu^{2+}$ show luminescence in the red spectral range peaking at 638 and 634 nm, respectively, with *fwhm* =1513–1532 cm^{-1} (~62 nm, nominal Eu-content 1%), developing comparable emission intensity. An image of a luminescent single crystal of $Li_2(Ca_{1.88}Sr_{0.12})[Mg_2Si_2N_6]:Eu^{2+}$ being excited with blue light (λ_{exc} = 460 nm) is shown in Figure 1b.

With the introduction of Sr into $Li_2(Ca_{1-x}Sr_x)_2[Mg_2Si_2N_6]:Eu^{2+}$ (x = 0–0.06), excitation and emission maxima are shifted slightly toward shorter wavelengths. The effect is influenced by the size of larger Sr^{2+} compared to Ca^{2+}. By introducing Sr, cell parameters and Eu–N distances are enlarged. Reduced crystal field splitting causes blue-shifted absorption and due to a comparable Stokes shift also a blue-shifted emission band. This fits well to the assumption that the activator ion occupies the alkaline earth atom position.

A comparison of the local coordinations of the alkaline earth ions (Figure 3a) with that of Ca and Sr in the commercially available phosphors $Ca_{1-x}Sr_xSiAlN_3:Eu^{2+}$ (SCASN) shows extensive similarities. However, Stokes shift and emission bandwidth of the title compounds are significantly smaller.[7] This observation can be explained by the fact that the host lattice ions Li, Mg, and Si all occupy distinct lattice sites while Si and Al in SCASN show a statistical distribution over the same lattice site leading to larger Stokes shifts and inhomogeneous broadening of the emission bands.[24]

Compounds with cube-like N coordination of AE^{2+} like $Sr[Mg_3SiN_4]:Eu^{2+}$ and $Sr[LiAl_3N_4]:Eu^{2+}$ still show unrivalled emission bandwidth (1170 cm^{-1}, 1180 cm^{-1}) compared to compounds with distorted octahedral coordination like $Li_2Ca_2[Mg_2Si_2N_6]:Eu^{2+}$ and $Ca_{1-x}Sr_xSiAlN_3:Eu^{2+}$ (>1500 cm^{-1}).[4,7,8] This is likely caused by different void sizes in the crystal structure provided for Eu^{2+} by octahedral and 8-fold coordination of N, assuming Eu occupies *AE* sites. Cube-like coordination on a Sr site is close to the energetic equilibrium geometry of Eu^{2+}, while octahedral coordination on a Ca site with shorter Eu^{2+}–ligand distances leads to an increased local structure relaxation around the activator in its excited state. As a consequence higher vibrational levels contribute to the emission energy spectrum (increased Huang-Rhys coupling factor *S*). With increasing *S* the Stokes shift (E_{Stokes}) increases linearly according to eq 1, with ω as the angular frequency of vibration around the emission center in the simplified configurational coordinate model.[25,26]

$$E_{Stokes} = (2S - 1)\hbar\omega \qquad (1)$$

Recently found $Ca_{18.75}Li_{10.5}[Al_{39}N_{55}]:Eu^{2+}$ with three different *AE* sites, which are in trigonal prismatic (1x) and distorted octahedral (2×) coordination, shows remarkable narrow-band red emission (1280 cm^{-1}) as well. It is assumed that Eu^{2+} partially occupies all Ca sites, while emission only occurs from distorted octahedrally coordinated Ca sites. If the 4*f* levels are comparably positioned in the band gap emission from the trigonal prismatically coordinated site, they are quenched due to the excited state being energetically located in the conduction band.[27]

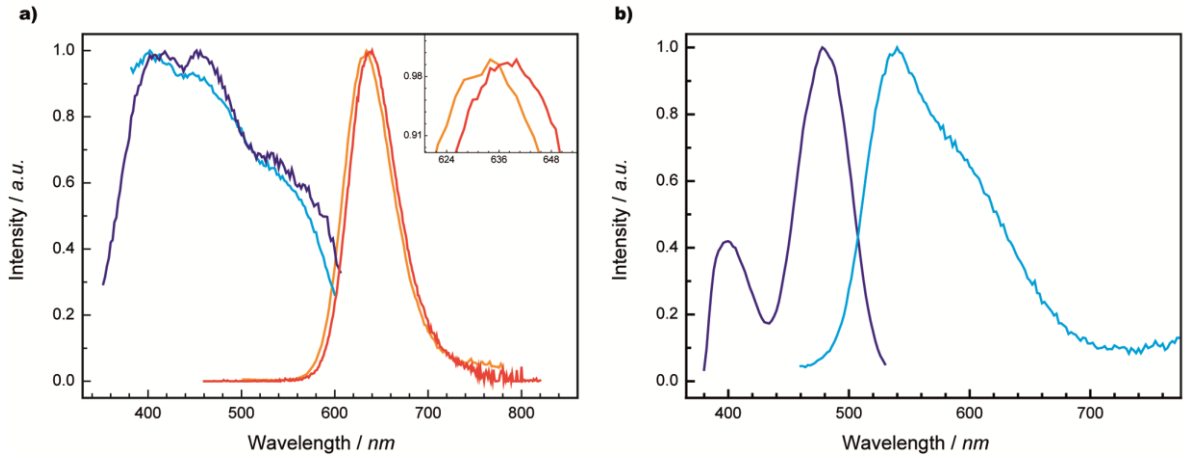

Figure 4. Luminescence spectra of a) $Li_2Ca_2[Mg_2Si_2N_6]:Eu^{2+}$ (exc.: dark blue line, em.: red line) and $Li_2(Ca_{1.88}Sr_{0.12})[Mg_2Si_2N_6]:Eu^{2+}$ (exc.: light blue line, em: orange line) and b) $Li_2Ca_2[Mg_2Si_2N_6]:Ce^{3+}$ (exc.: dark blue line, em.: light blue line).

2.2.2.6 Ce^{3+}-Luminescence

Samples of Ce^{3+}-doped $Li_2Ca_2[Mg_2Si_2N_6]$ show green luminescence with a maximum around 540 nm and a shoulder at ~600 nm due to the energetically split ground states of Ce^{3+} ($^2F_{5/2}$ and $^2F_{7/2}$) (Figure 4b). The excitation spectrum also shows two distinct maxima at ~400 and ~480 nm. Therefore, the phosphor is excitable with low energy blue light. The energetic difference of the lowest lying $4f^{n-1} \rightarrow 5d^1$ absorption bands of Ce^{3+} and Eu^{2+} in $Li_2Ca_2[Mg_2Si_2N_6]$ is ~4170 cm^{-1} and confirms that both activator ions occupy the same lattice site in the title compound's crystal structure.[28]

In Figure S2, emission spectra of YAG:Ce^{3+} and $Li_2Ca_2[Mg_2Si_2N_6]:Ce^{3+}$ are compared. Emission spectra of both compounds are very similar. Due to the red-shifted absorption of the title compound (~477 nm compared to ~455 nm in YAG:Ce^{3+}) a smaller Stokes shift is determined.

2.2.2.7 Luminescence Decay

Lifetime investigations of $Li_2Ca_2[Mg_2Si_2N_6]:Eu^{2+}$ emission are shown in Figure 5. Fitting of the measurement curves reveal an initial fast component with $\tau_1 \approx 0.2$ µs followed by a slower component $\tau_2 \sim 0.9$ µs. This is possibly attributed to energy transfer of neighboring Eu^{2+} centers or reabsorption effects and is comparable to state of the art red phosphors with the activator Eu^{2+}, e.g., commercial $Ca_{1-x}Sr_xSiAlN_3:Eu^{2+}$ ($\tau_1 \approx 0.3$ µs, $\tau_2 \approx 0.8$ µs) and $SrLiAl_3N_4:Eu^{2+}$ (monoexponential decay with $\tau \sim$

0.8 µs).[29] The observed lifetime of the Eu^{2+} luminescence of the title compound thus point toward high internal quantum efficiencies and make the materials attractive candidates for practical application as LED phosphors. Regarding decay time of red phosphors, the dopant Eu^{2+} shows advantage over slower decaying emitters like Eu^{3+} or Mn^{4+} that show decay time constants in the ms range due to emission saturation under high excitation densities.[30]

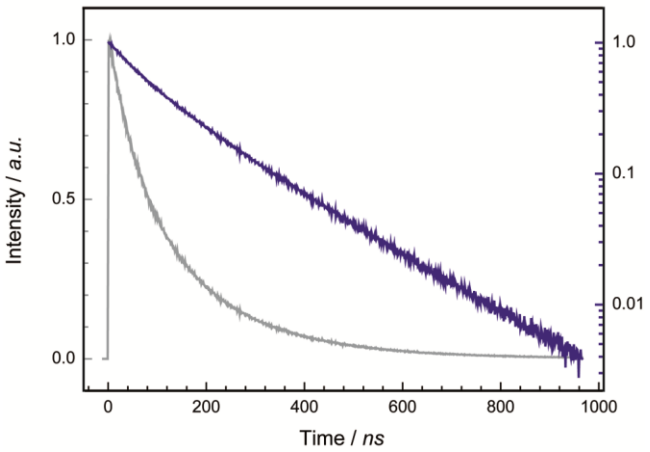

Figure 5. Luminescence decay of $Li_2Ca_2[Mg_2Si_2N_6]:Eu^{2+}$ (1 mol % Eu^{2+}, nominal composition). Linear (gray line) and logarithmic (blue line) plot.

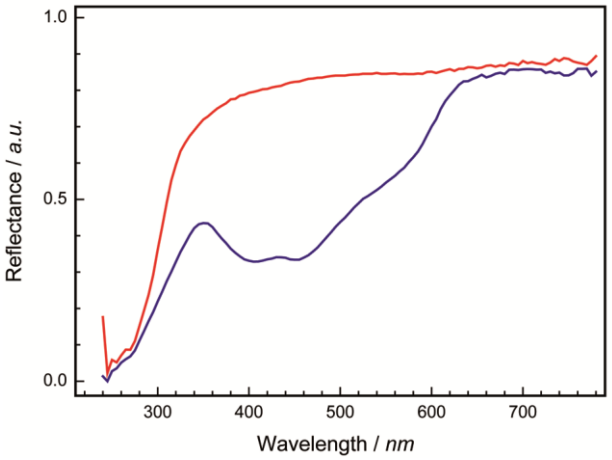

Figure 6. UV/vis reflectance spectra of undoped (red line) and doped (blue line, 1 mol % Eu^{2+}, nominal composition) $Li_2Ca_2[Mg_2Si_2N_6]$.

2.2.2.8 UV/vis Spectroscopy

Band gap investigations on Eu^{2+}-doped and undoped samples of $Li_2Ca_2[Mg_2Si_2N_6]$ were carried out by UV/vis reflectance spectroscopy. Reflectance spectra (Figure 6) show two absorption bands in the spectrum of the doped sample. One broad band is found in the blue to yellow region of the visible spectrum and is attributed to the $4f^7 \rightarrow 4f^{7-n}5d^n$ absorptions in Eu^{2+}. The strong absorption maxima at ~410 and ~460 nm are in good accordance with the red body color of the crystalline sample.

The absorption band around 240–280 nm is attributed to the host lattice absorption and can be found in the spectra of the doped and the undoped sample. The optical band gap was estimated to a value of ~4.6 eV. The excited 5*d*-state of Eu^{2+} should have a significant distance to the conduction band edge for high quantum efficiency (QE), which is a main condition for phosphor application in LEDs.[31,32] At ambient temperature internal quantum efficiency of initial powder sample of $Li_2Ca_2[Mg_2Si_2N_6]:Eu^{2+}$ shows values around 50.0% (±0.5%) for as-synthesized samples.

2.2.3 Conclusions

The nitridomagnesosilicate $Li_2(Ca_{1.88}Sr_{0.12})[Mg_2Si_2N_6]$ was successfully synthesized by solid-state metathesis in Ta ampules. The compound crystallizes isomorphic to the nitridomagnesosilicate $Li_2Ca_2[Mg_2Si_2N_6]$ in space group *C*2/*m*. Upon doping with Eu^{2+} and Ce^{3+}, respectively, luminescence in the visible spectral range is obtained in both compounds. Ce^{3+}-doped samples show broad band green emission. Eu^{2+}-doped compounds of $Li_2(Ca_{1-x}Sr_x)_2[Mg_2Si_2N_6]$ (x = 0–0.06) show exceptional narrow-band red emission (*fwhm* =1513–1532 cm^{-1}; ~62 nm). Successful synthesis of crystalline samples with x = 0 and 0.06 exhibit emission peaking at 638 and 634 nm. The emission maximum can be tuned in the red spectral range by varying the amount of Sr in $Li_2(Ca_{1-x}Sr_x)_2[Mg_2Si_2N_6]$ series in a range from 0 to 6%. The optical band gap of the Eu^{2+}-doped compound of ~4.6 eV is similar to the value ~4.9 eV of $Sr_2Si_5N_8:Eu^{2+}$.[33] The luminescence lifetime ($\tau_1 \approx 0.2$ µs, $\tau_2 \approx 0.9$ µs) of $Li_2Ca_2[Mg_2Si_2N_6]:Eu^{2+}$ is comparable to other red emitting Eu^{2+} phosphors.

Phosphors emitting in the particular area around 630 nm and simultaneously exhibiting the ability of fine-tuning the emission precisely within a small spectral range are sought after candidates for application in pcLEDs. Stabilization against hydrolysis of the phosphor can possibly be improved by protective coatings, as demonstrated for various oxide and nitride phosphor materials.[34-36] Optimization of the synthesis protocol will likely improve the luminescence properties, e.g., QE, further. Subject of ongoing investigations is the further extension of compositional ranges of the title compound with focus on the related luminescence properties.

2.2.4 References

[1] Pust, P.; Schmidt, P. J.; Schnick, W. A revolution in lighting. *Nat. Mater.* **2015**, *14*, 454-458.

[2] Wang, X.-J.; Funahashi, S.; Takeda, T.; Suehiro, T.; Hirosaki, N.; Xie, R.-J. Structure and luminescence of a novel orange-yellow-emitting $Ca_{1.62}Eu_{0.38}Si_5O_3N_6$ phosphor for warm white LEDs, discovered by a single-particle-diagnosis approach. *J. Mater. Chem. C* **2016**, *4*, 9968-9975.

[3] Ding, J.; Wu, Q.; Li, Y.; Long, Q.; Wang, Y.; Wang, Y. Eu^{2+}-activated $Ca_5Si_2Al_2N_8$ – A novel nitridoalumosilicate red phosphor containing the special polyhedron of separated corner-shared $[Al_2N_6]$ and $[Si_2N_6]$. *Chem. Eng. J.* **2016**, *302*, 466-474.

[4] Pust, P.; Weiler, V.; Hecht, C.; Tücks, A.; Wochnik, A. S.; Henß, A. K.; Wiechert, D.; Scheu, C.; Schmidt, P. J.; Schnick, W. Narrow-band red-emitting $Sr[LiAl_3N_4]:Eu^{2+}$ as a next-generation LED-phosphor material. *Nat. Mater.* **2014**, *13*, 891-896.

[5] Schmiechen, S.; Pust, P.; Schmidt Peter, J.; Schnick, W. Weißes Licht aus Nitriden. *Nachr. Chem.* **2014**, *62*, 847-851.

[6] Höppe, H. A.; Lutz, H.; Morys, P.; Schnick, W.; Seilmeier, A. Luminescence in Eu^{2+}-doped $Ba_2Si_5N_8$: fluorescence, thermoluminescence, and upconversion. *J. Phys. Chem. Solids* **2000**, *61*, 2001-2006.

[7] Watanabe, H.; Kijima, N. Crystal structure and luminescence properties of $Sr_xCa_{1-x}AlSiN_3:Eu^{2+}$ mixed nitride phosphors. *J. Alloys Compd.* **2009**, *475*, 434-439.

[8] Schmiechen, S.; Schneider, H.; Wagatha, P.; Hecht, C.; Schmidt, P. J.; Schnick, W. Toward New Phosphors for Application in Illumination-Grade White pc-LEDs: The Nitridomagnesosilicates $Ca[Mg_3SiN_4]:Ce^{3+}$, $Sr[Mg_3SiN_4]:Eu^{2+}$, and $Eu[Mg_3SiN_4]$. *Chem. Mater.* **2014**, *26*, 2712-2719.

[9] Strobel, P.; Schmiechen, S.; Siegert, M.; Tücks, A.; Schmidt, P. J.; Schnick, W. Narrow-Band Green Emitting Nitridolithoalumosilicate $Ba[Li_2(Al_2Si_2)N_6]:Eu^{2+}$ with Framework Topology whj for LED/LCD-Backlighting Applications. *Chem. Mater.* **2015**, *27*, 6109-6115.

[10] Takeda, T.; Hirosaki, N.; Funahshi, S.; Xie, R.-J. Narrow-Band Green-Emitting Phosphor $Ba_2LiSi_7AlN_{12}:Eu^{2+}$ with High Thermal Stability Discovered by a Single Particle Diagnosis Approach. *Chem. Mater.* **2015**, *27*, 5892-5898.

[11] Schmiechen, S.; Strobel, P.; Hecht, C.; Reith, T.; Siegert, M.; Schmidt, P. J.; Huppertz, P.; Wiechert, D.; Schnick, W. Nitridomagnesosilicate $Ba[Mg_3SiN_4]:Eu^{2+}$ and Structure–Property Relations of Similar Narrow-Band Red Nitride Phosphors. *Chem. Mater.* **2015**, *27*, 1780-1785.

[12] Schmiechen, S.; Nietschke, F.; Schnick, W. Structural Relationship between the Mg-Containing Nitridosilicates $Ca_2Mg[Li_4Si_2N_6]$ and $Li_2Ca_2[Mg_2Si_2N_6]$. *Eur. J. Inorg. Chem.* **2015**, 1592-1597.

[13] Bachmann, V.; Ronda, C.; Oeckler, O.; Schnick, W.; Meijerink, A. Color Point Tuning for $(Sr,Ca,Ba)Si_2O_2N_2:Eu^{2+}$ for White Light LEDs. *Chem. Mater.* **2009**, *21*, 316-325.

[14] Xia, Z.; Meijerink, A. Ce^{3+}-Doped garnet phosphors: composition modification, luminescence properties and applications. *Chem. Soc. Rev.* **2017**, *46*, 275-299.

[15] Lange, H.; Wötting, G.; Winter, G. Silicon Nitride – From Powder Synthesis to Ceramic Materials. *Angew. Chem. Int. Ed. Engl.* **1991**, *30*, 1579-1597.

[16] Fair, H. D.; Walker, R. F., *Energetic Materials 1: Physics and Chemistry of the Inorganic Azides*, 1st ed., Plenum Press: New York, London, **1997**.

[17] Grill, A. Effect of current pulses on the temperature distribution and microstructure in TIG tantalum welds. *Metall. Trans. B* **1981**, *12*, 187-192.

[18] Schmiechen, S., Dissertation, LMU Munich **2015**.

[19] Sheldrick, G. M., *SADABS, v. 2: Multi-Scan Absorption Correction*, Bruker-AXS, **2012**.

[20] Sheldrick, G. M., *SHELXS-97: A program for crystal structure solution*, University of Göttingen, **1997**.

[21] Sheldrick, G. M., *SHELXL-97: A program for crystal structure refinement*, University of Göttingen, **1997**.

[22] Sheldrick, G. M. A short history of SHELX. *Acta Crystallogr. Sect. A* **2008**, *64*, 112-122.

[23] Zeuner, M.; Pagano, S.; Hug, S.; Pust, P.; Schmiechen, S.; Scheu, C.; Schnick, W. $Li_2CaSi_2N_4$ and $Li_2SrSi_2N_4$ – a Synthetic Approach to Three-Dimensional Lithium Nitridosilicates. *Eur. J. Inorg. Chem.* **2010**, 4945-4951.

[24] Tsai, Y.-T.; Chiang, C.-Y.; Zhou, W.; Lee, J.-F.; Sheu, H.-S.; Liu, R.-S. Structural Ordering and Charge Variation Induced by Cation Substitution in (Sr,Ca)$AlSiN_3$:Eu Phosphor. *J. Am. Chem. Soc.* **2015**, *137*, 8936-8939.

[25] de Jong, M.; Seijo, L.; Meijerink, A.; Rabouw, F. T. Resolving the ambiguity in the relation between Stokes shift and Huang-Rhys parameter. *Phys. Chem. Chem. Phys.* **2015**, *17*, 16959-16969.

[26] Blasse, G.; Bril, A. Characteristic luminescence. *Philips Tech. Rev.* **1970**, *31*, 304-314.

[27] Wagatha, P.; Pust, P.; Weiler, V.; Wochnik, A. S.; Schmidt, P. J.; Scheu, C.; Schnick, W. $Ca_{18.75}Li_{10.5}[Al_{39}N_{55}]:Eu^{2+}$ - Supertetrahedron Phosphor for Solid-State Lighting. *Chem. Mater.* **2016**, *28*, 1220-1226.

[28] Dorenbos, P. Ce^{3+} 5*d*-centroid shift and vacuum referred 4*f*-electron binding energies of all lanthanide impurities in 150 different compounds. *J. Lumin.* **2013**, *135*, 93-104.

[29] Cui, D.; Xiang, Q.; Song, Z.; Xia, Z.; Liu, Q. The synthesis of narrow-band red-emitting $SrLiAl_3N_4:Eu^{2+}$ phosphor and improvement of its luminescence properties. *J. Mater. Chem. C* **2016**, *4*, 7332-7338.

[30] Smet, P. F.; Parmentier, A. B.; Poelman, D. Selecting Conversion Phosphors for White Light-Emitting Diodes. *J. Electrochem. Soc.* **2011**, *158*, R37-R54.

[31] Tolhurst, T. M.; Schmiechen, S.; Pust, P.; Schmidt, P. J.; Schnick, W.; Moewes, A. Electronic Structure, Bandgap, and Thermal Quenching of $Sr[Mg_3SiN_4]:Eu^{2+}$ in Comparison to $Sr[LiAl_3N_4]:Eu^{2+}$. *Adv. Opt. Mater.* **2016**, *4*, 584-591.

[32] Dorenbos, P. Thermal quenching of Eu^{2+} 5*d*–4*f* luminescence in inorganic compounds. *J. Phys.: Condens. Matter* **2005**, *17*, 8103-8111.

[33] Fang, C. M.; Hintzen, H. T.; With, G. d.; Groot, R. A. d. Electronic structure of the alkaline-earth silicon nitrides $M_2Si_5N_8$ (M = Ca and Sr) obtained from first-principles calculations and optical reflectance spectra. *J. Phys.: Condens. Matter* **2001**, *13*, 67-76.

[34] Shi, X.; Dou, R.; Ma, T.; Liu, W.; Lu, X.; Shea, K. J.; Song, Y.; Jiang, L. Bioinspired Lotus-like Self-Illuminous Coating. *ACS Appl. Mater. Interfaces* **2015**, *7*, 18424-18428.

[35] Tsai, Y.-T.; Nguyen, H.-D.; Lazarowska, A.; Mahlik, S.; Grinberg, M.; Liu, R.-S. Improvement of the Water Resistance of a Narrow-Band Red-Emitting $SrLiAl_3N_4:Eu^{2+}$ Phosphor Synthesized under High Isostatic Pressure through Coating with an Organosilica Layer. *Angew. Chem. Int. Ed.* **2016**, *128*, 9804-9808.

[36] Liu, H.; Xia, Z.; Zhuang, J.; Zhang, Z.; Liao, L. Surface treatment investigation and luminescence properties of SiO_2-coated $Ca_2BO_3Cl:0.02Eu^{2+}$ phosphors via sol–gel process. *J. Phys. Chem. Solids* **2012**, *73*, 104-108.

3 Narrow-band emitting Nitridosilicates Investigated by Synchrotron X-ray Spectroscopy

3.1 Preface

Fundamental investigations on the physical processes of host and dopant interactions were conducted extensively by *Blasse* and *Bril* in the 1960's and *Dorenbos* since 2000.[1-8] Their research has considerably advanced the understanding of characteristic luminescence by establishing simple models, such as the configurational coordinate model and energy-level diagrams of the *RE* energy states. They also have been decisive in the deduction of simple structure-property relations and their influence on luminescence profile and efficiency. Yet, not all apparent electronic processes in *RE*-doped phosphors are fully understood.

As foundation for the determination of electronic processes in luminescent materials, band gap determination is necessary. To obtain informative values, different methods can be combined. As a standard method for determination of the band gap UV/vis spectroscopy is applied. Additionally, theoretical calculations of the materials' electronic states in the valence band (VB) and conduction band (CB) can be performed using i.e. the density functional theory (DFT). To support calculations experimental determination of the band characteristics by soft X-ray spectroscopy measurements at a synchrotron source can be applied. The combination of calculations and measurements yields more detailed information about electronic states and give information, e.g., about the presence of direct or indirect band gaps, the density of states (DOS) as well as the influence of specific elements and their contribution to the energy bands.[9-12]

We have applied soft X-ray spectroscopy methods, such as X-ray absorption and emission spectroscopy (XAS, XES) in combination with X-ray excited optical luminescence (XEOL) to perform detailed investigations on the electronic structure of phosphor materials. Nowadays, XES and XAS are routinely applied at all synchrotron sources to solve scientific problems in physics, chemistry, material sciences, life sciences, geology, medicine, and engineering. Soft X-ray spectroscopy methods are powerful as they are element specific, nondestructive, and highly sensitive to the local bonding environment and geometric structure coordinating the absorbing atoms.[13] Experimental results about the investigation on $Sr[LiAl_3N_4]:Eu^{2+}$, $Sr[Mg_3SiN_4]:Eu^{2+}$, as well as $Ca_2Li_2[Mg_2Si_2N_6]:Eu^{2+}$ and $BaLi_2[Al_2Si_2N_6]:Eu^{2+}$, characterized in chapter 2, are condensed in the next chapter. Measurements of never before experimentally observed electronic states, such as the excited Eu(II) 5*d* state, and state-of-the-art determination of VB and CB are used to supplement present models of excitation and emission processes in phosphor materials.

References

[1] Blasse, G.; Bril, A. Characteristic luminescence. *Philips Tech. Rev.* **1970**, *31*, 304-314.

[2] Dorenbos, P. The 5*d* level positions of the trivalent lanthanides in inorganic compounds. *J. Lumin.* **2000**, *91*, 155-176.

[3] Dorenbos, P. Relating the energy of the [Xe]5d^1 configuration of Ce^{3+} in inorganic compounds with anion polarizability and cation electronegativity. *Phys. Rev. B* **2002**, *65*, 235110.

[4] Dorenbos, P. Anomalous luminescence of Eu^{2+} and Yb^{2+} in inorganic compounds. *J. Phys.: Condens. Matter* **2003**, *15*, 2645-2665.

[5] Dorenbos, P. Energy of the first $4f^7 \rightarrow 4f^6 5d$ transition of Eu^{2+} in inorganic compounds. *J. Lumin.* **2003**, *104*, 239-260.

[6] Dorenbos, P. $f \rightarrow d$ transition energies of divalent lanthanides in inorganic compounds. *J. Phys.: Condens. Matter* **2003**, *15*, 575-594.

[7] Dorenbos, P. Systematic behaviour in trivalent lanthanide charge transfer energies. *J. Phys.: Condens. Matter* **2003**, *15*, 8417-8434.

[8] Dorenbos, P. Thermal quenching of Eu^{2+} 5*d*–4*f* luminescence in inorganic compounds. *J. Phys.: Condens. Matter* **2005**, *17*, 8103-8111.

[9] Braun, C.; Seibald, M.; Börger, S. L.; Oeckler, O.; Boyko, T. D.; Moewes, A.; Miehe, G.; Tücks, A.; Schnick, W. Material Properties and Structural Characterization of $M_3Si_6O_{12}N_2$:Eu^{2+} (M=Ba, Sr) - A Comprehensive Study on a Promising Green Phosphor for pc-LEDs. *Chem. Eur. J.* **2010**, *16*, 9646 – 9657.

[10] Hintze, F.; Johnson, N. W.; Seibald, M.; Muir, D.; Moewes, A.; Schnick, W. Magnesium Double Nitride Mg_3GaN_3 as New Host Lattice for Eu^{2+} Doping: Synthesis, Structural Studies, Luminescence, and Band-Gap Determination. *Chem. Mater.* **2013**, *25*, 4044-4052.

[11] Tolhurst, T. M.; Boyko, T. D.; Pust, P.; Johnson, N. W.; Schnick, W.; Moewes, A. Investigations of the Electronic Structure and Bandgap of the Next-Generation LED-Phosphor Sr[$LiAl_3N_4$]:Eu^{2+} – Experiment and Calculations. *Adv. Opt. Mater.* **2015**, *3*, 546-550.

[12] Tolhurst, T. M.; Schmiechen, S.; Pust, P.; Schmidt, P. J.; Schnick, W.; Moewes, A. Electronic Structure, Bandgap, and Thermal Quenching of Sr[Mg_3SiN_4]:Eu^{2+} in Comparison to Sr[$LiAl_3N_4$]:Eu^{2+}. *Adv. Opt. Mater.* **2016**, *4*, 584-591.

[13] Moewes, A., in *Handbook of Solid State Chemistry, Vol. 3* (Eds.: R. Dronskowski, S. Kikkawa,A. Stein), Wiley-VCH, Weinheim, Germany, **2017**.

3.2 Designing Luminescent Materials and Band Gaps: A Soft X‑ray Spectroscopy and Density Functional Theory Study of $Li_2Ca_2[Mg_2Si_2N_6]:Eu^{2+}$ and $Ba[Li_2(Al_2Si_2)N_6]:Eu^{2+}$

published in: *J. Phys. Chem. C* **2017**, *121*, 14296-14301

authors: Thomas M. Tolhurst, Philipp Strobel, Peter J. Schmidt, Wolfgang Schnick and Alexander Moewes

DOI: 10.1021/acs.jpcc.7b03814

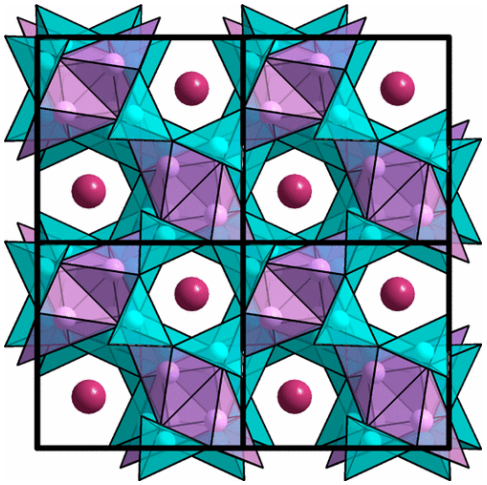

Abstract. A large band gap is a prerequisite for efficient emissions from a rare earth doped phosphor and is consequently a prerequisite for its application in high-quality lighting. We present a detailed characterization of luminescent materials $Li_2Ca_2[Mg_2Si_2N_6]:Eu^{2+}$ and $Ba[Li_2(Al_2Si_2)N_6]:Eu^{2+}$ using soft X-ray spectroscopy and density functional theory calculations, including a rigorous experimental determination, and theory-based elucidation, of their band gaps. The band gap of $Li_2Ca_2[Mg_2Si_2N_6]:Eu^{2+}$ is determined to be 4.84 ± 0.20 eV, while that of $Ba[Li_2(Al_2Si_2)N_6]:Eu^{2+}$ is 4.82 ± 0.20 eV. The origin of the band gaps is discussed in the context of the calculated DOS of each material and compared to benchmark luminescent materials $Sr[LiAl_3N_4]:Eu^{2+}$ and $Sr[Mg_3SiN_4]:Eu^{2+}$. Critically, the elements determining the band gaps are identified using the calculated density of states, as well as experimental resonant X-ray emission measurements. This allows for predictive power when searching for new nitridosilicates and related host structures, which upon doping with rare earth elements, may find application in the next-generation of phosphor converted light emitting diodes.

3.2.1 Introduction

Lighting is a leading consumer of energy globally, following only transportation and building temperature control. Solid state lighting, the phosphor converted light emitting diode (pcLED) in particular, is poised to reduce energy consumption in the lighting sector by 40% within the next decade and half.[1] In order to achieve or even exceed this goal, several advances are wanting. Improvements to device architecture are important,[2] but there are also considerable gains to be made in both phosphor efficiency and the luminous efficacy of the devices.[1] The former is accessible through improved quantum efficiency of the phosphors, but the latter requires narrow, red emitting phosphors.

The discovery of the highly efficient red emitter $M_2Si_5N_8:Eu^{2+}$ (M = Ca,Sr,Ba) and its demonstration as an LED phosphor were milestones in the field.[3,4] The recent discovery of narrow emitting $Sr[LiAl_3N_4]:Eu^{2+}$ (SLA) and $Sr[Mg_3SiN_4]:Eu^{2+}$ (SMS) has made ultrahigh color rendering pcLEDs realizable.[5,6] There are still improvements that can be made, and efficient phosphors emitting in different regions of the visible spectrum are highly desirable. This is a study of two new phosphors: narrow green-emitting $Ba[Li_2(Al_2Si_2)N_6]:Eu^{2+}$ (BLAS) and narrow red-emitting $Li_2Ca_2[Mg_2Si_2N_6]:Eu^{2+}$ (LCMS).[7-9] Either material emits in highly desirable regions of the visible spectrum and BLAS shows a promising quantum efficiency. Accurate measurements of their band gaps, arguably one of the most important material characteristics, are made through the use of soft X-ray spectroscopy. The density functional theory calculations for each phosphor are presented and used to explain the origins of their band gaps, while relating them to the values of other important benchmark phosphors. The comparison between phosphors is used to form an understanding of the structure–property relationships that underpin the useful properties of LCMS and BLAS. This understanding can guide the search for the next generation of efficient, narrow-emitting phosphors.

3.2.1.1 Synthesis and Structure Models

The powder samples of BLAS and LCMS where synthesized in sealed tantalum ampules through a modified solid-state metathesis reaction. Full synthesis details and characterization of crystal structures are described elsewhere.[7,9] Crystal structures derived from single crystal X-ray diffraction (XRD) are the primary input to the density functional theory (DFT) calculations presented here. Due to the statistical occupation of the Si/Al sites in BLAS, half of the sites in the unit cell were assigned to each element for the DFT calculations. The experimentally determined lattice parameters were taken as the best representation of the samples, and no DFT-based structure optimization was carried out. This approach is seen to lead to excellent agreement between the experimental and calculated spectra, supporting the accuracy of the structures determined with XRD. Both samples in this study are doped with Eu^{2+}, which leads to $4f^7 \rightarrow 5d^1 4f^6$ emissions in each sample in the red (LCMS) and green (BLAS) spectral regions, respectively.

3.2.2 Experimental Section

3.2.2.1 X-ray Spectroscopy

The X-ray absorption measurements were collected at the spherical grating monochromator beamline at the Canadian Light Source in Saskatoon, Saskatchewan, Canada.[10] The absorption intensity was measured as the partial fluorescence yield (PFY), determined by postprocessing the emission spectra collected using Si drift detectors. The beamline monochromator has a resolving power of about 5000 at the N K-edge. The X-ray emission spectroscopy (XES) measurements were collected at Beamline 8.0.1.1 of the Advanced Light Source in Berkeley, California, USA.[11] The beamline monochromator has a resolving power of about 5000. The emission spectrometer is in the Rowland Circle configuration and has a resolving power of about 1000. Samples were prepared for measurement under Ar or N_2 atmospheres to avoid hydrolysis of LCMS, which is mildly hygroscopic. The powder samples were pressed into clean In foil, prior to transfer to the vacuum chambers used for the measurements. All measurements were conducted under a vacuum of 10^{-6} Torr or better.

3.2.2.2 Calculations

The density functional theory calculations presented here used the WIEN2k software package.[12] This package uses linearized augmented plane waves (LAPW) and augmented plane waves with local orbitals (APW+lo) to solve the Kohn–Sham equations. The generalized gradient approximation of Perdew, Burke, and Ernzerhof (GGA-PBE) was used throughout to model the exchange-correlation energies. Additional calculations using the modified Becke–Johnson (mBJ) potential were conducted, in order to obtain accurate estimates of the band gap.[13] The *k*-mesh for each sample was determined by increasing the mesh size until the total energy of the unit cell converged to 10^{-5} Ry. Core hole calculations used 2 × 1 × 1 supercells, with an appropriately scaled *k*-mesh.

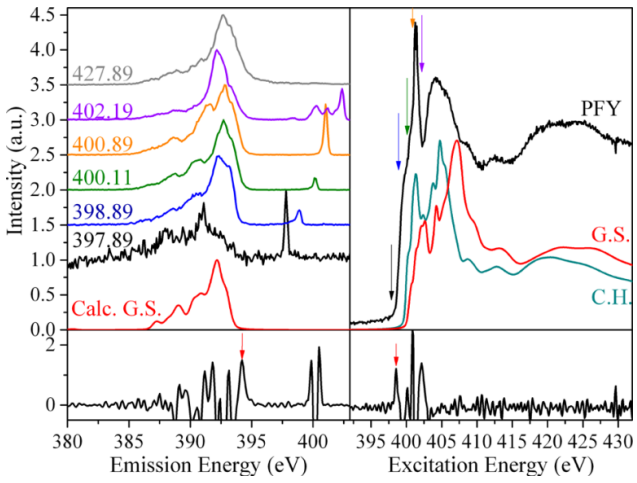

Figure 1. X-ray emission and absorption spectra of LCMS. The XES (left) and XAS (right) are shown alongside DFT calculations, while the second derivatives of the 400.11 eV RXES spectrum and the XAS spectrum are shown in the lower panels. The calculated ground state (g.s.) and excited state (core hole, c.h.) spectra are shown as red and cyan curves, respectively.

3.2.2.3 Nitrogen K-edge and the Band Gap

Soft X-ray emission and absorption measurements for each sample were conducted at the N K-edge and are shown in Figures 1 and 2. The X-ray absorption spectroscopy (XAS) measurements were collected as partial fluorescence yield (PFY). The X-ray emission spectroscopy (XES) measurements can be divided into two types, based on the excitation energy that was used. Those spectra excited near the onset of the XAS will contain resonant effects and are referred to here as RXES (resonant X-ray emission spectroscopy) spectra. They will be discussed in a subsequent section. The spectrum collected with an excitation energy of 427.89 eV, which is well above the absorption edge, should contain no resonant effects and represents a normal X-ray emission spectroscopy (NXES) spectrum. Both the XAS and the NXES have intensities that to first order are proportional to the density of states of the material.[14] Calculated spectra are shown alongside the measurements. A calculation for the ground state (g.s.) of each system is given, as is an excited state (core hole, c.h.) calculation that includes a N 1s hole and an electron added to the conduction band. The former is sufficient for describing the XES spectra, whereas an excited state calculation with a core hole is generally needed to properly describe the XAS spectra.[15-17] The band gaps and other properties of LCMS and BLAS can now be discussed in turn.

It can be seen that there is excellent agreement between the measured and calculated spectra of LCMS in Figure 1. There is a small apparent disagreement between the measured and calculated XES spectra in the region from about 395 to 405 eV. The peaks present in the measured spectra are due to X-ray scattering, which is not captured in the DFT models of the spectra. There is a small region of apparent disagreement in the XAS around 402 eV. However, this is simply due to absorption from N_2 gas that results from small amounts of radiation damage to the sample. As discussed elsewhere for similar phosphors, this is of no consequence to the results of interest here.[18] Outside of the narrow region of N_2 absorption the calculations and experiment match exceptionally well. It is also clear that the core hole calculation provides the best match to the XAS data. The proportionality of the X-ray spectra to the density of states, along with a successful model of the excited state, allows for a determination of the band gap. The band gap is defined by the energy difference between the onsets of the valence and conduction band densities of states. To determine the valence and conduction band onsets, the second derivatives of the XES and XAS spectra are taken, respectively. The band onsets are taken to be the first peaks above the noise level at the upper edge of the XES and lower edge of the XAS spectra, as indicated with red arrows in the bottom of Figure 2. This gives an experimentally determined gap of 4.33 ± 0.20 eV. Applying a DFT-derived correction for the effect of the core hole (the calculated energy difference between the CB onset in the ground and excited states) and nonequivalent site splitting of 0.51 eV to the band separation provides an accurate band gap measurement. In this way the band gap of LCMS is found to be 4.84 ± 0.20 eV. The main contributions to the error is the uncertainty in energy calibration when bringing emission and absorption energies to a common energy axis. It should be noted that in order to avoid influence of N_2

emissions in the determined valence band onset, the second derivative of the XES spectrum excited at 400.11 eV has been used, as no N_2 will be excited at this energy. The contributions of N_2 to spectra excited at higher energies is evident.[19] The calculated band gap for this system is 3.04 eV. This underestimation is typical and can be improved upon by using the mBJ exchange-correlation potential.[13] In this case a band gap of 4.15 eV results, in much better agreement with experiment.

Comparing the measured and calculated spectra for BLAS in Figure 2, it can be seen that there is again excellent agreement. The core hole effect is somewhat overestimated and leads to the usual conclusion that the band gap given here will represent an upper limit. Using the same methodology as above the band gap of BLAS is found to be 4.82 ± 0.20 eV. The calculated band gap using the GGA potential is found to be 3.26 eV, and the band gap resulting from use of the mBJ potential is 4.43 eV. Given that the mBJ potential is expected to be accurate to within about 10%, the agreement here is good. The experiment and calculations suggest that the band gaps of LCMS and BLAS are nearly identical, with that of BLAS perhaps being slightly larger by a few tenths of an electronvolt. The band gaps measured here are in good agreement with those from optical measurements in the literature, which yielded band gaps of about 4.6 eV for each sample.[7,9]

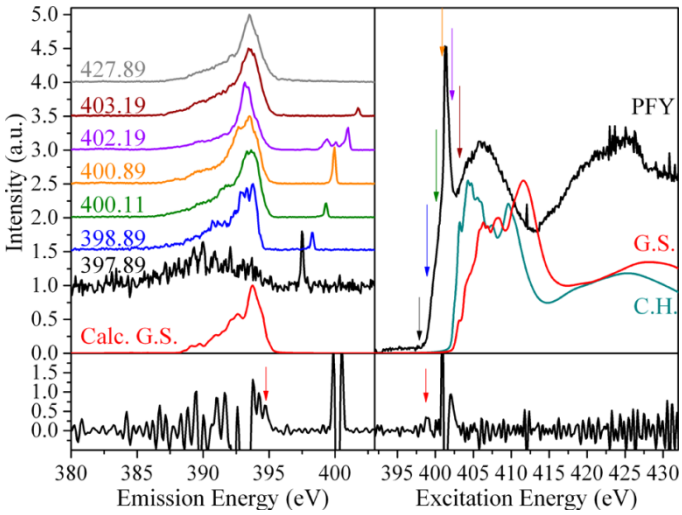

Figure 2. X-ray emission and absorption spectra of BLAS. The XES (left) and XAS (right) are shown alongside DFT calculations, while the second derivatives of the 400.11 eV RXES spectrum and the XAS spectrum are shown in the lower panels.

3.2.2.4 Density of States and Band Structure

Given the good agreement between the experimental and calculated spectra, it is worthwhile to look at the density of states (DOS) of each system in order to try to develop a deeper understanding of their electronic structures. In particular, why these materials, despite having different compositions and crystal structures, have similar band gaps. Further, why LCMS has a relatively large band gap when compared to the compositionally similar phosphor SMS. The band gap of the latter, which is 3.28 ± 0.20 eV, is detrimental to the efficiency of its $4f^7 \rightarrow 5d^14f^6$ emissions when doped with Eu^{2+}.[18] In this case both LCMS and BLAS have band gaps similar to the ultraefficient phosphor SLA, which has an

elemental composition similar to BLAS.[20] The similarity, and subtle differences, of all of these compounds make their comparison very informative.

The density of states of LCMS and BLAS are shown in Figure 3. The DOS of LCMS can be considered first. Gross features of the DOS are quite similar to SLA and SMS.[18,20] The N *p*-states dominate the upper VB. There is a strong presence of Si p-states in the middle VB and *s*-states toward the lower VB. The Si *p*-states are also strong in the middle of the CB. These features are characteristic of strong N *p*–Si sp^3 hybridization, as seen in SMS. There is comparatively little presence of the Mg states, which is due to it being largely ionized. The lower CB is dominated by the Ca *d*-states. It is common for the alkaline earth ion d-states to contribute heavily to the lower CB.[18,20]

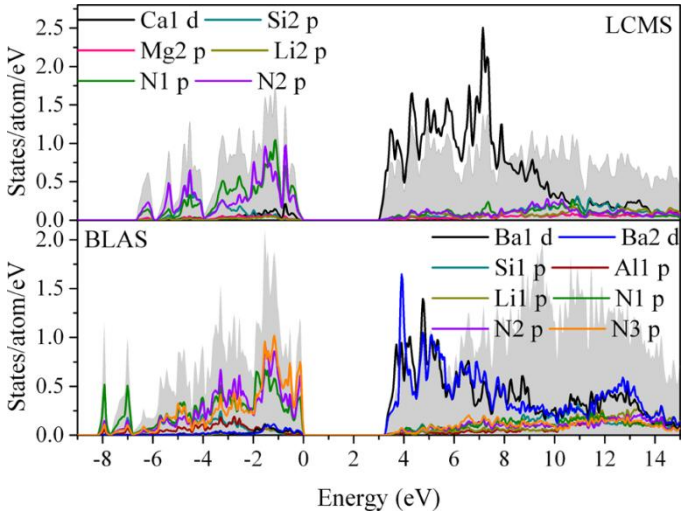

Figure 3. Calculated density of states for LCMS (top) and BLAS (bottom). The structures derived from XRD were used for both.

There is again tremendous similarity between the gross features of the DOS of BLAS and the other systems being discussed. There is evidence for strong interaction between N *p*-states and sp^3-hybridized Si states. Similar to LCMS, the Ba *d*-states are dominant in the lower CB. There is a noticeable presence of the Li states near the nonbonding N *p*-states at the upper edge of the VB, as well as higher in the CB. This implies relatively weak orbital overlap and that the Li is largely ionized. The Al states show the same general structure as the Si states. However, their intensity is lower than the Si states, which is to be expected from the lower electronegativity of Al. It can be concluded that the Al states are also modeled well by sp^3 hybrids, though their bonding with N is slightly more ionic.

Ignoring the alkaline earth cations for the moment, all other cations that are contributing to the network structure are tetrahedrally coordinated by N atoms. The DOS support the intuitive notion that in moving along the sequence Si → Al → Mg → Li, the bonds become more ionic, and the approximation of local sp^3 hybrid orbitals becomes less appropriate for describing the DOS. Indeed, the coordination of Li is not even tetrahedral in BLAS, but has the higher coordination that is expected from more ionic bonding. The strong bonding between Si, Al, and N leads to sp^3 hybridization of the Si and Al, but also leads to Si and Al playing a prominent role in determining the orbital character at the N sites. Careful analysis of the relative intensity of nonbonding N p-states for the nonequivalent

sites, and contributions to different regions of the VB and CB support this readily.[21] The influence of the Mg and Li will be secondary.

A few final points are worth noting. The well-defined peaks in the N *p*-states in the lower VB of BLAS suggests that the covalency of its lattice is slightly higher than in LCMS.[22] This is supported by the red optical emissions for LCMS, which must also stem from the smaller Eu–N distance and consequently higher crystal field splitting.[23,24] The analysis of SLA and SMS in the literature would suggest that the band gap of LCMS should be much smaller than that of BLAS. It has been found that the band gap of SMS is small as a result of the small energetic separation of the Mg *s*- and N *p*-states.[18] The band gap of LCMS is about 1 eV larger than that of SMS, despite containing Mg. The central problem in need of explanation here is whether Mg still limits the band gap of LCMS, and if so, why it is larger than in SMS. There are two phenomena that offer an explanation, both related to the N–Mg separation in the two materials; it is much smaller in LCMS. This is quite natural, as one generally expects a reduction in bond lengths if smaller alkaline earth metals are used, here Ca as opposed to Sr.[25] The reduction of the N–Mg bond length will increase the bond-antibond splitting, which in general varies as the square of the bond length.[22] As well, the increasing covalency of the N–Mg bond will drive the hybridization of the Mg *s*- and *p*-states, leading to orbitals that more closely resemble sp^3 hybrids. This also increases the energy of the unoccupied Mg states. These two effects in concert can account for the band gap increase seen in LCMS, when compared to SMS. Given the comparatively high energy of Ca *d*-states, one still expects the CB minimum to be determined by the Mg states, though the presence of the emptied Li *s*-states should be born in mind.[18,20] From the analysis of SLA in literature,[18,20] it can be expected that BLAS should have a band gap about the size of SLA, which is seen. At the same time, one would also expect that the CB minimum will be determined by the Ba d-states. The DOS are suggestive of this, but it is worthwhile to view the band structures of these materials in order to get a more detailed view of their electronic structures.

3.2.2.5 Band Structures

The calculated band structures of LCMS and BLAS are shown in Figure 4. The low-lying conduction bands of both materials are largely composed of the alkaline earth d-states, with one exception in LCMS. The lowest-lying conduction band is of predominantly s-character. This is in keeping with the idea that the tetrahedral cation sites, Mg and Li, will determine the CB minimum in this material. Thus, BLAS is a type I material like SLA, and LCMS a type II material like SMS. Materials are, according to Dorenbos, designated as type I if those alkaline earth ions that will be replaced by rare-earth ions determine the CB minimum, and type II materials otherwise.[26] It is also interesting to note the curvature of the bands at the VB and CB edges of LCMS. The low lying s-band of LCMS has a high curvature and therefore should have a relatively high electron mobility.[22] However, relatively low particle mobilities can be expected at the VB maxima of LCMS. This is to be expected with the VB maxima determined by the nonbonding N *p*-states. Both have indirect band

gaps, which should be conducive to high quantum efficiency; indirect band gaps discourage CB-VB transitions for the Eu^{2+} emission. The VB maxima of LCMS and BLAS are at the I and M-Γ points, respectively. Likewise the CB minima are respectively at Γ and Γ-Z.

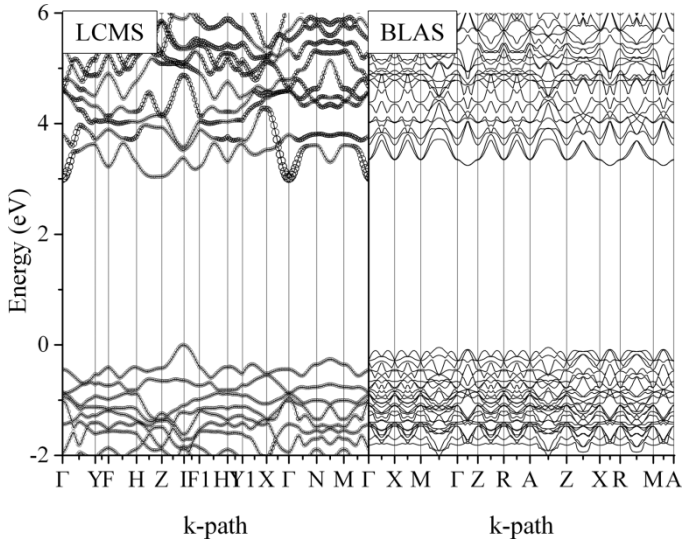

Figure 4. Calculated band structure of LCMS (left) and BLAS (right). The s-character states are plotted for LCMS, where the thickness of the lines in the plot indicates the relative contribution of the s-states to the total DOS at each point.

3.2.2.6 RXES

There are two main phenomena leading to the variations in spectral shape of the RXES spectra in Figures 1 and 2: resonant inelastic X-ray scattering (RIXS) and nonequivalent site excitation. The former manifests itself as peaks at some energy loss below the elastic scattering peaks, which results from the creation of, or scattering from, quasiparticles. They can be seen to follow the excitation energy, as indicated by the elastic scattering peak itself in the energy region from about 395 to 405 eV. The exact elastic peak energies will be given by the excitation energies shown above each spectrum. The low energy RIXS excitations present in the spectra will be discussed in another contribution. The RXES shows up as changes in the shape of the constant-energy fluorescence spectrum, which is proportional to the DOS of the states involved. It is the changes in the shape of this constant energy portion of the spectra that are of interest here. It can be seen in the above figures that there is little change in spectral shape for most spectra excited above 398 eV, implying all nonequivalent N-sites are excited in rough proportion to their concentrations, as with the NXES spectrum. There is an obvious change in shape for the lowest-energy excitation at 397.89 eV. The spectral shape is clearer in LCMS, and so it will be the point of focus. In Figure 5 this spectrum is shown alongside several models.

Usual explanations would be that either the variation in spectral shape is due to nonequivalent site excitation or crystal momentum-conserving RIXS. Here, an accurate explanation is offered by the DOS of the tetrahedral cation s-states, when they are compared to the measured spectrum. It would seem that the spectral shape is directly proportional to the *s*-state density of Mg and Li. This is reminiscent of the results for RIXS in molecular systems, where the transitions are governed by orbital

symmetry.[19,27] Keeping in mind that the DOS calculations suggest the CB minimum of LCMS is associated with the same states, this RXES excitation is clearly the result of excitation to the (|N *p*⟩ + |Mg/Li *s*⟩)* and de-excitation from the |N *p*⟩ + |Mg/Li *s*⟩ states. This strongly reinforces that the CB minimum of LCMS is determined by the Mg s- and Li *s*-states. To exclude alternative explanations, nonequivalent site excitation and momentum-conserving RIXS are considered in turn. The calculated spectra for nonequivalent site excitation are shown in the middle panel of the figure and show little variation in spectral shape, in keeping with the experimental spectra in earlier figures. Clearly nonequivalent site excitation does not describe the spectrum. As for the *k*-conserving RIXS,[28] it leads to emission from only those states with the same crystal momentum as the state to which the core electron was excited. A calculation for this type of emission, assuming excitation at the Γ point, is shown in the lower panel of the figure. Again this offers little explanation of the spectral shape.

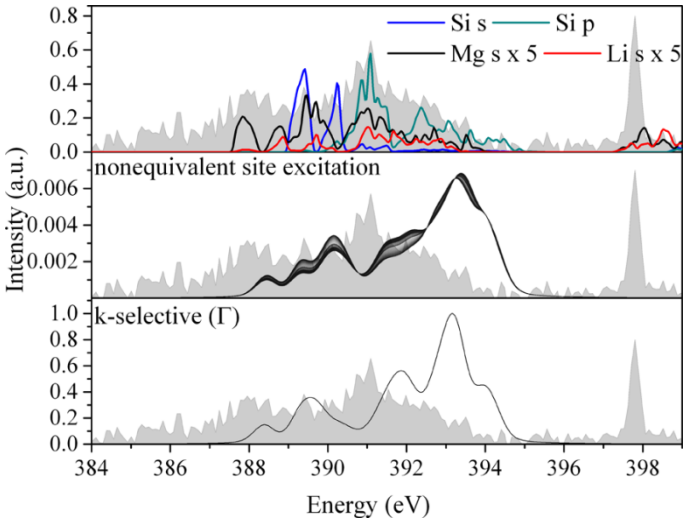

Figure 5. Top: select calculated DOS of LCMS. The RXES spectrum excited at 397.89 eV is shown as the shaded gray curve in each panel. Middle: calculated RXES spectra for excitations over the first 8 eV of the CB, which form a contour plot. The spectra are derived from weighting the contributions from nonequivalent N sites by their relative absorption intensities at each incident X-ray energy. Bottom: spectra due only to those states near the Γ point.

Based on this and the preceding discussion of the DOS and band structures, the energy level diagram in Figure 6 has been constructed. It is based on atomic term energies and is simply qualitative, but summarizes the energetic ordering of states for LCMS and BLAS in a useful manner.[22] The utility of such a diagram is rooted in the linear combinations of atomic orbitals model of electronic structure, as well as the general importance of nearest neighbor bonds in forming electronic structures in solids.[22,29-31]

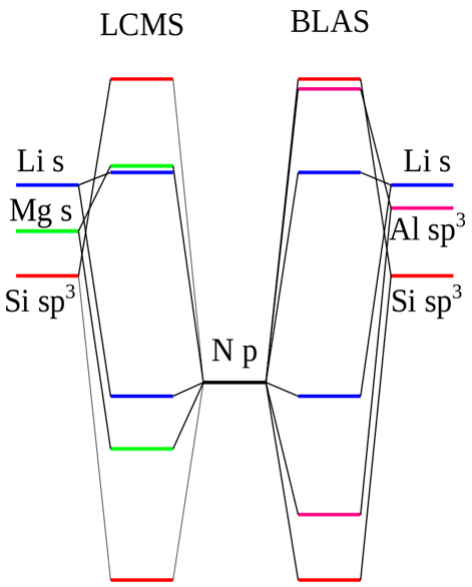

Figure 6. Energy level diagram for LCMS and BLAS based on tabulated term energies and the orbital mixing described above.[22]

There has been a sustained push to develop new phosphors, with new electronic structures and thus new emission and absorption properties.[1,32,33] Nitrides have fostered particular interest, as a result of their structural variation and demonstrated eminent luminescence properties.[5,25,34] It is well-known at this point that the band gap and relative positions of intragap states are key properties, holding sway over the luminescence characteristics of a given material.[26,35,36] The ability to predict or understand the band gap and positions of energy levels in the gap is invaluable, as is an understanding of the effect of elemental substitutions, which are generally applied to influence luminescence properties.[37] Herein lies the importance of studies providing accurate band gap measurements, linked to the underlying structure–property relationships of the material.

3.2.3 Conclusions

The band gaps of LCMS and BLAS have been found to be 4.84 ± 0.20 and 4.82 ± 0.20 eV, respectively. They therefore have the large band gaps that are a prerequisite for efficient emissions from the Eu^{2+} dopant. The DOS of the nonequivalent N sites show only small variations in intensity with energy, which suggest they will have the narrow emissions that are desirable in the next generation of LED-phosphors. LCMS has been determined by RXES measurements and DFT calculations to be a type II material, while BLAS is a type I material. Importantly, this designation predicts their properties, such as changes in their band gaps and thus TQ characteristics, under doping and use as the base of solid-solution series for tuning optical properties. Finally, it has been clarified that LCMS has a large band gap when compared to SMS because of its decreased N–Mg separation that drives orbital hybridization at the Mg site, and increased bond–antibond splitting. It is clear that both of these materials have high potential for use as phosphors, or as the conceptual parents of phosphors, in the next generations of high-efficiency phosphors for solid-state lighting.

3.2.4 References

[1] Pust, P.; Schmidt, P. J.; Schnick, W. A revolution in lighting. *Nat. Mater.* **2015**, *14*, 454-458.

[2] Kitai, A., *Luminescent Materials and Applications*, John Wiley and Sons Ltd: England, U.K., **2008**.

[3] Mueller-Mach, R.; Mueller, G.; Krames, M. R.; Höppe, H. A.; Stadler, F.; Schnick, W.; Juestel, T.; Schmidt, P. Highly efficient all-nitride phosphor-converted white light emitting diode. *Phys. Status Solidi A* **2005**, *202*, 1727.

[4] Huppertz, H.; Schnick, W. $Eu_2Si_5N_8$ and $EuYbSi_4N_7$. The First Nitridosilicates with a Divalent Rare Earth Metal. *Acta Crystallogr. Sect. C* **1997**, *53*, 1751-1753.

[5] Pust, P.; Weiler, V.; Hecht, C.; Tücks, A.; Wochnik, A. S.; Henß, A. K.; Wiechert, D.; Scheu, C.; Schmidt, P. J.; Schnick, W. Narrow-band red-emitting $Sr[LiAl_3N_4]:Eu^{2+}$ as a next-generation LED-phosphor material. *Nat. Mater.* **2014**, *13*, 891-896.

[6] Schmiechen, S.; Schneider, H.; Wagatha, P.; Hecht, C.; Schmidt, P. J.; Schnick, W. Toward New Phosphors for Application in Illumination-Grade White pc-LEDs: The Nitridomagnesosilicates $Ca[Mg_3SiN_4]:Ce^{3+}$, $Sr[Mg_3SiN_4]:Eu^{2+}$, and $Eu[Mg_3SiN_4]$. *Chem. Mater.* **2014**, *26*, 2712-2719.

[7] Strobel, P.; Schmiechen, S.; Siegert, M.; Tücks, A.; Schmidt, P. J.; Schnick, W. Narrow-Band Green Emitting Nitridolithoalumosilicate $Ba[Li_2(Al_2Si_2)N_6]:Eu^{2+}$ with Framework Topology whj for LED/LCD-Backlighting Applications. *Chem. Mater.* **2015**, *27*, 6109-6115.

[8] Schmiechen, S.; Nietschke, F.; Schnick, W. Structural Relationship between the Mg-Containing Nitridosilicates $Ca_2Mg[Li_4Si_2N_6]$ and $Li_2Ca_2[Mg_2Si_2N_6]$. *Eur. J. Inorg. Chem.* **2015**, 1592-1597.

[9] Strobel, P.; Weiler, V.; Hecht, C.; Schmidt, P. J.; Schnick, W. Luminescence of the Narrow-Band Red Emitting Nitridomagnesosilicate $Li_2(Ca_{1-x}Sr_x)_2[Mg_2Si_2N_6]:Eu^{2+}$ (x = 0–0.06). *Chem. Mater.* **2017**, *29*, 1377-1383.

[10] Regier, T.; Krochak, J.; Sham, T. K.; Hu, Y. F.; Thompson, J.; Blyth, R. I. R. Performance and capabilities of the Canadian Dragon: The SGM beamline at the Canadian Light Source. *Nucl. Instrum. Methods Phys. Res.* **2007**, *582*, 93-95.

[11] Jia, J. J.; Callcott, T. A.; Yurkas, J.; Ellis, A. W.; Himpsel, F. J.; Samant, M. G.; Stöhr, J.; Ederer, D. L.; Carlisle, J. A.; Hudson, E. A.; Terminello, L. J.; Shuh, D. K.; Perera, R. C. C. First experimental results from IBM/TENN/TULANE/LLNL/LBL undulator beamline at the advanced light source. *Rev. Sci. Instrum.* **1995**, *66*, 1394-1397.

[12] Schwarz, K.; Blaha, P. Solid state calculations using WIEN2k. *Comput. Mater. Sci.* **2003**, *28*, 259-273.

[13] Tran, F.; Blaha, P. Accurate Band Gaps of Semiconductors and Insulators with a Semilocal Exchange-Correlation Potential. *Phys. Rev. Lett.* **2009**, *102*, 226401.

[14] F. de Groot, A. K., *Core Level Spectroscopy of Solids*, Taylor & Francis Group, USA, **2008**.

[15] Mahan, G. D. Final-state potential in x-ray spectra. *Phys. Rev. B* **1980**, *21*, 1421-1431.

[16] Kurmaev, E. Z.; Wilks, R. G.; Moewes, A.; Finkelstein, L. D.; Shamin, S. N.; Kuneš, J. Oxygen x-ray emission and absorption spectra as a probe of the electronic structure of strongly correlated oxides. *Phys. Rev. B* **2008**, *77*, 165127.

[17] von Barth, U.; Grossmann, G. The effect of the core hole on x-ray emission spectra in simple metals. *Solid State Commun.* **1979**, *32*, 645-649.

[18] Tolhurst, T. M.; Schmiechen, S.; Pust, P.; Schmidt, P. J.; Schnick, W.; Moewes, A. Electronic Structure, Bandgap, and Thermal Quenching of $Sr[Mg_3SiN_4]:Eu^{2+}$ in Comparison to $Sr[LiAl_3N_4]:Eu^{2+}$. *Adv. Opt. Mater.* **2016**, *4*, 584-591.

[19] Nordgren, J.; Glans, P.; Gunnelin, K.; Guo, J.; Skytt, P.; Såthe, C.; Wassdahl, N. Resonant soft X-ray fluorescence spectra of molecules. *Appl. Phys. A* **1997**, *65*, 97-105.

[20] Tolhurst, T. M.; Boyko, T. D.; Pust, P.; Johnson, N. W.; Schnick, W.; Moewes, A. Investigations of the Electronic Structure and Bandgap of the Next-Generation LED-Phosphor $Sr[LiAl_3N_4]:Eu^{2+}$ – Experiment and Calculations. *Adv. Opt. Mater.* **2015**, *3*, 546-550.

[21] Tolhurst, T. M.; Braun, C.; Boyko, T. D.; Schnick, W.; Moewes, A. Experiment-Driven Modeling of Crystalline Phosphorus Nitride P_3N_5: Wide-Ranging Implications from a Unique Structure. *Chem. Eur. J.* **2016**, *22*, 10475-10483.

[22] Harrison, W. A., *Electronic Structure and the Properties of Solids*, W. H. Freeman and Company: San Francisco, CA, **1980**.

[23] Gauthier, G.; Jobic, S.; Evain, M.; Koo, H. J.; Whangbo, M. H.; Fouassier, C.; Brec, R. Syntheses, Structures, and Optical Properties of Yellow Ce_2SiS_5, $Ce_6Si_4S_{17}$, and $Ce_4Si_3S_{12}$ Materials. *Chem. Mater.* **2003**, *15*, 828-837.

[24] Dorenbos, P. Energy of the first $4f^7 \rightarrow 4f^6 5d$ transition of Eu^{2+} in inorganic compounds. *J. Lumin.* **2003**, *104*, 239-260.

[25] Pucher, F. J.; Marchuk, A.; Schmidt, P. J.; Wiechert, D.; Schnick, W. Luminescent Nitridophosphates $CaP_2N_4:Eu^{2+}$, $SrP_2N_4:Eu^{2+}$, $BaP_2N_4:Eu^{2+}$, and $BaSr_2P_6N_{12}:Eu^{2+}$. *Chem. Eur. J.* **2015**, *21*, 6443-6448.

[26] Dorenbos, P. Thermal quenching of Eu^{2+} $5d$–$4f$ luminescence in inorganic compounds. *J. Phys.: Condens. Matter* **2005**, *17*, 8103-8111.

[27] Rubensson, J.-E. RIXS dynamics for beginners. *J. Electron Spectrosc. Relat. Phenom.* **2000**, *110-111*, 135-151.

[28] Eisebitt, S.; Eberhardt, W. Band structure information and resonant inelastic soft X-ray scattering in broad band solids. *J. Electron Spectrosc. Relat. Phenom.* **2000**, *110–111*, 335-358.

[29] Hart, G. L. W.; Zunger, A. Electronic structure of BAs and boride III-V alloys. *Physical Review B* **2000**, *62*, 13522-13537.

[30] Gupta, R. P. Electronic structure of crystalline and amorphous silicon dioxide. *Physical Review B* **1985**, *32*, 8278-8292.

[31] Weaire, D.; Thorpe, M. F. Electronic properties of an amorphous solid. I. A simple tight-binding theory. *Phys. Rev. B* **1971**, *4*, 2508-2520.

[32] Huang, A.; Yang, Z.; Yu, C.; Chai, Z.; Qiu, J.; Song, Z. Tunable and White Light Emission of a Single-Phased $Ba_2Y(BO_3)_2Cl:Bi^{3+},Eu^{3+}$ Phosphor by Energy Transfer for Ultraviolet Converted White LEDs. *J. Phys. Chem. C* **2017**, *121*, 5267-5276.

[33] Gao, X.; Li, W.; Yang, X.; Jin, X.; Xiao, S. Near-Infrared Emission of Er^{3+} Sensitized by Mn^{4+} in $Ca_{14}Zn_6Al_{10}O_{35}$ Matrix. *J. Phys. Chem. C* **2015**, *119*, 28090-28098.

[34] Zeuner, M.; Pagano, S.; Schnick, W. Nitridosilicates and Oxonitridosilicates: From Ceramic Materials to Structural and Functional Diversity. *Angew. Chem. Int. Ed.* **2011**, *50*, 7754-7775.

[35] Dorenbos, P. A Review on How Lanthanide Impurity Levels Change with Chemistry and Structure of Inorganic Compounds. *ECS J. Solid State Sci. Technol.* **2013**, *2*, R3001-R3011.

[36] Sun, Y.; Li, P.; Wang, Z.; Cheng, J.; Li, Z.; Wang, C.; Tian, M.; Yang, Z. Tunable Emission Phosphor $Ca_{0.75}Sr_{0.2}Mg_{1.05}(Si_2O_6):Eu^{2+}$, Mn^{2+}: Luminescence and Mechanism of Host, Energy Transfer of $Eu^{2+} \rightarrow Mn^{2+}$, $Eu^{2+} \rightarrow$ Host, and Host $\rightarrow Mn^{2+}$. *J. Phys. Chem. C* **2016**, *120*, 20254-20266.

[37] Lin, C. C.; Liu, R. S. Advances in Phosphors for Light-emitting Diodes. *J. Phys. Chem. Lett.* **2011**, *2*, 1268-1277.

3.3 Direct Measurements of Energy Levels and Correlation with Thermal Quenching Behavior in Nitride Phosphors

published in: *Chem. Mater.* **2017**, *29*, 7976-7983

authors: Thomas M. Tolhurst, Philipp Strobel, Peter J. Schmidt, Wolfgang Schnick and Alexander Moewes

DOI: 0.1021/acs.chemmater.7b02974

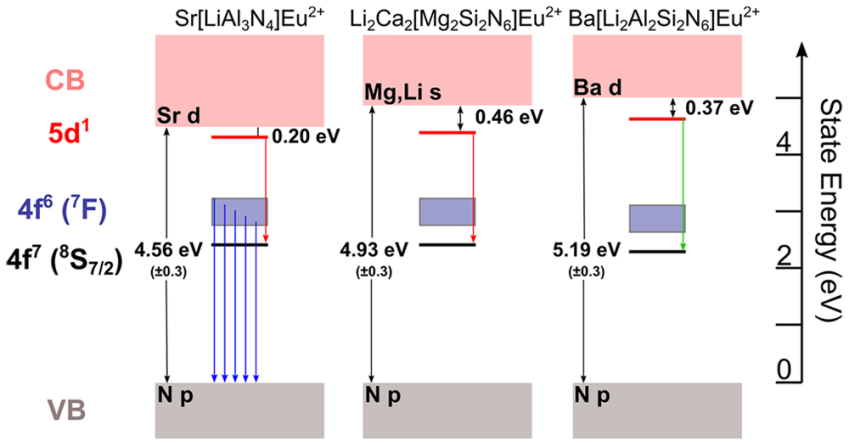

Abstract. Highly efficient narrow-band red emitting (*RE*) phosphors are the most desired and requested materials for developing illumination grade phosphor-converted light emitting diodes (pcLEDs). This study presents direct measurements of *RE* energy levels, critical to the color and efficiency of LED phosphors. For the first time, we experimentally determine the energetic separation of the Eu 5*d* state and the conduction band, which is the key indicator of quantum efficiency. This was achieved for the next-generation pcLED phosphors $Li_2Ca_2[Mg_2Si_2N_6]:Eu^{2+}$, $Ba[Li_2(Al_2Si_2)N_6]:Eu^{2+}$, and $Sr[LiAl_3N_4]:Eu^{2+}$ using resonant inelastic X-ray scattering. Band to band and 4*f* to valence band transitions are directly observed in X-ray excited optical luminescence spectra of $Sr[LiAl_3N_4]:Eu^{2+}$ and $Sr[Mg_3SiN_4]:Eu^{2+}$. These techniques are widely applicable and create a comprehensive, experimental picture of the Eu^{2+} energy levels in these compounds, leading to a complete understanding of all pertinent electronic processes. This study forms the base needed for a detailed discussion of the structure–property relationships, such as specific atoms, coordination and density of states, underpinning phosphor color and efficiency.

3.3.1 Introduction

Phosphor-converted light emitting diodes (pcLEDs) are positioned to significantly reduce global energy consumption, as they stand to become the dominant commercial lighting technology in the near future.[1,2] This trend is enhanced through the tailorability of pcLEDs enabled by combining different phosphors emitting throughout the visible spectrum, as well as improvements in device architecture.[1,3-6] There is extraordinary interest in efficient and narrow-band red phosphors, which reduce energy consumption and allow high color rendition (CRI, R_a >90).[1] Recently, the red emitting nitridoaluminate $Sr[LiAl_3N_4]:Eu^{2+}$ was developed, promising an increase of 14% in luminous efficacy when compared to state of the art high CRI LEDs.[7]

The synthesis and characterization of band emitting LED phosphors has become a vibrant research domain, and many advances have been made in understanding the useful and diverse properties of phosphors. Rare earth (*RE*)-doped materials have received particular favor for their tunable and, oftentimes, efficient emissions throughout the visible spectrum.[2,8-10] The luminescence of interest in Eu^{2+}-doped phosphors is due to the $5d^14f^6 \rightarrow 4f^7$ transition. The participation of the 5*d* leads to their tunability and eminence as next-generation phosphors. The crystal structure of the host material strongly influences the energetic position of the 5*d* state, responsible for emission tailoring, by two factors. First is the nephelauxetic effect. With N allowing a more covalent bonding, a smaller energetic distance between the $5d^14f^6$ and the $4f^7$ is obtained, leading to a red-shifted emission compared to ligands O or F. Second, the ligand crystal field splitting (CFS) is strongly dependent on the coordination of the dopant. The larger the CFS, the stronger the red shift of emission. This is in contrast to the more localized *RE* 4*f* states, which are not influenced by the crystal structure. Emission of Eu^{3+}-doped phosphors, as an example, where emission is only due to 4*f* state transitions, gives technically less relevant line emission. The *f* states are mainly localized and therefore miss the possibility of tailoring emission properties.

The high variability of the excited 5*d* energy state makes the structure–property relationships leading to efficient emissions and stable compounds complex and difficult to model. It is of the utmost importance to understand these relationships in order to expedite the discovery and engineering of new, desirable phosphors. It has long been understood that the band gap plays a significant role in the efficiency of phosphors.[8,11-13] However, the problem is multidimensional and has been pursued aggressively, albeit largely empirically, in many earlier works.[8,14-18] There is therefore a relatively strong empirical framework in place for predicting the energetic positions of the *RE* 4*f* and 5*d* states in a general way in the band gaps of luminescent materials. It is the interplay of the locations of band edges of the host material and the rare-earth ion states that leads to the manifold luminescence properties in these compounds and, critically, phosphor efficiency through the 5*d*–conduction band (CB) separation.[7,10,19] Dorenbos showed that thermal quenching (TQ) is caused by thermal excitation of the 5*d* electron to the CB, refuting other discussed mechanisms.[8] The knowledge of the precise location of the *RE* 5*d* states is therefore indispensible, and this precision has to date eluded the

aforementioned empirical methods. The 5*d*–CB separation has most often been estimated semiquantitatively and indirectly by referring to TQ data. TQ measurements of a phosphor give an overview of the emission intensity loss at elevated temperatures. Most important for application in LEDs is a phosphor's strong emission up to 200 °C, which is the average operating temperature. TQ data are often not reliable, as they strongly depend on the purity of the investigated sample, since defect states lead to an augmented TQ effect, e.g., by trapping of electrons. Direct measurements of RE state energies are completely lacking, as only few are accessible through standard optical spectroscopy experiments. This is especially so for the Eu 5d^1 state, as it is an excited state and therefore not accessible by standard methods. X-ray spectroscopy techniques allow the measurement of these state energies and therefore are a powerful complement to optical studies. In this work, a new method to experimentally determine the energetic positions of the Eu 5*d* states is described, leading to a complete and comprehensive understanding of all processes involved.

This study of next-generation phosphors $Sr[LiAl_3N_4]:Eu^{2+}$ (SLA), $Sr[Mg_3SiN_4]:Eu^{2+}$ (SMS), $Li_2Ca_2[Mg_2Si_2N_6]:Eu^{2+}$ (CLMS), and $Ba[Li_2(Al_2Si_2)N_6]:Eu^{2+}$ (BLSA) uses resonant inelastic X-ray scattering (RIXS) and X-ray excited optical luminescence (XEOL).[7,11,20-24] The samples themselves represent a cross section of the current frontier in the development of luminescent materials, each possessing ideal characteristics for application in pcLEDs, ranging from highly efficient emissions, to narrow band emissions, to emissions in different spectral regions. SMS exhibits the narrowest emission bandwidth (λ_{em} = 615 nm; *fwhm* ~ 43 nm, 1170 cm^{-1}) of any Eu^{2+}-doped nitrides discovered to date but also shows insufficient thermal quenching (TQ) behavior.[11] SLA is an attractive phosphor for industrial application, as it shows narrow-band red emission at 650 nm (*fwhm* ~ 50 nm, 1180 cm^{-1}) and a superior relative quantum efficiency (QE) >95% at 200 °C.[7] Narrow-band red emitting CLMS (λ_{em} = 638 nm, *fwhm* ~ 62 nm, 1510 cm^{-1}) shows high TQ despite a sufficiently large band gap.[21] Green emitting BLSA (λ_{em} = 532 nm, *fwhm* ~ 57 nm, 1960 cm^{-1}) exhibits a relative emission intensity of ~70% at 200 °C.[20] These phosphors are therefore compelling for this investigation, as they all have similar crystal structure characteristics, with slight differences leading to widely varying properties. The depth to which the origins of these properties are understood varies considerably. Emission efficiency in particular is a quagmire, being highly dependent on the *RE* energy level relative positions to others in the host lattice and heretofore difficult to measure.

The energetic separation between the 5d and conduction band—the key parameter determining thermal quenching behavior—in each sample is measured using RIXS. This adds a new aspect to the RIXS method that is used to identify quasi-particles such as magnons and orbitons, which are otherwise difficult to observe.[23] Additional energy states are probed with XEOL, allowing confirmation of the previously reported band gaps of SLA and SMS, as well as the measurement of intragap states that are typically not observed in optical spectroscopy measurements. The direct measurement of rare earth energy levels on a case-by-case basis provides the foundation needed for a detailed discussion of the structure–property relationships that lead to exceptional phosphor

performance. This work also demonstrates the wide applicability and power of RIXS and XEOL for understanding and directly measuring key phosphor properties, highlighting their potential to become prominent experimental techniques in phosphor research. These highly suitable X-ray techniques are not an obvious choice for phosphor research since the X-ray energies are far from the energies of the optical transitions.

3.3.2 Results and Discussion

3.3.2.1 Determination of the 5d–CB Separation by RIXS

In this section we introduce a new experimental method to obtain detailed information on RE energy levels by synchrotron X-ray spectroscopy. Resonant X-ray emission spectroscopy (RXES) and corresponding X-ray absorption spectroscopy (XAS) data were collected at the N K-edge for CLMS, BLSA, and SLA. Low excitation energy, resonant X-ray emission spectra are displayed in Figure 1a. The principal characteristic of XAS spectra is that they are roughly proportional to the unoccupied partial density of states (DOS),[25] and at the N K-edge the XAS spectra are proportional to the unoccupied density of *p*-character states. There are two main effects noticeable in the RXES spectra. First there are the variations in spectral shape that result from the excitation of nonequivalent N sites in each sample.[26] This is the strongest contribution to the spectra; it simply gives information about the VB density of states of the nonequivalent N sites. Here the focus will be entirely on the second, more subtle observable phenomenon: the RIXS. This process appears as subsidiary peaks at energies just below the elastic scattering peak. They represent energy losses of the incident X-rays to low-energy (optical) excitations.[23] This portion of the spectra is shown on an energy loss scale in Figure 1b.

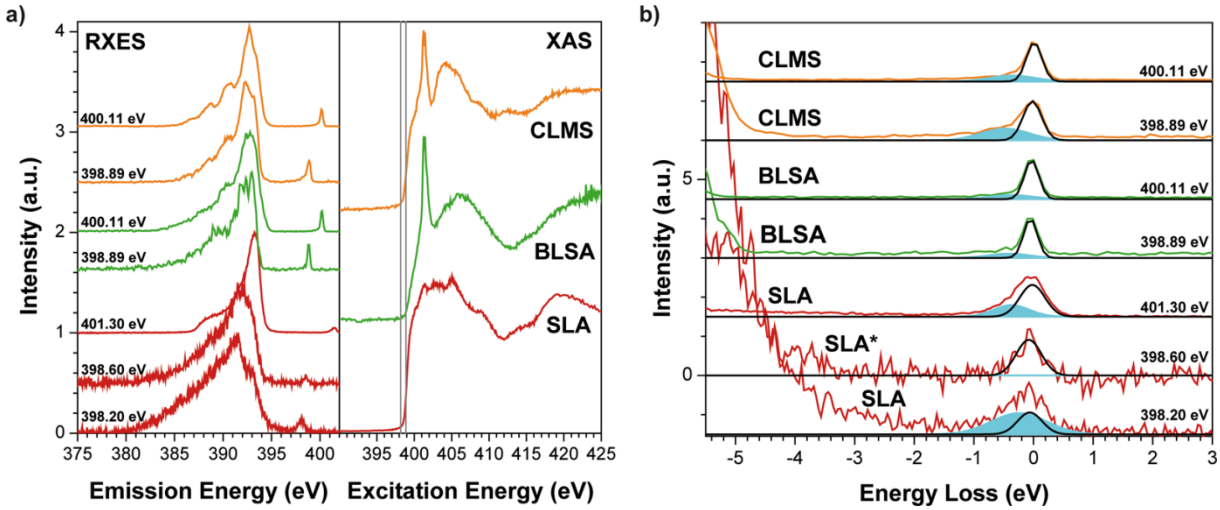

Figure 1. Resonant X-ray emission and absorption spectroscopy measurements. (a) Resonant X-ray emission spectra (left) and absorption (right) at the N K-edge. The 398.20 and 398.89 eV excitations are marked on the absorption spectra as gray, vertical lines. (b) Comparison of the RIXS spectra on an energy loss scale. The peaks from a least-squares fit of two Gaussians to the RIXS are shown as black (elastic) and cyan (loss feature) curves. CLMS (orange), BLSA (green), and SLA (red) spectra are shown.

Excitations using at least two different incident X-ray energies are shown for each sample, one at the CB onset and one at a slightly higher energy. For SLA, data were also collected for an undoped sample (SLA*), and one spectrum is shown in Figure 1. Unless explicitly stated otherwise, the Eu^{2+}-doped samples are those to which the discussion refers. Exact excitation energies are indicated for each RXES spectrum. There are two spectral features in each of the doped samples—elastically scattered radiation and an energy loss feature. We will show in the following that the energy loss arises due to excitations from the rare earth 5*d* level to the conduction band.

The fit results and uncertainties derived from the fitting are given in Table 1. As opposed to quoting the E_0 values for each peak and sample, the energy loss of the RIXS feature, $\Delta E_{RIXS} = E_{0,1} - E_{0,2}$, is given for each sample. For comparison, the ΔE_{TQ} values derived from the thermal quenching (TQ) data on each sample are also given in Table 1. The TQ data and the fit of a typical Arrhenius curve to the data,[7] which was used to obtain the ΔE_{TQ} values in the table, are shown in Figure 2a. Experimental details and details of the fits to the TQ data are given in the Supporting Information.

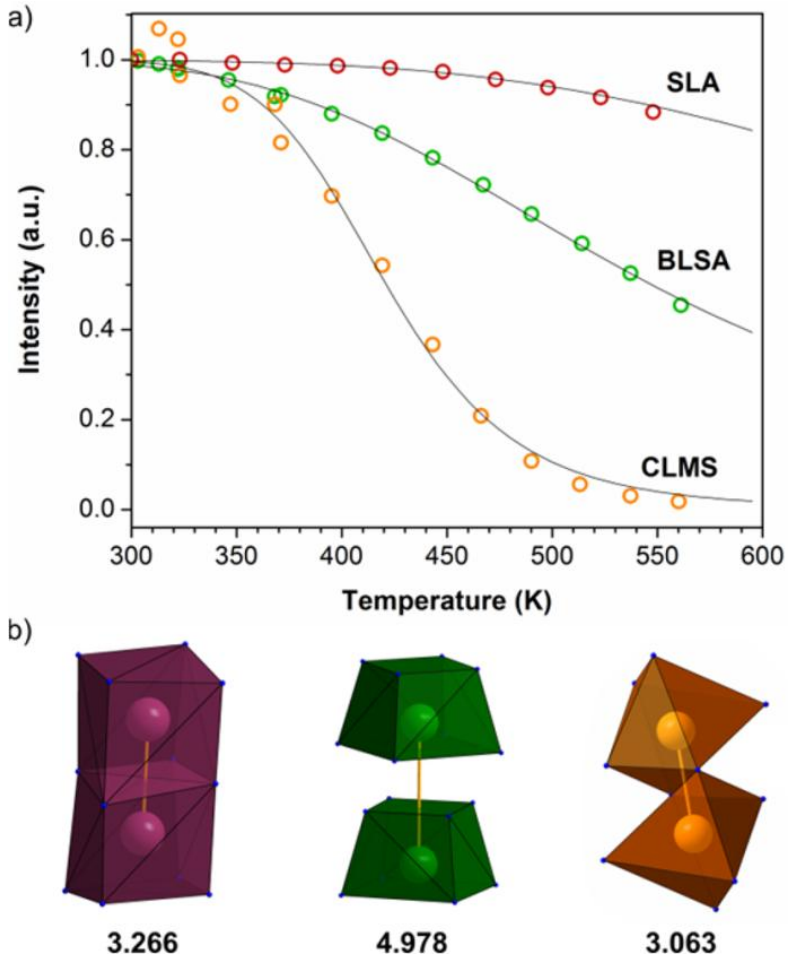

Figure 2. Thermal quenching behavior. (a) Fits of standard Arrhenius-type curves to the thermal quenching data of SLA, BLSA, and CLMS; (b) *AE* coordination by N in SLA (violet), BLSA (blue), and CLMS (orange); shortest *AE*–*AE* distances given in Å.

In the cases at hand all N atoms coordinate with alkaline earth metal ions, or the rare-earth dopants that occupy some of those same sites. Due to the low dopant concentrations (~1%) it is also likely that most N atoms will coordinate with at most one rare earth ion. When combined with previous results showing that the CB minimum in many phosphors, including SLA, consists largely of alkaline earth metal *d*-states,[12,13] it is seen that the *RE* 5*d* to CB transition is effectively a RE 5*d* → M *nd* (M = Ca (*n* = 3), Sr (*n* = 4), Ba (*n* = 5)) transition. It can therefore be proposed that the energy loss in the low excitation energy RIXS spectra is due to the 5*d*–CB transition in each material, which is analogous to an orbital excitation. This also agrees well with previous work using O K-edge RIXS to study intragap states in WO_3, where the defect-associated energy loss was strongest when exciting at the band edge and the intensity of the peak also scaled with the defect concentration.[27] The defect concentrations in this WO_3 study were similar to those of the *RE* dopants here. One would also expect the peak intensity in the case at hand to scale with the degree of N–*RE* orbital overlap, and thus the *RE*–ligand distance. The relative peak intensities in Figure 1b decrease from CLMS to SLA to BLSA, in accordance with the *RE*–ligand distances.

Table 1. Comparison of the Standard Deviations (σ_1, the elastic peak; σ_2, the inelastic peak) and peak Separations from the Fits Shown in Figure 1b[a]

sample	σ_1 (eV)	σ_2 (eV)	ΔE_{RIXS} (eV)	ΔE_{TQ} (eV)
$CLMS_{398.89}$	0.155	0.4	0.46 ± 0.03	0.49 ± 0.03
$CLMS_{400.11}$	0.129	0.375	0.370	
$BLSA_{398.89}$	0.115	0.347	0.37 ± 0.03	0.253 ± 0.008
$BLSA_{400.11}$	0.120	0.355	0.338	
$SLA_{398.20}$	0.205	0.464	0.2 ± 0.1	0.291 ± 0.009
$SLA^*_{398.60}$	0.210	0	n.a.	
$SLA_{401.30}$	0.211	0.302	0.353	

[a] The 5d–CB separations derived from least squares fits to TQ data for each sample are shown in the far right column for comparison. A full explanation is found in the Supporting Information. The TQ data for SLA has been reported previously.[7,12] The undoped SLA sample is denoted as SLA*. Excitation energy is given in eV (subscript).

Further support is provided considering the effect of increasing the excitation energies slightly, as well as by comparing to the data for the undoped SLA sample. The low energy excitation for undoped SLA shows no energy loss feature and an elastic peak with a width that corresponds to that determined from the fits for the other samples. The only difference between the doped and undoped SLA should be the Eu^{2+} dopant, correlating the energy loss feature for low energy excitations to the doping with Eu. The 401.30 eV excitation of SLA and undoped SLA (see Supporting Information Figure 1) is then interesting to consider. The spectra, including the energy loss peak location and width, are identical. The energy loss at higher excitation energies therefore cannot be due to the Eu dopant. Combining this with the observation above that a different energy loss is seen for all samples between the low and the high energy excitations and that the high-energy excitations show similar energy loss for all samples suggests another mechanism is responsible for the energy loss in the latter cases. The energy loss for the low energy excitation varies sample to sample, as would be expected for the 5*d*–CB separation.

The constancy of the energy loss at excitation energies increasingly above the CB minimum is well explained by losses to phonons. It is known that the phonon density rises rapidly over the first few tenths of an eV above the CB minimum and quickly dominates the RIXS spectrum at ligand edges.[28] This explains the quenching of the 5*d*–CB energy loss peak with increasing excitation energy and the differences between SLA and undoped SLA, as well as the differences between samples. Combining this with the good match between the energy loss of the low excitation energy spectra and what is ideally the 5*d*–CB separation derived from the TQ data provides strong support that these RIXS measurements have indeed recorded the 5*d*–CB separation in SLA, CLMS, and BLSA.

This measurement is critical to understanding how the host lattice influences the RE ion, such as that the 5*d* position is highly sensitive to its surroundings in contrast to the 4*f* states. It is interesting to now look at how the determination of the 5*d*–CB separation provides deeper insight into phosphor properties, by looking at the thermal quenching data in Figure 2a. It can be seen that despite its larger ΔE_{RIXS} CLMS shows more dramatic overall thermal quenching. Referring to Supporting Information eq 1, this is readily disentangled. In addition to the ΔE_{TQ} there is a free parameter *A* in the TQ fits, which is proportional to the nonradiative decay rate. The ΔE_{TQ} determines at what temperature the TQ initiates, while *A* determines the slope of the curve, determining how quickly the TQ becomes severe. Now that ΔE_{TQ} can be independently determined, the platform is set to more thoroughly understand other influences on TQ. Since $\Delta E_{TQ} = \Delta E_{RIXS}$ the influence of defects can be inferred to be minimal in the TQ of CLMS and SLA shown here. It follows that the TQ difference is due to intrinsic structural characteristics of the samples. One expects transition rates between states on nearby atoms to be proportional to the overlap of the participating orbitals and, thus, the *RE–AE* (alkaline earth) distance. In SLA the shortest *AE–AE* distance is 3.266 Å, while it is 3.063 Å in CLMS (see Figure 2b). The crystal geometry allows the overlap of d_z^2 states of nearby metal centers and, in conjunction with the last point, indicates that strong orbital overlap with neighboring metal sites causes a large *A* and increased TQ in CLMS.

3.3.2.2 Optical transitions Provided by XEOL

In this section XEOL (X-ray excited optical luminescence) is used to investigate additional optical transitions in the nitride materials. XEOL spectra excited at the Eu $M_{4,5}$-edge for all the samples being considered here are given in Figure 3. XEOL data for the $N_{2,3}$-edge are discussed in Supporting Information Discussion S3. The spectra are divided into regions A, B, and C for ease of discussion. Region A is due to the $5d^1 4f^6 \rightarrow 4f^7$ transition, in agreement with the literature.[7,11,20] It is the emission in the visible spectral region that is usually observed in the optical spectroscopy studies of the investigated phosphors. However, the peaks in regions B and C are not usually observed in the optical spectroscopy data, excited with blue light.

The emission peak in C is only seen in the undoped SLA sample. Given its energetic location and shape it can be assigned to the CB–valence band (VB) transition in the sample.[7,12] This should only be

observed in a high quality sample with few relevant intragap defect states. It can be concluded that the defect concentration in the undoped sample is low and that the Eu states will represent the only relevant intragap states in SLA. Note that this peak is absent in all doped samples, indicating that the Eu states become the preferred pathway for electron–hole recombination whenever present, which is an ideal characteristic for an LED phosphor.

The emission feature in B is only seen in SLA, which based on the results for the undoped sample, should be attributed to Eu states. Given their energetic position it is reasonable to assign the peak to $4f^7\underline{L} \rightarrow 4f^6$ transitions. This would constitute a metal to ligand charge transfer (MLCT). The broad peak is fit well by a sum of Gaussian curves. These are in keeping with the expectations for the energetic locations and widths of charge transfer peaks involving 4*f* states in materials doped with *RE* ions.[8] To assign the peaks in B to particular 4*f* states, the oxidation state of the Eu must be considered in conjunction with the 4*f* occupation, since they determine the relevant state energies.[8,29] It can be inferred from the band structure of SLA that the hole mobility in the VB of SLA will be lower than the electron mobility in the CB. This gives rise to the sequence of possible transitions shown in Figure 3 and further described in the Supporting Information Discussion S4. With the initial trapping of an electron by the Eu 5*d* state, a MLCT of the form $Eu^{1+} + \underline{L} \rightarrow Eu^{2+} + \gamma$ will occur, where the γ is giving rise to one of the peaks in region **B**. It is most likely that the 4*f* electrons are in the ^7F configuration of the $4f^6$ states. The transitions in the diagram are labeled to match the observed peaks in the optical emission spectra. This follows readily from considering the partial screening of the 4*f* states by the singly occupied 5*d*, in conjunction with the measured width and energetic locations of these states in the literature.[29-32]

Further support is built for the preceding results by considering the XEOL measurements made for a high quality, Eu^{2+}-doped powder sample of SMS. The compound is known for its uniquely narrow emissions in the red spectral region and similar crystal structure to SLA.[11] The XEOL spectrum of SMS is shown alongside the preceding spectra in Supporting Information Figure 2. In addition to the expected $5d^14f^6 \rightarrow 4f^7$ emission line, an emission peak in region B is seen. However, its shape is quite different than the peaks seen in the SLA spectrum.

One expects the character of the 4*f* states in both samples to be approximately the same, due to their rather atomic nature. Charge transfer (CT) features should therefore be quite similar. However, there is a substantial difference between SLA and SMS, their band gaps. This has already been correlated to their drastically different thermal quenching behaviors. The band gap of SMS has been measured to be 3.28 ± 0.20 eV in comparison to the 4.56 ± 0.20 eV band gap of SLA.[12,13] Comparing the 3.12 eV spectral position of the peak in region B of the SMS spectrum to these band gap values and noting its similarity in shape to the CB–VB transition in the XEOL of undoped SLA indicate directly that this is the CB–VB transition of SMS, not a MLCT involving the 4*f* states.

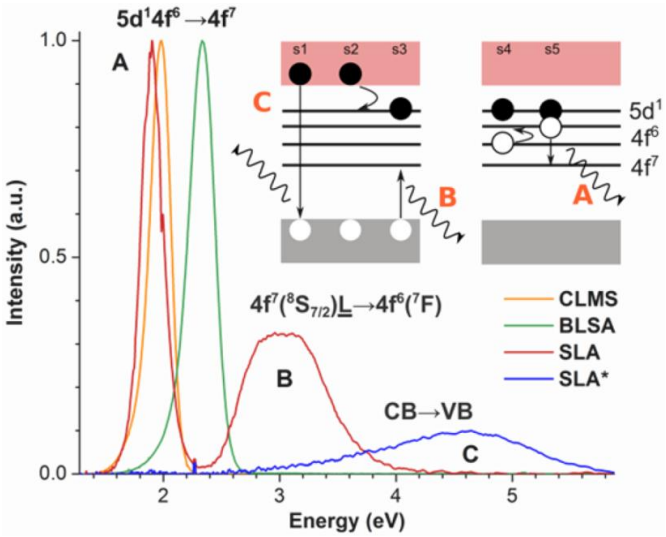

Figure 3. Determination of energy level structure with XEOL. Spectral regions are labeled as A, B, and C, with the corresponding transitions indicated. The diagram in the upper right shows the sequence of transitions expected to follow X-ray absorption and also lead to the transitions observed. Path s1 is a simple CB–VB transition, as seen in the undoped SLA sample. Paths s2 to s5 are the sequence facilitating electron–hole recombination in the doped samples. Straight arrows denote optical transitions, while curved arrows indicate nonradiative transitions.

That the CB–VB transition should be favored over the 4*f*–VB transition in SMS is clear from the band diagram in Figure 3. The overlap of the excited 4*f* states with the CB, combined with the close proximity of the SMS 5*d* states to the CB, lead to the CB–VB transition being favored over the sequence of decays seen in SLA. This not only re-enforces the band diagram constructed above but also provides strong confirmation of the band gap measured with X-ray spectroscopy.[13] Further, it solidifies why the thermal quenching of SMS is stronger than that of SLA; the excited states of the Eu^{2+} ion overlap strongly with the CB at elevated temperatures in SMS, due to its small band gap.

3.3.3 Conclusion

3.3.3.1 Comprehensive Picture

Synchrotron-based optical and X-ray investigations conducted on next-generation LED phosphors enable the presentation of a more comprehensive picture of the physics influencing the overall luminescence properties of Eu^{2+}-doped nitride phosphors, depending on crystal structure and elemental composition. The 5*d*–CB energetic separation in $Sr[LiAl_3N_4]:Eu^{2+}$ (SLA), $Sr[Mg_3SiN_4]:Eu^{2+}$ (SMS), $Li_2Ca_2[Mg_2Si_2N_6]:Eu^{2+}$ (CLMS), and $Ba[Li_2(Al_2Si_2)N_6]:Eu^{2+}$ (BLSA) has been determined through direct measurement, provided by RIXS (XAS). The separations measured through RIXS for SLA, CLMS, and BLSA are 0.2 ± 0.1 eV, 0.46 ± 0.03 eV, and 0.37 ± 0.03 eV, respectively. The optical band-to-band transitions were observed directly in undoped SLA, as well as in doped SMS. At the same time, the doped SLA sample showed metal to ligand charge transfer features that are not usually seen in optical measurements. This is a dramatic step forward in a field that often relies on empirical

models to predict the location of excited rare-earth states in the band gap of a host material. A summarizing schematic illustrating the above points is given in Figure 4. This shows the experimentally determined RE state positions in the band gap that heretofore have been largely inaccessible. The details of the energy level determination are included in Supporting Information Discussion S6. This thorough determination of dopant energy levels in the band gaps of these materials gives the needed experimental basis for a deeper understanding of the structure–property relationships that are critical for tailoring the luminescence properties of phosphors. Important structural parameters that influence functional properties, such as emission color and thermal quenching behavior, are elemental composition, dopant coordination, interatomic distances, and the density of states. In discussing thermal quenching properties of solid-state phosphors there are two principle considerations. First is the host material's band gap. This is influenced by the elements at the edges of VB and CB. At the CB edge, these can either be the elements that form the base of the rigid lattice, like tetrahedrally coordinated Li, Mg, Al, Si, Ga, or Ge, or the elements that fill the voids in the network structures, mostly alkaline earth metals Ca, Sr, and Ba. Some of those elements cause an intrinsic small band gap (<3–4 eV; e.g., Ga, Ge), others allow large band gaps >4 eV that are crucial for high QE. At the VB edge, the band gap is influenced by the O or N p states. In former studies the influence of crystal structure and elements on the host materials band gap was shown.[8,12,13,33-35] A small band gap can be connected to high TQ, e.g., caused by exciton self-trapping effects in the CB,[8,11] while a large band gap is usually connected to a rigid network structure and low TQ.[7]

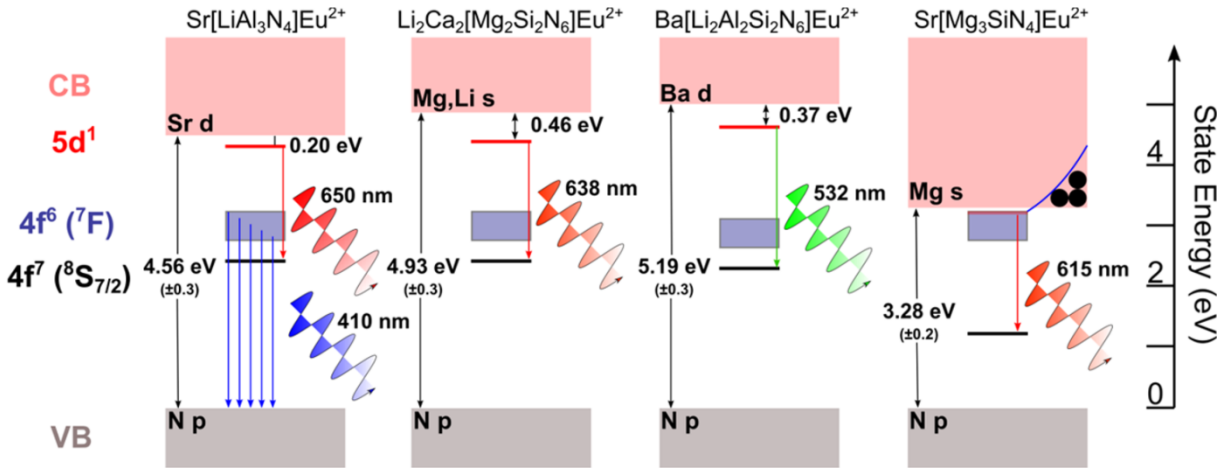

Figure 4. Comprehensive picture of energy levels in frontier phosphors. Experimentally determined RE states in the band gaps of SLA, SMS, CLMS, and BLSA. Band gaps of SLA and SMS are from the literature, and the others are predicted from the results herein.[12,13] SLA, CLMS, and SMS exhibit red luminescence, while SMS already shows strong TQ at ambient conditions, due to its small bad gap. BLSA emits in the green spectral area. The Eu $5d^1$ states (red line) were added to the picture by RIXS analysis. XEOL investigations show $4f^6$–VB transitions in SLA, resulting from a defect free crystalline compound and $5d^1$–$4f^7$ optical emission in all phosphors. While the upper edge of the VB is largely influenced from N *p* states in all phosphors, the lower edge of the CB is either determined by *AE d* states (SLA, BLSA; Type I) or tetrahedral centers Li and Mg *s* states (CLMS, SMS; Type II). The valence and conduction bands in the figure are labeled so as to indicate those states which are the principal contributors, giving a full picture of all the states relevant to luminescence.

Second, the influence of the elemental composition on the position of the intragap defect states is responsible for luminescence. These additional energy states, which here is the Eu 5*d* state, resulting from doping with *RE* elements, and allowing band emission, are a crucial prerequisite for application in illumination grade LEDs.[36] The nephelauxetic effect and CFS largely influence the position of the 5*d* state, as described above. Up to now, it was not possible, except for indirect estimation from TQ data or Eu^{3+} charge transfer band and Eu^{2+} 5*d*–4*f* emission, to determine the energetic position of the Eu 5*d* state in the band gap.[8] Through acquisition of RIXS data on phosphors it will be possible to connect the position of the 5*d* state, with respect to the band gap of the host material, directly to the influence of the environment.

This newly employed method of determining the 5*d*–CB separation stands to revolutionize how phosphors are studied and understood, while allowing the discernment of whether thermal quenching is an intrinsic material property or if it can be reduced by optimized synthesis conditions and reducing the concentration of defect states in the host material. That is to say that if the 5*d*–CB separation is determined to be large with RIXS, poor efficiency can be quickly tied to other influences, such as defects or electron transfer between metal sites. This is a critical distinction that can now be quickly made and facilitates the assessment of a material's potential for use in illumination grade LEDs. An excellent example in the present case is CLMS, which has a large 5*d*–CB separation. Coupling this with its thermal quenching data points to the nonradiative decay rate, as discussed in the Supporting Information, is the source of its poor thermal performance. Analysis of its crystal structure then links this to the small nearest-neighbor separation of the metal sites, an intrinsic material property. This disentanglement hinges on the independent determination of the 5*d*–CB separation. The methods used here can be applied across the gamut of LED phosphors, like Ce^{3+}-doped phosphors and Eu^{2+}-doped oxides, and they therefore represent a powerful tool for the quantitative and experimental analysis of phosphor properties. Understanding the influence of a host material's composition and structure on the Eu 5*d* level position allows a controlled synthesis of novel materials that possess desired features, while maintaining optimum control of emission characteristics.

3.3.4 Experimental Section

3.3.4.1 Analysis of Experimental Data

The energy loss in RIXS spectra is due to the excitation of electrons and quasiparticles in a crystal. In Figure 1a the excitation energy has been subtracted from the abscissa in Figure 1, moving the elastic peaks to an energy loss of 0 eV. Typical energy losses range from <0.1 eV for phonons, to ~0.1 eV for orbital excitations, to ~1.0 eV for crystal field excitations, and >1.0 eV for charge transfer excitations.[23] Many of these transitions are accessible to optical spectroscopy, though some are more effectively studied with RIXS, due to the selection rules involved.

It is critical to note that the fits to the data give the same elastic peak widths for all data collected under the same beamline conditions. This is necessary for the logical consistency of the results and supports the accuracy of the fitting to the peaks shown in Figure 1b. This also immediately suggests that any other breadth to the peaks must be due to inelastic scattering, which will be captured by the second Gaussian peak included in each fit. With this consistent result for the elastic peaks, the inelastic peaks can be regarded as representative of real excitations in the samples. Inelastic peaks are seen in all spectra except for the low energy excitation of undoped SLA. At the same time, the energy losses seen for the high-energy excitations are about the same in each sample, while those for the low energy excitations vary considerably. The energy losses seen for the high and low energy excitation in each sample are thus also different in general.

To make the identification of peak locations and widths as precise as possible, they have been fit with a sum of two Gaussian distributions, with centers E_0 and standard deviations σ, as seen in Figure 1b. The elastic peak and RIXS peaks will be referred to with subscripts 1 and 2, respectively. The parameters were allowed to vary freely during the fitting procedure to minimize any bias in the results.

RIXS measurements at ligand edges tend to emphasize intersite excitations, such as magnons or orbitons, or between metal sites in a crystal.[23,37] They have also been used to measure the location of defect states in the band gaps of metal oxides,[27] which could be enabled by the same superexchange process that makes ligand RIXS sensitive to intersite excitations.[23] The direct measurement of the 5*d*–CB separation will be unaffected by defects in the samples and thus represents a robust and generally applicable method for determining this critical material parameter.

XEOL has proven to be a tremendously useful tool for understanding the electronic structure, presence of defects, and luminescence properties of solids.[38,39] It provides an opportunity to observe luminescence not usually seen in optical excitations due to the high electron–hole density that is introduced into the system during measurement. Combining this with the potential for site-specific information inherent in XAS makes XEOL a formidable technique.[24] For the XEOL experiments the basic experimental technique is to collect an XAS measurement as above, while also recording the optical photon spectra emitted from the sample at every step in the raster scan.[24] The SMS XEOL data were collected in rapid succession with the above XEOL data for CLMS and BLSA. The data shown here for SLA were collected on a separate occasion. In all cases the peaks observed in Region B of Figure 3 and Supporting Information Figure 2 were found to be sensitive to sample decomposition and, thus, defect formation.

3.3.4.2 X-ray Absorption Spectroscopy

The X-ray absorption spectroscopy measurements were conducted at the Spherical Grating Monochromator (SGM) Beamline at the Canadian Light Source, in Saskatoon, Canada.[40] The X-ray emission measurements were conducted at Beamline 8.0.1.1 of the Advanced Light Source in Berkeley, CA, U.S.A.[41] The SGM beamline has a monochromator resolving power of about 5000 at

the N K-edge, while the PFY spectra were collected using an array of silicon drift detectors. The XEOL data were collected with the beamline's Ocean Optics QE 65000 spectrophotometer.[24] Beamline 8.0.1.1 has a monochromator resolving power of 5000, and a Rowland circle X-ray spectrometer for collecting the emission measurements. The spectrometer resolving power is about 800 at the N K-edge. The powder samples were prepared for measurement under N_2 or Ar atmospheres. Once pressed into clean wafers of In foil, the samples were transferred to the vacuum chambers used for the measurements. All measurements were conducted at ambient temperature. The data for CLMS and BLSA were collected under the same beamline conditions in rapid succession. On a separate occasion the data for SLA, including the undoped sample, were collected under the same beamline conditions in rapid succession.

3.3.4.3 Synthesis

All sample preparations were conducted in argon-filled gloveboxes (Unilab, MBraun, Garching; O_2 <1 ppm, H_2O <1 ppm) or in dry Schlenck-type glassware attached to a vacuum line (10^{-3} mbar). This was necessary due to the starting material's high sensitivity against moisture and air. Purification of argon (Air Liquide, 5.0) was performed by streaming of Ar through columns filled with silica gel (Merck), molecular sieve (Fluka, 4 Å), KOH (Merck, ≥85%), P_4O_{10} (Roth, ≥99%), and titanium sponge (Johnsen Matthey, 99.5%) at 700 °C. All reaction mixtures were ground before placing in the reaction vessel.[7,11]

$Sr[LiAl_3N_4]$ was synthesized in a forming gas atmosphere (5% H_2) by heating a stoichiometric mixture of $LiAlH_4$, AlN, and SrH_2. For the synthesis of $Sr[LiAl_3N_4]:Eu^{2+}$ (0.4 mol % nominal composition), EuF_3 was added. The reaction mixture was heated in a tungsten crucible in a radio-frequency furnace (type IG 10/200, frequency 200 kHz, max electrical output 12 kW, Hüttinger, Freiburg) at a rate of 50 °C/min to a target temperature of 1000 °C and maintained for 2 h.[7]

$Sr[Mg_3SiN_4]:Eu^{2+}$ was synthesized with a stoichiometric reaction mixture of $Sr(NH_2)_2$, Mg_3N_2, and "$Si(NH)_2$". The reaction mixture was heated in a tungsten crucible in a rf-furnace under nitrogen atmosphere. The temperature was raised to 1000 °C within 30 min, kept for 6 h, and subsequently quenched to room temperature by switching off the furnace.[11]

$Li_2Ca_2[Mg_2Si_2N_6]:Eu^{2+}$ was synthesized under forming gas (5% H_2) at 1100 °C for 2 h. Starting materials were a mixture of 5.531 g (131.4 mmol) of CaH_2, 5.611 g (40 mmol) of Si_3N_4, 1.393 g (40 mmol) of Li_3N, and 2.917 g (120 mmol) of Mg. For doping, EuF_3 (1 mol %) was added to the reaction mixture. CaO secondary phase is removed by washing with ammonia solution.[42]

$Ba[Li_2(Al_2Si_2)N_6]:Eu^{2+}$ was synthesized in a molybdenum crucible. A mixture of 11.553 g of $Ba_{0.99}AlSi:Eu_{0.01}$, 1.394 g of Li_3N, 2.460 g of AlN, and 2.806 g of Si_3N_4 was fired for 2 h at 1150 °C in forming gas (5% H_2).[43]

3.3.4.4 Thermal Quenching

TQ data were obtained with an AvaSpec-2048 Spectrometer. For excitation, a LED light source (450 nm) was used. Samples were measured in a temperature range from 300 to 560 K with a step size of ~24 K, heated with an IR lamp.

3.3.5 References

[1] Pust, P.; Schmidt, P. J.; Schnick, W. A revolution in lighting. *Nat. Mater.* **2015**, *14*, 454-458.

[2] Ye, S.; Xiao, F.; Pan, Y. X.; Ma, Y. Y.; Zhang, Q. Y. Phosphors in phosphor-converted white light-emitting diodes: Recent advances in materials, techniques and properties. *Mater. Sci. Eng., R* **2010**, *71*, 1-34.

[3] Cui, Y.; Song, T.; Yu, J.; Yang, Y.; Wang, Z.; Qian, G. Dye Encapsulated Metal-Organic Framework for Warm-White LED with High Color-Rendering Index. *Adv. Funct. Mater.* **2015**, *25*, 4796-4802.

[4] Zhang, X.; Xu, B.; Zhang, J.; Gao, Y.; Zheng, Y.; Wang, K.; Sun, X. W. All-Inorganic Perovskite Nanocrystals for High-Efficiency Light Emitting Diodes: Dual-Phase $CsPbBr_3$-$CsPb_2Br_5$ Composites. *Adv. Funct. Mater.* **2016**, *26*, 4595-4600.

[5] Zhuang, Z.; Guo, X.; Liu, B.; Hu, F.; Li, Y.; Tao, T.; Dai, J.; Zhi, T.; Xie, Z.; Chen, P.; Chen, D.; Ge, H.; Wang, X.; Xiao, M.; Shi, Y.; Zheng, Y.; Zhang, R. High Color Rendering Index Hybrid III-Nitride/Nanocrystals White Light-Emitting Diodes. *Adv. Funct. Mater.* **2016**, *26*, 36-43.

[6] Bhardwaj, J.; Cesaratto, J. M.; Wildeson, I. H.; Choy, H.; Tandon, A.; Soer, W. A.; Schmidt, P. J.; Spinger, B.; Deb, P.; Shchekin, O. B.; Götz, W. Progress in high-luminance LED technology for solid-state lighting. *Phys. Status Solidi A* **2017**, 1600826-n/a.

[7] Pust, P.; Weiler, V.; Hecht, C.; Tücks, A.; Wochnik, A. S.; Henß, A. K.; Wiechert, D.; Scheu, C.; Schmidt, P. J.; Schnick, W. Narrow-band red-emitting $Sr[LiAl_3N_4]:Eu^{2+}$ as a next-generation LED-phosphor material. *Nat. Mater.* **2014**, *13*, 891-896.

[8] Dorenbos, P. Thermal quenching of Eu^{2+} 5*d*–4*f* luminescence in inorganic compounds. *J. Phys.: Condens. Matter* **2005**, *17*, 8103-8111.

[9] Zeuner, M.; Pagano, S.; Schnick, W. Nitridosilicates and Oxonitridosilicates: From Ceramic Materials to Structural and Functional Diversity. *Angew. Chem. Int. Ed.* **2011**, *50*, 7754-7775.

[10] Kim, Y. H.; Arunkumar, P.; Kim, B. Y.; Unithrattil, S.; Kim, E.; Moon, S.-H.; Hyun, J. Y.; Kim, K. H.; Lee, D.; Lee, J.-S.; Im, W. B. A zero-thermal-quenching phosphor. *Nat. Mater.* **2017**, *16*, 543–550.

[11] Schmiechen, S.; Schneider, H.; Wagatha, P.; Hecht, C.; Schmidt, P. J.; Schnick, W. Toward New Phosphors for Application in Illumination-Grade White pc-LEDs: The Nitridomagnesosilicates $Ca[Mg_3SiN_4]:Ce^{3+}$, $Sr[Mg_3SiN_4]:Eu^{2+}$, and $Eu[Mg_3SiN_4]$. *Chem. Mater.* **2014**, *26*, 2712-2719.

[12] Tolhurst, T. M.; Boyko, T. D.; Pust, P.; Johnson, N. W.; Schnick, W.; Moewes, A. Investigations of the Electronic Structure and Bandgap of the Next-Generation LED-Phosphor $Sr[LiAl_3N_4]:Eu^{2+}$ – Experiment and Calculations. *Adv. Opt. Mater.* **2015**, *3*, 546-550.

[13] Tolhurst, T. M.; Schmiechen, S.; Pust, P.; Schmidt, P. J.; Schnick, W.; Moewes, A. Electronic Structure, Bandgap, and Thermal Quenching of $Sr[Mg_3SiN_4]:Eu^{2+}$ in Comparison to $Sr[LiAl_3N_4]:Eu^{2+}$. *Adv. Opt. Mater.* **2016**, *4*, 584-591.

[14] Dorenbos, P. The 5*d* level positions of the trivalent lanthanides in inorganic compounds. *J. Lumin.* **2000**, *91*, 155-176.

[15] Dorenbos, P. Relating the energy of the [Xe]5d^1 configuration of Ce^{3+} in inorganic compounds with anion polarizability and cation electronegativity. *Phys. Rev. B* **2002**, *65*, 235110.

[16] Dorenbos, P. $f \rightarrow d$ transition energies of divalent lanthanides in inorganic compounds. *J. Phys.: Condens. Matter* **2003**, *15*, 575-594.

[17] Dorenbos, P. Locating lanthanide impurity levels in the forbidden band of host crystals. *J. Lumin.* **2004**, *108*, 301-305.

[18] Dorenbos, P. A Review on How Lanthanide Impurity Levels Change with Chemistry and Structure of Inorganic Compounds. *ECS J. Solid State Sci. Technol.* **2013**, *2*, R3001-R3011.

[19] Zhang, Y.; Xu, J.; Cui, Q.; Yang, B. Eu^{3+}-doped $Bi_4Si_3O_{12}$ red phosphor for solid state lighting: microwave synthesis, characterization, photoluminescence properties and thermal quenching mechanisms. *Sci. Rep.* **2017**, *7*, 42464.

[20] Strobel, P.; Schmiechen, S.; Siegert, M.; Tücks, A.; Schmidt, P. J.; Schnick, W. Narrow-Band Green Emitting Nitridolithoalumosilicate $Ba[Li_2(Al_2Si_2)N_6]:Eu^{2+}$ with Framework Topology whj for LED/LCD-Backlighting Applications. *Chem. Mater.* **2015**, *27*, 6109-6115.

[21] Strobel, P.; Weiler, V.; Hecht, C.; Schmidt, P. J.; Schnick, W. Luminescence of the Narrow-Band Red Emitting Nitridomagnesosilicate $Li_2(Ca_{1-x}Sr_x)_2[Mg_2Si_2N_6]:Eu^{2+}$ (x = 0–0.06). *Chem. Mater.* **2017**, *29*, 1377-1383.

[22] Schmiechen, S.; Nietschke, F.; Schnick, W. Structural Relationship between the Mg-Containing Nitridosilicates $Ca_2Mg[Li_4Si_2N_6]$ and $Li_2Ca_2[Mg_2Si_2N_6]$. *Eur. J. Inorg. Chem.* **2015**, 1592-1597.

[23] Ament, L. J. P.; van Veenendaal, M.; Devereaux, T. P.; Hill, J. P.; van den Brink, J. Resonant inelastic x-ray scattering studies of elementary excitations. *Rev. Mod. Phys.* **2011**, *83*, 705-767.

[24] Ward, M. J.; Smith, J. G.; Regier, T. Z.; Sham, T. K. 2D XAFS-XEOL Spectroscopy – Some recent developments. *J. Phys.: Conf. Ser.* **2013**, *425*, 132009.

[25] F. de Groot, A. K., *Core Level Spectroscopy of Solids*, Taylor & Francis Group, USA, **2008**.

[26] Tolhurst, T. M.; Braun, C.; Boyko, T. D.; Schnick, W.; Moewes, A. Experiment-Driven Modeling of Crystalline Phosphorus Nitride P_3N_5: Wide-Ranging Implications from a Unique Structure. *Chem. Eur. J.* **2016**, *22*, 10475-10483.

[27] Johansson, M. B.; Kristiansen, P. T.; Duda, L.; Niklasson, G. A.; Österlund, L. Band gap states in nanocrystalline WO_3 thin films studied by soft x-ray spectroscopy and optical spectrophotometry. *J. Phys.: Condens. Matter* **2016**, *28*, 475802.

[28] Eisebitt, S.; Eberhardt, W. Band structure information and resonant inelastic soft X-ray scattering in broad band solids. *J. Electron Spectrosc. Relat. Phenom.* **2000**, *110–111*, 335-358.

[29] Dieke, G. H.; Crosswhite, H. M. The Spectra of the Doubly and Triply Ionized Rare Earths. *Appl. Opt.* **1963**, *2*, 675-686.

[30] Ma, C. G.; Brik, M. G.; Liu, D. X.; Feng, B.; Tian, Y.; Suchocki, A. Energy level schemes of fN electronic configurations for the di-, tri-, and tetravalent lanthanides and actinides in a free state. *J. Lumin.* **2016**, *170*, 369-374.

[31] Dorenbos, P. Energy of the first $4f^7 \rightarrow 4f^6 5d$ transition of Eu^{2+} in inorganic compounds. *J. Lumin.* **2003**, *104*, 239-260.

[32] Dorenbos, P. Systematic behaviour in trivalent lanthanide charge transfer energies. *J. Phys.: Condens. Matter* **2003**, *15*, 8417-8434.

[33] Pösl, C.; Niklaus, R.; Schnick, W. Nitridomagnesogermanate $Ba[Mg_3GeN_4]:Eu^{2+}$: Crystal Structure and Theoretical Calculations of Electronic Properties. *Eur. J. Inorg. Chem.* **2017**, 2422–2427.

[34] Niklaus, R.; Minar, J.; Häusler, J.; Schnick, W. First-principles and experimental characterization of the electronic properties of $CaGaSiN_3$ and $CaAlSiN_3$: the impact of chemical disorder. *Phys. Chem. Chem. Phys.* **2017**.

[35] Hintze, F.; Johnson, N. W.; Seibald, M.; Muir, D.; Moewes, A.; Schnick, W. Magnesium Double Nitride Mg_3GaN_3 as New Host Lattice for Eu^{2+} Doping: Synthesis, Structural Studies, Luminescence, and Band-Gap Determination. *Chem. Mater.* **2013**, *25*, 4044-4052.

[36] Blasse, G.; Bril, A. Characteristic luminescence. *Philips Tech. Rev.* **1970**, *31*, 304-314.

[37] Benckiser, E.; Fels, L.; Ghiringhelli, G.; Moretti Sala, M.; Schmitt, T.; Schlappa, J.; Strocov, V. N.; Mufti, N.; Blake, G. R.; Nugroho, A. A.; Palstra, T. T. M.; Haverkort, M. W.; Wohlfeld, K.; Grüninger, M. Orbital superexchange and crystal field simultaneously at play in YVO_3: Resonant inelastic x-ray scattering at the V L edge and the O K edge. *Phys. Rev. B* **2013**, *88*, 205115.

[38] Wang, D.; Yang, J.; Li, X.; Wang, J.; Li, R.; Cai, M.; Sham, T. K.; Sun, X. Observation of Surface/Defect States of SnO_2 Nanowires on Different Substrates from X-ray Excited Optical Luminescence. *Cryst. Growth Des.* **2012**, *12*, 397-402.

[39] Wang, Z.; Li, C.; Liu, L.; Sham, T.-K. Probing defect emissions in bulk, micro- and nano-sized α-Al_2O_3 via X-ray excited optical luminescence. *J. Chem. Phys.* **2013**, *138*, 084706.

[40] Regier, T.; Krochak, J.; Sham, T. K.; Hu, Y. F.; Thompson, J.; Blyth, R. I. R. Performance and capabilities of the Canadian Dragon: The SGM beamline at the Canadian Light Source. *Nucl. Instrum. Methods Phys. Res.* **2007**, *582*, 93-95.

[41] Jia, J. J.; Callcott, T. A.; Yurkas, J.; Ellis, A. W.; Himpsel, F. J.; Samant, M. G.; Stöhr, J.; Ederer, D. L.; Carlisle, J. A.; Hudson, E. A.; Terminello, L. J.; Shuh, D. K.; Perera, R. C. C. First experimental results from IBM/TENN/TULANE/LLNL/LBL undulator beamline at the advanced light source. *Rev. Sci. Instrum.* **1995**, *66*, 1394-1397.

[42] P. J. Schmidt, P. S., S. Schmiechen, C. Hecht, V. Weiler, W. Schnick Led phosphor comprising bow-tie shaped a2n6 building blocks. *PCT Int. Appl.* **2016**, WO 2016075021A.

[43] A. Tücks, B.-J. S., P. J. Schmidt, S. F. Schmiechen, W. Schnick New nitridoalumosilicate phosphor for solid state lighting. *PCT Int. Appl.* **2015**, WO 2015044106A

4 Narrow-band emitting oxo-, oxonitrido- and nitridoberyllates

4.1 Sr[$BeSi_2N_4$]:Eu^{2+}/Ce^{3+} and Eu[$BeSi_2N_4$]: Nontypical Luminescence in Highly Condensed Nitridoberyllosilicates

published in: *Chem. Eur. J.* **2018**, *24*, 7243-7249
authors: Philipp Strobel, Volker Weiler, Peter J. Schmidt, and Wolfgang Schnick
DOI: 10.1002/chem.201800912

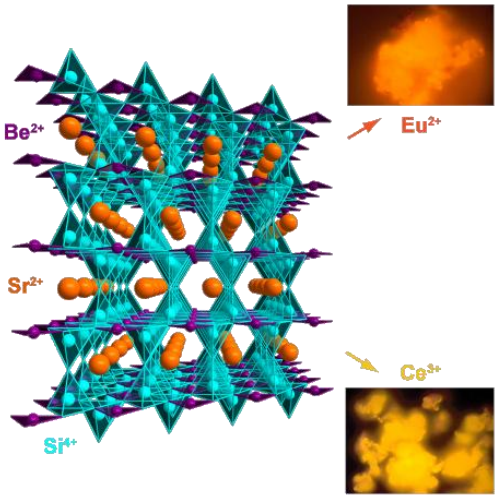

Abstract. *M*[$BeSi_2N_4$] (*M* = Sr,Eu), crystallizing in the hexagonal space group $P\bar{6}2c$, was synthesized from $Sr(NH_2)_2$, Be_3N_2, and "$Si(NH)_2$" in W crucibles under a N_2 atmosphere in a radio-frequency furnace. The crystal structure was solved from powder X-ray diffraction data by the charge-flipping method (Sr[$BeSi_2N_4$]: *a* = 4.86082(2), *c* = 9.42264(4) Å, *Z* = 2; Eu[$BeSi_2N_4$]: *a* = 4.85848(1), *c* = 9.41615(4) Å). *M*[$BeSi_2N_4$] contains a highly condensed rigid network of trigonal planar [BeN_3] units that are connected to Si_2N_7 double tetrahedra by common vertices. *M*[$BeSi_2N_4$] (*M* = Sr,Eu) are the first examples of nitridoberyllosilicates and are isotypic to the oxoberyllate Sr[Be_3O_4]. Eu^{2+}-doped Sr[$BeSi_2N_4$] and Eu[$BeSi_2N_4$] show orange-trapped exciton emission (λ_{em} = 605 nm, *fwhm* ≈ 126 nm), whereas Ce^{3+}-doped samples of Sr[$BeSi_2N_4$] show nontypical yellowish-orange luminescence. Sr[$BeSi_2N_4$] has a large band gap of ≈ 4.4 eV and shows high chemical and thermal stability. Eu^{2+}-doped beryllates with regular $4f^6 5d^1 \rightarrow 4f^7$-emission could be interesting for future application in LEDs upon doping with Eu^{2+} or Ce^{3+} due to large band gaps, rigid networks, and chemical and thermal stability.

4.1.1 Introduction

Solid-state host materials play a significant role in the development and improvement of LEDs, as they allow the conversion of blue light to generate illumination-grade white light. Phosphor converted (pc)LEDs significantly reduce global energy consumption and are already the most common light sources in the global lighting market with a market penetration rate of 52 %.[1,2] For application in pcLEDs, eligible phosphors need to fulfill challenging requirements like high quantum efficiency (QE) as well as chemical and thermal stability. Additionally, a transparent host lattice that allows doping, for example, with *RE* elements like Eu^{2+} and Ce^{3+}, is required.[3] In particular, novel red-emitting phosphors with reduced emission in the IR range, exhibiting exceptional chemical and thermal stability, need to be developed to improve long-time stability of pcLEDs and further reduce energy consumption.

As a materials' stability depends strongly on covalence and a rigid network structure, nitridosilicates and -aluminates appeared as an excellent material class upon doping with Eu^{2+}. They grant higher degrees of condensation, compared to oxo(alumo)silicates, due to the higher connectivity and larger size of the nitride ion and are more covalent and, therefore, contain more rigid bonds, leading to an increased nephelauxetic effect.[4] Red-emitting $(Ba,Sr)_2Si_5N_8:Eu^{2+}$ is already industrially applied. Further investigations showed that with exchange of Si and Al by the light elements Li and Mg novel, large band gap host materials for doping with *RE* became accessible: Recent examples are $Sr[Mg_3SiN_4]:Eu^{2+}$, $Li_2Ca_2[Mg_2Si_2N_6]:Eu^{2+}$, $Ba[Li_2(Al_2Si_2)N_6]:Eu^{2+}$ and $Ca_3Mg[Li_2Si_2N_6]:Eu^{2+}$, $Sr_4[LiAl_{11}N_{14}]:Eu^{2+}$, and isotypic α-$Sr_2[MgAl_5N_7]:Eu^{2+}$.[5-10] $Sr[LiAl_3N_4]:Eu^{2+}$, with exceptional narrow-band emission, is a red phosphor used in recently developed pcLEDs.[1,3,11] The outstanding luminescence properties of these phosphors are based on their rigid nitride networks containing various tetrahedrally coordinated atoms.

Latest investigations on nitridophosphate materials showed that structures built of condensed PN_4 tetrahedra are promising solid-state phosphors.[12-14] Furthermore, experiments introducing Ga and Ge into tetrahedra network structures resulted in part in luminescence upon Eu^{2+}-doping with poor QE due to small band gaps.[15-17]

Promising large band gaps are again predicted when Be is included in tetrahedral coordination in highly condensed crystal structures. Due to the strong covalent character of Be–ligand bonds that are comparable to Al– and Si–ligand bonds, rigid network structures allowing narrow-band emission upon RE-doping could be accessible. A great diversity of novel beryllate structures is expected, since there are two known coordination modes of Be in solid-state materials, namely trigonal planar and tetrahedral coordination. In naturally occurring minerals, several stable solid-state oxides containing tetrahedrally coordinated Be are well known. The most famous is the cyclohexasilicate *beryl*,[18] and its varieties *goshenite* (colorless), *emerald* (green), and *aquamarine* (blue), that are popular gemstones.[19] Oxoberyllates showing both, tetrahedral and trigonal planar coordinated Be, are, for example, layered $Na_6[Be_8O_{11}]$ and $Sr[Be_3O_4]$ with a 3D-network structure.[20,21]

Up to now, only few Be-containing nitrides are described in the literature. The double nitride $BeSiN_2$ crystallizes in a *wurtzite*-type superstructure with *chalcopyrite* (*sphalerite* type) analogous cation ordering.[22] In Li[BeN], layers of $^2_\infty[(Be_{3/3}N_{3/3})^-]$ are connected by LiN_4 tetrahedra, forming a rigid network.[23] MBe_2N_2 (*M* = Mg,Ca,Sr,Ba) compounds are classified as nitridoberyllates. $MgBe_2N_2$ crystallizes in the *anti*-La_2O_3 structure type and exclusively shows tetrahedrally coordinated Be. On the contrary, $AEBe_2N_2$ (*AE* = Ca,Sr,Ba) adopts the CaB_2C_2 structure type containing Be only in trigonal-planar coordination by N, and both elements form planar 4.8^2 nets with edge- and vertex-sharing triangles.[24]

In this contribution we present novel nitridoberyllosilicates with the composition $M[BeSi_2N_4]$ (*M* = Sr,Eu). Their crystal structure is isotypic to that of the oxoberyllate $Sr[Be_3O_4]$ and the nitridoalumoborosilicate $Sr_{1.9}Eu_{0.1}Si_2Al_2B_2N_8$.[21,25] The crystal structure of $Sr[Be_3O_4]$ contains two different Be sites. One site is trigonal planar, the other one has tetrahedral coordination by O. In $Sr[BeSi_2N_4]$, the additional negative charge, when replacing O by N, is compensated by full substitution of Be on the tetrahedrally coordinated site with Si. The remaining Be site with trigonal-planar coordination is not substituted.

Upon doping with Eu^{2+} and Ce^{3+}, $Sr[BeSi_2N_4]$ shows nontypical orange and yellowish-orange emission, respectively. $Eu[BeSi_2N_4]$ again shows emission in the orange spectral region. Crystal structures were investigated by powder X-ray diffraction methods. Elemental composition and morphology were investigated by SEM, EDS, and complementary ICP-OES analyses. Optical and electronic properties are investigated by luminescence and optical reflection spectroscopy.

4.1.2 Results and Discussion

4.1.2.1 Synthesis and elemental analysis

Powder samples of $Sr[BeSi_2N_4]:Eu^{2+}$, $Sr[BeSi_2N_4]:Ce^{3+}$, and $Eu[BeSi_2N_4]$ were synthesized in tungsten crucibles in a rf furnace. Analyses of the products were conducted under an air atmosphere as they have a proved stability under ambient conditions and in an *i*PrOH/glacial acetic acid mixture with a 1:1 ratio. Beige powder samples of $Sr[BeSi_2N_4]:Eu^{2+}$ show red luminescence upon excitation with highly energetic blue light. Powder samples of $Sr[BeSi_2N_4]:Ce^{3+}$ with a beige color emit yellowish-orange light. A Be_3N_2 side-phase with usually less than 4 wt % fraction was obtained in the synthesis of $Sr[BeSi_2N_4]$ samples. Phase-pure powder samples of $Eu[BeSi_2N_4]$ show a mustard yellow body color and poor red emission, due to concentration quenching. Morphology and elemental composition were investigated by electron microscopy, associated by EDS (Energy-dispersive X-ray spectroscopy; Sr,Eu,Si,N,O) and complementary ICP-OES (inductively coupled plasma optical emission spectrometry; Sr,Eu,Be,Si) investigations. SEM pictures of $M[BeSi_2N_4]$ (*M* = Sr,Eu) suggest hexagonal metrics of the nitridoberyllosilicate compounds (Figure S1, Supporting Information). Results of EDS and ICP analyses are compared in Table S1, Supporting Information. Complementary

measurements agree within the accuracy of the measurement method, considering methodical errors, when analyzing light elements.

4.1.2.2 Crystal structure determination

The crystal structure of microcrystalline $Sr[BeSi_2N_4]$ powder was elucidated on the basis of powder X-ray diffraction methods. A hexagonal unit cell with a = 4.86082(2) and c = 9.42264(4) Å was derived after indexing of a diffraction pattern of $Sr[BeSi_2N_4]$. Rietveld refinement was performed using TOPAS-Academic V4.1.[26] $Sr[BeSi_2N_4]$ is isotypic to $Sr[Be_3O_4]$ crystallizing in space group $P\bar{6}2c$ (no. 190). According to PXRD data, the same structural model is valid for $Eu[BeSi_2N_4]$. Summarized crystallographic data of $Sr[BeSi_2N_4]$ and $Eu[BeSi_2N_4]$ are given in Tables 1 and 2, detailed data is given in the Supporting Information. A graphical presentation of the Rietveld refinement of $Sr[BeSi_2N_4]$ and $Eu[BeSi_2N_4]$ is depicted in Figure 1. Atomic positions, bond lengths and angles, and anisotropic displacement parameters are listed in Tables S2–S5, Supporting Information.

Table 1. Crystallographic data of $Sr[BeSi_2N_4]$ and $Eu[BeSi_2N_4]$.[a]

	$Sr[BeSi_2N_4]$	**$Eu[BeSi_2N_4]$**
Crystal system / space group	hexagonal, $P\bar{6}2c$ (no. 190)	
Z	2	
Lattice parameters [Å,°]	a = 4.86082(2)	a = 4.85848 (1)
	c = 9.42264(4)	c = 9.41615 (4)
V [Å^3]	192.807(1)	192.489(1)
ρ [g cm^{-3}]	3.59707(4)	4.71319(6)

[a] Estimated standard deviations are given in parentheses.

Table 2. Atomic coordinates and isotropic displacement parameters of $Sr[BeSi_2N_4]$[a]

Atom (*Wyck.*)	***x***	***y***	***z***	**U_{eq} (Å^2)**	***sof***
Sr (2*d*)	2/3	1/3	1/4	0.0500	1
Si (4*f*)	1/3	2/3	0.07014(1)	0.0500	1
Be (2*a*)	0	0	0	1.08(14)	1
N1 (6*g*)	1/3	0	0	0.96(5)	1
N2 (2*c*)	1/3	2/3	1/4	0.96(5)	1

[a] Estimated standard deviations are given in parentheses.
[b] sof = site occupancy factor.

Applying the Madelung part of the lattice energy (MAPLE) concept, the crystal structure of $Sr[BeSi_2N_4]$ was compared to $Sr[Be_3O_4]$.[27] MAPLE values were calculated for each ion type and for the entire structure. The sum formula $Sr[BeSi_2N_4]$ was formally decomposed to the known ternary compounds $SrSiN_2$ and $BeSiN_2$.[22,28] The deviation of the total lattice energies (Table S6, Supporting Information) of $Sr[BeSi_2N_4]$ is 1.8 %, compared to the sum of total MAPLE values of $SrSiN_2$ and $BeSiN_2$. This proves fair electrostatic consistency with respect to the differing coordination of Be in $BeSiN_2$ (tetrahedral) and in $Sr[BeSi_2N_4]$ (trigonal planar).[4] The results are comparable to the MAPLE value deviations that are found for $Sr[Be_3O_4]$, when decomposed to SrO and three formula units of BeO, giving a deviation of 2.6 %. This even larger discrepancy is deduced to the decrease of the coordination of $O^{[4]}$ in BeO to $O^{[3]}$ in $SrBe_3O_4$.[29]

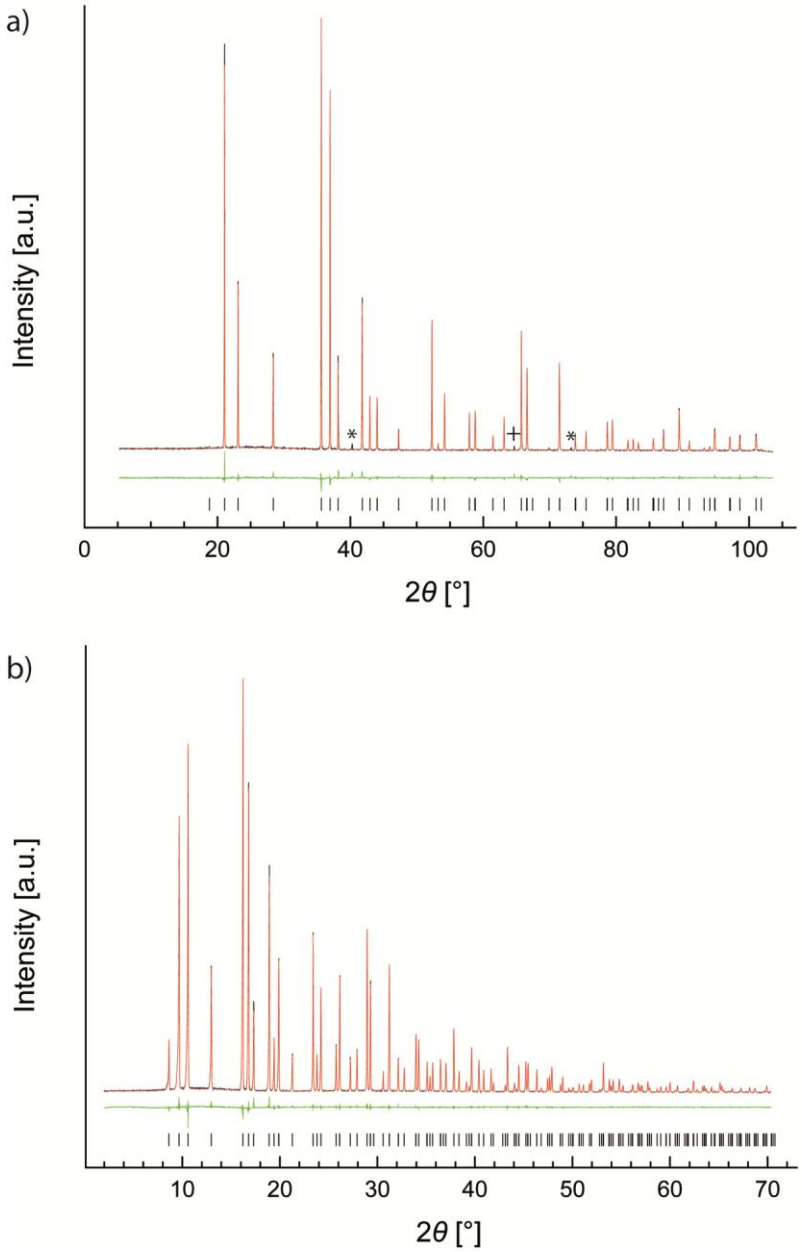

Figure 1. Rietveld refinement of a) $Sr[BeSi_2N_4]$ (Cu $K\alpha_1$ radiation) and b) $Eu[BeSi_2N_4]$ (Mo $K\alpha_1$ radiation) in $P\bar{6}2c$. Experimental data: black line, calculated pattern: red line, and difference curve: green line; black tickmarks: positions of Bragg reflections of $M[BeSi_2N_4]$. Be_3N_2 impurity (+) and unknown side phase (*) are marked.

4.1.2.3 Crystal structure description

$M[BeSi_2N_4]$ (M = Sr,Eu) crystallizes in the hexagonal space group $P\bar{6}2c$ and is isotypic to the oxoberyllate $Sr[Be_3O_4]$.[21] The structure is displayed in Figure 2, coordination of cations are illustrated in Figure 3.

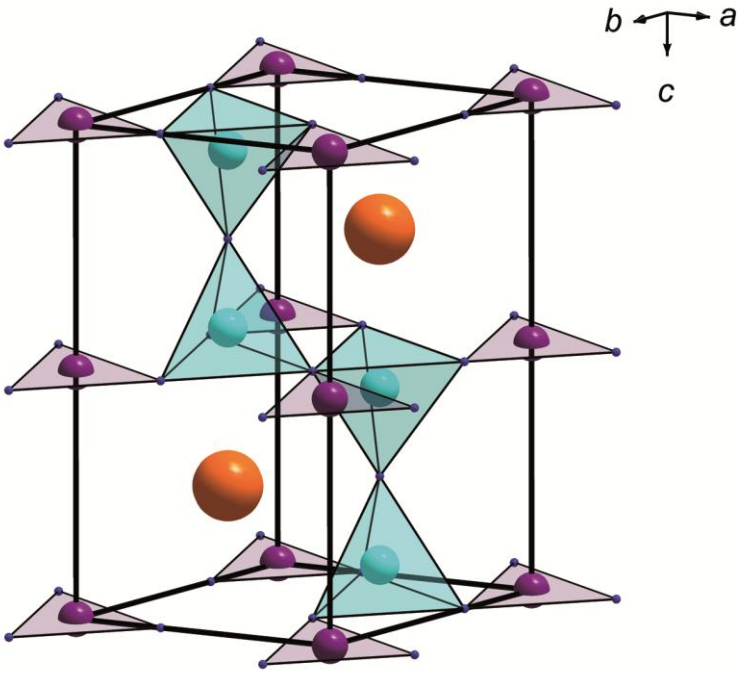

Figure 2. Crystal structure of $M[BeSi_2N_4]$ (M = Sr,Eu); SiN_4 tetrahedra (turquoise), BeN_3 units (violet), Sr (orange).

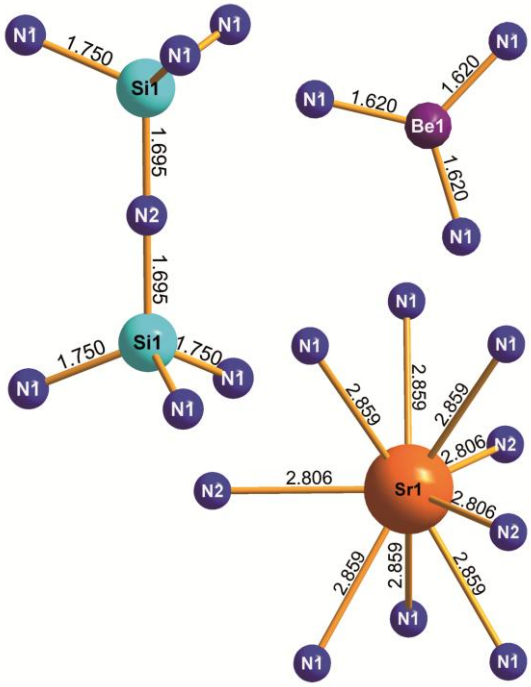

Figure 3. Coordination spheres of Si, Be, and Sr; bond lengths given in Å.

Trigonal planar $[BeN_3]$ units are connected by common vertices to $[Si_2N_7]$ units, built from two vertex-sharing SiN_4 tetrahedra. Base areas of SiN_4 tetrahedra, BeN_3 triangles, and empty rings of three N1 atoms form layers of equilateral triangles in the (001) plane. Regular N1-Be-N1 angles of 120° and their arrangement in the crystal structure lead to the highly symmetric hexagonal crystal structure. The Be–N distance is 1.62 Å and is, therefore, comparable to known bond lengths in trigonal planar units, for example, in $SrBe_2N_2$ (1.63–1.67 Å).[24] The Si–N2–Si angle of 180° is rather uncommon, although a linear angle was observed in, for example, $Ba_2Nd_7Si_{11}N_{23}$ and $La_{16}[Si_8N_{22}][SiON_3]_2$.[30,31] The Si–N2 distance is 1.69 Å and the Si–N1 distance is 1.75 Å, leading to a slightly distorted tetrahedron. Both distances correspond with typical values in nitridosilicates.[4,32] The described ordering of BeN_3 units and Si_2N_7 double tetrahedra leads to a nine-fold coordinated Sr site. Three N2 atoms are positioned in the equatorial plane, with a N2–Sr–N2 angle of 120°. Six N1 atoms, three contributing each from the upper and lower layer, form a regular trigonal prism. Overall, $Sr[BeSi_2N_4]$ is the first nitridoberyllosilicate and the first compound containing trigonal planar BeX_3 units and tetrahedral SiX_4 units (X = N,O).

As discussed earlier by Funahashi et al. in the crystal structure description of $Sr_{2-y}Eu_yB_{2-2x}Si_{2+3x}Al_{2-x}N_{8+x}$ (x < M > 0.12, y < M > 0.10), two trigonal planar BN_3 units, which are analogous to the BeN_3 units, can be exchanged by a Si_2N_7 unit, leading to a higher degree of condensation.[25] While $Sr_2B_2Si_2Al_2N_8$ is isotypic to $Sr[BeSi_2N_4]$, an increasing Si content, combined with reduced B and Al contents, leads to an increase of Sr ligands from nine, up to twelve. By applying the Rietveld method, we have investigated if this structural change applies for $Sr[BeSi_2N_4]$ and $Eu[BeSi_2N_4]$ as well. However, refinement results gave no evidence for additional electron density between Be atoms along *c*. Thus, $M[BeSi_2N_4]$ is confirmed to be isotypic to $Sr[Be_3O_4]$.

4.1.2.4 Luminescence

Microcrystalline samples of $Sr[BeSi_2N_4]$ and $Eu[BeSi_2N_4]$ show luminescence in the visible spectral region upon doping with *RE* elements Eu^{2+} and Ce^{3+} (1 % nominal dopant concentration). Figure 4 shows excitation and emission spectra of $Sr[BeSi_2N_4]:Eu^{2+}$. Spectra of $Sr[BeSi_2N_4]:Ce^{3+}$ are displayed in the Supporting Information. Due to low quantum efficiency (QE), the spectrum of the Eu^{2+}-doped sample is smoothed for presentation.

The obtained Eu^{2+}-containing compounds are highly excitable in the UV to the blue spectral region with $\lambda_{exc} \approx 400$ nm. $Sr[BeSi_2N_4]:Eu^{2+}$ exhibits broadband emission in the orange to red spectral region around 620 nm with a *fwhm* of ≈ 130 nm (≈ 3400 cm^{-1}) due to a large Stokes-shift. The luminescence spectrum of $Sr[BeSi_2N_4]:Eu^{2+}$ shows two distinguishable emission signals. Raw data and a deconvoluted emission spectrum of $Sr[BeSi_2N_4]:Eu^{2+}$ are displayed in Figure S3, Supporting Information. Two emission maxima are found at 594 (*fwhm* ≈ 87 nm) and 651 nm (*fwhm* ≈ 93 nm). The ratio of both emission signals varies in different crystal agglomerates, as is shown in Figure S4, Supporting Information.

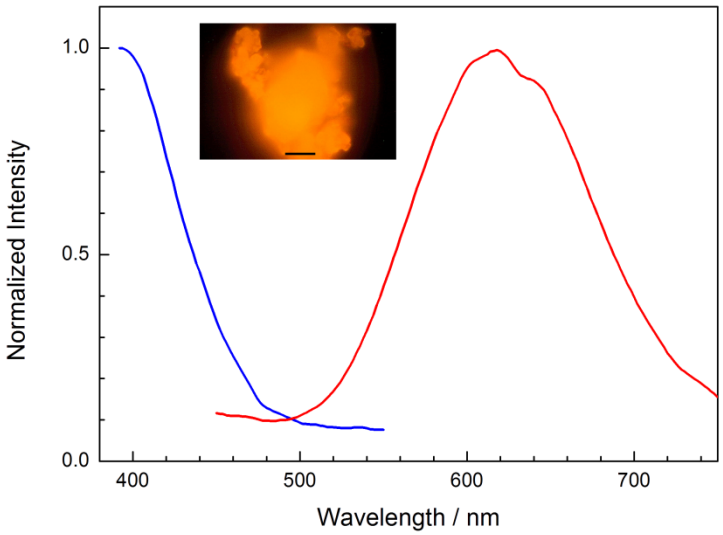

Figure 4. Luminescence spectra and photograph (scale bar: 20 µm) of $Sr[BeSi_2N_4]:Eu^{2+}$ (exc.: dark-blue line, em.: red line).

These nontypical luminescence properties, identified by the large Stokes shift as well as the broad luminescence spectrum with two observed emission signals were investigated in detail by temperature-dependent luminescence measurements, displayed in Figure S5, Supporting Information. $Sr[BeSi_2N_4]:Eu^{2+}$ shows a significant spectroscopic redshift of emission at low temperatures. Up to 100 K, nearly identical spectra with a maximum at λ_{em} = 670 nm with *fwhm* ≈ 112 nm (≈ 2560 cm^{-1}) are obtained. Above 100 K, emission was shifted towards 620 nm, with an increased *fwhm* of 121 nm (≈ 3030 cm^{-1}). With rising temperatures, the relative emission intensity first increases above 100 K and then decreases. The luminescence properties and the complex thermal quenching behavior of $Sr[BeSi_2N_4]:Eu^{2+}$ is, therefore, similar to that of the nitridomagnesoaluminates and -silicates $M[Mg_2Al_2N_4]:Eu^{2+}$ (*M* = Ca–Ba) and $Ba[Mg_3SiN_4]:Eu^{2+}$, and can be explained by nontypical trapped exciton emission.[5,17] At low temperatures ($T \leq 100$ K) emission was observed in $Sr[BeSi_2N_4]:Eu^{2+}$ resulting only from a trapped exciton state, whereas normal Eu^{II} emission from the $4f^6 5d^1$ state was additionally obtained at temperatures >100 K. The increase of relative emission intensity occurs due to arising $4f^6 5d^1 \rightarrow 4f^7$ emission next to the trapped exciton emission, whereas the decrease of emission above 200 K is assigned to thermal quenching of the regular Eu^{II} emission.

When Eu^{II} 5d levels are located close to the bottom of the host lattice conduction band trapped exciton emission has been observed repeatedly.[33] Trapped exciton states are stabilized by large coordination numbers ≥8 of the dopant and increased dopant–ligand distances.[17,33] This phenomenon frequently occurs in Ba compounds, but extraordinarily long Sr–N distances >2.9 Å and a coordination number of nine in $Sr[BeSi_2N_4]$ explain trapped exciton emission in this case.

The spectral luminescence properties of red-emitting $Sr[BeSi_2N_4]:Eu^{2+}$ are comparable to those of other Eu^{2+}-doped nitride phosphors, for example, $(Sr,Ba)_2Si_5N_8:Eu^{2+}$ (λ_{em} = 590–625 nm; *fwhm* ≈ 2050–2600 cm^{-1})[34] and $(Ca,Sr)AlSiN_3:Eu^{2+}$ (λ_{em} ≈ 610–660 nm; *fwhm* ≈ 2100–2500 cm^{-1}).[35]

Ce^{3+}-doped powder samples show broadband yellowish-orange emission, ranging from 500 nm to the IR region, covering nearly the entire visible spectral range (Figure S6, Supporting Information). $Sr[BeSi_2N_4]:Ce^{3+}$ is excitable with UV light. The broadened emission signal was explained by the overlap of two emission signals due to the split ground state of Ce^{3+} in $^2F_{5/2}$ and $^2F_{7/2}$. Additionally, for $Sr[BeSi_2N_4]:Ce^{3+}$ trapped exciton emission was also expected due to an observed large Stokes shift.

4.1.2.5 UV/Vis spectroscopy

$Sr[BeSi_2N_4]$ was investigated by UV/Vis reflectance spectroscopy for band gap determination. Eu^{2+}-doped and nondoped samples were analyzed. The reflectance spectrum of Eu^{2+}-doped $Sr[BeSi_2N_4]$ (Figure S7 a, red line, Supporting Information) with a broad absorption band around 280 nm gives an estimated band gap of approximately 4.4 eV. The intersection of two line tangents gives the experimental value. Additionally, a broad absorption band was displayed in the orange to red spectral region. This band was attributed to the $4f^7 \rightarrow 4f^6\ 5d^1$ absorption in Eu^{2+}. An undoped sample of $Sr[BeSi_2N_4]$ (Figure S7a, black line, Supporting Information) only shows the absorption caused by the host lattice.

The optical band gap was additionally determined by the Kubelka–Munk method. The reflectance spectrum was converted through the Kubelka–Munk function $F(R)=(1-R)^2/2R$.[36] The band gap was then determined with a Tauc plot by drawing a line tangent at the inflection point (Figure S7 b, Supporting Information).[37] For the calculations, the Kubelka–Munk exponent n = 1/2 for a direct allowed transition was used. Although $Sr[BeSi_2N_4]$ has a large band gap, which is a prerequisite for high QE, relatively low QE was observed. This can be explained by a direct band gap that can lead to decreased efficiency, as CB–VB transitions for the Eu^{2+} emission can be encouraged.[38] The band gap size that is evaluated from both methods is approximately in a range of 4.2–4.4 eV.

Further investigations with X-ray spectroscopy methods using synchrotron radiation combined with DFT calculations are planned for a more precise band gap determination. A newly developed method applying RIXS will additionally be used to determine the conduction band–$5d^1$ (Eu^{2+}) separation to further investigate the poor QE behavior of $Sr[BeSi_2N_4]:Eu^{2+}$.[39]

4.1.3 Conclusions

In this contribution, we present the first nitridoberyllosilicates with formula type $M[BeSi_2N_4]$ (M = Sr,Eu). $Sr[BeSi_2N_4]:Eu^{2+}$, $Sr[BeSi_2N_4]:Ce^{3+}$, and $Eu[BeSi_2N_4]$ show nontypical orange and yellowish-orange emission, respectively, upon excitation with UV to blue light. The highly covalent network of $M[BeSi_2N_4]$ provides a large band gap, required for luminescent materials, and proves high chemical and thermal stability. Working with the starting materials under an Ar atmosphere, as is required for air-sensitive reactants, allows a safe handling of Be-containing compounds for synthesis as well as transport to the furnace. The obtained product was stable in water and in a 1:1 *i*PrOH/glacial acetic acid solution. The strong, covalent bonding of Be in combination with SiN_4 tetrahedra in the

highly condensed network structure result in an outstanding increase of chemical stability, compared to the binary compounds Be_3N_2 and BeO that are soluble in water and diluted acids, respectively.

As usual for phosphor host lattices, network structures are described with vertex- or edge-sharing tetrahedra. In $Sr[BeSi_2N_4]$ and isotypic $Sr[Be_3O_4]$, the building units, forming the highly condensed network, were expanded by trigonal planar BeN_3 units. Therefore, introducing Be^{2+} into the solid-state host structures adds a new dimension to structural variability by the combination of trigonal planar Be and tetrahedral coordinated Be, Si, Al, and so forth. Boron was also found in trigonal planar coordination in solid-state materials, but is usually limited to this coordination at ambient pressure. In *c*-BN, compounds synthesized at increased pressure or due to stabilization by, for example, sulfate ions, B is also found in tetrahedral coordination.[25,40-42] Access to new types of networks makes Be a very interesting network-building element for luminescent materials, by approaching two different types of coordination, even in the same crystal structure.[21]

The high chemical stability and the rigid network structure of $M[BeSi_2N_4]$ is an interesting starting point for ongoing investigations for highly efficient narrow-band phosphors, based on beryllate structures. Phosphors, ranging from the blue over green to the red spectral area by varying the O and N content can be accessed. Strong covalent bonds and large band gaps cause us to expect high QE in beryllate compounds, making them highly promising materials class for application in pcLEDs.

4.1.4 Experimental Section

4.1.4.1 Safety assessment

Be containing compounds are known to cause diseases, such as berylliosis, chronic beryllium disease (CBD), and cancer.[43] In particular, Be dusts and soluble salts are hazardous. Small beryllium particles can be inhaled into the lungs and upper respiratory tract, and dissolved Be can accumulate in the human body, leading to chronic diseases. Nevertheless, Be compounds are widely spread in industrial applications, for example, ceramics, automotive materials, and electronics.[43] To reduce the risk of exposure, working with Be in closed systems, such as Schlenk-lines and glove boxes is suitable and required. Insoluble solid-state compounds, such as the mineral and gemstone beryl (*emerald, aquamarine*), with strongly bound Be are less dangerous.[43] Therefore we assess insoluble, coarse-grained Be-containing solid-state compounds with a large density to be less dangerous and handling with appropriate safety measures is feasible. In principle, application of beryllate phosphors in pcLEDs is conceivable, as same coatings for sensitive phosphors, for example, with silica, could protect from exposure and intoxication due to accidental incorporation.[44]

4.1.4.2 Synthesis

Due to the starting materials' high sensitivity to moisture and air, and toxicity of Be dusts, experiments were performed in argon-filled glove boxes (Unilab, MBraun, Garching; O_2 <1 ppm, H_2O <1 ppm) or in dry Schlenk-type glassware attached to a vacuum line (10^{-3} mbar). Purification of argon

gas (Air Liquide, 5.0) was performed in columns filled with silica gel (Merck), molecular sieves (Fluka, 4 Å), KOH (Merck, ≥85 %), P_4O_{10} (Roth, ≥99 %), and titanium sponge (Johnsen Matthey, 99.5 %), heated to 700 °C. As starting materials for the synthesis of $Sr[BeSi_2N_4]$, 0.30 mmol of $Sr(NH_2)_2$ (35.9 mg, synthesized according to the method reported by Zeuner et al.),[45] 0.07 mmol Be_3N_2 (3.6 mg, synthesized from Be (ABCR, 99+%, 325. mesh) in a radio-frequency (rf-)furnace under a N_2-atmosphere at 1300 °C),[46] and 0.30 mmol "$Si(NH)_2$" (17.4 mg, synthesized according to the method by Lange et al.)[47] were ground under an argon atmosphere in a glove box. For the synthesis of doped compounds, 1 mol % EuF_3 (Sigma–Aldrich, 99.99 %) or CeF_3 (Sigma–Aldrich, 99.99 %) were added. $Eu[BeSi_2N_4]$ was synthesized from a mixture of 0.23 mmol $Eu(NH_2)_2$ (42.3 mg, synthesized analogous to $Sr(NH_2)_2$), 0.08 mmol Be_3N_2 (4.2 mg), and 0.35 mmol "$Si(NH)_2$" (20.3 mg). The mixtures were placed in tungsten crucibles and transferred into a water-cooled quartz reactor of a rf furnace (type IG 10/600, frequency 600 kHz, max electrical output 10 kW, Hüttinger Freiburg). The reaction mixtures were heated to 1500 °C under a N_2 atmosphere within 45 min, maintained at this temperature for 6 h, subsequently cooled to 700 °C in 10 h, and finally quenched to room temperature by switching off the furnace.

4.1.4.3 Elemental analysis

The title compounds' elemental composition was determined by energy dispersive X-ray spectroscopy (EDS) and complementary ICP-OES analysis. For EDS a Dualbeam Helios Nanolab G3 UC scanning electron microscope (SEM, FEI) with X-Max 80 SDD detector (Oxford Instruments) was used. The EDS data were obtained from several particles at an accelerating voltage of 20 kV. Morphology of the microcrystalline samples was additionally investigated by SEM. Inductively coupled plasma optical emission spectrometry (ICP-OES) was conducted with a Varian Vista RL spectrometer, to determine the atomic cation ratio (Be:Sr:Eu:Si).

4.1.4.4 Powder X-ray diffraction

The obtained powder samples were ground and sealed in a glass capillary (Hilgenberg, d = 0.2 mm). PXRD data were collected on a STOE STADI P diffractometer (Mo $K\alpha_1$ or Cu $K\alpha_1$ radiation, Ge(111) monochromator, Mythen 1K detector) in a modified Debye–Scherrer geometry. Crystal structure solution via charge flipping, extraction of the peak positions, pattern indexing, structure solution, Fourier calculations, and Rietveld refinements were carried out using the TOPAS package.[48-50] Reflection intensities were extracted with the Pawley method. A cylindrical absorption correction was applied during the refinement. Peak profiles were calculated with the fundamental parameters approach, a direct convolution of source emission profiles, axial instrument contributions, crystallite size, and microstrain effects. Texture was included with a spherical harmonics function. The background was adapted with a shifted Chebyshev function with 12 polynomials. The Sr, Eu, and Si sites were refined with anisotropic displacement parameters. Be and N sites were refined isotropically. Isotropic displacement parameters of N1 and N2 were refined with a common value.

Further details on the crystal structure investigations may be obtained from the Fachinformationszentrum Karlsruhe, 76344 Eggenstein-Leopoldshafen, Germany (fax: (+49) 7247-808-666; e-mail: crysdata@fiz-karlsruhe.de), on quoting the depository number CSD-434198 ($Sr[BeSi_2N_4]$) and CSD-434199 ($Eu[BeSi_2N_4]$).

4.1.4.5 Luminescence

Luminescence properties of powder samples were investigated with a HORIBA Fluoromax4 Spectrofluorimeter system connected to an Olympus BX51 microscope by optical fibers. Emission spectra were obtained in a wavelength range between 450 and 750 nm with 2 nm step size. The spectral width of the excitation wavelength at 440 nm is 10 nm. Excitation spectra were obtained with a monitoring wavelength of 664 nm for $Sr[BeSi_2N_4]:Eu^{2+}$ and 628 nm for $Sr[BeSi_2N_4]:Ce^{3+}$. Photoluminescence measurements on powder samples were carried out using an in-house built system based on a 5.3“ integrating sphere and a spectrofluorimeter equipped with a 150 W Xe lamp, two 500 mm Czerny-Turner monochromators, 1800 L mm^{-1} lattices, and 250/500 nm lamps with a spectral range from 230 to 820 nm. Low-temperature emission spectra of a $Sr[BeSi_2N_4]:Eu^{2+}$ powder sample were recorded with an Ocean Optics HR2000 + ES spectrometer (2.048 pixels, grating UA (200–1.100 nm), slit 50) with the samples mounted in a closed-cycle He cryostat. The spectra were obtained in a range from 380–850 nm (0.5 nm step size).

4.1.4.6 UV/Vis spectroscopy

The optical band gap of $Sr[BeSi_2N_4]$ was estimated from UV/Vis-reflectance data by two methods: First, applying a Tauc-plot diagram and second from the intersection of line tangents in the reflectance spectrum.[6,37] Reflectance spectra of Eu^{2+}-doped and undoped powder samples were obtained with an Edinburgh Photonics FLS920-s spectrometer equipped with a 450 W Xe900 arc lamp (single photon-photomultiplier detector, Czerny-Turner monochromator with triple grating turret). The spectra were measured in the wavelength range from 230 to 800 nm (5 nm step size).

4.1.5 References

[1] Pust, P.; Weiler, V.; Hecht, C.; Tücks, A.; Wochnik, A. S.; Henß, A. K.; Wiechert, D.; Scheu, C.; Schmidt, P. J.; Schnick, W. Narrow-band red-emitting $Sr[LiAl_3N_4]:Eu^{2+}$ as a next-generation LED-phosphor material. *Nat. Mater.* **2014**, *13*, 891-896.

[2] http://www.ledinside.com/newsletter/1286, 10/13/2017,

[3] Pust, P.; Schmidt, P. J.; Schnick, W. A revolution in lighting. *Nat. Mater.* **2015**, *14*, 454-458.

[4] Zeuner, M.; Pagano, S.; Schnick, W. Nitridosilicates and Oxonitridosilicates: From Ceramic Materials to Structural and Functional Diversity. *Angew. Chem. Int. Ed.* **2011**, *50*, 7754-7775.

[5] Schmiechen, S.; Strobel, P.; Hecht, C.; Reith, T.; Siegert, M.; Schmidt, P. J.; Huppertz, P.; Wiechert, D.; Schnick, W. Nitridomagnesosilicate $Ba[Mg_3SiN_4]:Eu^{2+}$ and Structure–Property Relations of Similar Narrow-Band Red Nitride Phosphors. *Chem. Mater.* **2015**, *27*, 1780-1785.

[6] Strobel, P.; Weiler, V.; Hecht, C.; Schmidt, P. J.; Schnick, W. Luminescence of the Narrow-Band Red Emitting Nitridomagnesosilicate $Li_2(Ca_{1-x}Sr_x)_2[Mg_2Si_2N_6]:Eu^{2+}$ (x = 0–0.06). *Chem. Mater.* **2017**, *29*, 1377-1383.

[7] Poesl, C.; Schnick, W. Crystal Structure and Nontypical Deep-Red Luminescence of $Ca_3Mg[Li_2Si_2N_6]:Eu^{2+}$. *Chem. Mater.* **2017**, *29*, 3778-3784.

[8] Wilhelm, D.; Baumann, D.; Seibald, M.; Wurst, K.; Heymann, G.; Huppertz, H. Narrow-Band Red Emission in the Nitridolithoaluminate $Sr_4[LiAl_{11}N_{14}]:Eu^{2+}$. *Chem. Mater.* **2017**, *29*, 1204-1209.

[9] Strobel, P.; Schmiechen, S.; Siegert, M.; Tücks, A.; Schmidt, P. J.; Schnick, W. Narrow-Band Green Emitting Nitridolithoalumosilicate $Ba[Li_2(Al_2Si_2)N_6]:Eu^{2+}$ with Framework Topology whj for LED/LCD-Backlighting Applications. *Chem. Mater.* **2015**, *27*, 6109-6115.

[10] Wagatha, P.; Weiler, V.; Schmidt, P. J.; Schnick, W. Tunable Red Luminescence in Nitridomagnesoaluminates α-$Sr_2[MgAl_5N_7]:Eu^{2+}$, β-$Sr_2[MgAl_5N_7]:Eu^{2+}$ and $Sr_8[LiMg_2Al_{21}N_{28}]:Eu^{2+}$. *Chem. Mater.* **2018**, *30*, 1755-1761.

[11] Lumileds, Narrow Red Phosphor Technology, **2016**

[12] Marchuk, A.; Schnick, W. $Ba_3P_5N_{10}Br:Eu^{2+}$: A Natural-White-Light Single Emitter with a Zeolite Structure Type. *Angew. Chem. Int. Ed.* **2015**, *54*, 2383-2387.

[13] Marchuk, A.; Wendl, S.; Imamovic, N.; Tambornino, F.; Wiechert, D.; Schmidt, P. J.; Schnick, W. Nontypical Luminescence Properties and Structural Relation of $Ba_3P_5N_{10}X:Eu^{2+}$ (X = Cl, I): Nitridophosphate Halides with Zeolite-like Structure. *Chem. Mater.* **2015**, *27*, 6432-6441.

[14] Pucher, F. J.; Marchuk, A.; Schmidt, P. J.; Wiechert, D.; Schnick, W. Luminescent Nitridophosphates $CaP_2N_4:Eu^{2+}$, $SrP_2N_4:Eu^{2+}$, $BaP_2N_4:Eu^{2+}$, and $BaSr_2P_6N_{12}:Eu^{2+}$. *Chem. Eur. J.* **2015**, *21*, 6443-6448.

[15] Poesl, C.; Niklaus, R.; Schnick, W. The Crystal Structure of Nitridomagnesogermanate $Ba[Mg_3GeN_4]:Eu^{2+}$ and Theoretical Calculations of Its Electronic Properties. *Eur. J. Inorg. Chem.* **2017**, *2017*, 2422-2427.

[16] Hintze, F.; Johnson, N. W.; Seibald, M.; Muir, D.; Moewes, A.; Schnick, W. Magnesium Double Nitride Mg_3GaN_3 as New Host Lattice for Eu^{2+} Doping: Synthesis, Structural Studies, Luminescence, and Band-Gap Determination. *Chem. Mater.* **2013**, *25*, 4044-4052.

[17] Pust, P.; Hintze, F.; Hecht, C.; Weiler, V.; Locher, A.; Zitnanska, D.; Harm, S.; Wiechert, D.; Schmidt, P. J.; Schnick, W. Group (III) Nitrides $M[Mg_2Al_2N_4]$ (M = Ca, Sr, Ba, Eu) and $Ba[Mg_2Ga_2N_4]$ – Structural Relation and Nontypical Luminescence Properties of Eu^{2+} Doped Samples. *Chem. Mater.* **2014**, *26*, 6113-6119.

[18] Bragg, W. L.; West, J. The Structure of Beryl, $Be_3Al_2Si_6O_{18}$. *Proc. R. Soc. London, Ser. A* **1926**, *111*, 691-714.

[19] Jarnot, M.; Simmons, W. S.; Staebler, G.; Wilson, T.; Wise, M., *Extra Lapis English, No. 7: Beryl and Its Color Varieties*: Lapis International, LLC, **2005**.

[20] Hoppe, R.; Schuldt, D. Neue Beryllate der Alkalimetalle: $Na_6Be_8O_{11}$. *Z. Anorg. Allg. Chem.* **1988**, *564*, 61-71.

[21] Harris, L. A.; Yakel, H. L. The crystal structure of $SrBe_3O_4$. *Acta Crystallogr. Sect. B* **1969**, *25*, 1647-1651.

[22] Eckerlin, P. Zur Kenntnis des Systems Be_3N_2-Si_3N_4, IV. Die Kristallstruktur von $BeSiN_2$. *Z. Anorg. Allg. Chem.* **1967**, *353*, 225-235.

[23] Somer, M.; Carrillo-Cabrera, W.; Peters, E.-M.; Peters, K.; von Schnering, H. G. Crystal structure of lithium beryllium nitride, LiBeN. *Z. Kristallogr.* **1996**, *211*, 635.

[24] Somer, M.; Yarasik, A.; Akselrud, L.; Leoni, S.; Rosner, H.; Schnelle, W.; Kniep, R. Ae[Be_2N_2]: Nitridoberyllates of the Heavier Alkaline-Earth Metals. *Angew. Chem. Int. Ed.* **2004**, *43*, 1088-1092.

[25] Funahashi, S.; Michiue, Y.; Takeda, T.; Xie, R.-J.; Hirosaki, N. Substitutional disorder in $Sr_{2-y}Eu_yB_{2-2x}Si_{2+3x}Al_{2-x}N_{8+x}$ (x≃0.12, y≃0.10). *Acta Crystallogr. Sect. C* **2014**, *70*, 452-454.

[26] Coelho, A. A., *TOPAS-Academic*, Version 4.1: A program for Rietveld refinement: Brisbane, Australia, **2007**.

[27] Hübenthal, R., *MAPLE: A program for calculation of Madelung part of lattice energy, Vol. 4*: University of Gießen, Germany, **1993**.

[28] Gál, Z. A.; Mallinson, P. M.; Orchard, H. J.; Clarke, S. J. Synthesis and Structure of Alkaline Earth Silicon Nitrides: $BaSiN_2$, $SrSiN_2$, and $CaSiN_2$. *Inorg. Chem.* **2004**, *43*, 3998-4006.

[29] Superscripted numbers specify connectivity, that is, the number of directly connected network-building cations.

[30] Huppertz, H.; Schnick, W. $Ba_2Nd_7Si_{11}N_{23}$ — A Nitridosilicate with a Zeolite-Analogous Si–N Structure. *Angew. Chem. Int. Ed. Engl.* **1997**, *36*, 2651-2652.

[31] Schmolke, C.; Lupart, S.; Schnick, W. $La_{16}[Si_8N_{22}][SiON_3]_2$ – A nitridosilicate with isolated, corner-sharing and edge-sharing tetrahedra. *Solid State Sci.* **2009**, *11*, 305-309.

[32] Schmiechen, S.; Schneider, H.; Wagatha, P.; Hecht, C.; Schmidt, P. J.; Schnick, W. Toward New Phosphors for Application in Illumination-Grade White pc-LEDs: The Nitridomagnesosilicates $Ca[Mg_3SiN_4]:Ce^{3+}$, $Sr[Mg_3SiN_4]:Eu^{2+}$, and $Eu[Mg_3SiN_4]$. *Chem. Mater.* **2014**, *26*, 2712-2719.

[33] Dorenbos, P. $f \rightarrow d$ transition energies of divalent lanthanides in inorganic compounds. *J. Phys.: Condens. Matter* **2003**, *15*, 575-594.

[34] Höppe, H. A.; Lutz, H.; Morys, P.; Schnick, W.; Seilmeier, A. Luminescence in Eu^{2+}-doped $Ba_2Si_5N_8$: fluorescence, thermoluminescence, and upconversion. *J. Phys. Chem. Solids* **2000**, *61*, 2001-2006.

[35] Uheda, K.; Hirosaki, N.; Yamamoto, Y.; Naita, A.; Nakajima, T.; Yamamoto, H. Luminescence Properties of a Red Phosphor, $CaAlSiN_3:Eu^{2+}$, for White Light-Emitting Diodes *Electrochem. Solid State Lett.* **2006**, *9*, H22-H25.

[36] López, R.; Gómez, R. Band-gap energy estimation from diffuse reflectance measurements on sol–gel and commercial TiO_2: a comparative study. *J. Sol-Gel Sci. Technol.* **2012**, *61*, 1-7.

[37] Tauc, J.; Grigorovici, R.; Vancu, A. Optical Properties and Electronic Structure of Amorphous Germanium. *Phys. Status Solidi B* **1966**, *15*, 627-637.

[38] Tolhurst, T. M.; Strobel, P.; Schmidt, P. J.; Schnick, W.; Moewes, A. Designing Luminescent Materials and Band Gaps: A Soft X-ray Spectroscopy and Density Functional Theory Study of $Li_2Ca_2[Mg_2Si_2N_6]:Eu^{2+}$ and $Ba[Li_2(Al_2Si_2)N_6]:Eu^{2+}$. *J. Phys. Chem. C* **2017**, *121*, 14296-14301.

[39] Tolhurst, T. M.; Strobel, P.; Schmidt, P. J.; Schnick, W.; Moewes, A. Direct Measurements of Energy Levels and Correlation with Thermal Quenching Behavior in Nitride Phosphors. *Chem. Mater.* **2017**, 7976-7983.

[40] Bruns, J.; Podewitz, M.; Schauperl, M.; Joachim, B.; Liedl, K. R.; Huppertz, H. $CaB_2S_4O_{16}$: A Borosulfate Exhibiting a New Structure Type with Phyllosilicate Analogue Topology. *Chem. Eur. J.* **2017**, *23*, 16773-16781.

[41] Bruns, J.; Podewitz, M.; Schauperl, M.; Liedl, K. R.; Janka, O.; Pöttgen, R.; Huppertz, H. $Ag[B(SO_4)_2]$ – Synthesis, Crystal Structure, and Characterization of the First Precious-Metal Borosulfate. *Eur. J. Inorg. Chem.* **2017**, *2017*, 3981-3989.

[42] Wentorf, R. H. Cubic Form of Boron Nitride. *J. Chem. Phys.* **1957**, *26*, 956-956.

[43] Agency for Toxic Substances and Disease Registry (ATSDR) - Case Studies in Environmental Medicine - Beryllium Toxicity **2018**.

[44] Tsai, Y.-T.; Nguyen, H.-D.; Lazarowska, A.; Mahlik, S.; Grinberg, M.; Liu, R.-S. Improvement of the Water Resistance of a Narrow-Band Red-Emitting $SrLiAl_3N_4:Eu^{2+}$ Phosphor Synthesized under High Isostatic Pressure through Coating with an Organosilica Layer. *Angew. Chem. Int. Ed.* **2016**, *128*, 9804-9808.

[45] Zeuner, M.; Pagano, S.; Hug, S.; Pust, P.; Schmiechen, S.; Scheu, C.; Schnick, W. $Li_2CaSi_2N_4$ and $Li_2SrSi_2N_4$ – a Synthetic Approach to Three-Dimensional Lithium Nitridosilicates. *Eur. J. Inorg. Chem.* **2010**, 4945-4951.

[46] García-Gutiérrez, R.; Barboza-Flores, M.; Berman-Mendoza, D.; Contreras-López, O. E.; Ramos-Carrazco, A. Synthesis and characterization of highly luminescent beryllium nitride. *Mater. Lett.* **2014**, *132*, 179-181.

[47] Lange, H.; Wötting, G.; Winter, G. Silicon Nitride – From Powder Synthesis to Ceramic Materials. *Angew. Chem. Int. Ed. Engl.* **1991**, *30*, 1579-1597.

[48] Coelho, A. A charge-flipping algorithm incorporating the tangent formula for solving difficult structures. *Acta Crystallogr. Sect. A* **2007**, *63*, 400-406.

[49] Oszlanyi, G.; Suto, A. Ab initio structure solution by charge flipping. *Acta Crystallogr. Sect. A* **2004**, *60*, 134-141.

[50] Oszlanyi, G.; Suto, A. The charge flipping algorithm. *Acta Crystallogr. Sect. A* **2008**, *64*, 123-134.

4.2 Luminescence of an Oxonitridoberyllate: A Study of Narrow-Band Cyan Emitting $Sr[Be_6ON_4]:Eu^{2+}$

published in: *Chem. Mater.* **2018**, *30*, 3122-3130

authors: Philipp Strobel, Tristan de Boer, Volker Weiler, Peter J. Schmidt, Alexander Moewes, and Wolfgang Schnick

DOI: 10.1021/acs.chemmater.8b01256

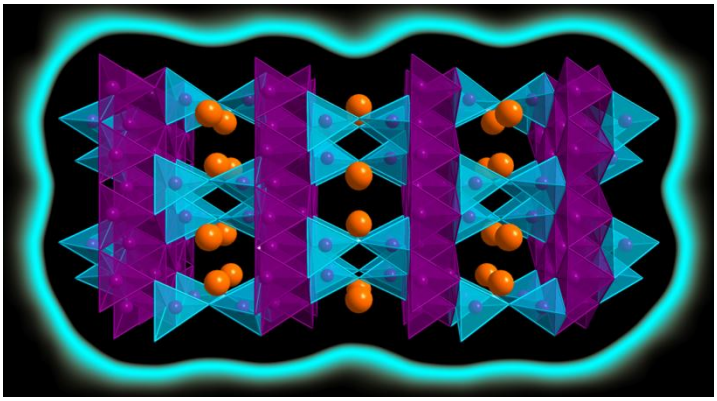

Abstract. Oxo- and (oxo)nitridoberyllates show exceptional potential as host lattices for application in illumination grade phosphor converted (pc)LEDs due to their remarkable electronic and structural characteristics, allowing highly efficient narrow-band emission upon doping with Eu^{2+}. $Sr[Be_6ON_4]:Eu^{2+}$, the first example of an oxonitridoberyllate phosphor, exhibits narrow-band cyan emission (λ_{em} = 495 nm; full width at half-maximum, *fwhm* = 35 nm; ≈ 1400 cm^{-1}), comparable to the emission of the oxonitridosilicate $BaSi_2O_2N_2:Eu^{2+}$ (*fwhm* = 35 nm) or a cyan-emitting primary LED (*fwhm* = 27 nm). $Sr[Be_6ON_4]:Eu^{2+}$ reveals a highly condensed rigid 3D network with a remarkably large degree of condensation [i.e., atomic ratio Be:(O,N)] of κ = 1.2 that is achieved by interconnection of highly condensed layers of BeN_4 tetrahedra by Be_2ON_6 units via common edges. The crystal structure of $Sr[Be_6ON_4]:Eu^{2+}$ was solved on the basis of single-crystal and powder XRD data (*C*2/*c*, no. 15, *a* = 13.9283(14), *b* = 5.7582(6), *c* = 4.9908(5) Å, β = 90.195(1)°, *Z* = 4, R_1 = 0.033, wR_2 = 0.065, GoF = 1.046). $Sr[Be_6ON_4]:Eu^{2+}$ shows a close structural relationship to other nitride as well as oxide compounds, and therefore closes a structural gap helping to understand relations in Be-containing solid-state materials. The electronic structure of $Sr[Be_6ON_4]:Eu^{2+}$ was characterized by X-ray spectroscopy measurements, supported by density functional theory (DFT) calculations. Due to its excellent emission properties, large band gap, rigid 3D network, as well as chemical and thermal stability, $Sr[Be_6ON_4]:Eu^{2+}$ is a promising phosphor to close the cyan gap in efficient high-CRI pcLEDs (CRI, color rendering index).

4.2.1 Introduction

In recent years, investigation of narrow-band red luminophores has been in the focus of LED phosphor development for improving the CRI (color rendering index, R_a8) and reducing IR spillover of white light-emitting LEDs.[1,2] In most common LEDs blue-emitting InGaN chips are used to excite light-converting phosphors that add green–yellow and orange–red spectral components. After the discovery of highly efficient red-emitting BSSNE ($(Ba,Sr)_2Si_5N_8:Eu^{2+}$) and SCASN ($(Sr,Ca)AlSiN_3:Eu^{2+}$), as well as narrow-band red-emitting SLA ($Sr[LiAl_3N_4]:Eu^{2+}$), a good base for highly efficient pcLEDs with good color rendition and CRI values around 90 was established.[1-4] At the same time there is need for narrow-band green, yellow, and blue phosphors for various LED application fields like illumination, consumer electronics, and display backlighting technology.[1]

CRI values of common LEDs are usually limited in blue excited pcLEDs.[5] This can be explained by missing emission intensity between the blue light of the InGaN-LED and the emission of common green–yellow phosphors, e.g., YAG:Ce and LuAG:Ce, the so-called cyan gap.[6] To overcome this limitation, a phosphor emitting in this particular spectral region with narrow-band emission between 490 and 500 nm and a strong absorption in the blue spectral range is required.

Prerequisites for phosphors emitting in the blue to green region are not different from those for red phosphors and include chemical and thermal stability, high conversion efficiency, and narrow-band emission as a consequence of the small Stokes shift needed for efficient excitation with blue light.[7] Several specific requirements for solid-state materials leading to highly efficient, narrow-band emitting phosphors with a small Stokes shift have been identified over the last years: a rigid host lattice providing a highly symmetric dopant site (e.g., Eu^{2+}, Ce^{3+}) with a high coordination number and a large band gap for gaining high QE (quantum efficiency).[1,8] These properties are often provided by (oxo)nitridosilicate and -aluminate host structures. For obtaining emission in the blue to green spectral region only few Eu^{2+}-doped oxide and oxonitride compounds are available.[5,9] An important phosphor with tunable emission in the required spectral region is the oxonitridosilicate $MSi_2O_2N_2$ (M = Ca, Sr, Ba).[10] By replacing Ca with the larger Sr or Ba the initially yellow–green emission with an emission maximum of 560 nm can be blue-shifted to 537 nm (Sr) and even 495 nm (Ba) accompanied by structural changes.[10-13] A drawback of this compound group is its layered crystal structure leading to insufficient thermal and chemical stability.[14] To increase stability and therefore retain optimum luminescence properties of LED phosphors at operating conditions, host materials with 3D-network structures would be preferable.[14]

Recently, we have proposed nitridoberyllates as a new class of materials exhibiting the required structural and optical characteristics of efficient host lattices for Eu^{2+}-doped LED phosphors. $Sr[BeSi_2N_4]:Eu^{2+}$, which is isotypic to $SrBe_3O_4$,[15] exhibits a highly condensed 3D-network structure, made up of trigonal planar and tetrahedral building units with strongly covalent Be–N and Si–N bonds. Its symmetric, rigid host lattice offers a large band gap; however, due to exceptionally long Sr–N bonds, trapped exciton emission is obtained.[16] Nevertheless, exploration of $Sr[BeSi_2N_4]:Eu^{2+}$ with

its highly condensed, rigid network was the starting point for extensive investigations on (oxo)nitridoberyllate compounds.

In this work, we present a novel Eu^{2+}-doped oxonitridoberyllate phosphor, structurally related to $Sr[BeSi_2N_4]:Eu^{2+}$, with exceptional luminescence properties. $SrBe_6ON_4:Eu^{2+}$ exhibits a similarly narrow emission (λ_{em} = 495 nm; *fwhm* = 35 nm; ≈ 1400 cm^{-1}) as $BaSi_2O_2N_2:Eu^{2+}$ (Ba222),[10] but shows increased thermal stability of the emission. This improvement results from the highly condensed structure of $SrBe_6ON_4:Eu^{2+}$ with a 3D network of $BeON_3$ and BeN_4 tetrahedra. Excellent emission properties of narrow-band cyan-emitting $Sr[Be_6ON_4]:Eu^{2+}$ make this novel oxonitridoberyllate phosphor a highly promising material for application in, e.g., high-CRI white pcLEDs.

4.2.2 Experimental Section

4.2.2.1 Safety Assessment

Beryllium dusts and soluble salts are hazardous and can cause diseases, such as cancer, berylliosis, and chronic beryllium disease (CBD).[16,17] When small particles of a beryllium compound are inhaled or dissolved the element can be incorporated. Beryllium can accumulate in the human body, leading to chronic diseases. Nevertheless, Be-containing materials are common in industrial applications, such as ceramics, automotive, aerospace, and electronics or semiconductors.[17,18] Schlenk-lines and glove boxes are suitable and required to reduce risk of exposure, when working with Be. Appropriate safety measures are feasible, and we therefore assess insoluble, coarse-grained Be-containing solid-state compounds to be less dangerous. Natural examples are Be-containing gem stones, e.g., *beryl*, *aquamarine*, and *emerald*. Therefore, application of (oxo)nitridoberyllate phosphors in pcLEDs is conceivable.

4.2.2.2 Synthesis

All experiments requiring highly sensitive starting materials or Be-containing compounds were performed in Argon-filled glove boxes (Unilab, MBraun, Garching; O_2 <1 ppm, H_2O <1 ppm) or in dry Schlenk-type glassware attached to a vacuum line (10^{-3} mbar). Argon (Air Liquide, 5.0) was dried and purified in columns filled with silica gel (Merck), molecular sieve (Fluka, 4 Å), KOH (Merck, ≥85%), P_4O_{10} (Roth, ≥99%), and titanium sponge (700 °C, Johnsen Matthey, 99.5%).

Crystalline samples of $Sr[Be_6ON_4]:Eu^{2+}$ were synthesized by reacting SrO (103.6 mg, 1.0 mmol, Alfa Aesar, 99.5%) and Be_3N_2 [30.3 mg, 0.55 mmol, synthesized from Be (ABCR, 99+%, 325 mesh) in a radio frequency (rf) furnace under N_2 atmosphere at 1300 °C] after mixing in an agate mortar.[19] For doped compounds 1 mol % of SrO was replaced by Eu_2O_3 (ABCR, 99.99%). The reaction mixture was filled into W crucibles and subsequently heated in 1 h to 1400 °C in an rf furnace. The temperature was maintained at 1400 °C for 1 h, then cooled down to 700 °C in 0.5 h and subsequently to room temperature by shutting down the furnace.

Powder samples of $Sr[Be_6ON_4]:Eu^{2+}$ were synthesized in Ta ampules. $Sr(N_3)_2$ (25.7 mg, 0.15 mmol), Be_3N_2 (13.9 mg, 0.25 mmol), BeO (3.8 mg, 0.15 mmol), and Eu_2O_3 (0.3 mg, 0.005 mmol) were mixed, filled into Ta ampules that subsequently were weld shut and heated in evacuated silica tubes to 950 °C in 3 h. The temperature was kept for 24 h, cooled down to 500 °C in 3 h and then to room temperature by shutting down the furnace.

4.2.2.3 Elemental Analysis

Energy-dispersive X-ray spectroscopy (EDS) and complementary ICP-OES (inductively coupled plasma optical emission spectrometry) analysis were used to determine the elemental composition of $Sr[Be_6ON_4]:Eu^{2+}$. For EDS a Dualbeam Helios Nanolab G3 UC scanning electron microscope (SEM, FEI) with X-Max 80 SDD detector (Oxford Instruments) was used. The EDS data were obtained from several particles with an accelerating voltage of 20 kV. The morphology of the crystalline samples was additionally investigated by SEM.

ICP-OES analysis was conducted with a Varian Vista RL spectrometer to determine the atomic ratio of Sr, Be, and Eu.

4.2.2.4 Single-Crystal X-ray Diffraction

A green single crystal of $Sr[Be_6ON_4]:Eu^{2+}$ was selected and fixed on a micromount (MiTeGen). X-ray diffraction data were collected on a Bruker D8 Venture diffractometer with rotating anode. Goebel mirror optics were used to specifically select and focus the Mo Kα radiation (λ = 0.71073 Å). Integration and absorption correction was carried out with the program package APEX3.[20] The crystal structure was solved by Direct Methods (SHELXS)[21] and refined by full-matrix least-squares methods (SHELXL).[22,23] Eu was disregarded in the structure refinement due to its low amount and its therefore insignificant contribution to the scattering density. The O/N ordering was determined during the refinement. All atom sites were refined anisotropically. $Sr[Be_6ON_4]:Eu^{2+}$ was additionally refined as a two-component twin.

Further details on the structure investigation may be obtained from the Fachinformationszentrum Karlsruhe, 76344 Eggenstein-Leopoldshafen, Germany (Fax, (+49)7247-808-666; E-mail, crysdata@fiz-karlsruhe.de) upon quoting the depository number CSD-434259.

4.2.2.5 Powder X-ray Diffraction

The structural model obtained from single-crystal data was further investigated by powder X-ray diffraction methods. A powder sample of $Sr[Be_6ON_4]:Eu^{2+}$ was sealed in a glass capillary with 0.2 mm diameter and 0.01 mm wall thickness (Hilgenberg, Germany) and measured on a STOE STADI P diffractometer (Cu $K\alpha_1$ radiation, Ge(111) monochromator, Mythen1K detector) in Debye–Scherrer geometry. Data were refined with the TOPAS Academic 4.1 package.[24] The Rietveld method was used by applying the fundamental parameters approach (direct convolution of source emission profiles, axial instrument contributions, crystallite size, and microstrain effects). Capillary absorption correction (inner diameter 0.18 mm) was carried out using the calculated absorption coefficient.

4.2.2.6 Luminescence

Luminescence spectra of $Sr[Be_6ON_4]:Eu^{2+}$ were obtained with a HORIBA Fluoromax4 spectrofluorimeter system connected to an Olympus BX51 microscope by optical fibers. The spectral width of the excitation wavelength at 440 nm is 10 nm. Emission spectra were recorded in a wavelength range between 460 and 820 nm with 2 nm step size. Excitation spectra were obtained with a monitoring wavelength of 510 nm for $Sr[Be_6ON_4]:Eu^{2+}$.

For QE determination, an industrial setup was used with a $BaSO_4$ sample as reference (reflectance of 100%). Sample absorption was calculated from the difference in the reflectance of sample and reference. The QE is given as the quotient of sample emission and absorption.

4.2.2.7 UV/Vis Spectroscopy

A reflectance spectrum of a Eu^{2+}-doped powder sample was obtained with an Edinburgh Photonics FLS920-s spectrometer equipped with a 450 W Xe900 arc lamp (single photon-photomultiplier detector, Czerny-Turner monochromator with triple grating turret). The spectra were measured in the wavelength range from 240 to 780 nm (5 nm step size). The optical band gap was estimated from the intersection of line tangents in the reflectance spectrum.[25,26]

4.2.2.8 X-ray Spectroscopy

The X-ray absorption spectroscopy (XAS) measurements, which are probing the unoccupied partial density of states (PDOS), were conducted at the Spherical Grating Monochromator (SGM) beamline at the Canadian Light Source (CLS), Saskatoon, Canada.[27] X-ray emission spectroscopy (XES), which is sensitive to the occupied PDOS, and resonant inelastic X-ray scattering (RIXS) measurements were conducted at the Resonant Elastic and Inelastic X-ray Scattering (REIXS) beamline at the CLS. The SGM beamline has a monochromator resolving power ($E/\Delta E$) of about 5000 at the N K-edge, and partial fluorescence yield (PFY) XAS spectra were collected using an array of silicon drift detectors. REIXS has a monochromator resolving power of 5000, and a Rowland circle X-ray spectrometer for collecting the emission measurements with a resolving power of 1700 at the N K-edge. These measurements are performed by promoting core electrons to the conduction band and monitoring their scattering (RIXS) or subsequent decay (XAS, XES). Samples were pressed into clean wafers of In foil and transferred to the vacuum chambers used for the measurements. All measurements were conducted at ambient temperature, and data were collected in rapid succession. The XAS spectra were energy-calibrated using a peak value of 402.1 eV in hexagonal boron nitride. The XES spectra were calibrated using elastic scattering peaks.

4.2.2.9 Density Functional Theory

The electronic structure of $SrBe_6ON_4$ was modeled using WIEN2k, a full-potential, all-electron commercially available, density functional theory (DFT) software package which uses linearized augmented plane waves with local orbitals in a Kohn–Sham scheme.[28] Calculations were performed using the PBEsol generalized gradient approximation (GGA) exchange-correlation functional.[29] Since

the PBEsol exchange-correlation functional significantly underestimates the band gap of materials, the modified Becke–Johnson (mBJ) exchange-correlation functional is also used.[30] A basis set size of RK_{max} = 7 was used, and the *k*-mesh was selected so that the total energy per unit cell was stable within 10^{-5} Ry per unit cell, which corresponds to a 9 × 10 × 9 *k*-mesh.

The DFT calculations are used to calculate the density of states and band structure, as well as to directly calculate predicted XES and XAS spectra, allowing for a detailed comparison with experiment. The spectra are calculated by multiplying the PDOS with a dipole transition matrix and a radial transition probability.[31] Calculated spectra are broadened to reflect lifetime and instrumentation related broadening. XES and XAS spectra depend on the final state of the system, which for XAS spectra corresponds to a system perturbed by an X-ray injected core hole.[32] To account for this perturbation, a core hole is added to a 1 × 2 × 2 supercell of the unit cell with a compensating background electronic charge, and separate core hole calculations were performed for each nitrogen site.

4.2.3 Results and Discussion

4.2.3.1 Synthesis and Elemental Analysis

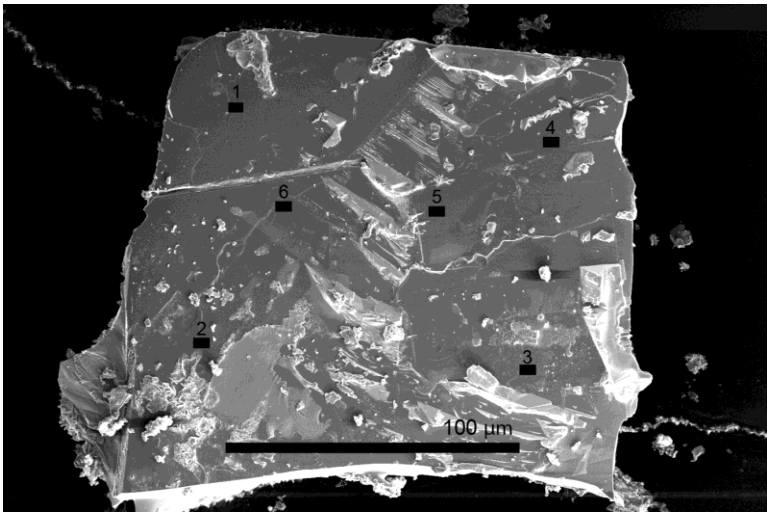

Figure 1. SEM image of platelet-like $Sr[Be_6ON_4]:Eu^{2+}$ crystal (scale bar 100 µm), numbers 1–6 mark locations of EDS scans.

Single-crystalline samples of $Sr[Be_6ON_4]:Eu^{2+}$ were synthesized by solid-state reactions in W crucibles in an rf furnace. A heterogeneous mixture containing air- and water-stable luminescent single crystals of $Sr[Be_6ON_4]:Eu^{2+}$ was obtained. Cyan-emitting powder samples of $Sr[Be_6ON_4]:Eu^{2+}$ were synthesized in Ta ampules. Morphology and elemental composition were investigated by electron microscopy, accompanied by EDS (Sr, O, N) and complementary ICP-OES (Sr, Eu, Be) investigations. SEM pictures of $Sr[Be_6ON_4]:Eu^{2+}$ show either platelet-like (Figure 1) or block-like morphology. Averaged results of EDS as well as ICP analysis are given in Table 1. Light elements (O,

N) might be underestimated especially by EDS, and Be usually cannot be quantified by this method. Results of individual measurements are given in the Supporting Information.

Table 1. Elemental Analysis of $Sr[Be_6ON_4]:Eu^{2+}$

	Sr	Eu	Be	O	N
EDS	1			1	3
ICP	1	<0.01	7		

4.2.3.2 Crystal Structure Determination

X-ray diffraction experiments were performed on single crystals of $Sr[Be_6ON_4]$. The oxonitridoberyllate crystallizes in the monoclinic space group *C*2/*c* (no. 15) and was refined as a two-component rotation twin. Structure solution was initially performed in *P*1. Crystal data obtained from single-crystal XRD show pseudo-orthorhombic metrics. Applying the Rietveld method on a powder sample of $Sr[Be_6ON_4]$, the monoclinic angle β = 90.195(1)° was confirmed (Figure 2).

Crystallographic data of the structure solution and refinement are summarized in Table 2. Atomic coordinates and isotropic displacement parameters are given in Table 3. Bond lengths and angles as well as anisotropic displacement parameters (ADPs) and a graphical presentation of the ADPs of $Sr[Be_6ON_4]$ are given in the Supporting Information.

The consistency of the structural model is supported by lattice-energy calculations (MAPLE, Madelung Part of Lattice Energy). MAPLE values were calculated for each ion type and for the entire structure. The results of the MAPLE calculations are summarized in the SI. The partial MAPLE values are in good agreement with reference data reported before, confirming O/N ordering in $Sr[Be_6ON_4]$.[12,16] Partial MAPLE values for Be^{2+}, O^{2-}, and N^{3-} are listed in the Supporting Information. The comparison of the MAPLE sum of $Sr[Be_6ON_4]$ with total MAPLE values of constituting SrO and Be_3N_2 shows only minor deviation of 0.33%.[19,33]

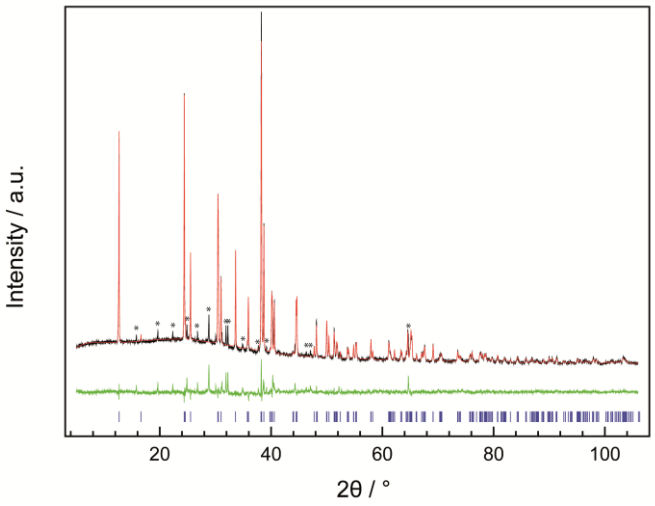

Figure 2. Rietveld refinement of the structural model of $Sr[Be_6ON_4]$ (Cu $K\alpha_1$ radiation). Experimental data (black line), calculated pattern (red line), and difference curve (green line). Tick marks: blue, positions of Bragg reflections of $Sr[Be_6ON_4]$; unidentified side-phases are marked with asterisks.

Table 2. Crystal Data for $Sr[Be_6ON_4]$[a]

formula mass [g mol^{-1}]	213.72
crystal system/space group	monoclinic, *C*2/*c* (no. 15)
lattice parameters [Å, deg]	*a* = 13.9283(14) *b* = 5.7582(6) *c* = 4.9908(5) *β* = 90.195(1)[b]
cell volume [Å^3]	400.27(7)
formula units per cell *Z*	4
X-ray density [g cm^{-1}]	3.547
linear absorption coefficient [cm^{-1}]	13.325
F(000)	392
crystal dimensions (mm^3)	0.05 × 0.02 × 0.01
diffractometer	D8 Venture
radiation	Mo Kα (λ = 0.710 73 Å)
temperature [K]	293(2)
Abs correction	multiscan
θ range [deg]	3.83–45.78
measured reflections	10 858
independent reflections	1676 [R_{int} = 0.0756]
observed reflections	1559
min/max transmission	0.716/1.000
refined parameters	57
GOF	1.046
R indices ($F_o^2 \geq 2\sigma(F_o^2)$)	R_1 = 0.0277, wR_2 = 0.0625
R indices (all data)	R_1 = 0.0333, wR_2 = 0.0645
min/max residual electron density (eÅ^{-3})	–1.454/1.327

[a]esd's are given in parentheses.
[b]Value obtained from PXRD Rietveld refinement; single-crystal data show pseudo-orthorhombic metrics.

Table 3. Atomic Coordinates, Equivalent Isotropic Displacement Parameters, and Site Occupancy Factors (sof's) of $Sr[Be_6ON_4]$[a]

atom (*Wyck.*)	***x***	***y***	***z***	U_{eq} **(Å^2)**	***sof***
Sr1 (4*e*)	0	0.796 93(3)	1/4	0.009 30(4)	1
Be1 (8*f*)	0.111 75(11)	0.3606(3)	0.2454(5)	0.0080(2)	1
Be2 (8*f*)	0.196 08(14)	0.1090(3)	0.4375(4)	0.0079(3)	1
Be3 (8*f*)	0.296 73(14)	0.1393(3)	0.1050(4)	0.0075(3)	1
O1 (4*e*)	0	0.3381(2)	1/4	0.0090(2)	1
N1 (8*f*)	0.333 42(8)	0.1126(2)	0.4333(2)	0.0061(2)	1
N2 (8*f*)	0.169 22(9)	0.1342(2)	0.0981(2)	0.0063(2)	1

[a]esd's are given in parentheses.

4.2.3.3 Crystal Structure Description

$Sr[Be_6ON_4]$ crystallizes in the monoclinic space group *C*2/*c* (no. 15). Pseudo-orthorhombic metrics are indicated by the Sr1 and O1 positions, but are disrupted by the arrangement of the BeN_4 tetrahedra. This leads to a monoclinic symmetry with β = 90.195(1)°. This angle is supported by PXRD Rietveld refinement (Figure 2) showing split reflections that confirm the monoclinic space group *C*2/*c*.

The crystal structure, displayed in Figure 3, can be described as a highly condensed 3D network. $Sr[Be_6ON_4]$ is built from layers of edge-sharing BeN_4 tetrahedra resulting in an exceptionally high degree of condensation [i.e., atomic ratio Be:(O,N)] of κ = 1.2 that exceeds possible values in nitridosilicate and -aluminate structures ($\kappa \leq 0.75$; 1.0). The maximum κ value in Be-containing oxonitride compounds can reach values between 1 (BeO) and 1.5 (Be_3N_2).

Decisive for the compound's high degree of condensation is the reduced formal charge of Be^{2+}, when compared to Si^{4+}, while the ion size is nearly identical.[34] As a result, each BeN_4 tetrahedron is capable of sharing common edges with three other BeN_4 tetrahedra resulting in highly condensed layers.

Beyond that, the layers are interconnected by pairs of edge-sharing tetrahedra with stoichiometry Be_2ON_6 that are further connected to the layers by common edges. As a result of this high connectivity of vertex-sharing BeN_4 and $BeON_3$ tetrahedra each N atom is bound to five Be atoms, which does not seem to be possible in nitridosilicate related structures.

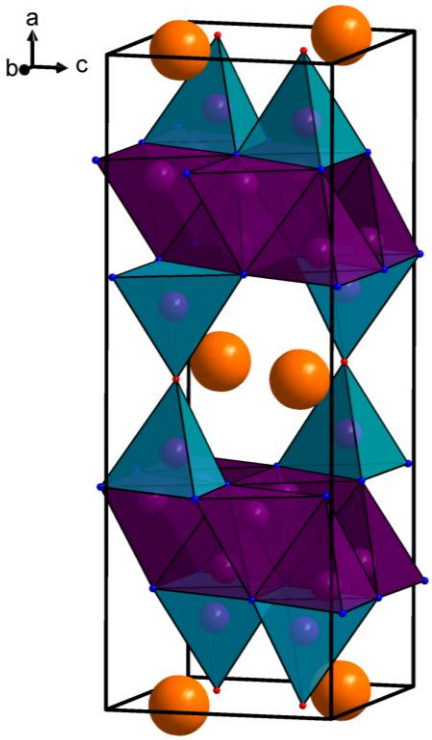

Figure 3. Crystal structure of $Sr[Be_6ON_4]$; BeN_4 tetrahedra (violet), $BeON_3$ tetrahedra (cyan), Sr atoms (orange), O atoms (red), N atoms (blue)

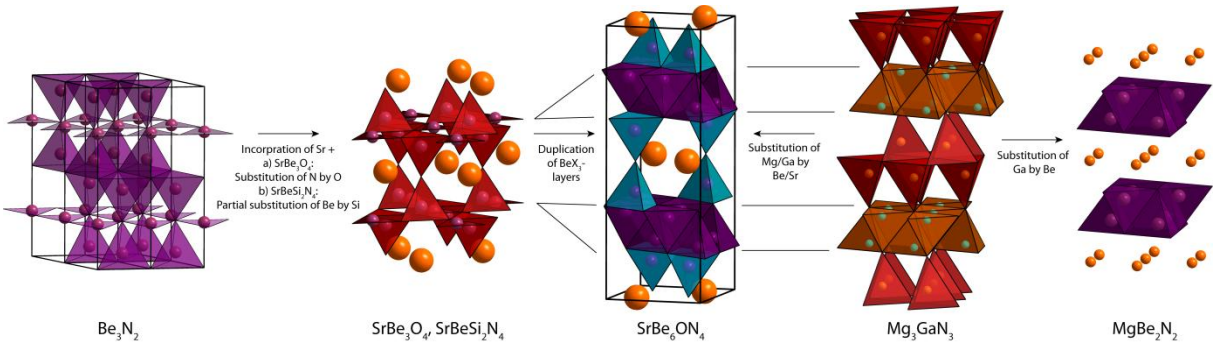

Figure 4. Starting from left: structural relations between β-Be_3N_2, $SrBe_3O_4$, and $SrBeSi_2N_4$ (isotypic, Be in trigonal planar, Si in tetrahedral coordination), $Sr[Be_6ON_4]$, Mg_3GaN_3, and $MgBe_2N_2$.

The crystal structure of $Sr[Be_6ON_4]$ can be derived from structurally related compounds, such as β-Be_3N_2, as well as $SrBe_3O_4$ or $SrBe[Si_2N_4]$.[15,16,35,36] All these compounds exhibit highly condensed 3D networks that can be interpreted as being built from layered frameworks of trigonal planar or tetrahedral units, interconnected by either edge- or vertex-sharing $(Be,Si)(O,N)_4$ tetrahedra. Additionally, analogous highly condensed types of tetrahedra layers found in $Sr[Be_6ON_4]$ were previously described in the nitridoberyllate $MgBe_2N_2$ and the nitride Mg_3GaN_3. Both compounds crystallize in trigonal space groups, $P\bar{3}m1$ (no. 164) and $R\bar{3}m$ (no. 166), respectively.[37,38] In $SrBe_6ON_4$ hexagonal symmetry is disrupted by the Sr and O atoms with its pseudo-orthorhombic metrics. A difference between the structures of $Sr[Be_6ON_4]$, β-Be_3N_2, Mg_3GaN_3, and $MgBe_2N_2$ is the interconnection of the highly condensed tetrahedra layers. While in $MgBe_2N_2$ layers are separated by Mg atoms, layers in β-Be_3N_2 and Mg_3GaN_3 are connected by the same arrangement of edge-sharing tetrahedra that are connected to the layers by common vertices. A comparison of all discussed crystal structures is displayed in Figure 4.

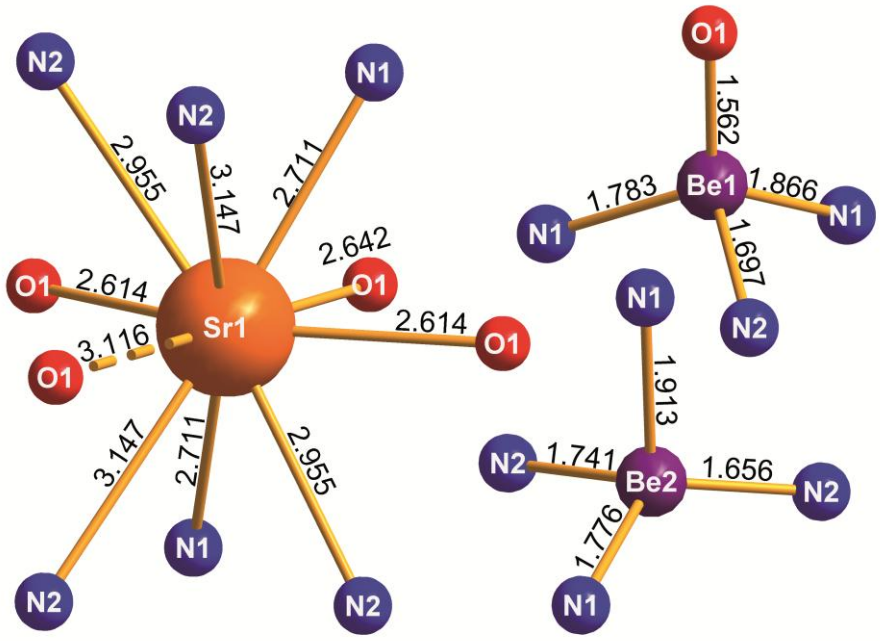

Figure 5. Coordination spheres of Be1, Be2, and Sr; bond lengths given in Å.

Bond lengths of Be–O and Be–N in $Sr[Be_6ON_4]$ are in the range expected for Be-containing solid-state compounds and are comparable to regular Si–*X* (*X* = O, N) distances (Figure 5).[15,38,39] The Be1–O distance is slightly shorter (1.56 Å) than Be1– and Be2–N distances (1.66–1.9 Å). The Be2–N1 distance of 1.9 Å is exceptionally long. This can be explained by the composition of the highly condensed tetrahedra layer deduced from the planar layers of the $SrBe_3O_4$ structure. Therefore, Be2 can be described to be in an intermediate state between sp^3-hybridization as in a tetrahedron and sp^2-hybridization as in trigonal planar coordination. A similar intermediate coordination has been observed for B, e.g., in $M_6B_{22}O_{39}\cdot H_2O$ (*M* = Fe, Co, Ni).[40,41] The Be3–N distances are in the range 1.72–1.78 Å, and the $Be3N_4$ tetrahedra therefore are close to regular. The additional space between the layers and between Be_2ON_6 units is occupied by Sr atoms. The Sr atoms are coordinated antiprismatically by six N atoms, with distances between 2.7 and 3.1 Å and four equatorial O atoms in a distance of ≈ 2.6 Å (3×) and 3.1 Å (1×).

4.2.3.4 Electronic Properties

The electronic properties of $Sr[Be_6ON_4]:Eu^{2+}$ have been investigated applying DFT calculations and soft-X-ray synchrotron radiation. Measured nonresonant XES and XAS spectra are shown in Figure 6, with black lines, together with spectra calculated using the PBEsol functional. For the absorption spectra, the core hole (c.h.) and ground state (g.s.) spectra are shown in solid and dashed lines, respectively. It is well-known that GGA exchange-correlation functionals underestimate the band gap of semiconductors, and so these spectra have been rigidly shifted to allow comparison of spectral features. Considering the absorption spectra, good agreement with experiment is obtained by the ground state calculation, while features in the core hole calculation are pushed closer together. This suggests that the core hole concentration has been overestimated in the core hole calculation. Similarly good agreement is also seen between the resonant and nonresonant features in the emission spectra.

Given that the absorption and emission spectra are proportional to the unoccupied and occupied PDOS, after accounting for the core hole perturbation, their separation can be used to determine the electronic band gap. Using the second derivative to determine the onset of spectral weight yields an XES–XAS separation of 4.2 ± 0.3 eV.[42] After accounting for a core hole shift of 0.4 eV, this yields an overall band gap of 4.6 ± 0.3 eV. This is in agreement with the band gap predicted by the mBJ functional, with a predicted value of 4.75 eV.

By performing RIXS measurements, a technique in which emission spectra are collected at various above-threshold excitation energies, insight into the nature of the band gap can be obtained. By comparing observed near-threshold spectra and nonresonant XES spectra, *k*-selective enhancements to the RIXS signal can be observed.[43] This allows direct and indirect band gaps to be distinguished without any further theoretical input. These resonant spectra are shown for four energies in the left panel of Figure 6. At the minimum excitation energy, shown in cyan, resonant enhancement at 394.0 eV is seen. As the excitation energy is increased, the relative importance of the peak diminishes, confirming that the band gap is direct. This is in agreement with the calculated electronic band

structure of $SrBe_6ON_4$, shown in Figure S2. The conduction band minimum is at the Γ point, while valence band maxima occur at the Γ point and between Y2 and Γ. Although the absolute maximum occurs between Y2 and Γ, the energy at the Γ point is within 20 meV of the Fermi energy level.

The optical band gap, additionally estimated from reflectance data (Figure 7, gray line), is approximately 4.8 eV, and is in the same range as the band gap obtained from DFT calculations and XAS–XES experiments. The absorption band below 300 nm is attributed to the host structure absorption; the second, broad absorption band, ranging from 300 to 600 nm, is caused by the $4f^7$ to $4f^6 5d^1$ absorption of Eu^{2+}.

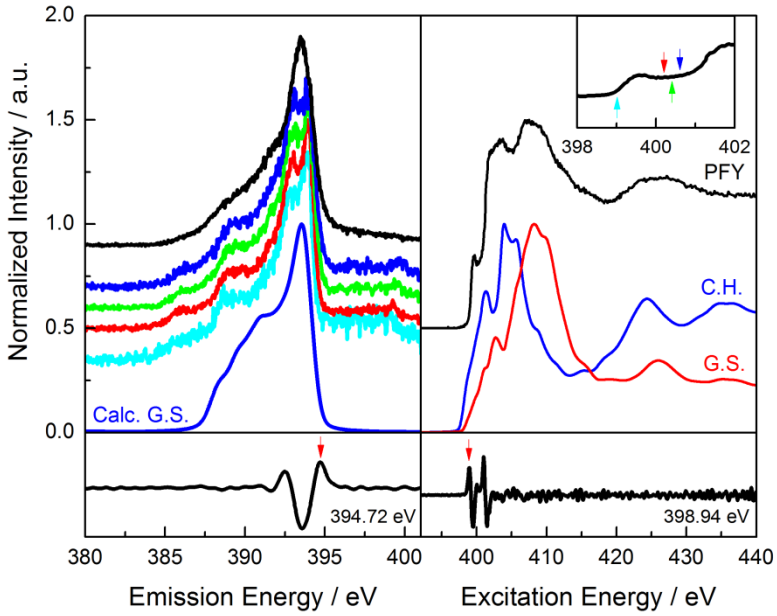

Figure 6. Top left: experimental and calculated X-ray emission spectra. From bottom to top, the calculated nonresonant emission spectrum of $Sr[Be_6ON_4]$ followed by RIXS spectra collected at the energy indicated by the arrow in the inset. The top line is the nonresonant emission spectrum. Top right: experimental and calculated XAS spectra of $Sr[Be_6ON_4]$. Black line is an experimental N K PFY XAS spectrum, while the blue and red lines correspond to calculated absorption spectra in the absence and presence of a core hole, respectively. Bottom panels: the bottom left and right panels show the second derivative of the nonresonant X-ray emission and absorption spectra, respectively.

4.2.3.5 Luminescence

The highly condensed network structure of $Sr[Be_6ON_4]:Eu^{2+}$ shows extraordinary effects on the oxonitridoberyllate luminescence properties. Due to a reduced nephelauxetic effect in oxonitrides compared to nitride structures, emission is observed in the blue to green spectral region. Upon excitation with UV to blue light, narrow-band cyan-emission at 495 nm with a *fwhm* of only 35 nm (≈ 1400 cm^{-1}) is detected. The nominal doping level is 1% with respect to Sr. Figure 7 shows excitation and emission spectra of a $Sr[Be_6ON_4]:Eu^{2+}$ single crystal. The narrow-band emission of $Sr[Be_6ON_4]:Eu^{2+}$ is a consequence of the crystal structure's high degree of condensation as well as the strongly covalent character of the Be–*X* (*X* = O, N) bonds. This results in a highly rigid crystal structure that provides the dopants constant ligand field.

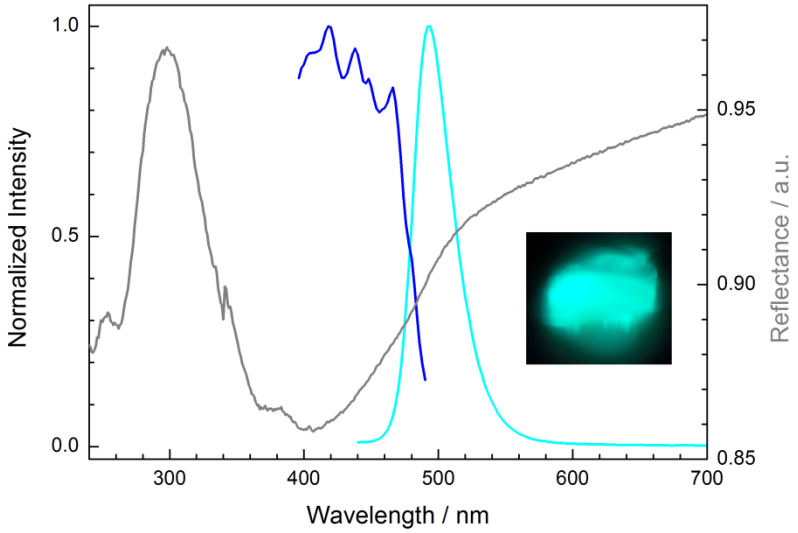

Figure 7. Luminescence, UV/vis spectra, and image of cyan-emitting crystal of $Sr[Be_6ON_4]:Eu^{2+}$ (excitation, blue line; emission, cyan line; reflectance, gray line). Partly resolved ^7F_J energy levels of Eu^{2+} are visible in the excitation spectrum.

Additionally, the network structure offers a single dopant site to partially occupy. As it is discussed in the literature, chemical disorder, multiple dopant sites, and strong lattice vibrations can lead to a varying crystal field around each activator ion and consequentially a broadened emission.[1,8] All these effects are therefore reduced in $Sr[Be_6ON_4]:Eu^{2+}$.

As a result, the luminescence properties of $Sr[Be_6ON_4]:Eu^{2+}$ are comparable to the emission of the oxonitridosilicate $BaSi_2O_2N_2:Eu^{2+}$ (Ba222, λ_{em} = 494 nm, *fwhm* ≈ 35 nm). Due to its layered structure Ba222 lacks efficiency at elevated temperatures and makes this class of materials susceptible for thermal degradation.[14] In contrast, $Sr[Be_6ON_4]:Eu^{2+}$ shows superior stability based on the highly covalent and therefore rigid 3D-network structure. Measurements on as-synthesized powder samples show decent QE values of 20%, which can be improved upon synthesis optimization.

The excellent thermal behavior of $Sr[Be_6ON_4]:Eu^{2+}$ emission is shown in Figure 8a. The narrow-band cyan-emitting phosphor shows only low thermal quenching at high temperatures with a relative emission intensity of >90% at 275 °C. The observed excellent emission stability over temperature is

corroborated by analysis of the collected RIXS spectra using a recently developed method by Tolhurst et al.[44] This technique allows directly determining the energetic separation of the Eu 5*d* state from the conduction band (CB). The separation can be evaluated from resonant X-ray emission spectroscopy at the ligand K-edge.

The RIXS signal appears as subsidiary peaks at energies just below the elastic scattering peak and represents energy losses of the incident X-rays to low-energy (optical) excitations (Figure 8b). This energy loss results from excitations from the lowest rare earth dopant (here: Eu^{2+}) 5*d* level to the conduction band.[44] This separation is a key value to obtaining proficient quantum efficiencies. A small separation allows thermal ionization of excited Eu electrons to the CB resulting in decreased emission efficiency while a large separation improves TQ behavior.

For $Sr[Be_6ON_4]:Eu^{2+}$ a value for the Eu 5*d*–CB separation of $\Delta E \approx 0.26(1)$ eV is observed. This value is similar to that found for, e.g., state-of-the-art narrow-band red luminescent $Sr[LiAl_3N_4]:Eu^{2+}$ ($\Delta E = 0.29$ eV). SLA also shows comparable thermal quenching behavior with 90% relative emission intensity at 275 °C.[2,44]

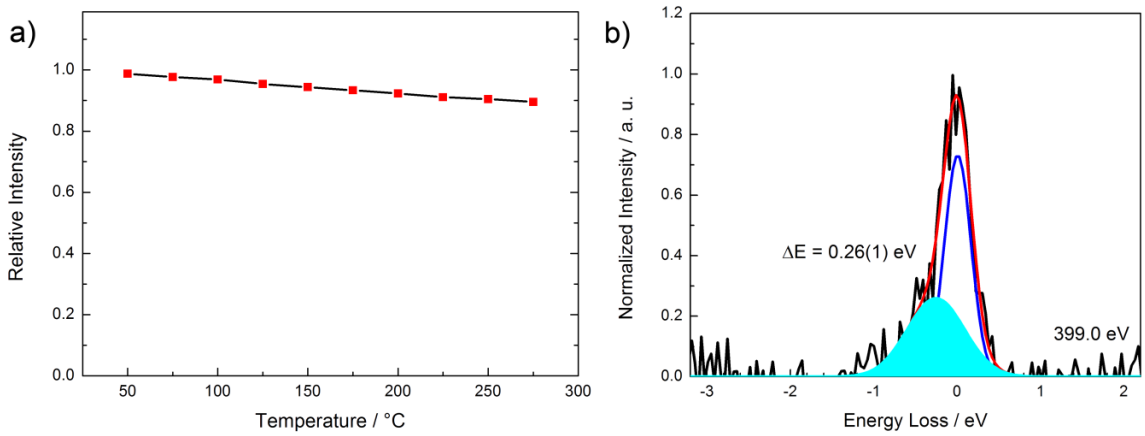

Figure 8. (a) Thermal quenching behavior of $Sr[Be_6ON_4]:Eu^{2+}$. (b) RIXS spectrum (399.0 eV excitation) on an energy loss scale, the peaks from a least-squares fit of two Gaussians to the RIXS are shown as blue (elastic) and cyan (loss feature) curves.

4.2.4 Conclusions

This work describes synthesis as well as investigation of luminescence and electronic properties of the first oxonitridoberyllate $Sr[Be_6ON_4]:Eu^{2+}$. The cyan-emitting phosphor shows excellent narrow-band emission with λ_{em} = 495 nm and *fwhm* = 35 nm, comparable to $BaSi_2O_2N_2:Eu^{2+}$.[10] The phosphor material shows superior thermal quenching behavior and superior long-time stability with a relative emission intensity of 90% at 275 °C even for nonoptimized samples, making $Sr[Be_6ON_4]:Eu^{2+}$ a promising, thermally and chemically stable narrow-band emitting phosphor to cover the cyan emission gap typically observed in blue pumped pcLEDs.

The oxonitridoberyllate's excellent emission characteristics are strongly related to the compound's crystal structure. Highly condensed layers of edge-sharing BeN_4 tetrahedra are connected by vertex-sharing $BeON_3$ tetrahedra forming a rigid 3D-network structure. This network provides for a regularly coordinated dopant site, resulting in the narrow-band cyan emission. Safe handling of Be-containing, air-sensitive as well as air-insensitive starting materials is guaranteed by handling in Ar-filled glove boxes. This method is already state-of-the-art for highly sensitive Si- and Al-containing starting materials for fabrication of Eu^{2+}- and Ce^{3+}-doped phosphors. Chemical stability under acidic conditions up to pH 1 which may be further improved by, e.g., particle coatings ensures safe handling and prevents unwanted release of Be into the environment.

$Sr[Be_6ON_4]:Eu^{2+}$ shows close structural relations to nitridosilicate- and aluminate as well as oxide structures, and the development of the novel narrow-band cyan phosphor is therefore the realization of structural evolution, comparable with the mineral-inspired prototype evolution method.[45,46] A highly condensed network is known from other phosphor materials, e.g., $(BaSr)_2Si_5N_8:Eu^{2+}$ and $Sr[LiAl_3N_4]:Eu^{2+}$.[2,4] The structure of $Sr[Be_6ON_4]:Eu^{2+}$ can be seen as an intermediate structure between β-Be_3N_2, Mg_3GaN_3, as well as $SrBe_3O_4$ and isotypic $SrBe[Si_2N_4]$.[15,37] These findings give deep insights into the structural chemistry of beryllium compounds and can help in finding and understanding the formation of novel, narrow-band emitting beryllate phosphors. Due to its large band gap, excellent QE is expected upon optimization of the synthesis procedure. Its stability, extraordinary luminescence characteristics, and excellent thermal behavior make $Sr[Be_6ON_4]:Eu^{2+}$ a highly promising phosphor for application in next-generation LEDs with CRI values >90.

4.2.5 References

[1] Pust, P.; Schmidt, P. J.; Schnick, W. A revolution in lighting. *Nat. Mater.* **2015**, *14*, 454-458.

[2] Pust, P.; Weiler, V.; Hecht, C.; Tücks, A.; Wochnik, A. S.; Henß, A. K.; Wiechert, D.; Scheu, C.; Schmidt, P. J.; Schnick, W. Narrow-band red-emitting $Sr[LiAl_3N_4]:Eu^{2+}$ as a next-generation LED-phosphor material. *Nat. Mater.* **2014**, *13*, 891-896.

[3] Watanabe, H.; Kijima, N. Crystal structure and luminescence properties of $Sr_xCa_{1-x}AlSiN_3:Eu^{2+}$ mixed nitride phosphors. *J. Alloys Compd.* **2009**, *475*, 434-439.

[4] Höppe, H. A.; Lutz, H.; Morys, P.; Schnick, W.; Seilmeier, A. Luminescence in Eu^{2+}-doped $Ba_2Si_5N_8$: fluorescence, thermoluminescence, and upconversion. *J. Phys. Chem. Solids* **2000**, *61*, 2001-2006.

[5] Kitai, A., *Materials for Solid State Lighting and Displays*, John Wiley and Sons: West Sussex, U.K., **2017**.

[6] High Color-Rendering, Full-Visible-Spectrum LEDs by Soraa. *LED professional Review* **2016**.

[7] McKittrick, J.; Hannah, M. E.; Piquette, A.; Han, J. K.; Choi, J. I.; Anc, M.; Galvez, M.; Lugauer, H.; Talbot, J. B.; Mishra, K. C. Phosphor Selection Considerations for Near-UV LED Solid State Lighting. *ECS J. Solid State Sci. Technol.* **2013**, *2*, R3119-R3131.

[8] Schmiechen, S.; Pust, P.; Schmidt Peter, J.; Schnick, W. Weißes Licht aus Nitriden. *Nachr. Chem.* **2014**, *62*, 847-851.

[9] Wang, Y.-F.; Liu, L.; Xie, R.-J.; Huang, Q. Microwave Assisted Sintering of Thermally Stable $BaMgAl_{10}O_{17}:Eu^{2+}$ Phosphors. *ECS J. Solid State Sci. Technol.* **2013**, *2*, R196-R200.

[10] Bachmann, V.; Ronda, C.; Oeckler, O.; Schnick, W.; Meijerink, A. Color Point Tuning for $(Sr,Ca,Ba)Si_2O_2N_2:Eu^{2+}$ for White Light LEDs. *Chem. Mater.* **2009**, *21*, 316-325.

[11] Seibald, M.; Rosenthal, T.; Oeckler, O.; Fahrnbauer, F.; Tücks, A.; Schmidt, P. J.; Schnick, W. Unexpected Luminescence Properties of $Sr_{0.25}Ba_{0.75}Si_2O_2N_2:Eu^{2+}$ – A Narrow Blue Emitting Oxonitridosilicate with Cation Ordering. *Chem. Eur. J.* **2012**, *18*, 13446-13452.

[12] Seibald, M.; Rosenthal, T.; Oeckler, O.; Maak, C.; Tücks, A.; Schmidt, P. J.; Wiechert, D.; Schnick, W. New Polymorph of the Highly Efficient LED-Phosphor $SrSi_2O_2N_2:Eu^{2+}$ – Polytypism of a Layered Oxonitridosilicate. *Chem. Mater.* **2013**, *25*, 1852-1857.

[13] Seibald, M.; Rosenthal, T.; Oeckler, O.; Schnick, W. Highly Efficient pc-LED Phosphors $Sr_{1-x}Ba_xSi_2O_2N_2:Eu^{2+}$ ($0<x<1$) - Crystal Structures and Luminescence Properties Revisited. *Crit. Rev. Solid State Mater. Sci.* **2014**, *39*, 215-229.

[14] Wang, C.-Y.; Xie, R.-J.; Li, F.; Xu, X. Thermal degradation of the green-emitting $SrSi_2O_2N_2:Eu^{2+}$ phosphor for solid state lighting. *J. Mater. Chem. C* **2014**, *2*, 2735-2742.

[15] Harris, L. A.; Yakel, H. L. The crystal structure of $SrBe_3O_4$. *Acta Crystallogr. Sect. B* **1969**, *25*, 1647-1651.

[16] Strobel, P.; Weiler, V.; Schmidt, P. J.; Schnick, W. $Sr[BeSi_2N_4]:Eu^{2+}/Ce^{3+}$ and $Eu[BeSi_2N_4]$: Nontypical Luminescence in Highly Condensed Nitridoberyllosilicates. *Chem. Eur. J.* **2018**, *24*, 7243-7249.

[17] Agency for Toxic Substances and Disease Registry (ATSDR) - Case Studies in Environmental Medicine - Beryllium Toxicity **2018**.

[18] Kreiss, K.; Day, G. A.; Schuler, C. R. Beryllium: A Modern Industrial Hazard. *Annu. Rev. Public Health* **2007**, *28*, 259-277.

[19] García-Gutiérrez, R.; Barboza-Flores, M.; Berman-Mendoza, D.; Contreras-López, O. E.; Ramos-Carrazco, A. Synthesis and characterization of highly luminescent beryllium nitride. *Mater. Lett.* **2014**, *132*, 179-181.

[20] BrukerAXS, *APEX3 v2016.5-0*: Billerica, **2016**.

[21] Sheldrick, G. M., *SHELXS-97: A program for crystal structure solution*, University of Göttingen, **1997**.

[22] Sheldrick, G. M., *SHELXL-97: A program for crystal structure refinement*, University of Göttingen, **1997**.

[23] Sheldrick, G. M. A short history of SHELX. *Acta Crystallogr. Sect. A* **2008**, *64*, 112-122.

[24] Coelho, A. A., *TOPAS-Academic*, Version 4.1: A program for Rietveld refinement: Brisbane, Australia, **2007**.

[25] Tauc, J.; Grigorovici, R.; Vancu, A. Optical Properties and Electronic Structure of Amorphous Germanium. *Phys. Status Solidi B* **1966**, *15*, 627-637.

[26] Strobel, P.; Weiler, V.; Hecht, C.; Schmidt, P. J.; Schnick, W. Luminescence of the Narrow-Band Red Emitting Nitridomagnesosilicate $Li_2(Ca_{1-x}Sr_x)_2[Mg_2Si_2N_6]:Eu^{2+}$ (x = 0–0.06). *Chem. Mater.* **2017**, *29*, 1377-1383.

[27] Regier, T.; Krochak, J.; Sham, T. K.; Hu, Y. F.; Thompson, J.; Blyth, R. I. R. Performance and capabilities of the Canadian Dragon: The SGM beamline at the Canadian Light Source. *Nucl. Instrum. Methods Phys. Res.* **2007**, *582*, 93-95.

[28] Schwarz, K.; Blaha, P.; Madsen, G. K. H. Electronic structure calculations of solids using the WIEN2k package for material sciences. *Comput. Phys. Commun.* **2002**, *147*, 71-76.

[29] Perdew, J. P.; Ruzsinszky, A.; Csonka, G. I.; Vydrov, O. A.; Scuseria, G. E.; Constantin, L. A.; Zhou, X.; Burke, K. Restoring the Density-Gradient Expansion for Exchange in Solids and Surfaces. *Phys. Rev. Lett.* **2008**, *100*, 136406.

[30] Tran, F.; Blaha, P. Accurate Band Gaps of Semiconductors and Insulators with a Semilocal Exchange-Correlation Potential. *Phys. Rev. Lett.* **2009**, *102*, 226401.

[31] Schwarz, K.; Neckel, A.; Nordgren, J. On the X-ray emission spectra from FeAl. *J. Phys. F: Met. Phys.* **1979**, *9*, 2509.

[32] von Barth, U.; Grossmann, G. Dynamical effects in x-ray spectra and the final-state rule. *Phys. Rev. B* **1982**, *25*, 5150-5179.

[33] Bashir, J.; Khan, R. T. A.; Butt, N. M.; Heger, G. Thermal atomic displacement parameters of SrO. *Powder Diffr.* **2012**, *17*, 222-224.

[34] Baur, W. H. Effective ionic radii in nitrides. *Crystallogr. Rev.* **1987**, *1*, 59-83.

[35] Eckerlin, P.; Rabenau, A. Zur Kenntnis des Systems Be_3N_2-Si_3N_4. Die Struktur einer neuen Modifikation von Be_3N_2. *Z. Anorg. Allg. Chem.* **1960**, *304*, 218-229.

[36] Hall, D.; Gurr, G. E.; Jeffrey, G. A. Zur Kenntnis des Systems Be_3N-Si_3N_4. V. A Refinement of the Crystal Structure of β-Beryllium Nitride. *Z. Anorg. Allg. Chem.* **1969**, *369*, 108-112.

[37] Hintze, F.; Johnson, N. W.; Seibald, M.; Muir, D.; Moewes, A.; Schnick, W. Magnesium Double Nitride Mg_3GaN_3 as New Host Lattice for Eu^{2+} Doping: Synthesis, Structural Studies, Luminescence, and Band-Gap Determination. *Chem. Mater.* **2013**, *25*, 4044-4052.

[38] Somer, M.; Yarasik, A.; Akselrud, L.; Leoni, S.; Rosner, H.; Schnelle, W.; Kniep, R. $Ae[Be_2N_2]$: Nitridoberyllates of the Heavier Alkaline-Earth Metals. *Angew. Chem. Int. Ed.* **2004**, *43*, 1088-1092.

[39] Leoni, S.; Niewa, R.; Akselrud, L.; Prots, Y.; Schnelle, W.; Göksuc, T.; Cetinkol, M.; Somer, M.; Kniep, R. Novel Barium Beryllates Ba[Be_2N_2] and Ba_3[Be_5O_8]: Syntheses, Crystal Structures and Bonding Properties. *Z. Anorg. Allg. Chem.* **2005**, *631*, 1818-1824.

[40] Schmitt Martin, K.; Huppertz, H. $Ni_6B_{22}O_{39}{\cdot}H_2O$ – extending the field of nickel borates. *Z. Naturforsch. B: J. Chem. Sci.* **2017**, *72*, 967.

[41] Neumair, S. C.; Knyrim, J. S.; Oeckler, O.; Glaum, R.; Kaindl, R.; Stalder, R.; Huppertz, H. Intermediate States on the Way to Edge-Sharing BO_4 Tetrahedra in $M_6B_{22}O_{39}{\cdot}H_2O$ (*M* = Fe,Co). *Chem. Eur. J.* **2010**, *16*, 13659-13670.

[42] Kurmaev, E. Z.; Wilks, R. G.; Moewes, A.; Finkelstein, L. D.; Shamin, S. N.; Kuneš, J. Oxygen x-ray emission and absorption spectra as a probe of the electronic structure of strongly correlated oxides. *Phys. Rev. B* **2008**, *77*, 165127.

[43] Eisebitt, S.; Eberhardt, W. Band structure information and resonant inelastic soft X-ray scattering in broad band solids. *J. Electron Spectrosc. Relat. Phenom.* **2000**, *110–111*, 335-358.

[44] Tolhurst, T. M.; Strobel, P.; Schmidt, P. J.; Schnick, W.; Moewes, A. Direct Measurements of Energy Levels and Correlation with Thermal Quenching Behavior in Nitride Phosphors. *Chem. Mater.* **2017**, 7976-7983.

[45] Xia, Z.; Liu, Q. Progress in discovery and structural design of color conversion phosphors for LEDs. *Prog. Mater. Sci.* **2016**, *84*, 59-117.

[46] Xia, Z.; Xu, Z.; Chen, M.; Liu, Q. Recent developments in the new inorganic solid-state LED phosphors. *Dalton Trans.* **2016**, *45*, 11214-11232.

4.3 Oxoberyllates $SrBeO_2$ and $Sr_{12}Be_{17}O_{29}$ as Novel Host Materials for Eu^{2+} Luminescence

published in: *Chem. Eur. J.*, **2018**, https://doi.org/10.1002/chem.201801951
authors: Philipp Strobel, Robin Niklaus, Peter J. Schmidt and Wolfgang Schnick
DOI: 10.1002/chem.201801951

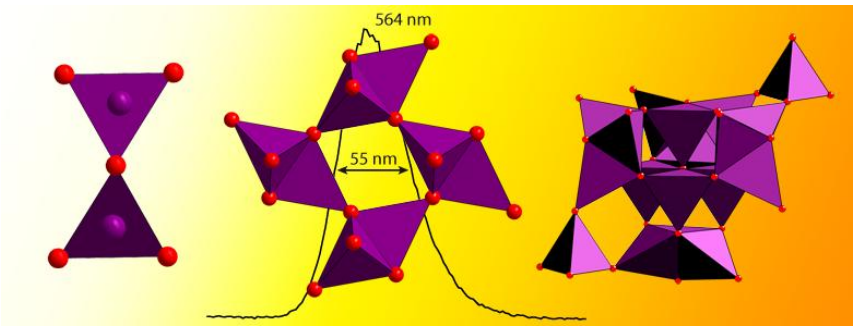

Abstract: Beryllate structures are marginally investigated, but show intriguing structural relations to oxo- and nitridosilicates. A typical feature is the coordination of Be both in trigonal planar and tetrahedral coordination by O. A broad range of structures is accessible by variable combinations of both building units. Three novel ternary Sr-oxoberyllates are characterized by single-crystal X-ray diffraction analysis, density functional theory calculations and investigations on luminescence properties: α-$SrBeO_2$, β-$SrBeO_2$ and $Sr_{12}Be_{17}O_{29}$ are obtained with oxoberyllate substructures made up of either BeO_3 triangles or BeO_4 tetrahedra. The compounds can be described as chain- and layer-type beryllates. When excited with blue light of (In,Ga)N LED chips β-$SrBeO_2$ and $Sr_{12}Be_{17}O_{29}$ show visible emission in the yellow and orange spectral range, respectively, upon doping with Eu^{2+}. Both are the first luminescent oxoberyllates reported so far. Exceptional narrow-band yellow emission (λ_{em} = 564 nm, *fwhm* = 55 nm) make $SrBeO_2$:Eu^{2+} a promising phosphor for application in phosphor converted (pc-)LEDs.

4.3.1 Introduction

Eu^{2+}-doped phosphors are widely applied in state-of-the-art illumination grade white phosphor converted (pc-)LEDs. Highly condensed oxo- and nitridosilicates as well as -aluminates are subject to intensive investigations.[1-4] Narrow-band emitting phosphors are required to increase the luminous efficacy of illumination grade LEDs, as well as to improve a LED's color gamut for application in backlight LCD (liquid crystal display) TVs.[1,5,6] To gain narrow-band emission with high luminous efficacy, symmetric Eu^{2+}-coordination and rigid host materials with large band gap are demanded. We recently demonstrated that Be-containing (oxo)nitridoberyllates are of significant interest, as Eu^{2+}-doped compounds show enormous potential for application in pc-LEDs.[7,8]

Yet, oxoberyllates have been barely investigated, even though Be-containing minerals are well known for almost 100 years.[9-11] Due to the toxicity of Be-containing dusts, only few synthetic Be-compounds have been investigated so far. Three ternary beryllates, containing a heavier alkaline earth metal (*AE* = Ca–Ba), are structurally characterized, namely $Ca_{12}Be_{17}O_{29}$, $SrBe_3O_4$ and $Ba_3Be_5O_8$.[12-14] Two more compositions, namely $Ca_2Be_3O_5$, possibly crystallizing in cubic space group $Fm\bar{3}m$, and $Sr_2Be_3O_5$, with orthorhombic metrics, are discussed, but not yet confirmed.[15] These ternary beryllates are first examples proposing great structural diversity, which could be even more diverse than the huge structural variability approached by silicates and aluminates. Foundation for this enhanced structural variability is a secondary building unit, namely BeO_3-triangles, which besides BeO_4-tetrahedra are part of the anionic beryllate network structures. A similar structural situation is not known from oxosilicates and –aluminates, but was similarly observed in oxo- and (oxo)nitridoberyllates.[7,8,13] In $Ca_{12}Be_{17}O_{29}$, $SrBe_3O_4$ and $Ba_3Be_5O_8$ both BeO_4-tetrahedra and BeO_3-triangles occur, while exclusively BeO_4-tetrahedra are found e.g. in binary BeO.[16] Yet, there are only few beryllates known exhibiting solely trigonal planar BeO_3-units, e.g. Y_2BeO_4.[17]

The most famous compound containing Be in tetrahedral coordination is the mineral beryl and its colored varieties emerald and aquamarine. $Be_3Al_2(SiO_3)_6$ is commonly described as a hexacyclosilicate.[10] Alternatively, beryl can be interpreted as highly condensed network of regular SiO_4- and distorted BeO_4-tetrahedra with a degree of condensation (i.e. molar ratio (Be,Si):O) $\kappa = 0.5$, offering space for octahedrally coordinated Al. $SrBe_3O_4$, the until now only known compound in the system Sr-Be-O, exhibits a 3D-network of triangles and tetrahedra isotypic to $Sr[BeSi_2N_4]$.[7] When heavier *AE* metals (Ca–Ba) are introduced into similar highly condensed network structures consisting of BeX_3- and BeX_4-units (X = N,O), doping with rare earth elements (*RE*, e.g., Eu^{2+}, Ce^{3+}) is possible to obtain luminescence in the visible part of the spectrum, comparable to diverse oxo/nitridosilicates and -aluminates.[7,8]

In this contribution, the first luminescent ternary beryllates, namely β-$SrBeO_2$:Eu^{2+} and $Sr_{12}Be_{17}O_{29}$:Eu^{2+} as well as non-luminescent α-$SrBeO_2$:Eu^{2+} are described and characterized. Crystal structures of the three novel ternary Sr-beryllates were solved and refined from single-crystal XRD data and confirmed by Rietveld analysis on PXRD data. The crystal structures show interesting

relations to known oxosilicate and nitridosilicate structures. Condensed building units form similarly designed structures of non-condensed units, chains, layers or networks, respectively. The title compounds crystallize as chain or layered beryllates of either triangles or tetrahedra. They are stable toward hydrolysis and have initially been observed as single-crystalline side-phases during the synthesis of the oxonitridoberyllate $SrBe_6ON_4$:Eu^{2+} that shows narrow-band cyan emission.[8] While α-$SrBeO_2$(:Eu^{2+}) is obtained as colorless transparent crystals, Eu^{2+}-doped β-$SrBeO_2$ exhibits narrow-band yellow luminescence, $Sr_{12}Be_{17}O_{29}$:Eu^{2+} orange luminescence. Its narrow-band yellow emission makes β-$SrBeO_2$:Eu^{2+} an interesting phosphor for application in yellow and white pc-LEDs, based on blue InGaN LED chips.

4.3.2 Results and Discussion

4.3.2.1 Synthesis and Elemental Analysis.

Single crystals of α-$SrBeO_2$ and β-$SrBeO_2$ as well as $Sr_{12}Be_{17}O_{29}$ were synthesized by high-temperature routes. The targeted phase pure synthesis of the title compounds is challenging. $Sr_{12}Be_{17}O_{29}$ and $SrBe_3O_4$ are obtained concomitantly at synthesis conditions of 950 °C in Ta-ampules or in W-crucibles at 1400 °C in Ar-atmosphere in a radio-frequency furnace, starting from SrO and BeO. Similar conditions are applied for the synthesis of α- and β-$SrBeO_2$ that appear only as by-products next to $SrBe_6ON_4$, when starting from a heterogeneous SrO-Be_3N_2 mixture. This leads to the assumption that both $SrBeO_2$ polymorphs are kinetically inert, while $Sr_{12}Be_{17}O_{29}$ and $SrBe_3O_4$ are thermodynamically stable products. All title compounds have proven stability at ambient conditions and against hydrolysis in water and 1M HCl (pH 1).

EDS (Energy-dispersive X-ray spectroscopy) was used for determination of the atomic ratio (Sr:N:O) of the single-crystalline compounds' elemental compositions. Besides O, no N was detected, leaving the conclusion of the formation of pure oxide phases. Beryllium was not detected by EDS due to methodical limits. While α-$SrBeO_2$ and β-$SrBeO_2$ gave a Sr/O ratio of 1:2.3, measurements of orange $Sr_{12}Be_{17}O_{29}$ crystals showed a value of 12:29.4. These findings are in good accordance with the specific sum formulas obtained from single-crystal refinement. Next to Sr no other metals were detected by EDS, leaving Li and Be as only possible elements on tetrahedral centers, as both cannot be determined by EDS. Li–O-distances are usually found with larger values (≈ 1.9 Å), which is not conform to crystallographic data. Supported by MAPLE calculations and according to bond lengths discussion, as discussed in detail below, as well as charge neutrality, Be is therefore confirmed as cation in all title compounds.

4.3.2.2 Crystal Structure Determination.

Single crystals of α-$SrBeO_2$, β-$SrBeO_2$ and $Sr_{12}Be_{17}O_{29}$ have been analyzed applying X-ray diffraction experiments. α-$SrBeO_2$ crystallizes in monoclinic space group $P2_1/m$ (no. 11) with cell parameters a = 3.5824(3), b = 5.1732(5), c = 5.5515(5) Å and β = 98.262(4)° and was refined as a

two-component inversion twin. This polymorph has been denominated as the *α*-polymorph as it is assumed to be the high-temperature form due to its less condensed building units and lower density. *β*-$SrBeO_2$, crystallizes in space group $P2_1/c$ (no. 14, a = 7.0045(9), b = 5.0697(11), c = 5.3127(7) Å and β = 98.935(6)°). $Sr_{12}Be_{17}O_{29}$, refined as a two-component inversion twin, shows tetragonal metrics ($I\bar{4}2m$, no. 121) with a = 11.0104(4) and c = 10.6208(10) Å.

Crystallographic data of the structure solution and refinement are displayed in Table 1. Supporting data, details of the structure solution and refinement, atomic coordinates and isotropic displacement parameters, selected bond lengths and angles, anisotropic displacement parameters (ADPs) as well as graphical presentations of Rietveld refinements are listed in the Supplementary Material.

Lattice-energy calculations (MAPLE, Madelung Part of Lattice Energy) were additionally performed to support the structural models' consistency. MAPLE values were calculated for each ion type and for the complete structure. The results of the MAPLE calculations are summarized in the Supplementary Material. The partial MAPLE values are in good agreement with reference data reported before. Partial MAPLE values for Sr^{2+}, Be^{2+} and O^{2-} are listed. The comparison of the MAPLE sums of the title compounds with total MAPLE values of constituting binary and ternary oxides show only minor deviations.[13,16,18]

Table 1. Crystallographic data of single-crystals of *α*-$SrBeO_2$, *β*-$SrBeO_2$ and $Sr_{12}Be_{17}O_{29}$.[a]

		***α*-SrBeO₂**	***β*-SrBeO₂**	**Sr₁₂Be₁₇O₂₉**
Crystal system		monoclinic		tetragonal
Space group		$P2_1/m$ (no. 11)	$P2_1/c$ (no.14)	$I\bar{4}2m$ (no. 121)
Z		2	4	2
Lattice parameters [Å,°]	a	3.5824(3)	7.0045(9)	11.0104(4)
	b	5.1732(5)	5.0697(11)	
	c	5.5515(5)	5.3127(7)	10.6208(10)
	β	98.262(4)	98.935(6)	
V [Å^3]		101.815(16)	186.37(5)	1287.55(15)
ρ [g cm^{-3}]		4.19549	4.58409	4.30373

[a]e.s.d.s are given in parentheses.

4.3.2.3 Crystal Structure Description.

The structure of *α*-$SrBeO_2$, displayed in Figure 1, crystallizes in monoclinic space group $P2_1/m$ (no. 11) and exhibits a chain-like structure. Infinite *zweier* single chains of BeO_3-units are observed, applying the nomenclature of silicates according to *Liebau* on structures with AX_3-units (A = B, Be, etc.; X = O, N, etc.).[19] Each triangle is connected to two other triangles by common vertices, one remaining vertex is terminal resulting in the presence of O2[2] and O1[1] sites.[20] The triangle chains are separated by Sr atoms that are in a 6+2 coordination by O, which can be described as a doubly capped trigonal prism. Be-O distances are in a range 1.53–1.55 Å. A long-range Be-O interaction with a distance of 3.05 Å presumably causes the deviation of the Be site from its trigonal planar coordination, giving a strong hint for a preferred tetrahedral coordination of Be. This observation is supported by prolate ADPs of the O2 site indicating additional binding forces towards a more distant Be atom. This effect has been closer investigated with low-temperature single-crystal XRD measurements corroborating that the ADP ellipsoids of the O2 position result from bending vibrations of Be–O as

elliptic deflection decreases upon cooling, shown in low temperature single-crystal X-ray diffraction experiments at 100 K.

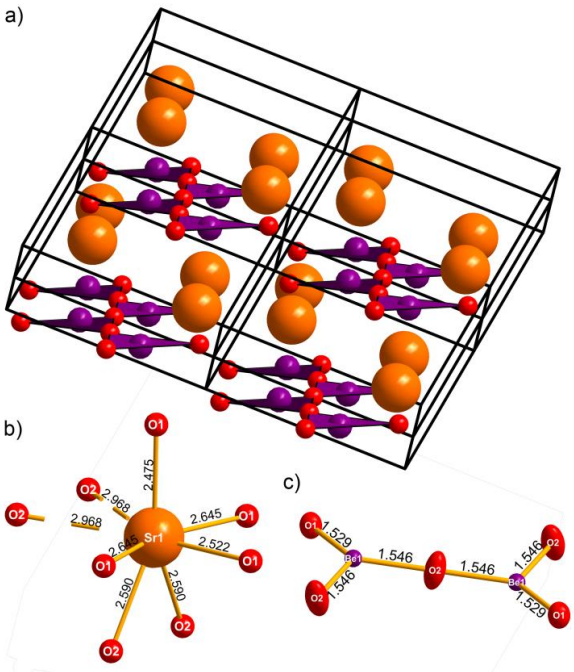

Figure 1. a) Crystal structure of α-$SrBeO_2$; b) Sr-O coordination; c) Be-O coordination. Sr (orange), Be (violet), O (red), BeO_3 units (violet). Distances are given in Å.

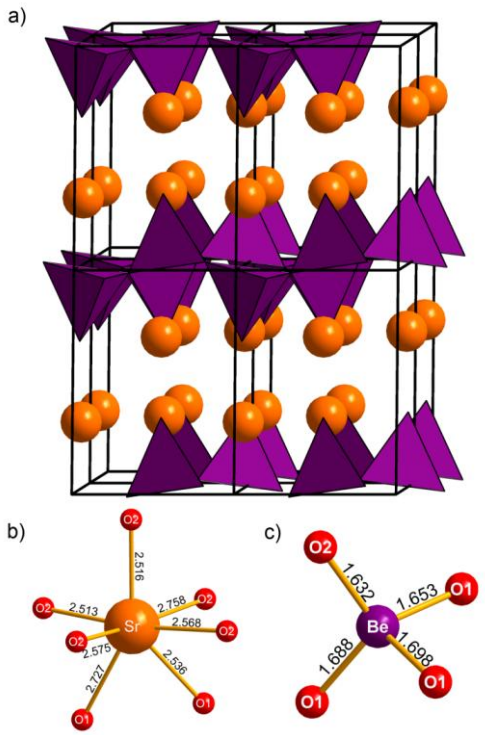

Figure 2. a) Crystal structure of β-$SrBeO_2$; b) Sr-O coordination; c) Be-O coordination. Sr (orange), Be (violet), O (red), BeO_4 tetrahedra (violet). Distances are given in Å.

The crystal structure of β-$SrBeO_2$ in monoclinic space group $P2_1/c$ (no. 14) consists of layers of condensed BeO_4-tetrahedra, shown in Figure 2. Two tetrahedra are connected via common edges, building $[Be_2O_6]$-"bow-tie" units. These units are linked twice by vertices to edge-connecting O of an adjacent "bow-tie"-unit. The two remaining O are terminal. This arrangement leads to the presence of one $O^{[1]}$ and three $O^{[3]}$ per tetrahedron. The layers form rhombic distorted *vierer* rings and are stacked on top of each other, forming *vierer* ring channels. Sr atoms in sevenfold O-coordination are found between the layers, with Sr–O distances between 2.51 and 2.76 Å. As a result of the coordination number increase of Be from 3 in the α-polymorph to 4, Be–O distances are elongated to 1.63–1.70 Å. Due to increased density and formation of tetrahedra, β-$SrBeO_2$ is discussed as the high-pressure and low-temperature polymorph.

With its sheet structure, β-$SrBeO_2$ is closely related to the nitridosilicates $MSiN_2$ (M = Sr,Ba) that show similar connectivity of SiN_4-tetrahedra.[21] $[Si_2N_6]$-"bow-tie" units are connected to adjacent "bow-ties" by four vertices, forming *sechser* rings. No terminal $O^{[1]}$ are found, but two different $O^{[2]}$ sites.

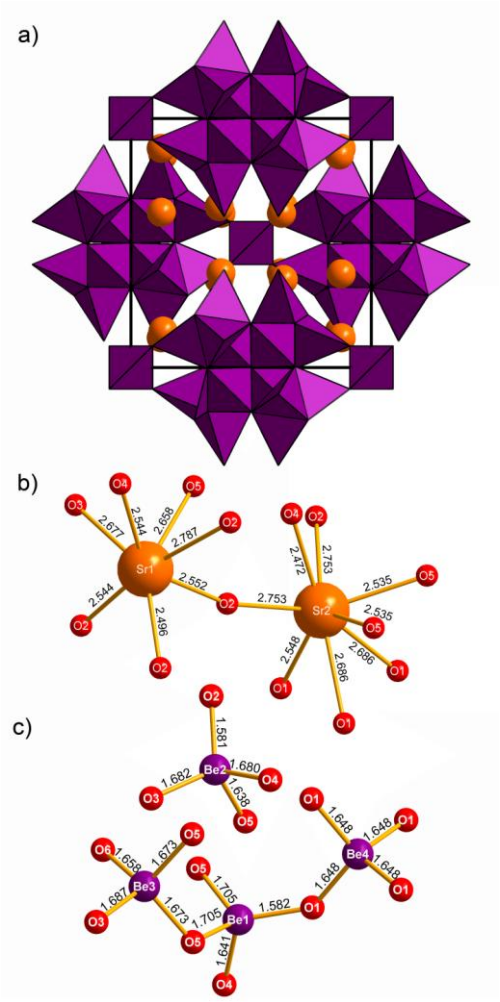

Figure 3. a) Crystal structure of $Sr_{12}Be_{17}O_{29}$ (viewing direction along [100]; b) Sr–O coordinations; c) Be-O coordinations. Sr (orange), Be (violet), O (red), BeO_4 tetrahedra (violet). Distances are given in Å.

$Sr_{12}Be_{17}O_{29}$ (Figure 3) crystallizing in the tetragonal space group $I\bar{4}2m$ (no. 121) shows striking similarities with $Ca_{12}Be_{17}O_{29}$ regarding stoichiometry and structure. Nevertheless, both structures are not isotypic. The structure of $Ca_{12}Be_{17}O_{29}$, crystallizing in the cubic space group $F\bar{4}3m$, resembles a zeolithic network of BeO_3-triangles and BeO_4-tetrahedra.[12] Cavities within the network are filled with building blocks of BeO_3- and BeO_4-units. In $Sr_{12}Be_{17}O_{29}$ as well as $Ca_{12}Be_{17}O_{29}$, this assembly of building blocks is related. The core element of the assembly in both structures is a detail of hypothetical *sphalerite*-type BeO, crystallizing in space group $F\bar{4}3m$; this BeO polymorph is predicted at very high pressures and temperatures:[22] Four BeO_4-tetrahedra are connected by one common oxygen forming star-shaped $[O^{[4]}(BeO_3)_4]$ units. In highly condensed silicate structures containing $X^{[4]}$ (X = O,N), only $N^{[4]}$, connecting four SiN_4 tetrahedra, is known.[23-26] In $Ca_{12}Be_{17}O_{29}$, these star-shaped units are isolated, but stabilized by four capping Be atoms, forming BeO_3-units. In $Sr_{12}Be_{17}O_{29}$, in contrast, triples of edge-sharing tetrahedra stabilize the $[O^{[4]}(BeO_3)_4]$ units, resulting in larger units of 16 condensed BeO_4-tetrahedra. These units are again connected by tetrahedra to strands along [001]. The setup of strands is displayed in Figure 4. The arrangement of strands can be described as closest packing, while strands are separated by Sr-atoms in seven- and eightfold O-coordination, respectively, with Sr–O distances between 2.50 and 2.79 Å. Be–O distances are in a range of 1.58–1.71 Å comparable to the values found for the regular tetrahedrally coordinated Be sites in $Ca_{12}Be_{17}O_{29}$.[12]

The beryllates consisting of tetrahedral networks, namely β-$SrBeO_2$ and $Sr_{12}Be_{17}O_{29}$ show close structural relationships to highly condensed nitridosilicate structures. Be^{2+} with the same ionic radius as Si^{4+} and similar electronegativity can effectively substitute Si on tetrahedrally coordinated crystallographic sites.[27] The increased structural variety of nitridosilicates, compared to oxosilicates is induced by the larger size of the nitride ion and its ability to link a larger number of cations than oxide ions.[4] In contrast, the higher connectivity of tetrahedra in beryllates is achieved by the reduced formal charge of Be, compared to Si, allowing the formation of edge-sharing tetrahedra and even the appearance of $O^{[3]}$ and $O^{[4]}$.

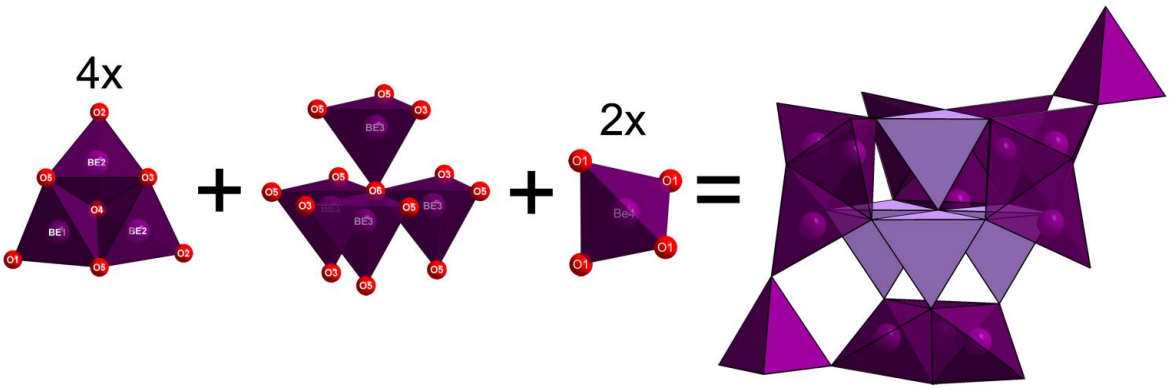

Figure 4. Setup of strands of BeO_4 tetrahedra in $Sr_{12}Be_{17}O_{29}$. Be (violet), O (red), BeO_4 tetrahedra (violet). Distances are given in Å.

As a result, structures with “bow-tie” units and highly condensed layers or networks are accessible in oxoberyllate structures. Additionally, structures with characteristics often found in borates can be obtained in beryllates, e.g., α-$SrBeO_2$ exhibiting only trigonal planarly coordinated Be.[28] A combination of tetrahedral and trigonal planar units in a single structure is found in e.g., $SrBe_3O_4$ as well as $Ca_{12}Be_{17}O_{29}$[12,13].

4.3.2.4 DFT calculations.

In order to investigate thermodynamic stabilities and to validate our experimental findings of all compounds in the ternary system Sr-Be-O, calculations based on the DFT (density functional theory) method using the program package VASP have been applied. The respective enthalpies of formation of α-$SrBeO_2$, β-$SrBeO_2$, $SrBe_3O_4$ and $Sr_{12}Be_{17}O_{29}$ have been calculated with respect to their O_2 content.[29,30]

Table 2. Enthalpies of formation and reaction from binary oxides (T = 0 K) of α-$SrBeO_2$, β-$SrBeO_2$, $SrBe_3O_4$ and $Sr_{12}Be_{17}O_{29}$ (f.u.: formula unit).

Formula	Enthalpy of formation (eV per O_2)	Enthalpy of reaction (eV per f.u.)	Enthalpy of reaction (eV per O_2)
SrO	-11.147		
BeO	-11.210		
α-$SrBeO_2$	-11.214	-0.036	-0.036
β-$SrBeO_2$	-11.222	-0.043	-0.043
$SrBe_3O_4$	-11.280	-0.171	-0.086
$Sr_{12}Be_{17}O_{29}$	-11.277	-1.348	-0.092

From Table 2 it becomes apparent that $SrBe_3O_4$ and $Sr_{12}Be_{17}O_{29}$ appear as the thermodynamically most stable structures. With respect to their enthalpy of formation both compounds differ only by 0.29 kJ/mol while both polymorphs of β- and α-$SrBeO_2$ are energetically elevated by 5.3 and 6.1 kJ/mol.

Hence, the experimentally observed formation of both $SrBe_3O_4$ and $Sr_{12}Be_{17}O_{29}$ is in line with their small difference in formation enthalpy and their respective synthesis temperatures above 1200 K. Considering the calculated total and further normalized enthalpies of reaction, the increased stability of $SrBe_3O_4$ and $Sr_{12}Be_{17}O_{29}$ of more than 4.1 kJ/mol with regard to both $SrBeO_2$ polymorphs is further demonstrated. Evidently, all compounds are also thermodynamically stable against phase separation into their binary oxides. In line with their elevated enthalpies of formation, both α-$SrBeO_2$ and β-$SrBeO_2$ appear to be inaccessible from pure SrO and BeO at the applied synthesis conditions. This corroborates the suggested kinetically controlled formation of both $SrBeO_2$ polymorphs from different starting materials like Be_3N_2.

The stability of both polymorphs was further examined through calculations of the phonon dispersion within the supercell approach. While β-$SrBeO_2$ is shown to be a dynamically stable structure showing no apparent imaginary modes, α-$SrBeO_2$ exhibits significant imaginary modes. This

is in line with the lower condensation degree making α-$SrBeO_2$ most likely an intermediate structure regarding a reconstructive formation of β-$SrBeO_2$.

With phase pure synthesis being out of reach for the luminescent beryllates described in this work an estimate of the band gaps was further calculated from theory. Band gaps from standard GGA-PBE yield E_g values of 3.7 eV (α-$SrBeO_2$), 4.4 eV (β-$SrBeO_2$) and 4.3 eV ($Sr_{12}Be_{17}O_{29}$) respectively. Due to the usual underestimation of exchange correlation effects by standard DFT, E_g values were also calculated with the help of the modified Becke-Johnson formalism (mbj) in order to arrive at corrected estimates for β-$SrBeO_2$ and $Sr_{12}Be_{17}O_{29}$.[31] β-$SrBeO_2$ and $Sr_{12}Be_{17}O_{29}$ exhibit direct band gaps at Γ with values for E_g of 6.0 eV (β-$SrBeO_2$) and 6.4 eV ($Sr_{12}Be_{17}O_{29}$) underlining the suitability of oxoberyllates as host materials for doping with rare earth elements, such as Eu^{2+} or Ce^{3+} for possible LED applications. For efficient phosphors a band gap ≥4 eV is beneficial.[32] Graphical representations can be found in the Supplementary Material.

4.3.2.5 Luminescence.

Luminescence characteristics of the three title compounds have been investigated upon doping with Eu. During synthesis under Ar gas atmosphere Eu^{3+} was reduced to Eu^{2+}. Occupation of the Sr site with Eu (1% nominal dopant concentration) and exclusion of oxygen during synthesis explain the presence of Eu^{2+}, which is confirmed by the detection of broadband Eu^{2+} emission. While α-$SrBeO_2$:Eu^{2+} does not exhibit visible luminescence, β-$SrBeO_2$:Eu^{2+} and $Sr_{12}Be_{17}O_{29}$:Eu^{2+} show emission in the visible spectral range.[1] Additionally, no luminescence was observed in $SrBe_3O_4$:Eu^{2+} powder samples. Figure 5 shows excitation and emission spectra of β-$SrBeO_2$:Eu^{2+}. Luminescence spectra of $Sr_{12}Be_{17}O_{29}$:Eu^{2+} are shown in the Supporting Material. Both phosphors are highly excitable in the UV to blue spectral region with λ_{exc} ≈ 400 nm. $Sr_{12}Be_{17}O_{29}$:Eu^{2+} shows inefficient broadband orange emission (λ_{em} = 580 nm, *fwhm* = 157 nm), originating from two irregularly coordinated Sr sites.[3]

β-$SrBeO_2$:Eu^{2+} exhibits intense, extraordinary narrow-band emission in the yellow spectral range. The emission maximum is found at 564 nm with a band width of only 55 nm (≈ 1680 cm^{-1}). The basis for the rather narrow emission band is only one crystallographic Sr site with a large coordination sphere and highly condensed layers leading to reduced lattice vibrations and therefore a small Stokes-shift. The spectral luminescence properties of yellow emitting β-$SrBeO_2$:Eu^{2+} exhibits narrower emission as comparable Eu^{2+}-doped (oxo)nitride phosphors, e.g., $CaSi_2O_2N_2$:Eu^{2+} (λ_{em} = 560 nm; *fwhm* ≈ 2330 cm^{-1}).[33] Other yellow phosphors are $Ba[(Mg_{2-x}Li_x)(Al_{4-x}Si_x)N_6]$:$Eu^{2+}$ (x = 0–0.4) with narrow-band yellow emission at ≈ 560 nm (*fwhm* ≈ 2000 cm^{-1}),[5] $CaGa_2S_4$:Eu^{2+} (λ_{em} = 550 nm, *fwhm* ≈ 1800 cm^{-1})[34,35] and Ca-α-SiAlON ($CaSi_9Al_3ON_{15}$:Eu^{2+}) with a broader emission band at 581 nm (*fwhm* ≈ 2890 cm^{-1}).[36]

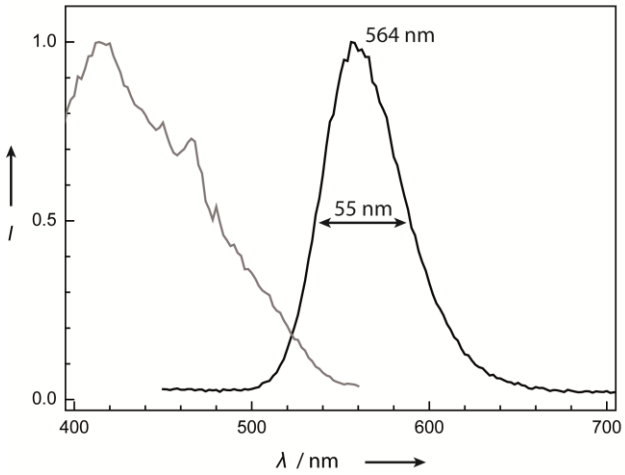

Figure 5. Excitation (gray) and emission spectrum (black) of narrow-band yellowβ-$SrBeO_2$:Eu^{2+}.

Two potential applications are discussed for such narrow-band yellow phosphors. Yellow pc-LEDs, based on blue InGaN chips are a promising replacement for yellow primary LEDs that still exhibit only low efficacy, resulting in the so-called "yellow gap".[37,38] Additionally, compared to broadband emitting phosphors, such as YAG:Ce^{3+}, narrow-band yellow phosphors guarantee the highest lumen equivalents in yellow as well as white pc-LEDs.[37]

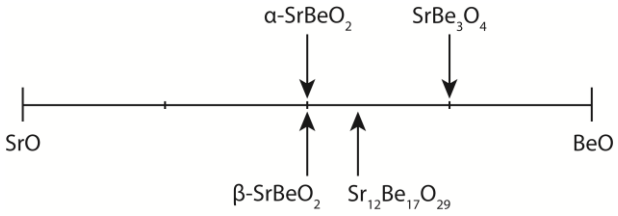

Scheme 1. Known compounds in the complemented quasi binary phase diagram of SrO-BeO**.**

4.3.3 Conclusions

In this contribution we report on three novel oxoberyllates α-$SrBeO_2$, β-$SrBeO_2$ and $Sr_{12}Be_{17}O_{29}$ in the ternary system Sr-Be-O, filling the quasi-binary phase diagram (Scheme 1). The beryllates consisting of tetrahedral networks, β-$SrBeO_2$ and $Sr_{12}Be_{17}O_{29}$, are closely related to nitridosilicates, while the structure of α-$SrBeO_2$ with trigonal planar BeO_3 units are comparable to borates. Eu^{2+}-doped samples of β-$SrBeO_2$ and $Sr_{12}Be_{17}O_{29}$ show visible emission. β-$SrBeO_2$:Eu^{2+} is a narrow-band yellow phosphor with λ_{em} = 564 nm (*fwhm* = 55nm), $Sr_{12}Be_{17}O_{29}$:Eu^{2+} exhibits broad orange emission at 580 nm (*fwhm* = 157 nm). Both phosphors are excitable by UV to blue light.

Thermodynamic stabilities of the three title compounds have been investigated by DFT methods and are compared to the stability of $SrBe_3O_4$. $Sr_{12}Be_{17}O_{29}$ appears as more stable phase compared to the so far only known ternary Sr-oxoberyllate, while α-$SrBeO_2$ and β-$SrBeO_2$ are less stable. These results support the observations during synthesis efforts. $SrBe_3O_4$ and $Sr_{12}Be_{17}O_{29}$ can be obtained starting from binary oxides SrO and BeO, while α-$SrBeO_2$ and β-$SrBeO_2$ can yet only be obtained starting

from SrO and Be_3N_2. Nevertheless, further optimization of the synthesis conditions of β-$SrBeO_2$:Eu^{2+} with its extremely narrow-band yellow emission will be necessary before detailed investigation of quantum efficiency and potential application in yellow or white pc-LEDs. Due to the intense response signal upon blue light excitation of β-$SrBeO_2$:Eu^{2+} high efficiency is expected.

The novel ternary beryllates indicate a huge structural variability of beryllate structures that could be even more diverse introducing additional elements during the synthetic access to quaternary and other multinary compound classes. Large band gaps ≥4 eV, as determined for the title compounds, high chemical and thermal stability, accessible highly condensed structures with a degree of condensation κ ≥0.5 (e.g., atomic ratio Be:(O,N)) and simple structures with a single dopant site make beryllate compounds interesting host materials for doping with rare earth elements such as Eu^{2+} and Ce^{3+}.

The high chemical stability and large band gaps of ternary beryllates is an interesting starting point for ongoing investigations for highly efficient narrow-band phosphors, based on beryllate structures. Strong covalent bonds as well as large band gaps cause us to expect high QE in beryllate compounds,[7,8] making them a highly promising materials class for application in pc-LEDs.

4.3.4 Experimental Section

4.3.4.1 Safety Assessment.

Be containing compounds are known to cause diseases, such as berylliosis, cancer and chronic beryllium disease (CBD).[39] Be dusts and soluble salts are particularly hazardous. Small beryllium particles can be inhaled into the lungs, and dissolved Be can accumulate in the human body, leading to chronic diseases. To reduce risk of exposure, working with Be in closed systems, such as Schlenk-lines and glove boxes is suitable and required. Insoluble solid-state compounds, such as the mineral and gemstone beryl (*emerald*, *aquamarine*), with strongly bound Be are less dangerous.[39] Additionally, Be compounds are widely spread in industrial applications, e.g., ceramics, automotive and electronics.[39] Therefore, we assess insoluble, coarse-grained Be containing solid-state compounds with large density to be less dangerous and handling with appropriate safety measures is feasible. In principle, application of beryllate phosphors in pc-LEDs is conceivable, as same coatings for sensitive phosphors, e.g., with silica, could protect from exposure and intoxication due to accidental incorporation.[7,40]

4.3.4.2 Synthesis.

Argon-filled glove boxes (Unilab, MBraun, Garching; O_2 <1 ppm, H_2O <1 ppm) and dry Schlenk-type glassware attached to a vacuum line (10^{-3} mbar) were used for sample preparation and experiments, due to the starting materials' high sensitivity to moisture and air, and toxicity of Be dusts. Purification of Ar gas (Air Liquide, 5.0) was performed in columns filled with silica gel (Merck), molecular sieve (Fluka, 4 Å), KOH (Merck, ≥85%), P_4O_{10} (Roth, ≥99%), and titanium sponge (Johnsen Matthey, 99.5%), heated to 700 °C. Crystalline samples of α- and β-$SrBeO_2$ were

synthesized by reaction of SrO (Alfa Aesar, 103.6 mg, 1.0 mmole, 99.5%) and Be_3N_2 (39.2 mg, 0.53 mmole, synthesized from Be (ABCR, 99+%, 325. mesh) in an rf-furnace under N_2 atmosphere at 1300 °C) after mixing in an agate mortar.[8] For doped compounds 1 mole% of SrO was replaced by Eu_2O_3 (ABCR, 99.99%). The reaction mixture was filled in W crucibles and subsequently heated in 1 h to 1400 °C in an rf-furnace. The temperature was maintained at 1400 °C for 1 h, then cooled down to 700 °C in 6 h and then to room temperature by shutting down the furnace. Crystalline samples of $Sr_{12}Be_{17}O_{29}$ were synthesized in Ta-ampules. SrO (31.1 mg, 0.3 mmole), BeO (10.6 mg, 0.43 mmole, Alfa Aesar, 99.95%) and Eu_2O_3 (0.1 mg, 0.005 mmole) were mixed in an agate mortar, filled into Ta ampules that subsequently were weld shut and heated in evacuated silica tubes to 950 °C in 3h. The temperature was kept for 24h, cooled down to 500 °C in 3h and then to room temperature by shutting down the furnace.

4.3.4.3 Elemental Analysis.

The title compounds' elemental composition was determined by energy dispersive X-ray spectroscopy (EDS). A Dualbeam Helios Nanolab G3 UC scanning electron microscope (SEM, FEI) with X-Max 80 SDD detector (Oxford Instruments) was used. The EDS data were obtained from several particles at an accelerating voltage of 20 kV. Morphology of the microcrystalline samples was additionally investigated by SEM.

4.3.4.4 Single crystal X-ray diffraction:

Single crystals of α- and β-$SrBeO_2$ as well as $Sr_{12}Be_{17}O_{29}$ were selected and fixed on micromounts (MiTeGen). X-ray diffraction data were collected on a Bruker D8 Venture diffractometer with rotating anode. Goebel mirror optics were used to specifically select and focus the Mo-Kα radiation (λ = 0.71073 Å). Integration and absorption correction was carried out with the program package APEX3.[41] The crystal structures were solved by Direct Methods (SHELXS)[42] and refined by full-matrix least-squares methods (SHELXL).[43,44] Eu^{2+} was disregarded in the structure determination due to its low amount and its therefore insignificant contribution to the scattering density. α-$SrBeO_2$ was refined as a 2-component perfect inversion twin, The α-$SrBeO_2$ single crystal was additionally measured at 100 K using the same conditions and settings as described for room temperature single crystal XRD. $Sr_{12}Be_{17}O_{29}$ was refined as 2-component inversion twin. Further details of the crystal structure investigations can be obtained from the Fachinformationszentrum Karlsruhe, 76344 Eggenstein-Leopoldshafen, Germany (Fax, (+49)7247-808-666; email, crysdata@fiz-karlsruhe.de) upon quoting the depository numbers CSD-434343 ($Sr_{12}Be_{17}O_{29}$), CSD-434344 (α-$SrBeO_2$), and CSD-434345 (β-$SrBeO_2$).

4.3.4.5 Powder X-ray diffraction.

The samples were sealed in glass capillaries with 0.2 mm diameter and 0.01 mm wall thickness (Hilgenberg, Germany) and measured on a Stoe Stadi P diffractometer (λ = 1.5406 Å, Cu-Kα_1, Ge(111)-monochromator) in a parafocussing Debye-Scherrer geometry using a MYTHEN 1K Si-strip

detector (Dectris, Baden, Switzerland). Rietveld refinements were carried out with TOPAS-Academic Version 4.1.[45] Peak shapes were fitted using a fundamental parameter approach (direct convolution of source emission profiles, axial instrument contributions, crystallite size, and micro-strain effects) and the background using a shifted Chebyshev function.[46] Capillary absorption correction (inner diameter 0.18 mm) was carried out using the calculated absorption coefficient.

4.3.4.6 DFT calculations.

All structural relaxations were performed with use of the Vienna ab initio simulation package (VASP) until the total energies of each respective unit cell were converged to 10^{-7} eV/atom while the residual atomic forces were ensured to be below 1×10^{-3} eV.[47-49] The generalized gradient approximation (GGA) of Perdew, Burke, and Ernzerhof (PBE) was used alongside the projector-augmented-wave (PAW) method to deal with the exchange correlation.[50-53] For band structure calculations the modified Becke-Johnson (mbj) exchange potential was used.[31,54] A plane-wave cutoff of 535 eV was chosen for all calculations. Respective Brillouin zones were sampled on different Γ-centered *k*-meshes, depending on unit cell dimensions, (SrO: 10 × 10 × 10; BeO: 22 × 20 × 12; *α*-$SrBeO_2$:14 × 10 × 10; *β*-$SrBeO_2$: 8 × 10 × 10; $SrBe_3O_4$: 11 × 13 × 6; $Sr_{12}Be_{17}O_{29}$: 5 × 5 × 5) produced by the method of Monkhorst and Pack.[55]

4.3.4.7 Luminescence.

Luminescence spectra of *β*-$SrBeO_2$:Eu^{2+} as well as $Sr_{12}Be_{17}O_{29}$:Eu^{2+} were obtained with a HORIBA Fluoromax4 Spectrofluorimeter system connected to an Olympus BX51 microscope by optical fibers. The spectral width of the excitation wavelength at 420 nm is 10 nm. Emission spectra were recorded in a wavelength range between 400–800 nm and 380–780 nm, respectively, with 2 nm step size. Excitation spectra were obtained with a monitoring wavelength of 584 nm for *β*-$SrBeO_2$:Eu^{2+} and 630 nm for $Sr_{12}Be_{17}O_{29}$:Eu^{2+}.

4.3.5 References

[1] Pust, P.; Schmidt, P. J.; Schnick, W. A revolution in lighting. *Nat. Mater.* **2015**, *14*, 454-458.

[2] Pust, P.; Weiler, V.; Hecht, C.; Tücks, A.; Wochnik, A. S.; Henß, A. K.; Wiechert, D.; Scheu, C.; Schmidt, P. J.; Schnick, W. Narrow-band red-emitting $Sr[LiAl_3N_4]:Eu^{2+}$ as a next-generation LED-phosphor material. *Nat. Mater.* **2014**, *13*, 891-896.

[3] Schmiechen, S.; Pust, P.; Schmidt Peter, J.; Schnick, W. Weißes Licht aus Nitriden. *Nachr. Chem.* **2014**, *62*, 847-851.

[4] Zeuner, M.; Pagano, S.; Schnick, W. Nitridosilicates and Oxonitridosilicates: From Ceramic Materials to Structural and Functional Diversity. *Angew. Chem. Int. Ed.* **2011**, *50*, 7754-7775.

[5] Strobel, P.; Schmiechen, S.; Siegert, M.; Tücks, A.; Schmidt, P. J.; Schnick, W. Narrow-Band Green Emitting Nitridolithoalumosilicate $Ba[Li_2(Al_2Si_2)N_6]:Eu^{2+}$ with Framework Topology whj for LED/LCD-Backlighting Applications. *Chem. Mater.* **2015**, *27*, 6109-6115.

[6] Xie, R.-J.; Hirosaki, N.; Takeda, T. Wide Color Gamut Backlight for Liquid Crystal Displays Using Three-Band Phosphor-Converted White Light-Emitting Diodes. *Appl. Phys. Express* **2008**, *2*, 022401-022403.

[7] Strobel, P.; Weiler, V.; Schmidt, P. J.; Schnick, W. $Sr[BeSi_2N_4]:Eu^{2+}/Ce^{3+}$ and $Eu[BeSi_2N_4]$: Nontypical Luminescence in Highly Condensed Nitridoberyllosilicates. *Chem. Eur. J.* **2018**, *24*, 7243-7249.

[8] Strobel, P.; de Boer, T.; Weiler, V.; Schmidt, P. J.; Moewes, A.; Schnick, W. Luminescence of an Oxonitridoberyllate: A Study of Narrow-Band Cyan Emitting $Sr[Be_6ON_4]:Eu^{2+}$. *Chem. Mater.* **2018**, *30*, 3122-3130.

[9] Bragg, W. L.; Brown, G. B. The Crystalline Structure of Chrysoberyl. *Proc. R. Soc. London, Ser. A* **1926**, *110*, 34-63.

[10] Bragg, W. L.; West, J. The Structure of Beryl, $Be_3Al_2Si_6O_{18}$. *Proc. R. Soc. London, Ser. A* **1926**, *111*, 691-714.

[11] McKeehan, L. W. The Crystal Structure of Beryllium and of Beryllium Oxide. *Proc. Natl. Acad. Sci. U. S. A.* **1922**, *8*, 270-274.

[12] Harris, L. A.; Yakel, H. L. The crystal structure of calcium beryllate, $Ca_{12}Be_{17}O_{29}$. *Acta Crystallogr.* **1966**, *20*, 295-301.

[13] Harris, L. A.; Yakel, H. L. The crystal structure of $SrBe_3O_4$. *Acta Crystallogr. Sect. B* **1969**, *25*, 1647-1651.

[14] Leoni, S.; Niewa, R.; Akselrud, L.; Prots, Y.; Schnelle, W.; Göksuc, T.; Cetinkol, M.; Somer, M.; Kniep, R. Novel Barium Beryllates $Ba[Be_2N_2]$ and $Ba_3[Be_5O_8]$: Syntheses, Crystal Structures and Bonding Properties. *Z. Anorg. Allg. Chem.* **2005**, *631*, 1818-1824.

[15] Harris, L. A.; Potter, R. A.; Yakel, H. L. Preliminary observations of mixed oxide compounds containing BeO. *Acta Crystallogr.* **1962**, *15*, 615-616.

[16] Zachariasen, W. Über die Kristallstruktur von BeO. *Norsk. Geol. Tidssk* **1925**, *8*, 189-200.

[17] Harris, L. A.; Yakel, H. L. The crystal structure of Y_2BeO_4. *Acta Crystallogr.* **1967**, *22*, 354-360.

[18] Bashir, J.; Khan, R. T. A.; Butt, N. M.; Heger, G. Thermal atomic displacement parameters of SrO. *Powder Diffr.* **2012**, *17*, 222-224.

[19] Liebau, F., *Structural Chemistry of Silicates*, Springer: Berlin, **1985**.

[20] Superscripted numbers specify connectivity: number of directly connected network building cations.

[21] Gál, Z. A.; Mallinson, P. M.; Orchard, H. J.; Clarke, S. J. Synthesis and Structure of Alkaline Earth Silicon Nitrides: $BaSiN_2$, $SrSiN_2$, and $CaSiN_2$. *Inorg. Chem.* **2004**, *43*, 3998-4006.

[22] Duman, S.; Sütlü, A.; Bağcı, S.; Tütüncü, H. M.; Srivastava, G. P. Structural, elastic, electronic, and phonon properties of zinc-blende and wurtzite BeO. *J. Appl. Phys.* **2009**, *105*, 033719.

[23] Maak, C.; Niklaus, R.; Friedrich, F.; Mähringer, A.; Schmidt, P. J.; Schnick, W. Efficient Yellow-Orange Phosphor $Lu_4Ba_2[Si_9ON_{16}]O:Eu^{2+}$ and Orange-Red Emitting $Y_4Ba_2[Si_9ON_{16}]O:Eu^{2+}$: Two Oxonitridosilicate Oxides with Outstanding Structural Variety. *Chem. Mater.* **2017**, *29*, 8377-8384.

[24] Huppertz, H.; Oeckler, O.; Lieb, A.; Glaum, R.; Johrendt, D.; Tegel, M.; Kaindl, R.; Schnick, W. $Ca_3Sm_3[Si_9N_{17}]$ and $Ca_3Yb_3[Si_9N_{17}]$ Nitridosilicates with Interpenetrating Nets that Consist of Star-Shaped $[N^{[4]}(SiN_3)_4]$ Units and $[Si_5N_{16}]$ Supertetrahedra. *Chem. Eur. J.* **2012**, *18*, 10857-10864.

[25] Lieb, A.; Schnick, W. $BaSm_5[Si_9Al_3N_{20}]O$ – a nitridoaluminosilicate oxide with a new structure type composed of "star-shaped" $[N^{[4]}((Si,Al)N_3)_4]$ units as secondary building units. *Solid State Sci.* **2006**, *8*, 185-191.

[26] Lieb, A.; Kechele, J. A.; Kraut, R.; Schnick, W. The Sialons $MLn[Si_{4-x}Al_xO_xN_{7-x}]$ with M = Eu, Sr, Ba and Ln = Ho-Yb – Twelve Substitution Variants with the $MYb[Si_4N_7]$ Structure Type. *Z. Anorg. Allg. Chem.* **2007**, *633*, 166-171.

[27] Shannon, R. D. Revised Effective Ionic Radii and Systematic Studies of Interatomic Distances in Halides and Chalcogenides. *Acta Crystallogr. Sect. A* **1976**, *32*, 751.

[28] Huppertz, H.; Keszler, D. A., *Borates: Solid-State Chemistry (Encyclopedia of Inorganic and Bioinorganic Chemistry)*, **2014**.

[29] Wang, L.; Maxisch, T.; Ceder, G. Oxidation energies of transition metal oxides within the GGA + U framework. *Phys. Rev. B* **2006**, *73*, 195107.

[30] Chevrier, V. L.; Ong, S. P.; Armiento, R.; Chan, M. K. Y.; Ceder, G. Hybrid density functional calculations of redox potentials and formation energies of transition metal compounds. *Phys. Rev. B* **2010**, *82*, 075122.

[31] Tran, F.; Blaha, P. Accurate Band Gaps of Semiconductors and Insulators with a Semilocal Exchange-Correlation Potential. *Phys. Rev. Lett.* **2009**, *102*, 226401.

[32] Tolhurst, T. M.; Strobel, P.; Schmidt, P. J.; Schnick, W.; Moewes, A. Designing Luminescent Materials and Band Gaps: A Soft X-ray Spectroscopy and Density Functional Theory Study of $Li_2Ca_2[Mg_2Si_2N_6]:Eu^{2+}$ and $Ba[Li_2(Al_2Si_2)N_6]:Eu^{2+}$. *J. Phys. Chem. C* **2017**, *121*, 14296-14301.

[33] Bachmann, V.; Ronda, C.; Oeckler, O.; Schnick, W.; Meijerink, A. Color Point Tuning for $(Sr,Ca,Ba)Si_2O_2N_2:Eu^{2+}$ for White Light LEDs. *Chem. Mater.* **2009**, *21*, 316-325.

[34] Aidaev, F. S. Synthesis and Luminescent Properties of Eu-Activated $CaGa_2S_4$ and $SrGa_2S_4$. *Inorganic Materials* **2003**, *39*, 96-98.

[35] Dobrowolska, A.; Dierre, B.; Fang, C. M.; Hintzen, H. T.; Dorenbos, P. Thermal quenching of Eu^{2+} emission in Ca- and Sr-Ga_2S_4 in relation with VRBE schemes. *J. Lumin.* **2017**, *184*, 256-261.

[36] Xie, R. J.; Hirosaki, N.; Takeda, T.; Suehiro, T. On the performance enhancement of nitride phosphors as spectral conversion materials in solid state lighting. *ECS J. Solid State Sci. Technol.* **2013**, *2*, R3031-R3040.

[37] Piquette, A.; Bergbauer, W.; Galler, B.; Mishra, K. C. On Choosing Phosphors for Near-UV and Blue LEDs for White Light. *ECS J. Solid State Sci. Technol.* **2016**, *5*, R3146-R3159.

[38] Mueller-Mach, R.; Mueller, G. O.; Krames, M. R.; Shchekin, O. B.; Schmidt, P. J.; Bechtel, H.; Chen, C. H.; Steigelmann, O. All-nitride monochromatic amber-emitting phosphor-converted light-emitting diodes. *Phys. Status Solidi RRL* **2009**, *3*, 215-217.

[39] Agency for Toxic Substances and Disease Registry (ATSDR) - Case Studies in Environmental Medicine - Beryllium Toxicity **2018**.

[40] Tsai, Y.-T.; Nguyen, H.-D.; Lazarowska, A.; Mahlik, S.; Grinberg, M.; Liu, R.-S. Improvement of the Water Resistance of a Narrow-Band Red-Emitting $SrLiAl_3N_4:Eu^{2+}$ Phosphor Synthesized under High Isostatic Pressure through Coating with an Organosilica Layer. *Angew. Chem. Int. Ed.* **2016**, *128*, 9804-9808.

[41] BrukerAXS, *APEX3 v2016.5-0*: Billerica, **2016**.

[42] Sheldrick, G. M., *SHELXS-97: A program for crystal structure solution*, University of Göttingen, **1997**.

[43] Sheldrick, G. M., *SHELXL-97: A program for crystal structure refinement*, University of Göttingen, **1997**.

[44] Sheldrick, G. M. A short history of SHELX. *Acta Crystallogr. Sect. A* **2008**, *64*, 112-122.

[45] Coelho, A. A., *TOPAS-Academic*, Version 4.1: A program for Rietveld refinement: Brisbane, Australia, **2007**.

[46] Cheary, R. W.; Coelho, A. A.; Cline, J. P. Fundamental Parameters Line Profile Fitting in Laboratory Diffractometers. *J. Res. Natl. Inst. Stand. Technol.* **2004**, *109*, 1-25.

[47] Kresse, G.; Hafner, J. Ab initio. *Phys. Rev. B* **1993**, *47*, 558-561.

[48] Kresse, G.; Hafner, J. Ab initio. *Phys. Rev. B* **1994**, *49*, 14251-14269.

[49] Kresse, G.; Furthmüller, J. Efficiency of ab-initio total energy calculations for metals and semiconductors using a plane-wave basis set. *Comput. Mater. Sci.* **1996**, *6*, 15-50.

[50] Perdew, J. P.; Burke, K.; Ernzerhof, M. Generalized Gradient Approximation Made Simple. *Phys. Rev. Lett.* **1996**, *77*, 3865-3868.

[51] Perdew, J. P.; Burke, K.; Ernzerhof, M. Generalized Gradient Approximation Made Simple [Phys. Rev. Lett. 77, 3865 (1996)]. *Phys. Rev. Lett.* **1997**, *78*, 1396-1396.

[52] Blöchl, P. E. Projector augmented-wave method. *Phys. Rev. B* **1994**, *50*, 17953-17979.

[53] Kresse, G.; Joubert, D. From ultrasoft pseudopotentials to the projector augmented-wave method. *Phys. Rev. B* **1999**, *59*, 1758-1775.

[54] Camargo-Martínez, J. A.; Baquero, R. Performance of the modified Becke-Johnson potential for semiconductors. *Phys. Rev. B* **2012**, *86*, 195106.

[55] Monkhorst, H. J.; Pack, J. D. Special points for Brillouin-zone integrations. *Phys. Rev. B* **1976**, *13*, 5188-5192.

4.4 Ultra-Narrow Band Blue Emitting Oxoberyllates $AELi_2[Be_4O_6]:Eu^{2+}$ (*AE* = Sr,Ba) Paving the Way to Efficient RGB pc-LEDs

published in: *Angew. Chem. Int. Ed.*, **2018**, https://doi.org/10.1002/anie.201804721

authors: Philipp Strobel, Christian Maak, Volker Weiler, Peter J. Schmidt and Wolfgang Schnick

DOI: 10.1002/anie.201804721

Abstract: Highly efficient phosphor-converted light-emitting diodes (pc-LEDs) are popular in lighting and high-tech electronics applications. The main goals of present LED research are increasing light quality, preserving color point stability and reducing energy consumption. For those purposes excellent phosphors in all spectral regions are required. Here, we report on ultra-narrow band blue emitting oxoberyllates $AELi_2[Be_4O_6]:Eu^{2+}$ (*AE* = Sr,Ba) exhibiting a rigid covalent network isotypic to the nitridoalumosilicate $BaLi_2[(Al_2Si_2)N_6]:Eu^{2+}$. The oxoberyllates' extremely small Stokes-shift and unprecedented ultra-narrow band blue emission with *fwhm* ≈ 25 nm (≈ 1200 cm^{-1}) at λ_{em} = 454–456 nm result from its rigid, highly condensed tetrahedra network. $AELi_2[Be_4O_6]:Eu^{2+}$ allows for using short-wavelength blue LEDs (λ_{em} <440 nm) for efficient excitation of the ultra-narrow band blue phosphor, for application in violet pumped white RGB phosphor LEDs with improved color point stability, excellent color rendering, and high energy efficiency.

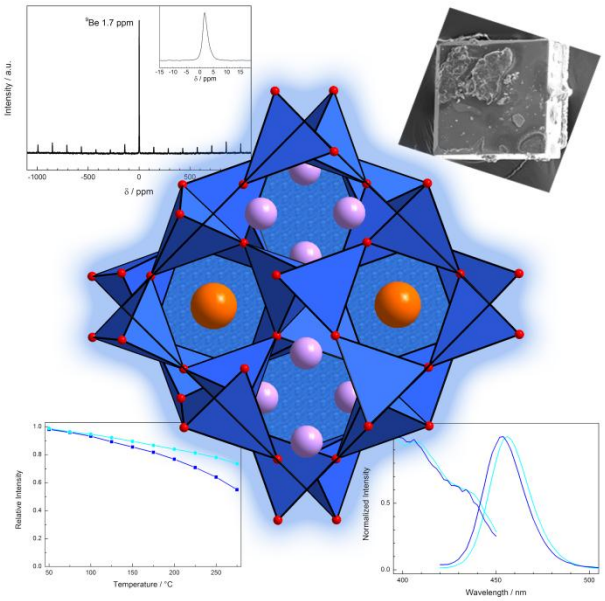

4.4.1 Article

Cost-effective and energy-efficient illumination-grade white phosphor converted (pc-)LEDs have nowadays been well established at the global lighting market.[1] The rapid distribution of LEDs has evolved from mass production of warm-white LEDs with innovative red phosphors, offering CRI (*color rendering index*) values beyond 80.[2] To gain increased luminous efficacy, exploration of narrow-band red emitting phosphors was in the focus of recent LED phosphor development reducing IR-spillover of white light emitting pc-LEDs.[2-7] With the discovery of highly efficient red emitting BSSNE ($(Ba,Sr)_2Si_5N_8:Eu^{2+}$) and SCASN ($(Sr,Ca)AlSiN_3:Eu^{2+}$) as well as narrow-band red emitting SLA ($Sr[LiAl_3N_4]:Eu^{2+}$), the base for highly efficient, high CRI pc-LEDs was established.[2,8,9] As was shown with application of SLA in high-power LEDs, an increase of 14% in luminous efficacy was achieved, when compared to standard red phosphors, such as BSSNE and SCASN, with a CRI >90.[2]

Understanding structure-property relations allows creating phosphors with efficient narrow-band emission to further improve emission characteristics of state-of-the-art pc-LEDs. A highly condensed network with a large degree of condensation (e.g., molar ratio of (Be,Al,Si):(O,N)) of $\kappa \geq 0.5$, cation ordering and only one crystallographic dopant site are prerequisites for narrow-band emission of wide band gap materials. Suitable compounds have been found in the materials classes of nitridosilicates as well as –aluminates, and recently, exploring (oxo)nitridoberyllate compounds.[2,7,10-14] Upon doping with Eu^{2+} highly efficient narrow-band phosphors for application in pc-LEDs have been developed in these compound classes.

An approach to further improve emission characteristics of pc-LEDs is the development of violet pumped white RGB (red-green-blue) phosphor converted LEDs. In such RGB pc-LEDs, near ultraviolet emitting (nUV-)LEDs (λ_{em} <420 nm) are combined with highly efficient phosphors covering the blue to red spectral region to obtain high quality illumination grade white light with high color point stability under varying application conditions and e.g. reduced glare.[15,16] Essential phosphors in the red spectral region are BSSNE, SCASN and SLA as well as $K_2SiF_6:Mn^{4+}$.[2,8,9,17] The main part of the visible spectrum is typically covered by broad-band yellow-green emitting phosphors, such as $(Y,Lu)_3Al_5O_{12}:Ce^{3+}$ (YAG:Ce, LuAG:Ce).[16] Further suitable phosphors in the cyan-yellow spectral region are e.g., $Sr[Be_6ON_4]:Eu^{2+}$, $(Ba,Sr)_2SiO_4:Eu^{2+}$, $SrSi_2O_2N_2:Eu^{2+}$, β-$SiAlON:Eu^{2+}$, $Ba_2LiSi_7AlN_{12}:Eu^{2+}$ and $BaLi_2[(Al_2Si_2)N_6]:Eu^{2+}$ (BLSA).[10,12,18-22]

To minimize the intrinsic down-conversion energy loss of a white pc-LED with an RGB phosphor mix a very small Stokes-shift for the blue phosphor is needed. The small Stokes-shift ideally allows shifting the emission of a nUV primary pump LED in the blue spectral range, very close to the emission of the blue phosphor. Yet, in the blue spectral region no commercial small Stokes-shift narrow-band phosphors are known. Conventional blue phosphors for RGB pc-LEDs with high quantum efficiency are $(Sr,Ba,Ca)_{10}(PO_4)_6Cl_2:Eu^{2+}$ (SCAP), $BaMgAl_{10}O_{17}:Eu^{2+}$ (BAM), $LiCaPO_4:Eu^{2+}$ (LCP), $Sr_3MgSi_2O_8:Eu^{2+}$ (SMSO) and $Ba_3MgSi_2O_8:Eu^{2+}$ (BMSO), all of them showing a relatively large Stokes-shift compared to ultra-narrow red emitters like SLA.[23-26] To further improve the overall

efficiency of white emitting RGB pc-LEDs a blue phosphor that can be efficiently excited by pump LEDs with only inconsiderably higher emission energies is thus required.

This goal was accomplished by the synthesis of the novel oxoberyllate compounds $AELi_2[Be_4O_6]:Eu^{2+}$ with *AE* = Sr and Ba exhibiting all postulated structural characteristics for efficient, ultra-narrow band emission. These extremely narrow-band blue emitting phosphors with an emission band width of only 25 nm (≈ 1200 cm^{-1}) and a maximum at 454–456 nm show comparable material properties as narrow-band red emitting SLA (*fwhm* ≈ 1180 cm^{-1}).[2]

$AELi_2[Be_4O_6]:Eu^{2+}$ (*AE* = Sr,Ba) is one of the first beryllate phosphors discussed for application in LEDs. Be compounds, such as metal alloys are widely spread in industrial applications, e.g., ceramics, automotive and electronics. It is known that Be-containing dusts can cause diseases such as berylliosis, cancer and chronic beryllium disease (CBD).[27] As a result, beryllate compounds have not been investigated in great detail so far. Be dusts and soluble salts are hazardous. Small beryllium particles can be inhaled, and dissolved Be can accumulate in the human body. Working in closed systems, such as Schlenk-lines and glove boxes is suitable and required to reduce risk of exposure. Insoluble, coarsely grained Be containing solid-state phosphors are therefore less dangerous, while handling with appropriate safety measures is practicable.[7,27] We therefore assess insoluble, coarse-grained Be containing solid-state compounds to be less dangerous. Natural examples are Be-containing gem stones, e.g., *beryl*, *aquamarine*, and *emerald*. Therefore, application of beryllate phosphors in pc-LEDs is conceivable.

The highly condensed beryllates $AELi_2[Be_4O_6]:Eu^{2+}$ (*AE* = Sr,Ba) were successfully synthesized by applying high-temperature routes, as it is generally used for the synthesis of silicate and aluminate host materials. Due to its highly condensed network structure, $AELi_2[Be_4O_6]:Eu^{2+}$ (*AE* = Sr,Ba) meets requirements for narrow-band emitting phosphors: chemical and thermal stability, a large band gap as well as high quantum efficiency (QE) and color point stability at elevated temperatures. Its rigid network is the base for the narrow-band emission, as it limits the local structural relaxation of the dopant (Eu^{2+}) site in its excited state and allows a small Stokes-shift for narrow-band emission.[2,28] Introduction of tetrahedrally coordinated Be into the crystal structures results in improved, targeted properties like a large band gap and a rigid network, due to the strong covalent character of Be-ligand bonds, when comparing to compounds with Li or Mg in tetrahedral coordination. This was also shown for the luminescent (oxo)nitridoberyllates $Sr[Be_6ON_4]:Eu^{2+}$ and $Sr[BeSi_2N_4]:Eu^{2+}$.[7,10]

$AELi_2[Be_4O_6]:Eu^{2+}$ (*AE* = Sr,Ba) crystallizes isotypically with the green emitting phosphor $BaLi_2[(Al_2Si_2)N_6]:Eu^{2+}$ (BLSA).[12] Exchange of N in BLSA by O in $AELi_2[Be_4O_6]:Eu^{2+}$ results in a decreased nephelauxetic effect leading to a larger energy difference between the Eu $4f^7\ 5d^0$ ground state and the excited Eu $4f^6\ 5d^1$ state. Accordingly, emission in the blue spectral region is observed for $AELi_2[Be_4O_6]:Eu^{2+}$ in contrast to the green emission of $BaLi_2[(Al_2Si_2)N_6]:Eu^{2+}$.[1,2,6,12,29] Excitation and emission spectra of BLBO ($BaLi_2[Be_4O_6]:Eu^{2+}$) and SLBO ($SrLi_2[Be_4O_6]:Eu^{2+}$) are compared in Fig. 1a. The nominal doping concentration is 1%. While SLBO exhibits maximum emission at

456 nm, BLBO emits blue light at 454 nm. Due to a small Stokes-shift of only ≈ 1200 cm^{-1} both compounds show remarkably narrow emission with *fwhm* of ≈ 1200 cm^{-1}. Both compounds show a broad absorption band, extending into the UV and reaching towards the blue spectral area. Like the emission spectrum, the excitation spectrum of BLBO is also slightly blue-shifted compared to the Sr compound. The phosphors are highly excitable up to ~440 nm and therefore are suitable for excitation with violet to short wavelength blue InGaN-LEDs.

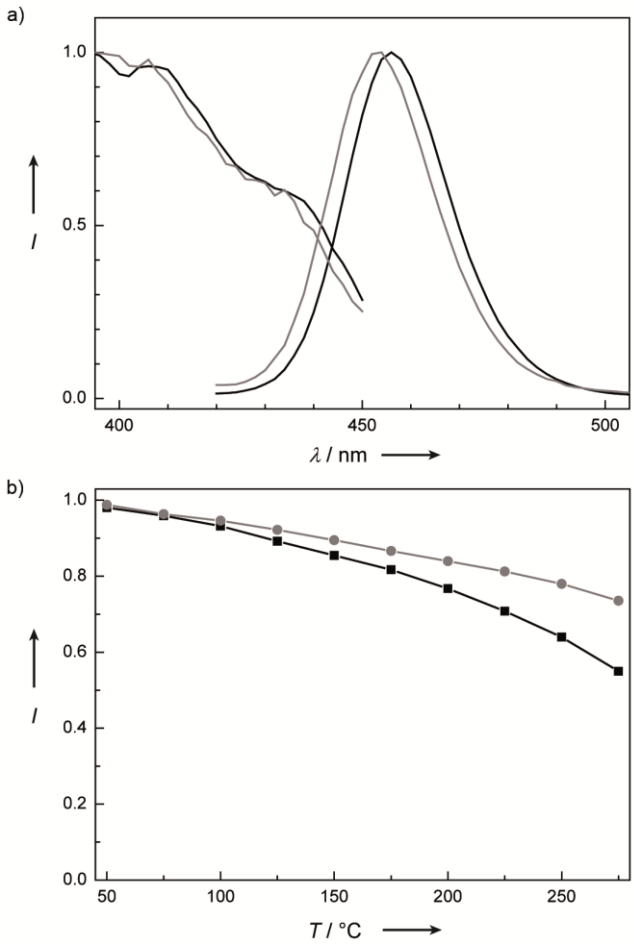

Figure 1. Photoluminescence properties of ultra-narrow band blue emitting $AELi_2[Be_4O_6]:Eu^{2+}$ (*AE* = Sr,Ba). a) Excitation and emission spectra of $BaLi_2[Be_4O_6]:Eu^{2+}$ (gray) and $SrLi_2[Be_4O_6]:Eu^{2+}$ (black) for λ_{exc} = 400 nm. b) Temperature dependence of the relative integrated photoluminescence intensity for BLBO (gray) and SLBO (black), revealing a decrease at 200 °C of only 17 and 24%, respectively, compared to room-temperature QE.

The narrow emission band width of only 1200 cm^{-1} of $AELi_2[Be_4O_6]:Eu^{2+}$ is comparable to the most narrow-band Eu^{2+}-phosphors, namely $Sr[LiAl_3N_4]:Eu^{2+}$ (*fwhm* = 1180 cm^{-1}) and $Sr[Mg_3SiN_4]:Eu^{2+}$ (1150 cm^{-1}). Compared to SCAP, BAM, LCP and BMSO, the two novel blue emitting phosphors BLBO and SLBO show an even narrower, unprecedented emission signal, resulting from the extremely small Stokes-shift. Powder layers of non-optimized BLBO exhibit proficient internal quantum efficiency of 64% (SLBO: ≈47%), when excited at 410 nm Temperature-dependent emission of samples of BLBO and SLBO (Figure 1b) show improved thermal quenching (TQ) behavior for BLBO. At 200 °C the relative emission intensity of BLBO is still 83%, while SLBO exhibits

proficient 76%. The low TQ is related to the sufficient band gap that was estimated to 3.8 eV for BLBO from undoped samples from diffuse reflectance spectra and analysis corresponding to the Tauc-method.[30] An indirect band gap was assumed, due to the structural analogy of $AELi_2[Be_4O_6]:Eu^{2+}$ and $BaLi_2[(Al_2Si_2)N_6]:Eu^{2+}$.[31]

Samples of $SrLi_2[Be_4O_6]:Eu^{2+}$ and $BaLi_2[Be_4O_6]:Eu^{2+}$ were investigated by single-crystal and powder X-ray diffraction (PXRD).[32] Both compounds show tetragonal metrics, crystallizing in space group *P*4/*ncc* (no. 130), isotypic with the nitridoalumosilicate $BaLi_2[(Al_2Si_2)N_6]$.[12] Rietveld refinement on PXRD data confirms the structural model. The calculated pattern and the experimental data are compared in Fig. 2. The calculated data disregards the Eu-content, due to its insignificant contribution to the structure factor. The crystallographic details are summarized in the Supporting Information.

The title compounds' morphology and elemental composition were investigated by electron microscopy, associated by EDS (Energy-dispersive X-ray spectroscopy; Sr,Ba,O) on single crystals and powder samples as well as complementary ICP-

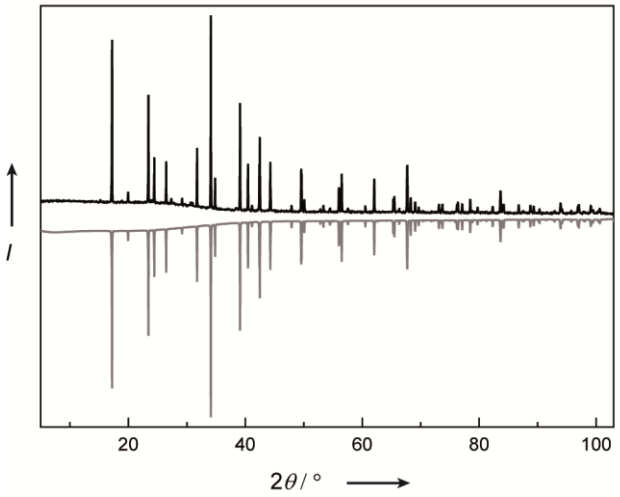

Figure 2. Crystal structure characterization of ultra-narrow band blue emitting $AELi_2[Be_4O_6]:Eu^{2+}$ (*AE* = Sr,Ba). X-ray powder pattern of BLBO with the measured data (black line) and calculated pattern based on Rietveld refinement data (gray line).

OES investigations (inductively coupled plasma optical emission spectrometry; Sr,Eu,Be) on powder samples. Results of EDS and ICP analysis are compared in Supplementary Table 6. The obtained results are in good accordance with the sum formula. Solid-state magic angle spinning nuclear magnetic resonance (MAS-NMR) investigations were conducted for ^6Li, ^7Li as well as ^9Be on an undoped sample of BLBO to confirm the incorporation of both elements as well as the high symmetry and ordering of each crystallographic position. The NMR spectra are displayed in Figure 4. All MAS-NMR spectra give one single isotropic signal, indicating the ordering of Li and Be in the network. For the ^7Li spectrum, a chemical shift of δ = 1.3 ppm is found which is comparable to Li in

highly condensed solid-state nitride structures (SLA: 2.6 ppm, $Li_2SrSi_2N_4$: 2.0 ppm).[2,33] For the ^9Be spectrum, a shift of 1.7 ppm is obtained.

The network structure of SLBO and BLBO is displayed in Figure 3. Corner- and edge-sharing BeO_4 tetrahedra form two different types of *vierer* ring channels that run along [001] and are filled with either Li or *AE* (Sr,Ba) atoms.[34] As was shown recently, Li atoms, which are in 4+1 coordination by anions, are better described as counter ions and should not be counted as network building atoms.[31] The strong ionic character of Li–N bonds was shown with DFT methods, accompanied by XAS/XES investigations, in $BaLi_2[(Al_2Si_2)N_6]$.[31] The highly symmetric crystal structure offers one crystallographic site each for AE^{2+} (*AE* = Sr,Ba) and Li^+ as counter ions in the highly condensed network. The *AE* site is in eight-fold coordination that is best described as square pyramid trunk.

Therefore, the title compounds structure shows striking similarities to SLA. Both structures contain two types of channels, formed by the tetrahedra network. One of these channels in each structure provides the regular symmetric eightfold coordination sphere for the *AE* site. While the second channel is unoccupied in SLA, in the title compounds structure type the second channel offers space for Li atoms that form a tetragonal bisphenoidal arrangement.[12] The regular eight-fold coordination of the *AE* site is essential for narrow-band emission. Eu^{2+} is expected to replace the *AE* ions, due to their similar structural chemical behavior.[2]

Lattice parameters of $SrLi_2[Be_4O_6]$ and $BaLi_2[Be_4O_6]$ show only little differences, despite different ionic radii of *AE*. Compared to $BaLi_2[(Al_2Si_2)N_6]$ lattice parameters are significantly shorter. Parameter *a* and *b* are decreased by approximately 0.6 Å, *c* by ~1.1 Å, leading to a reduced unit cell volume (*AE* = Ba: 77%, *AE* = Sr: 75%) compared to BLSA. This is caused by the decreased inter-atomic metal to ligand distances resulting from the replacement of N by O. Ba–O (2.77–2.84 Å), Be–O (1.6–1.7 Å) and Li–O distances (2.0–2.4 Å) are decreased compared to BLSA (Ba–N: 2.9–3.1 Å, (Al,Si)–N: 1.7–1.8 Å, Li–N: 2.1–2.5 Å), due to the reduced ionic radius of O.[35,36] Comparing both beryllates, Sr−O distances are decreased to 2.6 Å, while Be–O and Li–O distances are similar. The metal–ligand distances are in good accordance with literature: Be–O (1.65 Å)[37] and Li–O (2.0 Å).[38]

Oxoberyllate compounds with tetrahedrally coordinated Be show close relations to highly condensed nitridosilicate structures, and notably less similarity to oxosilicates. Even fourfold coordinated $O^{[4]}$ atoms are found in BeO crystallizing in the wurtzite structure type, or in ternary $Ca_{12}Be_{17}O_{29}$.[37,39] In particular, this structural relation is also shown in $AELi_2[Be_4O_6]$ (*AE* = Sr,Ba). In nitridosilicates, a highly condensed network structure with edge-sharing tetrahedra is achieved due to the large ionic radius of the nitride ligand. In oxide structures, the introduction of Be^{2+} with the same ionic radius, and decreased formal charge, compared to Si^{4+}, results in a higher degree of condensation.

When compared to $BaLi_2[(Al_2Si_2)N_6]:Eu^{2+}$, luminescence properties of $SrLi_2[Be_4O_6]:Eu^{2+}$ and $BaLi_2[Be_4O_6]:Eu^{2+}$ are significantly improved. Especially, the reduction of the emission band width from 1960 cm^{-1} (57 nm, green) in BLSA to 1200 cm^{-1} (25 nm, blue) is remarkable. This feature is strongly related to the chemical composition. While in BLSA the tetrahedra network is built up of

statistically distributed AlN_4- and SiN_4-tetrahedra in a molar 1:1 ratio, in SLBO and BLBO tetrahedra centers are solely occupied by Be. This has significant influence on the spectral shape. In general, the emission band width in Eu^{2+}-doped compounds is broadened due to electron-phonon coupling of the emission centers as well as fluctuations in the local Eu^{2+}-coordination sphere. A mixed occupied (Al,Si) site leads to a range of chemically differing second coordination spheres around Eu^{2+} resulting in inhomogeneous line broadening of the emission band. This effect, also observed for e.g., $MLiAl_3N_4:Eu^{2+}$ (*M* = Ca,Sr) and the higher symmetric UCr_4C_4 structure type compounds $MMg_2Al_2N_4:Eu^{2+}$ (*M* = Ca,Sr), is avoided by the substitution of Al and Si by Be in $AELi_2[Be_4O_6]:Eu^{2+}$ phosphors.

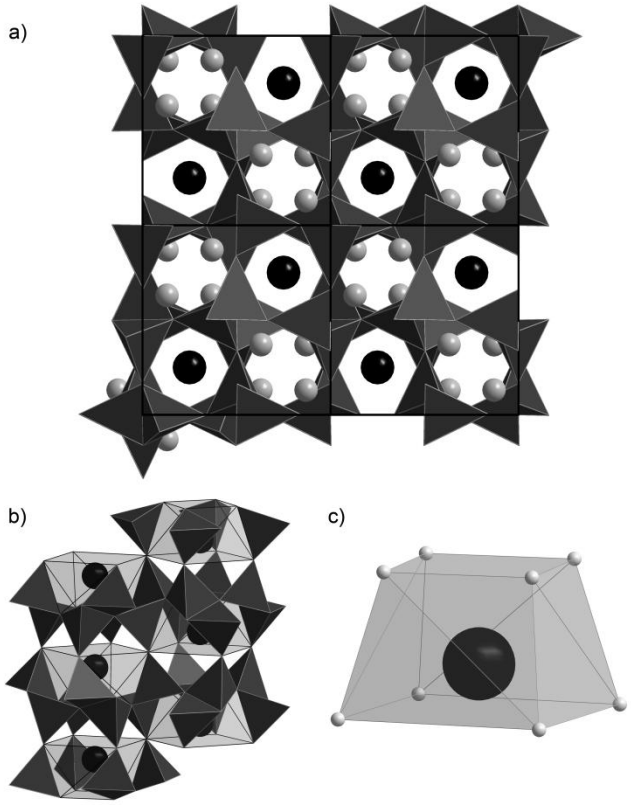

Figure 3. Structural overview of ultra-narrow band blue emitting $AELi_2[Be_4O_6]:Eu^{2+}$ (*AE* = Sr,Ba). a) 2 × 2 × 1 type supercell, view with two types of channels of *vierer* rings along [001]. b) Strands of corner-sharing $(Sr,Ba)O_8$ polyhedra coordinated by BeO_4 tetrahedra. c) $(Sr,Ba)O_8$ polyhedron. Black spheres are (Sr,Ba); gray spheres are Li; dark gray tetrahedra are BeO_4; light gray polyhedra are $(Sr,Ba)O_4$, white spheres are O.

The narrow-band emission is additionally supported by a rigid network structure, offering a highly symmetric Eu^{2+}-coordination. The strong covalent bonding between Be and its ligands, comparable to Al– and Si–ligand bonds, leads to an extremely rigid network. As a result, weak electron-phonon coupling and low local phonon frequencies lead to a small Stokes-shift. The rigid nature of the network is emphasized by the crystallographic data. Due to the larger ionic radius of Ba, when compared to Sr, the lattice parameters are expected to increase significantly. However, only little increase of the *a*-axis is observed, while the *c*-axis even decreases. This again is in accordance with

the results from luminescence measurements, where only a small shift of the emission band of 2 nm is detected. Nevertheless, the exchange of Sr by Ba leads to a slight blue-shifted emission, as expected. This can be explained by the larger ligand distances of Eu^{2+} on the Ba site, leading to a reduced ligand-field splitting and therefore higher energetic emission. This extraordinary small shift underlines the rigidity of the network, as emission shift due to substitutions on the *AE*-site can reach values of about 50 nm, e.g., in $(Sr_{1-x}Ca_x)Si_5N_8:Eu^{2+}$. or $(Sr_{2-x}Ba_x)Ga_2SiO_7:Eu^{2+}$.[40]

Summarizing, we present ultra-narrow band blue emitting oxoberyllate phosphors, synthesized at 1100°C with remarkably short reaction time of only 2h. $AELi_2[Be_4O_6]:Eu^{2+}$ (*AE* = Sr,Ba) phosphors show narrow-band emission with λ_{em} = 454–456 nm and *fwhm* of only 1200cm^{-1}. Because of a very small Stokes-shift the phosphors are highly excitable up to ~440 nm by e.g. InGaN LEDs. This difference to conventional blue phosphors with larger Stokes-shifts, such as SCAP, BAM, LCP and BMSO allows the substitution of violet LEDs emitting at ≈ 410 nm by primaries with longer wavelength emission. Hence, RGB phosphor converted light sources with an increased luminous efficacy and an increased overall conversion efficiency can be achieved, applying $AELi_2[Be_4O_6]:Eu^{2+}$ phosphors. The total amount of blue emitting phosphor in short wavelength blue pumped RGB light sources can also be lowered using e.g., common green to yellow emitting Ce^{3+} doped garnet phosphors with a rather narrow excitation band centered in the blue spectral range. Excitation from both, the blue emitting phosphor and the pump LED is possible if $AELi_2[Be_4O_6]:Eu^{2+}$ (*AE* = Sr,Ba) is being applied as blue emitting phosphor component. Therefore, application of $AELi_2[Be_4O_6]:Eu^{2+}$ (*AE* = Sr,Ba) in illumination-grade white LEDs seems highly promising, solving a number of recent problems in solid-state lighting.

4.4.2 References

[1] Pust, P.; Schmidt, P. J.; Schnick, W. A revolution in lighting. *Nat. Mater.* **2015**, *14*, 454-458.

[2] Pust, P.; Weiler, V.; Hecht, C.; Tücks, A.; Wochnik, A. S.; Henß, A. K.; Wiechert, D.; Scheu, C.; Schmidt, P. J.; Schnick, W. Narrow-band red-emitting $Sr[LiAl_3N_4]:Eu^{2+}$ as a next-generation LED-phosphor material. *Nat. Mater.* **2014**, *13*, 891-896.

[3] Wilhelm, D.; Baumann, D.; Seibald, M.; Wurst, K.; Heymann, G.; Huppertz, H. Narrow-Band Red Emission in the Nitridolithoaluminate $Sr_4[LiAl_{11}N_{14}]:Eu^{2+}$. *Chem. Mater.* **2017**, *29*, 1204-1209.

[4] Wagatha, P.; Pust, P.; Weiler, V.; Wochnik, A. S.; Schmidt, P. J.; Scheu, C.; Schnick, W. $Ca_{18.75}Li_{10.5}[Al_{39}N_{55}]:Eu^{2+}$ - Supertetrahedron Phosphor for Solid-State Lighting. *Chem. Mater.* **2016**, *28*, 1220-1226.

[5] Wagatha, P.; Weiler, V.; Schmidt, P. J.; Schnick, W. Tunable Red Luminescence in Nitridomagnesoaluminates α-$Sr_2[MgAl_5N_7]:Eu^{2+}$, β-$Sr_2[MgAl_5N_7]:Eu^{2+}$ and $Sr_8[LiMg_2Al_{21}N_{28}]:Eu^{2+}$. *Chem. Mater.* **2018**, *30*, 1755-1761.

[6] Strobel, P.; Weiler, V.; Hecht, C.; Schmidt, P. J.; Schnick, W. Luminescence of the Narrow-Band Red Emitting Nitridomagnesosilicate $Li_2(Ca_{1-x}Sr_x)_2[Mg_2Si_2N_6]:Eu^{2+}$ (x = 0–0.06). *Chem. Mater.* **2017**, *29*, 1377-1383.

[7] Strobel, P.; Weiler, V.; Schmidt, P. J.; Schnick, W. $Sr[BeSi_2N_4]:Eu^{2+}/Ce^{3+}$ and $Eu[BeSi_2N_4]$: Nontypical Luminescence in Highly Condensed Nitridoberyllosilicates. *Chem. Eur. J.* **2018**, *24*, 7243-7249.

[8] Höppe, H. A.; Lutz, H.; Morys, P.; Schnick, W.; Seilmeier, A. Luminescence in Eu^{2+}-doped $Ba_2Si_5N_8$: fluorescence, thermoluminescence, and upconversion. *J. Phys. Chem. Solids* **2000**, *61*, 2001-2006.

[9] Watanabe, H.; Kijima, N. Crystal structure and luminescence properties of $Sr_xCa_{1-x}AlSiN_3:Eu^{2+}$ mixed nitride phosphors. *J. Alloys Compd.* **2009**, *475*, 434-439.

[10] Strobel, P.; de Boer, T.; Weiler, V.; Schmidt, P. J.; Moewes, A.; Schnick, W. Luminescence of an Oxonitridoberyllate: A Study of Narrow-Band Cyan Emitting $Sr[Be_6ON_4]:Eu^{2+}$. *Chem. Mater.* **2018**, *30*, 3122-3130.

[11] Pust, P.; Hintze, F.; Hecht, C.; Weiler, V.; Locher, A.; Zitnanska, D.; Harm, S.; Wiechert, D.; Schmidt, P. J.; Schnick, W. Group (III) Nitrides $M[Mg_2Al_2N_4]$ (*M* = Ca, Sr, Ba, Eu) and $Ba[Mg_2Ga_2N_4]$ – Structural Relation and Nontypical Luminescence Properties of Eu^{2+} Doped Samples. *Chem. Mater.* **2014**, *26*, 6113-6119.

[12] Strobel, P.; Schmiechen, S.; Siegert, M.; Tücks, A.; Schmidt, P. J.; Schnick, W. Narrow-Band Green Emitting Nitridolithoalumosilicate $Ba[Li_2(Al_2Si_2)N_6]:Eu^{2+}$ with Framework Topology whj for LED/LCD-Backlighting Applications. *Chem. Mater.* **2015**, *27*, 6109-6115.

[13] Tolhurst, T. M.; Schmiechen, S.; Pust, P.; Schmidt, P. J.; Schnick, W.; Moewes, A. Electronic Structure, Bandgap, and Thermal Quenching of $Sr[Mg_3SiN_4]:Eu^{2+}$ in Comparison to $Sr[LiAl_3N_4]:Eu^{2+}$. *Adv. Opt. Mater.* **2016**, *4*, 584-591.

[14] Uheda, K.; Hirosaki, N.; Yamamoto, Y.; Naita, A.; Nakajima, T.; Yamamoto, H. Luminescence Properties of a Red Phosphor, $CaAlSiN_3:Eu^{2+}$, for White Light-Emitting Diodes *Electrochem. Solid State Lett.* **2006**, *9*, H22-H25.

[15] U.S. Department of Energy, Solid-State Lighting - R&D Plan, **2016**

[16] Kitai, A., *Materials for Solid State Lighting and Displays*, John Wiley and Sons: West Sussex, U.K., **2017**.

[17] Takahashi, T.; Adachi, S. Mn^{4+}-Activated Red Photoluminescence in K_2SiF_6 Phosphor. *J. Electrochem. Soc.* **2008**, *155*, E183-E188.

[18] Seibald, M.; Rosenthal, T.; Oeckler, O.; Schnick, W. Highly Efficient pc-LED Phosphors $Sr_{1-x}Ba_xSi_2O_2N_2:Eu^{2+}$ ($0<x<1$) - Crystal Structures and Luminescence Properties Revisited. *Crit. Rev. Solid State Mater. Sci.* **2014**, *39*, 215-229.

[19] Zhang, M.; Wang, J.; Zhang, Q.; Ding, W.; Su, Q. Optical properties of $Ba_2SiO_4:Eu^{2+}$ phosphor for green light-emitting diode (LED). *Mater. Res. Bull.* **2007**, *42*, 33-39.

[20] Hirosaki, N.; Xie, R.-J.; Kimoto, K.; Sekiguchi, T.; Yamamoto, Y.; Suehiro, T.; Mitomo, M. Characterization and properties of green-emitting β-$SiAlON:Eu^{2+}$ powder phosphors for white light-emitting diodes. *Appl. Phys. Lett.* **2005**, *86*, 211905.

[21] Seong, T.-Y.; Han, J.; Amano, H.; Morkoc, H., *III-Nitride Based Light Emitting Diodes and Applications*, Springer: Dordrecht, Germany, **2013**.

[22] Takeda, T.; Hirosaki, N.; Funahshi, S.; Xie, R.-J. Narrow-Band Green-Emitting Phosphor $Ba_2LiSi_7AlN_{12}:Eu^{2+}$ with High Thermal Stability Discovered by a Single Particle Diagnosis Approach. *Chem. Mater.* **2015**, *27*, 5892-5898.

[23] McKittrick, J.; Hannah, M. E.; Piquette, A.; Han, J. K.; Choi, J. I.; Anc, M.; Galvez, M.; Lugauer, H.; Talbot, J. B.; Mishra, K. C. Phosphor Selection Considerations for Near-UV LED Solid State Lighting. *ECS J. Solid State Sci. Technol.* **2013**, *2*, R3119-R3131.

[24] Piquette, A.; Bergbauer, W.; Galler, B.; Mishra, K. C. On Choosing Phosphors for Near-UV and Blue LEDs for White Light. *ECS J. Solid State Sci. Technol.* **2016**, *5*, R3146-R3159.

[25] Wang, Y.-F.; Liu, L.; Xie, R.-J.; Huang, Q. Microwave Assisted Sintering of Thermally Stable $BaMgAl_{10}O_{17}:Eu^{2+}$ Phosphors. *ECS J. Solid State Sci. Technol.* **2013**, *2*, R196-R200.

[26] Morimoto, K.; Kasugai, H.; Takizawa, T.; Yoshida, S.; Yamanaka, K.; Katayama, T.; Okuyama, K.; Shiraishi, S.; Mizuyama, Y. 60.2: Distinguished Paper:A 30 W Pure Blue Emission with NUV Laser-Diode-Pumped Phosphor for High-Brightness Projectors. *SID Symp. Dig. Tech. Pap.* **2013**, *44*, 832-835.

[27] Agency for Toxic Substances and Disease Registry (ATSDR) - Case Studies in Environmental Medicine - Beryllium Toxicity **2018**.

[28] Blasse, G.; Bril, A. Characteristic luminescence. *Philips Tech. Rev.* **1970**, *31*, 304-314.

[29] Schmiechen, S.; Pust, P.; Schmidt Peter, J.; Schnick, W. Weißes Licht aus Nitriden. *Nachr. Chem.* **2014**, *62*, 847-851.

[30] Tauc, J.; Grigorovici, R.; Vancu, A. Optical Properties and Electronic Structure of Amorphous Germanium. *Phys. Status Solidi B* **1966**, *15*, 627-637.

[31] Tolhurst, T. M.; Strobel, P.; Schmidt, P. J.; Schnick, W.; Moewes, A. Designing Luminescent Materials and Band Gaps: A Soft X-ray Spectroscopy and Density Functional Theory Study of $Li_2Ca_2[Mg_2Si_2N_6]:Eu^{2+}$ and $Ba[Li_2(Al_2Si_2)N_6]:Eu^{2+}$. *J. Phys. Chem. C* **2017**, *121*, 14296-14301.

[32]

[33] Zeuner, M.; Pagano, S.; Hug, S.; Pust, P.; Schmiechen, S.; Scheu, C.; Schnick, W. $Li_2CaSi_2N_4$ and $Li_2SrSi_2N_4$ – a Synthetic Approach to Three-Dimensional Lithium Nitridosilicates. *Eur. J. Inorg. Chem.* **2010**, 4945-4951.

[34] Liebau, F., *Structural Chemistry of Silicates*, Springer: Berlin, **1985**.

[35] Shannon, R. D. Revised Effective Ionic Radii and Systematic Studies of Interatomic Distances in Halides and Chalcogenides. *Acta Crystallogr. Sect. A* **1976**, *32*, 751.

[36] Baur, W. H. Effective ionic radii in nitrides. *Crystallogr. Rev.* **1987**, *1*, 59-83.

[37] Zachariasen, W. Über die Kristallstruktur von BeO. *Norsk. Geol. Tidssk* **1925**, *8*, 189-200.

[38] Zintl, E.; Harder, A.; Dauth, B. Gitterstruktur der Oxyde, Sulfide, Selenide und Telluride des Lithiums, Natriums und Kaliums. *Z. Elektrochem. Angew. Phys. Chem.* **1934**, *40*, 588-593.

[39] Harris, L. A.; Yakel, H. L. The crystal structure of calcium beryllate, $Ca_{12}Be_{17}O_{29}$. *Acta Crystallogr.* **1966**, *20*, 295-301.

[40] Li, G.; Tian, Y.; Zhao, Y.; Lin, J. Recent progress in luminescence tuning of Ce^{3+} and Eu^{2+}-activated phosphors for pc-WLEDs. *Chem. Soc. Rev.* **2015**, *44*, 8688-8713.

5 Conclusion and Outlook

Today, phosphor converted light emitting diodes (pc-LEDs) are at the heart of modern illumination technology. To further improve emission characteristics of pc-LEDs, it is of uttermost importance to control spectral properties of light converting materials. Development of narrow-band phosphors emitting across the entire visible spectrum is required to enhance properties, such as efficiency, color point stability and color rendering. The impact of narrow-band emitting phosphors was shown, e.g. by the invention of red emitting $Sr[LiAl_3N_4]:Eu^{2+}$ (SLA) with *fwhm* = 50 nm, gaining an increase of 14% in luminous efficacy.[1,2] Analyzing the relationship between crystal structures and spectral properties in Eu^{2+} doped phosphors was the decisive step for the development of SLA by *Pust* and structurally related $Sr[Mg_3SiN_4]:Eu^{2+}$ (SMS) with extremely narrow-band emission (*fwhm* = 43 nm) by *Schmiechen*.[1,3]

This thesis focuses on understanding the relationship of spectral and structural properties in highly condensed phosphor materials. The most important structural characteristics of previously developed state-of-the-art phosphors have been identified and transferred, yielding new classes of materials with novel crystal structures exhibiting unprecedented spectral qualities. Combination of structural analysis methods and characterization of spectral and electronic properties was successfully applied on Eu^{2+}- or Ce^{3+}-doped nitridosilicates and the hitherto only little or not yet examined classes of oxo-, nitrido- and oxonitridoberyllates. Single-crystal and powder X-ray diffraction methods as well as luminescence measurements, DFT calculations and soft X-ray spectroscopy, including a newly developed characterization method for Eu^{2+} doped phosphors using resonant inelastic X-ray spectroscopy (RIXS) were applied.

Based on previous investigations of nitridosilicates, exploration of multinary nitridosilicate and -aluminate compounds resulted in the development of narrow-band emitting $Ba(Mg_{2-x}Li_x)[(Al_{4-x}Si_x)N_6]:Eu^{2+}$ (x = 1.6–2; BLSA) and $Li_2(Ca_{1-x})_2[Mg_2Si_2N_6]:Eu^{2+}$ (x = 0–0.06; CLMS). Both compounds exhibit striking structural and chemical similarities to SLA and SMS.[4,5] Narrow-band emission was detected in the green spectral region at 532 nm with *fwhm* = 57 nm for BLSA and in the red region at 634-638 nm with *fwhm* = 62 nm for CLMS. Suitability of both phosphors for application in pc-LEDs was examined and parameters such as band gap and quantum efficiency have been investigated. For BLSA, DFT calculations suggest that the ionic character of Li–ligand bonds limits substitution of Li by the more electronegative Mg.[6] However, compounds crystallizing in the BLSA structure type, e.g. hypothetical "$BaMg_2[Al_4N_6]:Eu^{2+}$" are expected to result in even narrower emission due to the elimination of inhomogeneous line broadening. As discussed in previous cases, such line broadening results from the statistical distribution of tetrahedrally coordinated cations, e.g. Al and Mg in $AE[Mg_2Al_2N_4]:Eu^{2+}$ (*AE* = Ca,Sr,Ba) and Al and Si in $(Ca,Sr)SiAlN_3:Eu^{2+}$.[7] The mixed occupation then results in variable (Al,Mg)– or (Al,Si)–ligand bond lengths in the tetrahedral spheres, directly influencing the activator environment.[8-10]

For the determination of structure-property relations in nitridosilicates, electronic properties of SLA, SMS, BLSA as well as CLMS have been investigated and compared in detail by X-ray spectroscopy measurements and DFT calculations. For the first time, we were able to directly measure the energetic separation between the conduction band (CB) and the excited Eu(II) 5*d* level in all investigated phosphors. Up to now, experimentally determined excited activator energy states, located in the band gap, have been largely inaccessible and have only been determined indirectly by temperature-dependent luminescence investigations.[11] X-ray excited optical luminescence (XEOL) was additionally used to observe optically visible $5d^1\ 4f^6 \rightarrow 4f^7$ transitions, direct band to band transitions and 4*f* to valence band (VB) transitions. Applying X-ray spectroscopy in combination with DFT calculations allows drawing a comprehensive picture of the most important electronic processes in Eu^{2+}-doped phosphor materials giving rise to conclusions about the relation between electronic properties and critical phosphor qualities, such as color, efficiency and thermal quenching behavior.[6,12]

The extensive investigations on nitridosilicate compounds have demonstrated the impact of the crystal structure on luminescence properties: Large band gap host materials with a rigid network structure and a single dopant site are a prerequisite for efficient narrow-band emission. In this work, these findings have been successfully transferred to the development of novel beryllate phosphors. The nitridoberyllosilicate compound $Sr[BeSi_2N_4]:Eu^{2+}$ exhibits broad-band orange emission that was identified as anomalous trapped exciton emission.[13] Further investigations resulted in the development of the first oxonitridoberyllate compound $Sr[Be_6ON_4]:Eu^{2+}$, which structure is deduced from $Sr[BeSi_2N_4]$. The narrow-band cyan emission of $Sr[Be_6ON_4]:Eu^{2+}$ at 495 nm (*fwhm* = 35 nm) is comparable to the emission of the oxonitridosilicate $BaSi_2O_2N_2:Eu^{2+}$ or a cyan primary LED (*fwhm* = 27 nm).[14,15] A large band gap and its 3D network structure results in improved thermal quenching behavior enabling improved long-time stability under operating conditions, compared to $BaSi_2O_2N_2:Eu^{2+}$ with its layered structure.

During oxonitridoberyllate investigations several luminescent and non-luminescent, unknown side-phases have been detected and elucidated. In the quasi-binary system SrO-BeO three novel ternary oxoberyllates, namely non-luminescent α-$SrBeO_2:Eu^{2+}$, narrow-band yellow emitting β-$SrBeO_2:Eu^{2+}$ as well as broad-band orange emitting $Sr_{12}Be_{17}O_{29}:Eu^{2+}$ have been characterized.[16] The investigated oxoberyllates show structural features comparable to highly condensed nitridosilicate compounds. The layered structure of β-$SrBeO_2$, e.g. is comparable to the layered nitridosilicate $SrSiN_2$.

The systematic introduction of Li into oxoberyllate synthesis with analogy to before reported nitridosilicates and -aluminates resulted in an extraordinary narrow-band blue emitting oxoberyllate phosphor with nitridosilicate structure.[2,4,5,17,18] $AELi_2[Be_4O_6]:Eu^{2+}$ (*AE* = Sr,Ba) crystallizes in the $BaLi_2[(Al_2Si_2)N_6]$ structure type exhibiting exceptional narrow-band emission between 454 and 456 nm with *fwhm* ≈ 25 nm.[19] The reduction of emission band width by approximately 500 cm^{-1} in $AELi_2[Be_4O_6]:Eu^{2+}$ compared to BLSA results from the exchange of the statistically mixed occupied Al,Si site by Be, and demonstrates the effect of eliminating inhomogeneous line broadening.

Analyzing emission properties of the novel beryllate phosphors confirm assumptions that dopant coordination spheres' form as well as network rigidity are decisive for narrow-band emission. High rigidity resulting from a high degree of condensation as well as the strongly covalent character of the Be–*X* (*X* = O,N) bonds of the host structures can even compensate irregular coordinations of Eu leading to narrow-band emission. This is observed, e.g. in $Sr[Be_6ON_4]:Eu^{2+}$ with a rigid tetrahedral network of edge-sharing BeN_4 and $BeON_3$ tetrahedra, or in the supertetrahedron phosphor $Ca_{18.75}Li_{10.5}[Al_{39}N_{55}]:Eu^{2+}$, emitting at 647 nm with *fwhm* = 54 nm.[20]

The results described in this thesis demonstrate that crystal structure characteristics for efficient narrow-band emission obtained in (nitrido)silicates can be transferred onto other compound classes, such as the novel class of beryllate host materials, which structures and properties are investigated for the first time in this thesis. Consequently, synthesis concepts and structural characteristics of (nitrido)silicates have been successfully applied developing chemically and thermally stable, efficient narrow-band emitting beryllate phosphors covering the entire visible spectrum. The strong covalent character of Be–(O,N) bonds is comparable to (Al,Si)–(O,N) bonds. In combination with increased connectivity of ligand atoms, resulting from the reduced cation formal charge of Be^{2+} compared to Al^{3+} and Si^{4+}, these chemical and structural characteristics allow for the formation of highly condensed, rigid host materials offering an extended range for the degree of condensation (i.e. atomic ratio Be:(O,N); $0.5 \leq \kappa \leq 1.5$) and large band gaps. Oxo-, nitrido- and oxonitridoberyllates are therefore suitable for highly efficient, narrow-band luminescence in solid-state lighting. Ongoing investigations on narrow-band red emitting nitridoberyllates are promising and allow for even more efficient pc-LEDs. Finding a rigid nitridoberyllate structure adopting all required parameters, such as a symmetrically coordinated crystallographic *AE* site and high ordering of all present elements, even efficient, unprecedented narrow-band red Eu^{2+} emission <40 nm has now come into reach.

References

[1] Pust, P.; Schmidt, P. J.; Schnick, W. A revolution in lighting. *Nat. Mater.* **2015**, *14*, 454-458.

[2] Pust, P.; Weiler, V.; Hecht, C.; Tücks, A.; Wochnik, A. S.; Henß, A. K.; Wiechert, D.; Scheu, C.; Schmidt, P. J.; Schnick, W. Narrow-band red-emitting $Sr[LiAl_3N_4]:Eu^{2+}$ as a next-generation LED-phosphor material. *Nat. Mater.* **2014**, *13*, 891-896.

[3] Schmiechen, S.; Schneider, H.; Wagatha, P.; Hecht, C.; Schmidt, P. J.; Schnick, W. Toward New Phosphors for Application in Illumination-Grade White pc-LEDs: The Nitridomagnesosilicates $Ca[Mg_3SiN_4]:Ce^{3+}$, $Sr[Mg_3SiN_4]:Eu^{2+}$, and $Eu[Mg_3SiN_4]$. *Chem. Mater.* **2014**, *26*, 2712-2719.

[4] Strobel, P.; Schmiechen, S.; Siegert, M.; Tücks, A.; Schmidt, P. J.; Schnick, W. Narrow-Band Green Emitting Nitridolithoalumosilicate $Ba[Li_2(Al_2Si_2)N_6]:Eu^{2+}$ with Framework Topology whj for LED/LCD-Backlighting Applications. *Chem. Mater.* **2015**, *27*, 6109-6115.

[5] Strobel, P.; Weiler, V.; Hecht, C.; Schmidt, P. J.; Schnick, W. Luminescence of the Narrow-Band Red Emitting Nitridomagnesosilicate $Li_2(Ca_{1-x}Sr_x)_2[Mg_2Si_2N_6]:Eu^{2+}$ (x = 0–0.06). *Chem. Mater.* **2017**, *29*, 1377-1383.

[6] Tolhurst, T. M.; Strobel, P.; Schmidt, P. J.; Schnick, W.; Moewes, A. Designing Luminescent Materials and Band Gaps: A Soft X-ray Spectroscopy and Density Functional Theory Study of $Li_2Ca_2[Mg_2Si_2N_6]:Eu^{2+}$ and $Ba[Li_2(Al_2Si_2)N_6]:Eu^{2+}$. *J. Phys. Chem. C* **2017**, *121*, 14296-14301.

[7] Pust, P., Doctoral Thesis, Ludwig-Maximilians University, Munich **2014**.

[8] Pust, P.; Hintze, F.; Hecht, C.; Weiler, V.; Locher, A.; Zitnanska, D.; Harm, S.; Wiechert, D.; Schmidt, P. J.; Schnick, W. Group (III) Nitrides $M[Mg_2Al_2N_4]$ (*M* = Ca, Sr, Ba, Eu) and $Ba[Mg_2Ga_2N_4]$ – Structural Relation and Nontypical Luminescence Properties of Eu^{2+} Doped Samples. *Chem. Mater.* **2014**, *26*, 6113-6119.

[9] Uheda, K.; Hirosaki, N.; Yamamoto, H. Host lattice materials in the system Ca_3N_2–AlN–Si_3N_4 for white light emitting diode. *Phys. Status Solidi A* **2006**, *203*, 2712-2717.

[10] Uheda, K.; Hirosaki, N.; Yamamoto, Y.; Naita, A.; Nakajima, T.; Yamamoto, H. Luminescence Properties of a Red Phosphor, $CaAlSiN_3:Eu^{2+}$, for White Light-Emitting Diodes *Electrochem. Solid State Lett.* **2006**, *9*, H22-H25.

[11] Dorenbos, P. Thermal quenching of Eu^{2+} 5*d*–4*f* luminescence in inorganic compounds. *J. Phys.: Condens. Matter* **2005**, *17*, 8103-8111.

[12] Tolhurst, T. M.; Strobel, P.; Schmidt, P. J.; Schnick, W.; Moewes, A. Direct Measurements of Energy Levels and Correlation with Thermal Quenching Behavior in Nitride Phosphors. *Chem. Mater.* **2017**, 7976-7983.

[13] Strobel, P.; Weiler, V.; Schmidt, P. J.; Schnick, W. $Sr[BeSi_2N_4]:Eu^{2+}/Ce^{3+}$ and $Eu[BeSi_2N_4]$: Nontypical Luminescence in Highly Condensed Nitridoberyllosilicates. *Chem. Eur. J.* **2018**, *24*, 7243-7249.

[14] Kechele, J. A.; Oeckler, O.; Stadler, F.; Schnick, W. Structure elucidation of $BaSi_2O_2N_2$ – A host lattice for rare-earth doped luminescent materials in phosphor-converted (pc)-LEDs. *Solid State Sci.* **2009**, *11*, 537-543.

[15] Strobel, P.; de Boer, T.; Weiler, V.; Schmidt, P. J.; Moewes, A.; Schnick, W. Luminescence of an Oxonitridoberyllate: A Study of Narrow-Band Cyan Emitting $Sr[Be_6ON_4]:Eu^{2+}$. *Chem. Mater.* **2018**, *30*, 3122-3130.

[16] Strobel, P.; Niklaus, R.; Schmidt, P. J.; Schnick, W. Oxoberyllates $SrBeO_2$ and $Sr_{12}Be_{17}O_{29}$ as Novel Host Materials for Eu^{2+} Luminescence. *Chem. Eur. J.* **2018**, https://doi.org/10.1002/chem.201801951.

[17] Pust, P.; Wochnik, A. S.; Baumann, E.; Schmidt, P. J.; Wiechert, D.; Scheu, C.; Schnick, W. $Ca[LiAl_3N_4]:Eu^{2+}$ - A Narrow-Band Red-Emitting Nitridolithoaluminate. *Chem. Mater.* **2014**, *26*, 3544-3549.

[18] Zeuner, M.; Pagano, S.; Hug, S.; Pust, P.; Schmiechen, S.; Scheu, C.; Schnick, W. $Li_2CaSi_2N_4$ and $Li_2SrSi_2N_4$ – a Synthetic Approach to Three-Dimensional Lithium Nitridosilicates. *Eur. J. Inorg. Chem.* **2010**, 4945-4951.

[19] Strobel, P.; Maak, C.; Weiler, V.; Schmidt, P. J.; Schnick, W. Ultra-Narrow Band Blue Emitting Oxoberyllates $AELi_2[Be_4O_6]:Eu^{2+}$ (*AE* = Sr,Ba) Paving the Way to Efficient RGB pc-LEDs. *Angew. Chem. Int. Ed.* **2018**, https://doi.org/10.1002/anie.201804721.

[20] Wagatha, P.; Pust, P.; Weiler, V.; Wochnik, A. S.; Schmidt, P. J.; Scheu, C.; Schnick, W. $Ca_{18.75}Li_{10.5}[Al_{39}N_{55}]:Eu^{2+}$ - Supertetrahedron Phosphor for Solid-State Lighting. *Chem. Mater.* **2016**, *28*, 1220-1226.

6 Summary

1. Narrow-Band Green Emitting Nitridolithoalumosilicate $Ba[Li_2(Al_2Si_2)N_6]:Eu^{2+}$ with Framework Topology whj for LED/LCD-Backlighting Applications

Philipp Strobel, Sebastian Schmiechen, Markus Siegert, Andreas Tücks, Peter J. Schmidt, and Wolfgang Schnick

Chem. Mater. **2015**, *27*, 6109–6115

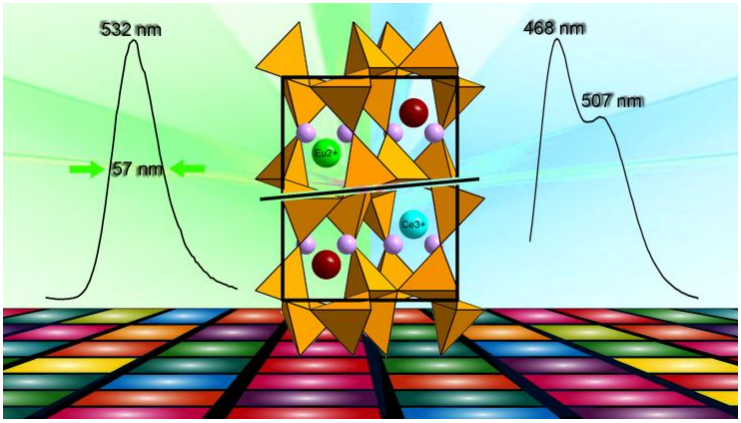

The Nitridolithoalumosilicate $Ba[Li_2(Al_2Si_2)N_6]:Eu^{2+}$ was synthesized under high-temperature conditions via metathesis reactions in weld-shut tantalum ampules at 950 °C. The crystal structure, crystallizing in space group *P*4/*ncc* (no. 130, a = 7.8282(4), c = 9.9557(5) Å, Z = 4) was solved on the basis of single-crystal X-ray diffraction data. The three-dimensional network structure offers two types of *vierer* ring channels occupied by either Ba or Li. The Ba coordination can be described as a truncated square pyramid trunk, similar to *AE* coordination spheres found in other narrow-band emitting nitridosilicates and -aluminates. For $Ba[Li_2(Al_2Si_2)N_6]:Eu^{2+}$, green emission is obtained at 532 nm with *fwhm* = 57 nm, and emission tuning towards the yellow spectral region is performed by substitution of Li by Mg in $Ba[(Mg_{2-x}Li_x)(Al_{4-x}Si_x)N_6]:Eu^{2+}$ (x = 1.6–2.0). Samples of $Ba[Li_2(Al_2Si_2)N_6]:Ce^{3+}$ exhibit broad-band blue-cyan emission. Due to its narrow-band green emission $Ba[Li_2(Al_2Si_2)N_6]:Eu^{2+}$ is discussed as phosphor for LED application i.e. in liquid crystal displays.

2. Luminescence of the Narrow-Band Red Emitting Nitridomagnesosilicate $Li_2(Ca_{1-x}Sr_x)_2[Mg_2Si_2N_6]:Eu^{2+}$ (x = 0–0.06)

Philipp Strobel, Volker Weiler, Cora Hecht, Peter J. Schmidt, and Wolfgang Schnick

Chem. Mater. **2017**, *29*, 1377–1383

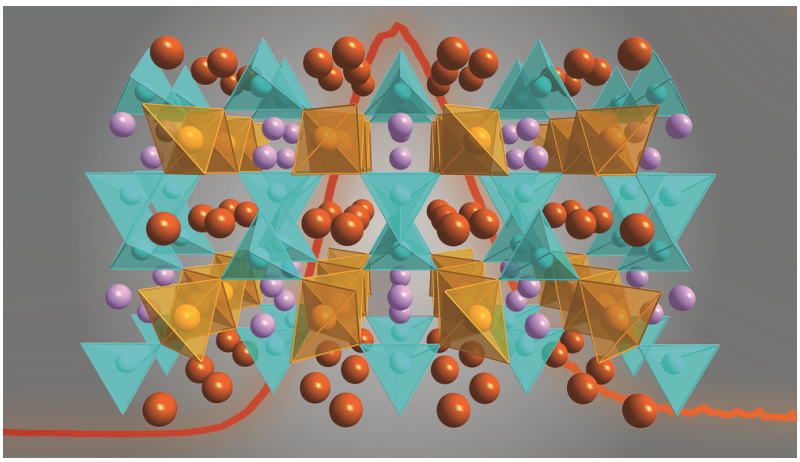

Efficient red-emitting phosphor materials are essential for improving next generation high-power pc-LEDs with increased luminous efficacy. $Li_2(Ca_{1.88}Sr_{0.12})[Mg_2Si_2N_6]:Eu^{2+}$ was synthesized by solid-state metathesis in Li melts in sealed tantalum ampules and was structurally characterized by single-crystal and powder X-ray diffraction ($C2/m$ (no. 12), a = 5.5744(2) Å, b = 9.8439(3) Å, c = 6.0170(2) Å, β = 97.2520(10)°, Z = 2). $Li_2(Ca_{1.88}Sr_{0.12})[Mg_2Si_2N_6]:Eu^{2+}$ is isotypic to $Li_2Ca_2[Mg_2Si_2N_6]$, the elemental composition was confirmed by EDS and ICP-OES measurements, while the substitution of Ca by Sr is limited. The three-dimensional network structure is built of $[Si_2N_6]$ bow-tie units that are connected by strands of MgN_4 tetrahedra by common vertices. The nitridomagnesosilicate phosphors $Li_2(Ca_{1-x}Sr_x)_2[Mg_2Si_2N_6]:Eu^{2+}$ (x = 0–0.06) show narrow-band red emission (λ_{em} ≈ 634-638 nm, *fwhm* ≈ 1513 cm^{-1} (≈ 62 nm)). Ce^{3+}-doped samples of $Li_2Ca_2[Mg_2Si_2N_6]$ emit light in the green spectral region (λ_{em} ≈ 540 nm). Red emitting $Li_2(Ca_{1-x}Sr_x)_2[Mg_2Si_2N_6]:Eu^{2+}$ (x = 0–0.06) are discussed for application in high power pc-LEDs with improved luminous efficacy and excellent color rendition.

3. Designing Luminescent Materials and Band Gaps: A Soft X−ray Spectroscopy and Density Functional Theory Study of $Li_2Ca_2[Mg_2Si_2N_6]:Eu^{2+}$ and $Ba[Li_2(Al_2Si_2)N_6]:Eu^{2+}$

Thomas M. Tolhurst, Philipp Strobel, Peter J. Schmidt, Wolfgang Schnick, and Alexander Moewes

J. Phys. Chem. C. **2017**, *121*, 14296–14301

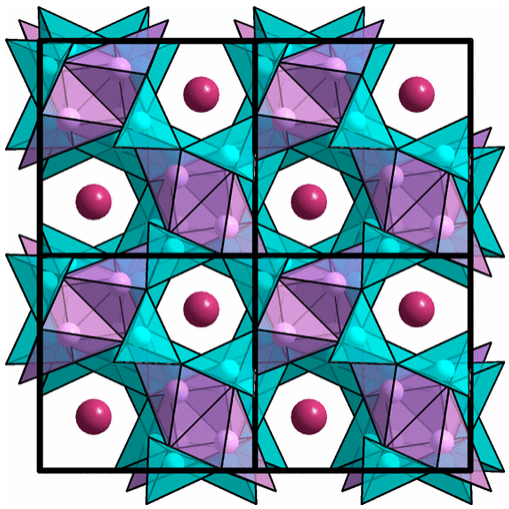

To improve understanding of complex structure-property relations and to enable further optimization of material properties of rare-earth doped solid-state phosphors, the band structures of $Li_2Ca_2[Mg_2Si_2N_6]:Eu^{2+}$ and $Ba[Li_2(Al_2Si_2)N_6]:Eu^{2+}$ have been investigated in detail by soft-X-ray spectroscopy methods as well as density functional theory calculations. Both materials exhibit similar indirect band gaps of ≈ 4.8 eV. The band gap of narrow-band red emitting $Li_2Ca_2[Mg_2Si_2N_6]:Eu^{2+}$ is therefore larger than the band gap of comparable narrow-band red emitting $Sr[Mg_3SiN_4]:Eu^{2+}$ due to decreased N–Mg separation and therefore increased bond–antibond splitting. A different constitution of the lowest lying bands of the conduction bands of $Li_2Ca_2[Mg_2Si_2N_6]:Eu^{2+}$ and $Ba[Li_2(Al_2Si_2)N_6]:Eu^{2+}$ is identified indicating a significant influence on the phosphors' thermal quenching behavior. The detailed investigation of the electronic structures underlines the high potential of both phosphors and related compounds for application in solid-state lighting.

4. Direct Measurements of Energy Levels and Correlation with Thermal Quenching Behavior in Nitride Phosphors

Thomas M. Tolhurst, Philipp Strobel, Peter J. Schmidt, Wolfgang Schnick, and Alexander Moewes
Chem. Mater. **2017**, *29*, 7976–7983

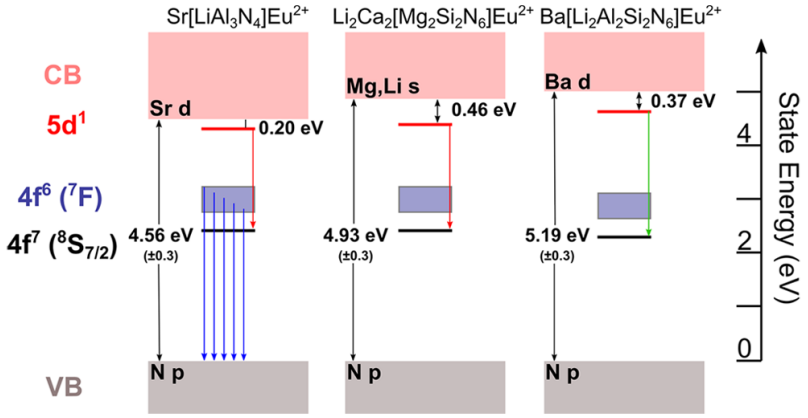

Electronic properties of the narrow-band emitting phosphors $Li_2Ca_2[Mg_2Si_2N_6]:Eu^{2+}$ (CLMS), $Ba[Li_2(Al_2Si_2)N_6]:Eu^{2+}$ (BLSA), $Sr[LiAl_3N_4]:Eu^{2+}$ (SLA) and $Sr[Mg_3SiN_4]:Eu^{2+}$ (SMS) are investigated applying Soft X-ray spectroscopy and DFT methods. X-ray excited optical luminescence (XEOL) experiments have been performed to directly observe band to band and 4*f* to valence band transitions. For the first time, direct measurements of the excited Eu(II) 5*d* state were conducted to obtain the energetic separation to the conduction band. Resonant inelastic X-ray scattering (RIXS) was employed for this purpose. The separations measured through RIXS for SLA, CLMS, and BLSA are 0.2 ± 0.1 eV, 0.46 ± 0.03 eV, and 0.37 ± 0.03 eV, respectively. Due to its small band gap no 5*d*-CB separation was resolved when investigating SMS. The development of this method is a great progress in a field that often relies on empirical models to predict the location of excited rare-earth states in the band gap of a host material. A comprehensive picture of all pertinent electronic processes was generated that can help understanding structure-property relations in phosphor materials, such as the influence of the crystal structure and density of states on a phosphor's luminescence properties.

5. $Sr[BeSi_2N_4]:Eu^{2+}/Ce^{3+}$ and $Eu[BeSi_2N_4]$: Nontypical Luminescence in Highly Condensed Nitridoberyllosilicates

Philipp Strobel, Volker Weiler, Peter J. Schmidt, and Wolfgang Schnick

Chem. Eur. J. **2018**, *24*, 2743-2749

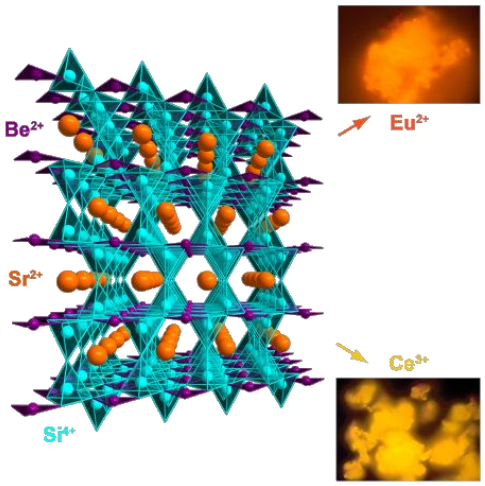

M[$BeSi_2N_4$] (*M* = Sr,Eu) synthesized from $Sr(NH_2)_2$, Be_3N_2 and "$Si(NH)_2$" under N_2 atmosphere in a rf furnace are the first ever observed nitridoberyllosilicates. Both compounds crystallize in the monoclinic space group $P\bar{6}2c$ (no. 190; Sr[$BeSi_2N_4$]: a = 4.86082(2), c = 9.42263(4) Å; Eu[$BeSi_2N_4$]: a = 4.85848(1), c = 9.41615(4) Å; Z = 2) and are isotypic to the beryllate $SrBe_3O_4$. The crystal structures were solved by the charge-flipping method from X-ray powder diffraction data and refined by the Rietveld method. *M*[$BeSi_2N_4$] (*M* = Sr,Eu) with their highly condensed 3D network built from BeN_3 triangles and Si_2N_7 double tetrahedra are phosphors exhibiting orange trapped exciton emission in Eu-containing compounds (λ_{em}= 605nm, *fwhm* ≈ 126nm) and yellowish-orange emission upon doping with Ce^{3+}. A large band gap and chemical as well as thermal stability make this beryllate compound a promising starting point for investigations on efficient beryllate phosphors, pointing towards highly efficient narrow-band phosphors for application in pc-LEDs.

6. Luminescence of an Oxonitridoberyllate: A Study of Narrow-Band Cyan Emitting $Sr[Be_6ON_4]:Eu^{2+}$

Philipp Strobel, Tristan de Boer, Volker Weiler, Peter J. Schmidt, Alexander Moewes, and Wolfgang Schnick

Chem. Mater. **2018**, *30*, 3122-3130

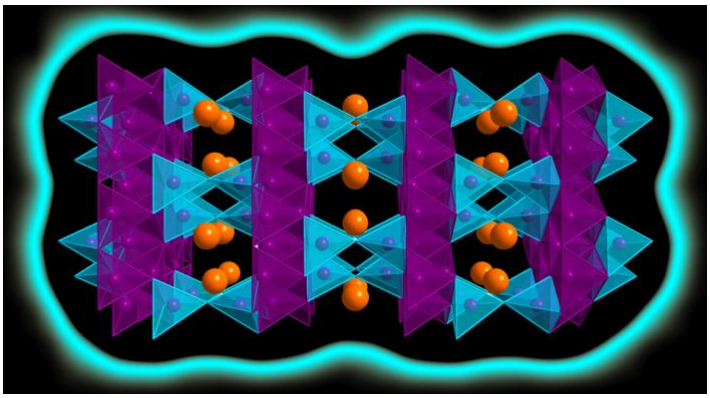

Narrow-band cyan emitting phosphors that are efficiently excitable by blue primary LEDs are highly demanded for covering the so called “cyan gap” in pc-LEDs to improve color rendering. $Sr[Be_6ON_4]:Eu^{2+}$ with its narrow-band cyan emission with λ_{em} = 495 nm and *fwhm* = 35 nm is therefore an highly promising phosphor for application in efficient high CRI pc-LEDs. $Sr[Be_6ON_4]:Eu^{2+}$ shows superior chemical and thermal stability compared to state of the art $Ba[Si_2O_2N_2]:Eu^{2+}$ phosphors due to its 3D network structure, built of BeN_4 and $BeON_3$ tetrahedra, with a remarkable degree of condensation κ = 1.2. $Sr[Be_6ON_4]$ is the first oxonitridoberyllate and crystallizes in the monoclinic space group *C*2/*c* (no. 15, *a* = 13.9283(14), *b* = 5.7582(6), *c* = 4.9908(5) Å, β = 90.195(5)°, *Z* = 4) with pseudo-orthorhombic metrics, solved from single-crystal XRD and supported by PXRD data. The phosphor was additionally investigated applying Soft X-ray spectroscopy methods and DFT calculations to determine the electronic structure. A large band gap and the rigid three-dimensional network underline the phosphor’s suitability for application.

7. Oxoberyllates $SrBeO_2$ and $Sr_{12}Be_{17}O_{29}$ as Novel Host Materials for Eu^{2+} Luminescence

Philipp Strobel, Robin Niklaus, Peter J. Schmidt, and Wolfgang Schnick

Chem. Eur. J. **2018**, https://doi.org/10.1002/chem.201801951

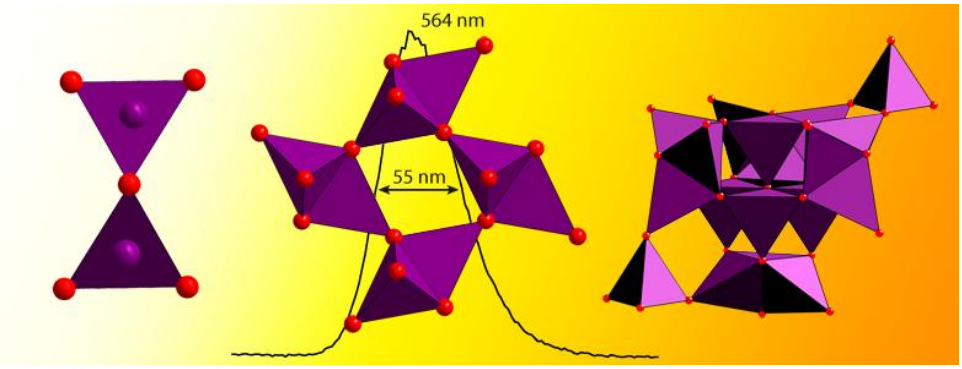

A broad range of structures is accessible by variable combinations of trigonal planar building units and tetrahedra. Three novel ternary Sr-oxoberyllates are characterized by single-crystal X-ray diffraction analysis, DFT calculations and luminescence investigations: α-$SrBeO_2$, ($P2_1/m$ (no. 11), a = 3.5824(3), b = 5.1732(5), c = 5.5515(5) Å, β = 98.262(4)°, Z = 2), β-$SrBeO_2$ ($P2_1/c$ (no. 14), a = 7.0045(9), b = 5.0697(11), c = 5.3127(7) Å, β = 98.935(6)°, Z = 4) and $Sr_{12}Be_{17}O_{29}$ ($I\bar{4}2m$ (no. 121), a = 11.0104(4) c = 10.6208(10) Å, Z = 2). The novel compounds can be described as chain- and layer-type beryllates. The beryllates consisting of tetrahedral networks, namely β-$SrBeO_2$ and $Sr_{12}Be_{17}O_{29}$, are closely related to nitridosilicates. The structure of α-$SrBeO_2$ with trigonal planar BeO_3 units is comparable to borates. DFT calculations have been applied to investigate the thermodynamic stability and electronic structure of the beryllate compounds. α-$SrBeO_2$ appears as colorless transparent crystals. $Sr_{12}Be_{17}O_{29}$:Eu^{2+} shows broad-band emission in the orange spectral range. β-$SrBeO_2$ exhibits exceptional narrow-band yellow emission (λ_{em} = 564 nm, *fwhm* = 55 nm) and is a promising material for application in yellow and white pc-LEDs with increased lumen equivalents. Both phosphors are the first luminescent oxoberyllates reported so far.

8. Ultra-Narrow Band Blue Emitting Oxoberyllates $AELi_2[Be_4O_6]:Eu^{2+}$ (*AE* = Sr,Ba) Paving the Way to Efficient RGB pc-LEDs

Philipp Strobel, Christian Maak, Volker Weiler, Peter J. Schmidt, and Wolfgang Schnick

Angew. Chem. Int. Ed. ***2018***, https://doi.org/10.1002/anie.201804721

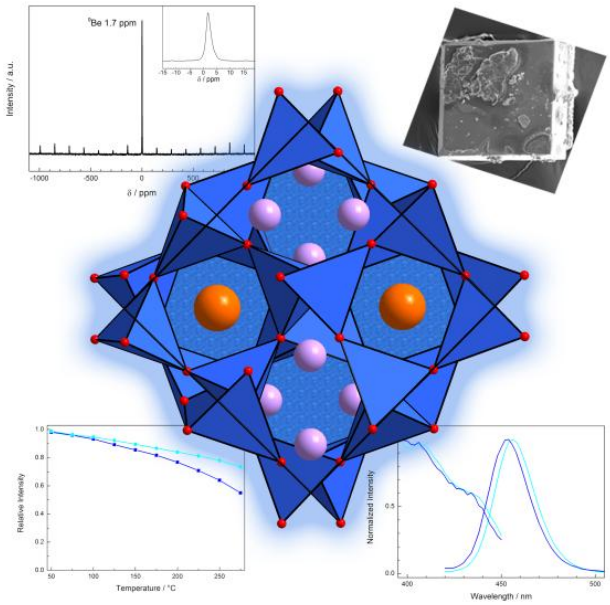

The novel quaternary oxoberyllates $AELi_2[Be_4O_6]:Eu^{2+}$ (*AE* = Sr,Ba) crystallizing in space group *P*4/*ncc* (no. 130; $SrLi_2[Be_4O_6]$: a = 7.1659(2), c = 8.9085(6) Å; $BaLi_2[Be_4O_6]$: a = 7.2770(4), c = 8.8872(5) Å; Z = 4) are isotypic to the highly condensed nitridoalumosilicate $BaLi_2[(Al_2Si_2)N_6]:Eu^{2+}$. The title compounds have been synthesized starting from binary oxides at 1100 °C in a radio-frequency furnace. An extremely small Stokes-shift and unprecedented ultra-narrow band blue emission with λ_{em} = 454–456 nm and *fwhm* ≈ 25 nm (≈ 1200 cm^{-1}) resulting from a rigid, highly condensed tetrahedral network is observed. Structural and elemental analysis was supported by NMR-spectroscopic investigations of ^6Li, ^7Li and ^9Be. Due to a decreased Stokes-shift, when compared to conventional blue emitting phosphors, $AELi_2[Be_4O_6]:Eu^{2+}$ allows for using blue primary LEDs with λ_{em} <440 nm in violet pumped white RGB (red, green, blue) phosphor LEDs. This new type of LED will have improved color point stability, enhanced color rendering and excellent energy efficiency.

7 Appendix

7.1 Supporting Information for Chapter 2.1

Philipp Strobel, Sebastian Schmiechen, Markus Siegert, Andreas Tücks, Peter J. Schmidt and Wolfgang Schnick, *Chem. Mater.* **2015**, *27*, 6109–6115.

Table S1. Atomic coordinates and isotropic displacement parameters of $Ba[(Mg_{0.2}Li_{1.8})(Al_{2.2}Si_{1.8})N_6]$ and $Ba[(Mg_{0.4}Li_{1.6})(Al_{2.4}Si_{1.6})N_6]$[a]

	Atom (*Wyck.*)	***x***	***y***	***z***	U_{eq}/Å^3	***sof***
$Ba[(Mg_{0.2}Li_{1.8})(Al_{2.2}Si_{1.8})N_6]$	Ba (4*c*)	1/4	1/4	0.3419(2)	0.0138(14)	1
	Mg (8*f*)	0.3722(3)	0.6278(3)	1/4	0.0091(6)	0.1
	Li (8*f*)	0.3722(3)	0.6278(3)	1/4	0.0091(6)	0.9
	Al (16*g*)	0.1225(7)	0.5332(7)	0.0819(5)	0.0074(17)	0.55
	Si (16*g*)	0.1225(7)	0.5332(7)	0.0819(5)	0.0074(17)	0.45
	N1 (8*f*)	0.5968(2)	0.4032(2)	1/4	0.0183(5)	1
	N2 (16*g*)	0.5064(2)	0.1566(2)	0.0445(19)	0.0169(4)	1
$Ba[(Mg_{0.4}Li_{1.6})(Al_{2.4}Si_{1.6})N_6]$	Ba (4*c*)	1/4	1/4	0.3424(3)	0.0146(16)	1
	Mg (8*f*)	0.3731(3)	0.6269(3)	1/4	0.0200(7)	0.2
	Li (8*f*)	0.3731(3)	0.6269(3)	1/4	0.0200(7)	0.8
	Al (16*g*)	0.1225(8)	0.5331(8)	0.0817(6)	0.0078(2)	0.6
	Si (16*g*)	0.1225(8)	0.5331(8)	0.0817(6)	0.0078(2)	0.4
	N1 (8*f*)	0.5979(3)	0.4021(3)	1/4	0.0184(6)	1
	N2 (16*g*)	0.5070(3)	0.1558(3)	0.0446(2)	0.0172(4)	1

[a] e.s.d.'s in parentheses

Table S2. Anisotropic displacement parameters (Å^2) of $Ba[Li_2(Al_2Si_2)N_6]$, $Ba[(Mg_{0.2}Li_{1.8})(Al_{2.2}Si_{1.8})N_6]$ and $Ba[(Mg_{0.4}Li_{1.6})(Al_{2.4}Si_{1.6})N_6]$[a]

	Atom	U_{11}	U_{22}	U_{33}	U_{12}	U_{13}	U_{23}
$Ba[Li_2(Al_2Si_2)N_6]$	Ba	0.00936(13)	0.00936(13)	0.01235(16)	0	0	0
	Li	0.0129(15)	0.0129(15)	0.015(2)	-0.004(2)	-0.0001(15)	-0.0001(15)
	Al	0.0042(3)	0.0067(3)	0.0048(3)	-0.0005(2)	0.0003(2)	-0.0006(2)
	Si	0.0042(3)	0.0067(3)	0.0048(3)	-0.0005(2)	0.0003(2)	-0.0006(2)
	N1	0.0125(9)	0.0078(8)	0.0119(9)	-0.0011(7)	-0.0025(7)	-0.0007(7)
	N2	0.0134(8)	0.0134(8)	0.0100(12)	0.0019(10)	-0.0002(8)	-0.0002(8)
$Ba[(Mg_{0.2}Li_{1.8})(Al_{2.2}Si_{1.8})N_6]$	Ba	0.01361(16)	0.01361(16)	0.0141(2)	0	0	0
	Mg	0.0103(9)	0.0103(9)	0.0067(14)	0.0001(8)	0.0001(8)	-0.0043(11)
	Li	0.0103(9)	0.0103(9)	0.0067(14)	0.0001(8)	0.0001(8)	-0.0043(11)
	Al	0.0058(3)	0.0094(3)	0.0071(3)	-0.00072(18)	0.00050(16)	-0.00008(18)
	Si	0.0058(3)	0.0094(3)	0.0071(3)	-0.00072(18)	0.00050(16)	-0.00008(18)
	N1	0.0210(8)	0.0104(7)	0.0194(10)	-0.0024(6)	-0.0036(8)	-0.0027(6)
	N2	0.0209(8)	0.0209(8)	0.0131(11)	-0.0001(7)	-0.0001(7)	-0.0006(10)
$Ba[(Mg_{0.4}Li_{1.6})(Al_{2.4}Si_{1.6})N_6]$	Ba	0.01439(18)	0.01439(18)	0.0150(2)	0	0	0
	Mg	0.0213(10)	0.0213(10)	0.017156	0.0008(9)	0.0008(9)	-0.0042(12)
	Li	0.0213(10)	0.0213(10)	0.017156	0.0008(9)	0.0008(9)	-0.0042(12)
	Al	0.0063(3)	0.0094(3)	0.0078(3)	-0.0009(2)	0.00035(19)	-0.0002(2)
	Si	0.0063(3)	0.0094(3)	0.0078(3)	-0.0009(2)	0.00035(19)	-0.0002(2)
	N1	0.0208(9)	0.0108(8)	0.0200(10)	-0.0034(7)	-0.0025(8)	-0.0035(7)
	N2	0.0208(9)	0.0208(9)	0.0137(13)	-0.0013(8)	-0.0013(8)	-0.0001(11)

[a] e.s.d.'s in parentheses

Table S3. Selected bond lengths (Å) of $Ba[Li_2(Al_2Si_2)N_6]$, $Ba[(Mg_{0.2}Li_{1.8})(Al_{2.2}Si_{1.8})N_6]$ and $Ba[(Mg_{0.4}Li_{1.6})(Al_{2.4}Si_{1.6})N_6]$ (*M* = Li; (Li,Mg))[a]

Bond name	**$Ba[Li_2(Al_2Si_2)N_6]$**	**$Ba[(Mg_{0.2}Li_{1.8})(Al_{2.2}Si_{1.8})N_6$**	**$Ba[(Mg_{0.4}Li_{1.6})(Al_{2.4}Si_{1.6})N_6]$**
Ba-N1 (4x)	2.934(18)	2.951(2)	2.959(2)
Ba-N2 (4x)	3.099(9)	3.125(9)	3.136(1)
(Si,Al)-N1	1.789(2)	1.793(19)	1.800(2)
(Si,Al)-N1	1.825(19)	1.837(2)	1.834(2)
(Si,Al)-N1	1.832(2)	1.846(2)	1.845(2)
(Si,Al)-N2	1.751(6)	1.763(6)	1.769(7)
M-N1 (2x)	2.298(2)	2.275(2)	2.272(2)
M-N2 (2x)	2.139(4)	2.184(3)	2.184(3)

[a] e.s.d.'s in parentheses

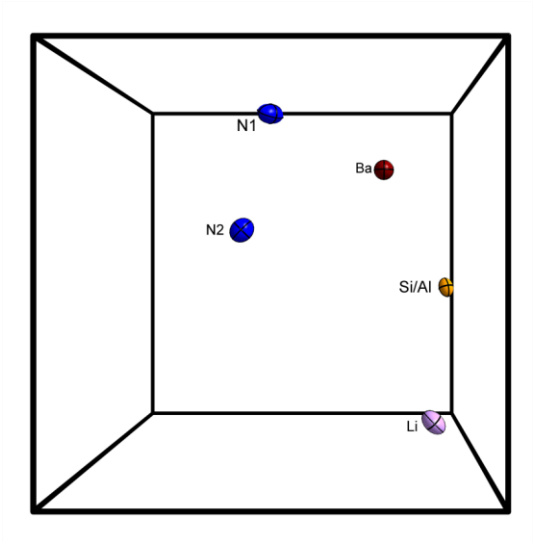

Figure S1. Presentation of the anisotropic refinement of each crystallographic position in $Ba[Li_2(Al_2Si_2)N_6]$; projection along [010]; ellipsoids with 70% probability.

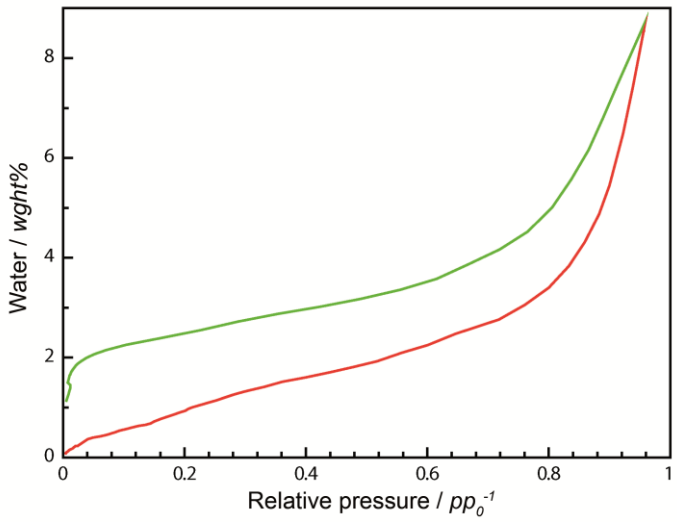

Figure S2. H_2O-sorption isotherm of $Ba[Li_2(Al_2Si_2)N_6]$; red line: adsorption, green line: desorption.

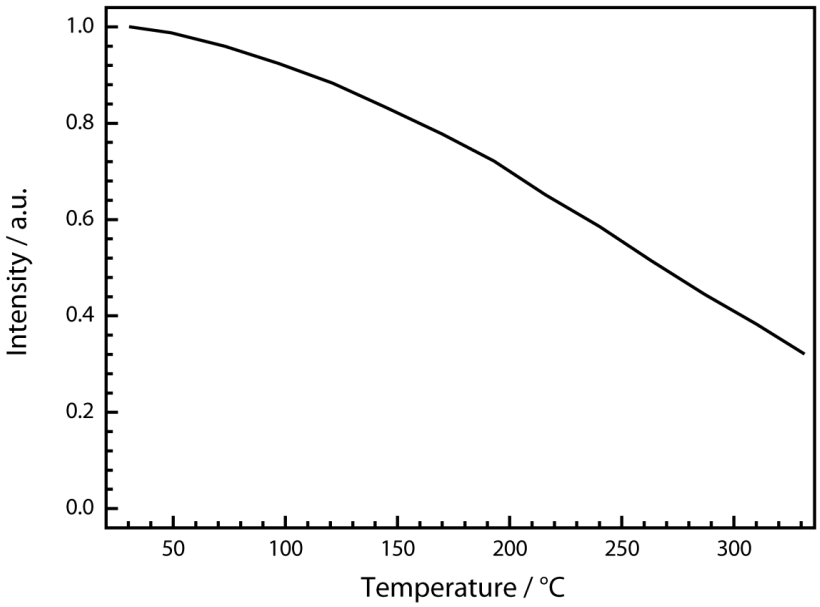

Figure S3. Thermal quenching of $Ba[Li_2(Al_2Si_2)N_6]:Eu^{2+}$ (1 mol% Eu^{2+}, nominal composition) as relative integrated emission intensity ($\lambda_{exc.}$ = 440 nm). At 200 °C the relative emission intensity is still ~70%.

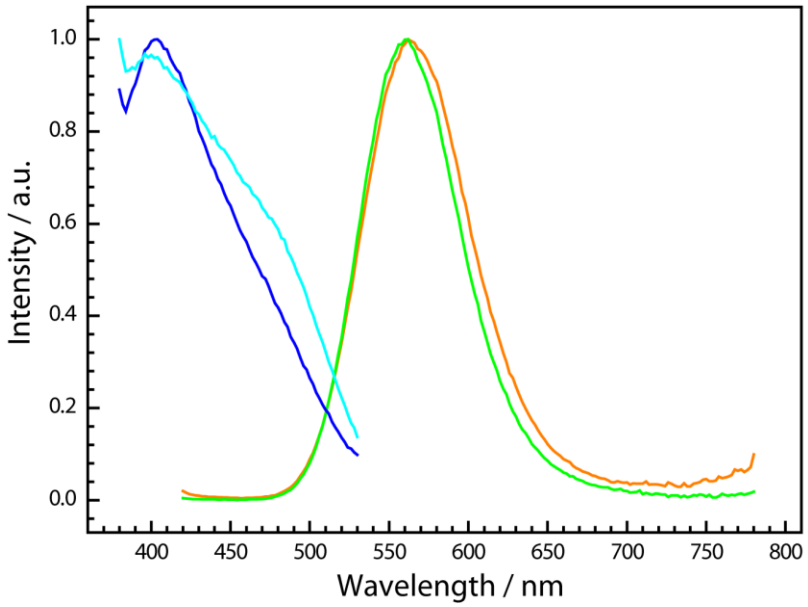

Figure S4. Excitation ($\lambda_{monitor}$ = 550 nm) and emission spectra of Eu^{2+}-doped $Ba[(Mg_{0.2}Li_{1.8})(Al_{2.2}Si_{1.8})N_6]$ (blue and orange curves) and $Ba[(Mg_{0.4}Li_{1.6})(Al_{2.4}Si_{1.6})N_6]$ (cyan and green curves); emission spectra were recorded at 400 nm excitation. Both compounds were doped with 2 mol% Eu^{2+} (nominal composition).

7.2 Supporting Information for Chapter 2.2

Philipp Strobel, Volker Weiler, Cora Hecht, Peter J. Schmidt and Wolfgang Schnick, *Chem. Mater.* **2017**, *29*, 1377–1383.

Table S1. Anisotropic displacement parameters (Å^2) of $Li_2(Ca_{1.88}Sr_{0.12})[Mg_2Si_2N_6]$[a]

Atom	U_{11}	U_{22}	U_{33}	U_{23}	U_{13}	U_{12}
Ca	0.00694(9)	0.01144(11)	0.00776(10)	0.000	0.00204(6)	0.000
Sr	0.00694(9)	0.01144(11)	0.00776(10)	0.000	0.00204(6)	0.000
Si	0.00352(12)	0.00455(13)	0.00407(13)	0.000	0.00003(9)	0.000
Mg	0.00489(16)	0.0066(2)	0.0071(2)	0.000	0.00097(12)	0.000
N1	0.0074(2)	0.0081(3)	0.0091(3)	0.0036(2)	0.0024(2)	0.0024(2)
N2	0.0041(3)	0.0112(4)	0.0052(3)	0.000	0.0006(3)	0.000

[a] e.s.d.s in parentheses

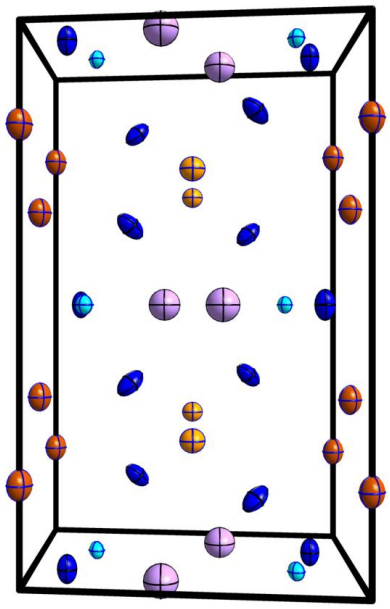

Figure S1. Presentation of the anisotropic refinement of each crystallographic position in $Li_2(Ca_{1.86}Sr_{0.14})[Mg_2Si_2N_6]$; projection along [100]; ellipsoids with 90% probability.

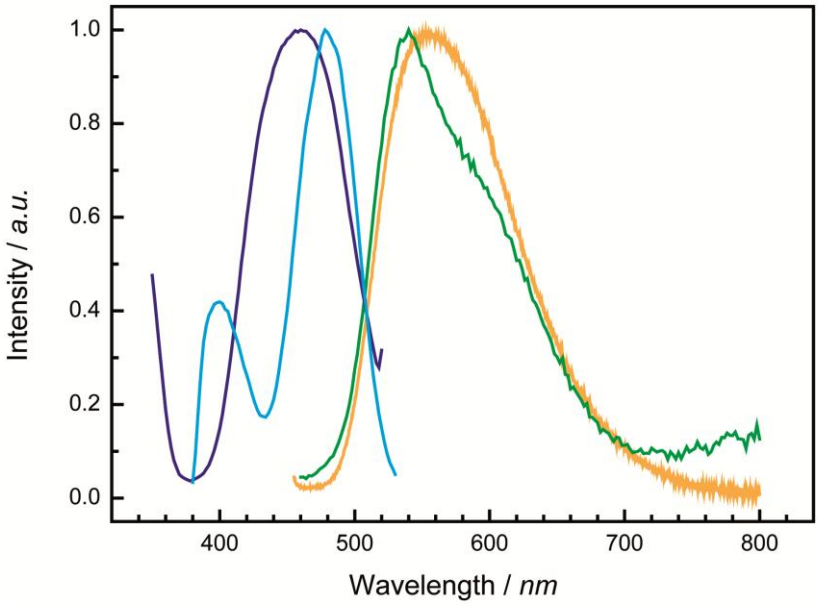

Figure S2. Luminescence spectra of YAG:Ce (excitation: dark blue, emission: orange) and $Li_2Ca_2[Mg_2Si_2N_6]:Ce^{3+}$ (excitation: light blue, emission: green).

7.3 Supporting Information for Chapter 3.3

Thomas M. Tolhurst, Philipp Strobel, Peter J. Schmidt, Wolfgang Schnick and Alexander Moewes, *Chem. Mater*. **2017**, *29*, 7976–7983.

S1: RIXS of undoped sample

As described in the experimental section, RXES measurements were also conducted for SLA* in rapid succession with those for the SLA sample. In Figure 1 their 401.30 eV-excited RIXS spectra are shown. In contrast to the low-energy excitations shown in Figure 1b, the spectra are identical at this higher excitation energy. This highlights that the phenomena leading to energy loss features when exciting further above the CB edge have the same source in both samples, and should be seen as being due to phonons.

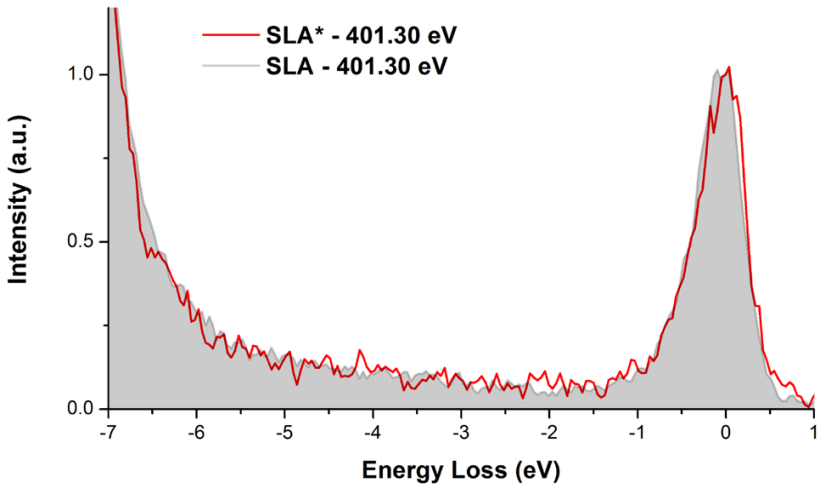

Figure 1. RIXS measurements for SLA and SLA* excited at 401.30 eV. As mentioned in the main text, the loss feature in each spectrum is identical within statistical uncertainty. The loss spectrum of SLA is the same as that shown in Figure 1 of the main text.

S2: Details of TQ fitting

The thermal quenching data in Figure 2a were fit with the standard relationship between the radiative and non-radiative rates given in Equation 1.[1] The two parameters that are varied in the least-squares fit to the data are *A* and *ΔE*. The latter determines at what temperature the TQ starts to become significant, while the former determines how rapidly the decay occurs with further temperature increase. The parameter *A* is simply related to the radiative (Γ_v) and non-radiative (Γ_0) rates by Equation 2.

$$I(T) = I_0/(1-Ae^{-\Delta E/kT}) \qquad \text{Eqn 1}$$

$$A = \Gamma_0/\Gamma_v \qquad \text{Eqn 2}$$

S3: XEOL at the Eu^{2+} $N_{2,3}$ edge

XEOL measurements were also conducted at the Eu $N_{2,3}$-edge for all samples, though not shown in Figure 4 or Supplementary Fig. 2, the same emission peaks appear in each case. There is however, an interesting difference that is seen at the two edges for SLA: the ratio of peak intensities in regions A and B is different. Denoting the emission intensity Λ, one finds at the $M_{4,5}$-edge that $\Lambda_B/\Lambda_A = 0.51 \pm 0.04$, while at the $N_{2,3}$-edge it is found that $\Lambda B/\Lambda A = 0.90 \pm 0.23$. Assuming the source of the peaks is electron-hole recombination in the sequence shown in Figure 4, one expects that $\Lambda_B/\Lambda_A = 1$. The principle difference in the edges as far as the XEOL measurements are concerned is the excitation energy itself and whether other atoms in the material can be excited, as well as the character of states to which the core electron is excited. At the low energy $N_{2,3}$-edge, only Eu has a substantial cross section for absorbing the incident X-rays, leading to a situation like that shown in the figure, where every absorbed X-ray leads to an electron in the CB and a hole in VB. At the $M_{4,5}$-edge, the other elements in the sample have a substantial photoabsorption cross section for the incident X-rays, leading to high energy photoelectrons that could directly excite the Eu 4f electrons into 5d states, as well as create electron-hole pairs.

S4: Discussion of transitions in Figure 3

The inset of Figure 3 shows the possible transitions that may occur in the process of electron-hole recombination in the materials considered in this work. In particular it focuses on explaining the transitions that lead to the emission peaks seen in SLA and SLA*. In the undoped sample the CB to VB transition is seen and is shown as transition s1 in the figure. This should only be seen where defect concentrations are low, as they will typically lead to non-radiative recombination of the electron and hole. Transitions s2 to s5 define a sequence that explains the XEOL emissions seen from SLA. First, an electron from the CB is captured by the Eu^{2+} 5*d* (transition s2). This is a non-radiative transition and leads to a change in the oxidation state of the Eu ion as already described above. At this point the Eu 4f states still contain 7 electrons and therefore should be in the $^8S_{7/2}$ ground state. Transition s3 shows a hole from the VB being promoted to the Eu 4*f* states in the band gap, through emission of a

photon. The emissions from this transition give rise to spectral peak B in Figure 3. The Eu ion is again in the 2+ oxidation state, with one fewer 4*f* electron. As discussed above it should be expected that the Eu has an outer electron configuration of $5d^1 4f^6 (^7F)$. Depending on the state in which the electrons were left in the ^7F manifold after the MLCT, relaxation will occur (s4). The electron and hole finally recombine through the ubiquitous $5d^1 4f^6 \rightarrow 4f^7$ transition, s5, giving rise to the well known emission peaks in region A of the figure. The Eu is left in the 2+ oxidation state and can participate in subsequent recombination events.

S5: XEOL of SMS and SLA compared

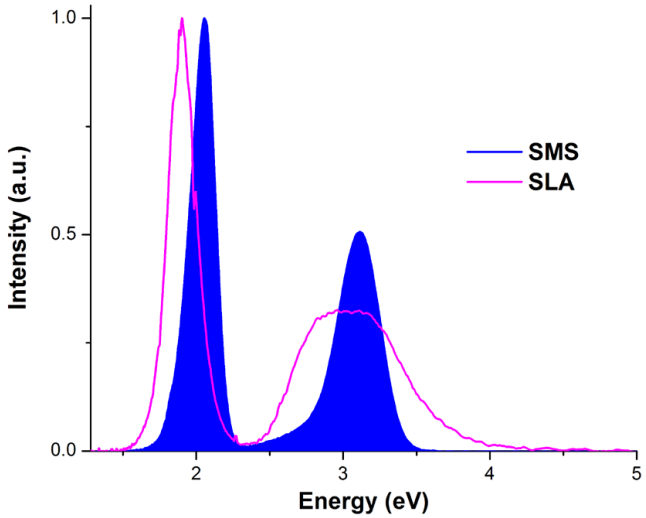

Figure 2. XEOL of SMS (shaded blue curve) and SLA (pink curve).

S6: Predicting energy levels from the RIXS and XEOL data

The band gap of SLA is known to be 4.56 ± 0.20 eV, [10] and the 5*d*–CB separation has been found through the RIXS data to be 0.2 ± 0.1 eV. Subtracting from the difference of these values the $5d^1 4f^6 \rightarrow 4f^7$ emission energy of SLA (650 nm = 1.90 eV) gives the $4f^7$ energy level with respect to the N *p*-states. The $4f^7$–VB separation should be similar for all compounds in this study and can be used, in conjunction with the known $5d^1 4f^6 \rightarrow 4f^7$ emission, and 5d–CB energies of the other samples to predict their band gaps. In this way band gaps of 4.93 ± 0.3 eV and 5.19 ± 0.3 eV are predicted for CLMS and BLSA, respectively. The separation of the $4f^7$ and excited $4f^6$ states is taken to be the same in all samples, due to the atomic nature of the 4*f* states.

References

[1] Dorenbos, P. Thermal quenching of Eu^{2+} 5*d*–4*f* luminescence in inorganic compounds. *J. Phys.: Condens. Matter* **2005**, *17*, 8103-8111.

7.4 Supporting Information for Chapter 4.1

Philipp Strobel, Volker Weiler, Peter J. Schmidt, and Wolfgang Schnick, *Chem. Eur. J.* **2018**, *24*, 7243-7249.

S1: Elemental Analysis of $Sr[BeSi_2N_4]$ and $Eu[BeSi_2N_4]$

Table S1. Elemental Analysis of $Sr[BeSi_2N_4]$ and $Eu[BeSi_2N_4]$ (Stoichiometric ratio)

		Sr	Eu	Be	Si	N
$Sr[BeSi_2N_4]$	EDS	1.0	-	-	1.9	2.4
	ICP	1.0	<0.01	1.4	1.8	-
$Eu[BeSi_2N_4]$	EDS	-	1.0	1.2	0.9	1.9
	ICP	-	0.5	1.2	2.0	-

S2: Additional crystallographic data for $Sr[BeSi_2N_4]$ and $Eu[BeSi_2N_4]$

Table S2. Atomic coordinates and isotropic displacement parameters of $Sr[BeSi_2N_4]$ and $Eu[BeSi_2N_4]$[a]

	Atom (Wyck.)	*x*	*y*	*z*	U_{eq} (A^2)	sof
$Sr[BeSi_2N_4]$	Sr (2*d*)	2/3	1/3	1/4	0.0500	1
	Si (4*f*)	1/3	2/3	0.07014(1)	0.0500	1
	Be (2*a*)	0	0	0	1.08(14)	1
	N1 (6*g*)	1/3	0	0	0.96(5)	1
	N2 (2*c*)	1/3	2/3	1/4	0.96(5)	1
$Eu[BeSi_2N_4]$	Eu (2*d*)	2/3	1/3	1/4	0	1
	Si (4*f*)	1/3	2/3	0.07009(1)	0	1
	Be (2*a*)	0	0	0	0.46(11)	1
	N1 (6*g*)	1/3	0	0	0.40(4)	1
	N2 (2*c*)	1/3	2/3	1/4	0.40(4)	1

[a]The e.s.d. values are given in parentheses.

Table S3. Anisotropic displacement parameters (Å^2) of $Sr[BeSi_2N_4]$ and $Eu[BeSi_2N_4]$[a]

	Atom	U_{11}	U_{22}	U_{33}	U_{12}	U_{13}	U_{23}
$Sr[BeSi_2N_4]$	Sr	0.0141(3)	0.0141(3)	0.0111(4)	0.0071(1)	0	0
	Si	0.0121(4)	0.0121(4)	0.0132(7)	0.0061(2)	0	0
$Eu[BeSi_2N_4]$	Eu	0.0072(1)	0.0072(1)	0.0046(2)	0.0036(5)	0	0
	Si	0.0032(3)	0.0032(3)	0.0026(5)	0.0016(2)	0	0

[a]The e.s.d. values are given in parentheses.

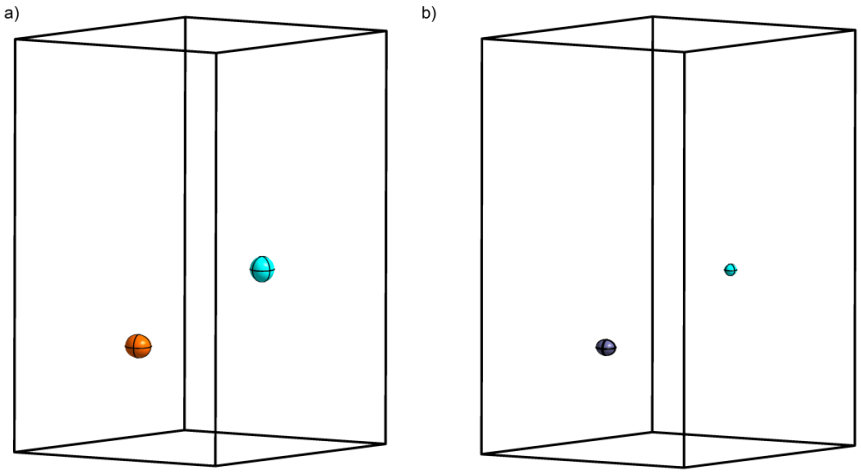

Figure S1: Presentation of the anisotropic refinement of the crystallographic positions of Sr and Si in a) $Sr[BeSi_2N_4]$ and b) $Eu[BeSi_2N_4]$; ellipsoids with 90% probability.

Table S4. Selected bond lengths and angles in $Sr[BeSi_2N_4]$ and $Eu[BeSi_2N_4]$[a]

	$Sr[BeSi_2N_4]$	**$Eu[BeSi_2N_4]$**
Bond name	**Bond length / Å**	
Sr/Eu-N2 (3x)	2.8064(1)	2.8050(1)
Sr/Eu-N1 (6x)	2.8591(1)	2.8573(1)
Si-N2 (1x)	1.6948(9)	1.6941(9)
Si-N1 (3x)	1.7499(4)	1.7488(4)
Be-N1 (3x)	1.6203(1)	1.6195(1)
Angle name	**Angle / °**	
N2-Sr/Eu-N2	120	
N1-Sr/Eu-N1	110.958(1)	110.95(1)
N1-Si-N1	106.622(1)	106.64(3)
N1-Si-N2	112.19(3)	112.17(3)
Si-N2-Si	180	

[a] e.s.d.'s in parentheses

S3: MAPLE calculations

Table S5. Results of MAPLE calculations [kJ/mol] for $Sr[BeSi_2N_4]$; Δ = MAPLE sum of constituting binary/ternary nitrides / MAPLE sum compound.

	$Sr[BeSi_2N_4]$
Sr^{2+}	1674
Be^{2+}	3261
Si^{4+}	9912
N^{3-}	5488- 5626
Total	47140
Δ	1.3 - 1.8%
Total MAPLE: $BeSiN_2$ + $SrSiN_2$ = 46326 kJ/mol; $SrSiN_2$ + 1/3 Be_3N_2 + 1/3 Si_3N_4 = 46535 kJ/mol	

The deviation Δ >1% can be explained by the change of coordination of Be. While Be is in trigonal planar coordination in $Sr[BeSi_2N_4]$, it is tetrahedrally coordinated in Be_3N_2 and $BeSiN_2$, leading to an increased deviation.

This can be seen when applying the MAPLE concept for $SrBe_3O_4$: The partial MAPLE value for the trigonal planarly coordinated Be yields decreased values (2880 kJ/mol), when compared to tetrahedrally coordinated (O^{2-} ligands) Be (2980 kJ/mol).

S4: Additional Luminescence data

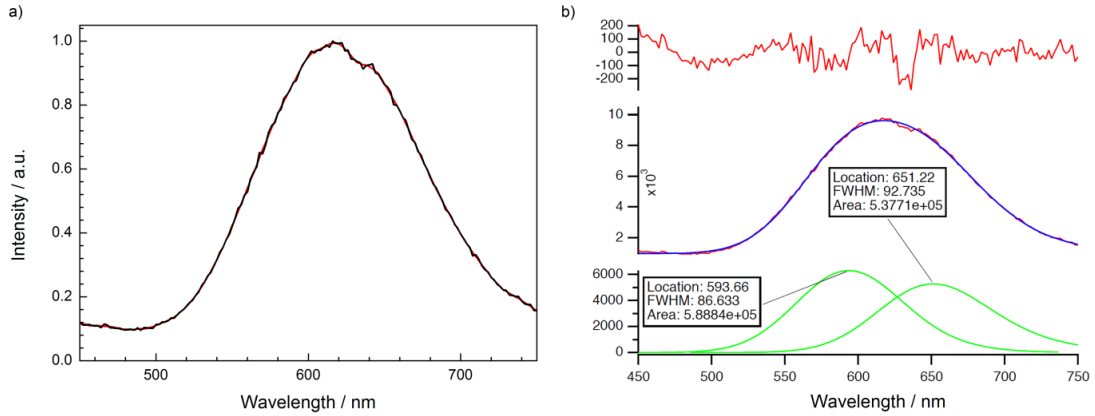

Figure S2: a) Emission spectrum of $SrBeSi_2N_4:Eu^{2+}$ (black: corrected data, red: smoothed curve); b) Deconvolution of the emission spectrum of $SrBeSi_2N_4:Eu^{2+}$ (1. red: difference plot, 2. red: corrected data, blue: fit, 3. green: deconvolution with two functions consisting of a Gaussian and an exponential part)

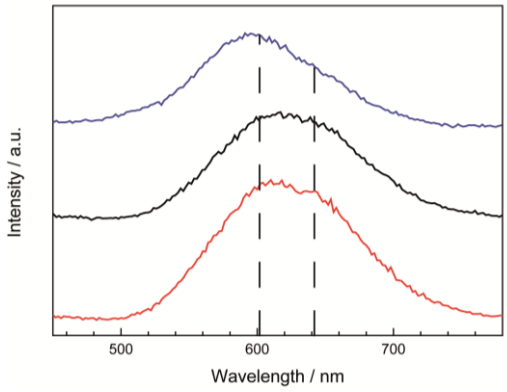

Figure S3: Emission spectra of three $SrBeSi_2N_4:Eu^{2+}$ crystal agglomerates. The ratio of two emission peaks (black dashed lines) varies in each sample.

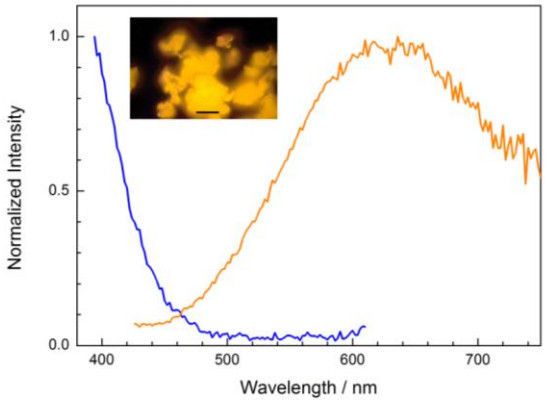

Figure S4: Luminescence spectra and photograph of $Sr[BeSi_2N_4]:Ce^{3+}$ (exc.: dark blue line, em.: orange line; scale bar 20 µm).

7.5 Supporting Information for Chapter 4.2

Philipp Strobel, Volker Weiler, Peter J. Schmidt, and Wolfgang Schnick, *Chem. Mater.* **2018**, *30*, 3122-3130.

Table S1. EDS results (atom%) via Point and ID on a $Sr[Be_6ON_4]$ single crystal with platelet-like morphology (Main Figure 1)

Scan #	Sr	N	O
1	19.39	60.98	19.63
2	19.38	61.51	19.1
3	19.41	60.74	19.85
4	19.13	61.4	19.47
5	18.86	61.02	20.12
6	19.31	61.07	19.63
Average	19.25	61.12	19.63
Ratio	1	3.2	1.0

Table S2. Anisotropic displacement parameters ($Å^2$) of $Sr[Be_6ON_4]$[a]

Atom	U_{11}	U_{22}	U_{33}	U_{12}	U_{13}	U_{23}
Sr	0.00998(7)	0.00950(6)	0.00843(6)	0	0.00106(8)	0
Be1	0.0068(5)	0.0081(5)	0.0091(5)	-0.0005(8)	-0.0002(7)	0.0003(4)
Be2	0.0098(7)	0.0067(6)	0.0073(6)	0.0000(5)	-0.0004(6)	-0.0008(5)
Be3	0.0072(6)	0.0083(6)	0.0070(6)	-0.0001(5)	0.0004(5)	0.0008(5)
O1	0.0061(4)	0.0119(4)	0.0089(4)	0	0.0005(6)	0
N1	0.0069(4)	0.0058(3)	0.0058(4)	-0.0005(3)	0.0001(3)	-0.0003(3)
N2	0.0071(4)	0.0058(4)	0.0059(3)	-0.0003(3)	0.0009(3)	0.0003(3)

[a] e.s.d.'s in parentheses

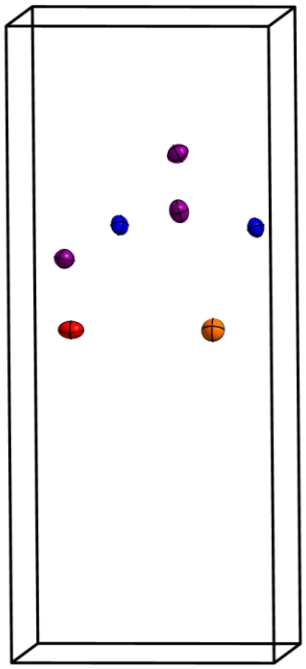

Figure S1: Presentation of the anisotropic refinement of the crystallographic positions in $Sr[Be_6ON_4]$; ellipsoids with 90% probability.

Table S3. Selected bond lengths and angles in $Sr[Be_6ON_4]$[a]

Bond name	**Bond length / Å**
Sr-O1 (2x)	2.6136(5)
Sr-O1 (1x)	2.6423(14)
Sr-N1 (2x)	2.7105(11)
Sr-N2 (2x)	2.9548(13)
Be1-O1 (1x)	1.5621(16)
Be1-N1 (1x)	1.783(3)
Be1-N2 (1x)	1.697(2)
Be1-N2 (1x)	1.866(2)
Be2-N1 (1x)	1.777(2)
Be2-N1 (1x)	1.913(2)
Be2-N2 (1x)	1.656(2)
Be2-N2 (1x)	1.741(2)
Be3-N1 (1x)	1.723(2)
Be3-N1 (1x)	1.761(2)
Be3-N2 (1x)	1.776(2)
Be3-N2 (1x)	1.718(2)
Angle names	**Angle / °**
O1-Sr-O1	72.70(3)
O1-Sr-N1	63.98(3)
O1-Be1-N2	114.36(12)
O1-Be1-N1	114.88(14)
N2-Be1-N1	101.37(12)
N2-Be2-N2	119.54(13)
N2-Be2-N1	122.36(12)
N2-Be2-N1	103.91(11)
N2-Be3-N1	123.15(13)
N2-Be3-N1	104.94(11)
N1-Be3-N1	107.65(11)

[a] e.s.d.'s in parentheses

Results of MAPLE calculations [kJ/mol] for $Sr[Be_6ON_4]$; Δ = MAPLE sum of constituting binary nitrides / MAPLE sum compound.

Table S4. MAPLE calculations of $Sr[Be_6ON_4]$

	$Sr[Be_6ON_4]$
Sr^{2+}	1602
Be^{2+}	2834-2858
O^{2-}	2537
N^{3-}	5533- 5536
Total	43371
Δ	0.33%
Total MAPLE: $SrO + 2\ Be_3N_2$ = 43515 kJ/mol	

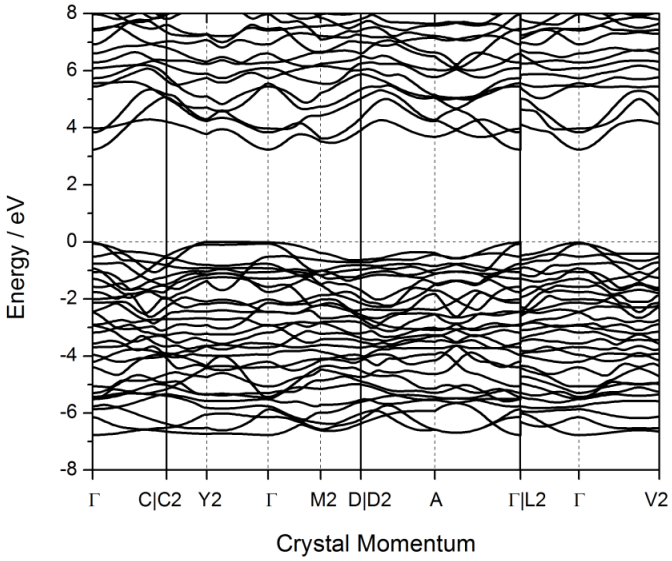

Figure S2: Band structure of $SrBe_6ON_4$ calculated using the PBEsol functional. The horizontal axis of the band structure corresponds to a path through high symmetry points in the Brillouin zone.[1]

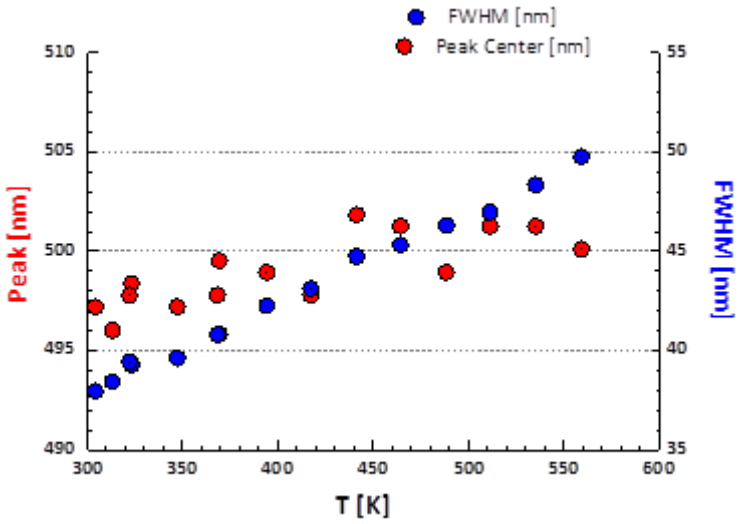

Figure S3: Temperature dependence of peak position and *fwhm* of $Sr[Be_6ON_4]:Eu^{2+}$ luminescence.

References

[1] Hinuma, Y.; Pizzi, G.; Kumagai, Y.; Oba, F.; Tanaka, I. Band structure diagram paths based on crystallography. *Comput. Mater. Sci.* **2017**, *128*, 140-184.

7.6 Supporting Information for Chapter 4.3

Philipp Strobel, Volker Weiler, Peter J. Schmidt, and Wolfgang Schnick, *Chem. Eur. J.* **2018**, https://doi.org/10.1002/chem.201801951.

Detailed crystallographic data for α-$SrBeO_2$

Table S1. Crystal data for α-$SrBeO_2$ [a]

Formula mass [g mol^{-1}]	128.63	
Crystal system / space group	Monoclinic, $P2_1/m$ (no. 11)	
Lattice parameters [Å, °]	a = 3.5824(3)	a = 3.5578(6)
	b = 5.1732(5)	b = 5.1651(9)
	c = 5.5515(5)	c = 5.5408(10)
	β = 98.262(4)	β = 98.640(7)
Cell volume [Å^3]	101.815(16)	100.66(3)
Formula units per cell Z	2	
X-ray density [g cm^{-1}]	4.196	4.244
Linear absorption coefficient [cm^{-1}]	26.065	26.363
F(000)	116	
Crystal dimensions (mm^3)	0.03 × 0.02 × 0.01	
Diffractometer	D8 Venture	
Radiation	Mo-Kα (λ = 0.71073 Å)	
Temperature [K]	**293(2)**	**100(2)**
Abs correction	multi-scan	
θ range [°]	3.71-30.0	3.72-26.73
Measured reflns	1476	1507
Independent reflns	326 [R_{int} = 0.0240]	323 [R_{int} = 0.0212]
Observed reflns	317	311
Min./max. transmission	0.645/1.000	
Refined params	25	
GOF	1.133	1.175
R indices ($F_o^2 \geq 2\sigma(F_o^2)$)	R_1 = 0.0145, wR_2 = 0.0365	R_1 = 0.0155, wR_2 = 0.0372
R indices (all data)	R_1 = 0.0150, wR_2 = 0.0367	R_1 = 0.0166, wR_2 = 0.0375
min./max. residual electron density (eÅ^{-3})	-0.638/0.742	-0.683/0.837

[a] e.s.d.s in parentheses.

Table S2. Atomic coordinates, equivalent isotropic displacement parameters and site occupancy factors (sof) of α-$SrBeO_2$, determined at room temperature [a]

Atom (*Wyck.*)	***x***	***y***	***z***	U_{eq}. (Å^3)	***sof***
Sr1 (2*e*)	0.35036(6)	3/4	0.19588(4)	0.01022(11)	1
Be1 (2*e*)	0.0532(11)	1/4	0.3563(7)	0.0124(6)	1
O1 (2*e*)	0.2294(6)	1/4	0.1212(4)	0.0115(4)	1
O2 (2*c*)	0	0	1/2	0.0175(4)	1

[a] e.s.d.s in parentheses.

Table S3. Atomic coordinates, equivalent isotropic displacement parameters and site occupancy factors (sof) of α-$SrBeO_2$, determined at 100 K [a]

Atom (*Wyck.*)	***x***	***y***	***z***	U_{eq}. (Å^3)	***sof***
Sr1 (2*e*)	0.35307(8)	3/4	0.19752(5)	0.00527(11)	1
Be1 (2*e*)	0.0524(13)	1/4	0.3555(8)	0.0079(7)	1
O1 (2*e*)	0.2310(7)	1/4	0.1211(4)	0.0072(4)	1
O2 (2*c*)	0	0	1/2	0.0091(4)	1

[a] e.s.d.s in parentheses.

Table S4. Anisotropic displacement parameters (Å^2) of α-$SrBeO_2$, determined at room temperature [a]

Atom	U_{11}	U_{22}	U_{33}	U_{12}	U_{13}	U_{23}
Sr1	0.01228(15)	0.00877(14)	0.00999(15)	0.000	0.00287(9)	0.000
Be1	0.0186(17)	0.0070(13)	0.0111(15)	0.000	0.0009(14)	0.000
O1	0.0138(9)	0.0094(8)	0.0119(9)	0.000	0.0036(8)	0.000
O2	0.0285(11)	0.0099(8)	0.0163(9)	0.0036(8)	0.0109(9)	0.0040(8)

[a]e.s.d.s in parentheses.

Table S5. Anisotropic displacement parameters (Å^2) of α-$SrBeO_2$, determined at 100 K [a]

Atom	U_{11}	U_{22}	U_{33}	U_{12}	U_{13}	U_{23}
Sr1	0.00589(15)	0.00467(14)	0.00548(15)	0.000	0.00159(9)	0.000
Be1	0.0115(18)	0.0033(15)	0.0085(17)	0.000	-0.0002(15)	0.000
O1	0.0078(10)	0.0058(9)	0.0080(10)	0.000	0.0009(9)	0.000
O2	0.0135(10)	0.0052(9)	0.0090(10)	0.0008(8)	0.0035(8)	0.0017(9)

[a]e.s.d.s in parentheses.

Table S6. Selected bond lengths and angles in α-$SrBeO_2$ [a]

Bond name	Bond length / Å room temperature	Bond length / Å 100 K
Sr-O1 (1x)	2.475(2)	2.468(2)
Sr-O1 (1x)	2.522(2)	2.516(2)
Sr-O1 (2x)	2.6455(5)	2.6424(7)
Sr-O2 (2x)	2.5899(3)	2.5859(4)
Sr-O2 (2x)	2.9682(3)	2.9351(4)
Be1-O1 (1x)	1.529(4)	1.529(5)
Be1-O2 (2x)	1.546(2)	1.545(3)
Angle names	**Angle / °**	
O1-Sr-O1	91.58(7)	91.07(8)
O1-Sr-O1	89.50(4)	89.27(5)
O1-Sr-O2	91.57(4)	91.40(5)
O2-Sr-O2	79.946(8)	79.970(13)
O1-Be1-O2 (2x)	122.49(14)	122.55(15)
O2-Be1-O2	113.6(3)	113.3(3)

[a]e.s.d.s in parentheses.

Detailed crystallographic data for β-$SrBeO_2$

Table S7. Crystal data for β-$SrBeO_2$ [a]

Formula mass [g mol^{-1}]	128.63
Crystal system / space group	Monoclinic, $P2_1/c$ (no. 14)
Lattice parameters [Å]	a = 7.0045(9)
	b = 5.0697(11)
	c = 5.3127(7)
	β = 98.935(6)
Cell volume [Å^3]	186.37(5)
Formula units per cell Z	4
X-ray density [g cm^{-1}]	4.584
Linear absorption coefficient [cm^{-1}]	28.479
F(000)	232
Crystal dimensions (mm^3)	0.02 × 0.015 × 0.01
Diffractometer	D8 Venture
Radiation	Mo-Kα (λ = 0.71073 Å)
Temperature [K]	293(2)
Abs correction	multi-scan
θ range [°]	2.944-29.940
Measured reflns	2746
Independent reflns	496 [R_{int} = 0.0315]
Observed reflns	539
Min./max. transmission	0.878/1.000
Refined params	22
GOF	1.245
R indices ($F_o^2 \geq 2\sigma(F_o^2)$)	R_1 = 0.0193, wR_2 = 0.0503
R indices (all data)	R_1 = 0.0218, wR_2 = 0.0508
min./max. residual electron density (eÅ^{-3})	-0.685/1.144

[a]e.s.d.s in parentheses.

Table S8. Atomic coordinates, equivalent isotropic displacement parameters and site occupancy factors (sof) of β-$SrBeO_2$ [a]

Atom (*Wyck.*)	***x***	***y***	***z***	U_{eq}. (Å^3)	***sof***
Sr1 (4*e*)	0.30784(4)	0.52102(6)	0.20210(6)	0.00684(12)	1
Be1 (4*e*)	0.0966(7)	0.0725(9)	0.1677(8)	0.0090(8)	1
O1 (4*e*)	0.0305(4)	0.2968(5)	0.3727(5)	0.0088(5)	1
O2 (4*e*)	0.3286(3)	0.0155(4)	0.2236(4)	0.0073(4)	1

[a]e.s.d.s in parentheses.

Table S9. Anisotropic displacement parameters (Å^2) of β-$SrBeO_2$ [a]

Atom	U_{11}	U_{22}	U_{33}	U_{12}	U_{13}	U_{23}
Sr1	0.00654(16)	0.00713(16)	0.00714(17)	0.00012(11)	0.00200(10)	-0.00039(11)

[a] e.s.d.'s in parentheses

Table S10. Selected bond lengths and angles in β-$SrBeO_2$ [a]

Bond name	**Bond length / Å**
Sr-O2 (1x)	2.513(2)
Sr-O2 (1x)	2.516(2)
Sr-O1 (1x)	2.536(3)
Sr-O2 (1x)	2.568(2)
Sr-O2 (1x)	2.575(2)
Sr-O1 (1x)	2.727(3)
Sr-O2 (1x)	2.758(2)
Sr-O1 (1x)	2.894(3)
Be1-O2 (1x)	1.632(5)
Be1-O1 (1x)	1.653(5)
Be1-O1 (1x)	1.688(5)
Be1-O1 (1x)	1.699(5)
Angle names	**Angle / °**
O1-Sr-O1	65.50(4)
O1-Sr-O1	73.19(8)
O1-Sr-O2	118.95(8)
O2-Sr-O2	172.31(11)
O1-Be1-O2	112.0(3)
O1-Be1-O2	11.5(3)
O1-Be1-O1	117.2(3)
O1-Be1-O2	111.0(3)

[a]e.s.d.s in parentheses.

Detailed crystallographic data for $Sr_{12}Be_{17}O_{29}$

Table S11. Crystal data for $Sr_{12}Be_{17}O_{29}$ [a]

Formula mass [g mol^{-1}]	1668.61
Crystal system / space group	Tetragonal, $I\bar{4}2m$ (no. 121)
Lattice parameters [Å]	a = 11.0104(4)
	c = 10.6208(10)
Cell volume [$Å^3$]	1287.55(15)
Formula units per cell Z	2
X-ray density [g cm^{-1}]	4.304
Linear absorption coefficient [cm^{-1}]	24.761
F(000)	1512
Crystal dimensions (mm^3)	0.03 × 0.02 × 0.01
Diffractometer	D8 Venture
Radiation	Mo-Kα (λ = 0.71073 Å)
Temperature [K]	293(2)
Abs correction	multi-scan
θ range [°]	3.701-32.499
Measured reflns	8283
Independent reflns	1184 [R_{int} = 0.0940]
Observed reflns	1236
Min./max. transmission	0.796/1.000
Refined params	46
GOF	1.103
R indices ($F_o^2 \geq 2\sigma(F_o^2)$)	R_1 = 0.0449, wR_2 = 0.0737
R indices (all data)	R_1 = 0.0473, wR_2 = 0.0747
min./max. residual electron density ($eÅ^{-3}$)	-2.685/2.041

[a]e.s.d.s in parentheses.

Table S12. Atomic coordinates, equivalent isotropic displacement parameters and site occupancy factors (sof) of $Sr_{12}Be_{17}O_{29}$ [a]

Atom (*Wyck.*)	*x*	*y*	*z*	$U_{eq.}$ (Å^3)	*sof*
Sr1 (16*j*)	0.88040(4)	0.62343(4)	0.62592(6)	0.00680(13)	1
Sr2 (8*i*)	0.64644(5)	0.64644(5)	0.86688(9)	0.00662(15)	1
Be1 (16*j*)	0.8882(6)	0.7486(6)	0.8762(7)	0.0062(11)	1
Be2 (8*i*)	0.8917(7)	0.8917(7)	0.7351(10)	0.0060(16)	1
Be3 (8*i*)	0.5889(6)	0.5889(6)	0.5866(9)	0.0040(17)	1
Be4 (2*b*)	0	0	1/2	0.008(4)	1
O1 (16*j*)	0.8923(4)	0.6057(4)	0.8875(4)	0.0076(6)	1
O2 (16*j*)	0.6774(4)	0.5051(4)	0.6813(4)	0.0058(7)	1
O3 (8*i*)	0.9136(4)	0.9136(4)	0.5893(6)	0.0083(11)	1
O4 (8*i*)	0.8210(4)	0.8210(4)	0.9974(6)	0.0057(10)	1
O5 (8*i*)	0.7884(4)	0.7884(4)	0.7636(6)	0.0060(10)	1
O6 (2*a*)	0	0	0	0.006(2)	1

[a]e.s.d.s in parentheses.

Table S13. Anisotropic displacement parameters (Å^2) of $Sr_{12}Be_{17}O_{29}$[a]

Atom	U_{11}	U_{22}	U_{33}	U_{12}	U_{13}	U_{23}
Sr1	0.0068(2)	0.0071(3)	0.0064(2)	-0.0001(2)	0.0001(2)	0.00031(12)
Sr2	0.00668(18)	0.00668(18)	0.0065(3)	-0.0003(2)	-0.0003(2)	-0.0002(2)

[a]e.s.d.s in parentheses.

Table S14. Selected bond lengths and angles in $Sr_{12}Be_{17}O_{29}$[a]

Bond name	Bond length / Å
Sr-O1 (1x)	2.491(5)
Sr-O5 (1x)	2.542(4)
Sr-O1 (1x)	2.543(4)
Sr-O1 (1x)	2.553(5)
Sr-O2 (1x)	2.653(4)
Sr-O3 (1x)	2.675(4)
Sr-O1 (1x)	2.788(4)
Be1-O1 (1x)	1.579(9)
Be1-O2 (1x)	1.641(8)
Be1-O5 (1x)	1.682(9)
Be1-O4 (1x)	1.685(9)
Be2-O2 (2x)	1.710(7)
Be2-O3 (1x)	1.585(12)
Be4-O3 (4x)	1.646(6)
Angle names	**Angle / °**
O1-Sr-O5	118.64(16)
O1-Sr-O1	83.02(15)
O1-Sr-O1	82.40(13)
O2-Sr-O4	61.79(16)
O1-Be1-O2	120.0(5)
O1-Be1-O5	109.4(5)

[a]e.s.d.s in parentheses.

Rietveld refinement of α- and β-$SrBeO_2$

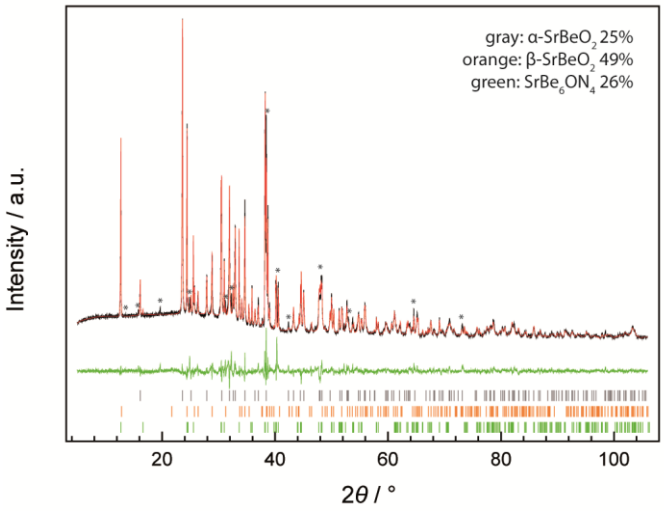

Figure S1. Rietveld refinement of α- and β-$SrBeO_2$ next to $SrBe_6ON_4$ (Cu-Kα_1 radiation).[1] Unidentified reflections are marked with asterisks.

Rietveld refinement of $Sr_{12}Be_{17}O_{29}$

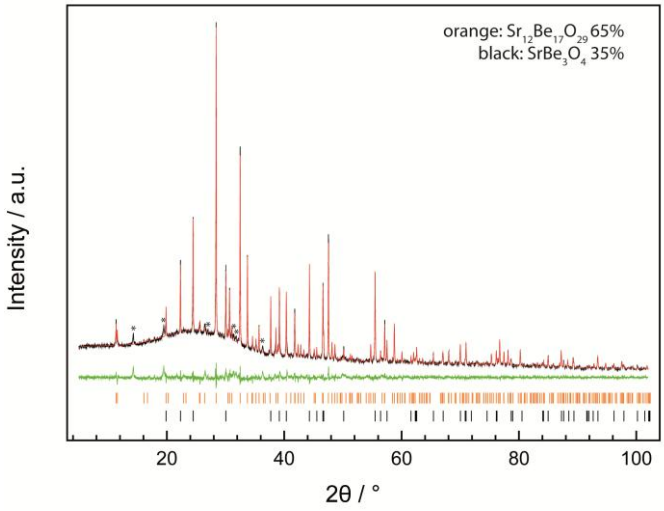

Figure S2. Rietveld refinement of $Sr_{12}Be_{17}O_{29}$ next to $SrBe_3O_4$ (Cu-Kα_1 radiation).[2] Unidentified reflections are marked with asterisks.

Details on SEM and EDS

Table S15. Averaged EDS results (atom%) of α- and β-$SrBeO_2$:Eu^{2+} as well as $Sr_{12}Be_{17}O_{29}$:Eu^{2+} single crystals

	Sr	O	Eu
α -$SrBeO_2$:Eu^{2+}	1	2.5	0.01
β-$SrBeO_2$:Eu^{2+}	1	2.3	-
$Sr_{12}Be_{17}O_{29}$:Eu^{2+}	1	2.5	-

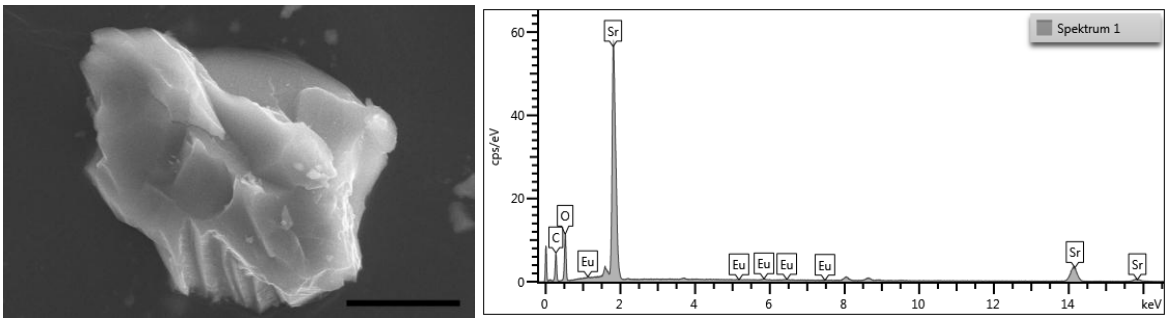

Figure S6. Left: Scanning electron micrograph of a α-$SrBeO_2$ crystal (scale bar 10 µm). Right: Exemplary EDS spectrum of α-$SrBeO_2$.

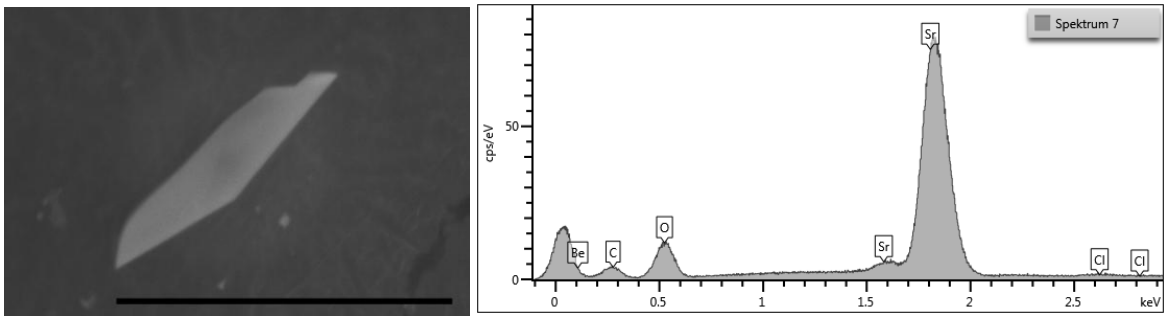

Figure S7. Left: Scanning electron micrograph of a β-$SrBeO_2$ crystal (scale bar 10 µm). Right: Exemplary EDS spectrum of β-$SrBeO_2$.

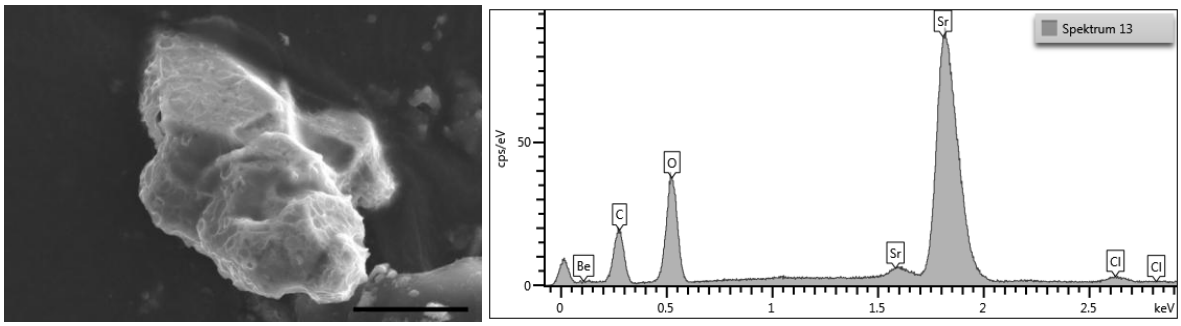

Figure S8. Left: Scanning electron micrograph of a $Sr_{12}Be_{17}O_{29}$ crystal (scale bar 10 µm). Right: Exemplary EDS spectrum of $Sr_{12}Be_{17}O_{29}$.

MAPLE calculations

Results of MAPLE calculations [kJ/mol] for α-$SrBeO_2$, β-$SrBeO_2$ and $Sr_{12}Be_{17}O_{29}$; Δ = MAPLE sum of constituting binary or ternary oxides / MAPLE sum compound.[2-4]

Table S16. MAPLE calculations of α-$SrBeO_2$

	α-$SrBeO_2$
Sr^{2+}	1816
Be^{2+}	2947
O^{2-}	2157-2454
Total	9387
Δ	[1] 1.55%, [2] 0.08%
Total MAPLE:	[1] SrO + BeO = 9535 kJ/mol
	[2] ($SrBe_3O_4$ + 3SrO + BeO)/4 = 9395 kJ/mol

Table S17. MAPLE calculations of β-$SrBeO_2$

	β-$SrBeO_2$
Sr^{2+}	1831
Be^{2+}	2863
O^{2-}	2132-2449
Total	9284
Δ	[1] 2.63%, [2] 1.17%, [3] 0.02%
Total MAPLE:	[1] SrO + BeO = 9535 kJ/mol
	[2] ($SrBe_3O_4$ + 3SrO + BeO)/4 = 9395 kJ/mol
	[3] ($Sr_{12}Be_{17}O_{29}$ + 5SrO)/17 = 9286 kJ/mol

Table S18. MAPLE calculations of $Sr_{12}Be_{17}O_{29}$

	$Sr_{12}Be_{17}O_{29}$
Sr^{2+}	1785-1864
Be^{2+}	2759-2884
O^{2-}	2119-2671
Total	139055
Δ	[1] 0.95%, [2] 0.03%
Total MAPLE:	[1] 12SrO + 17BeO = 143276 kJ/mol
	[2] 17β-$SrBeO_2$ − 5SrO = 139018 kJ/mol

DFT calculations

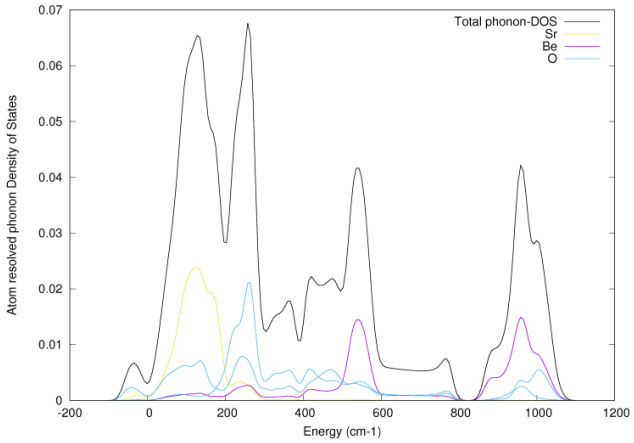

Figure S9. Total and partial phonon Density of States for α-$SrBeO_2$. Imaginary modes below 0 indicate structural instability.

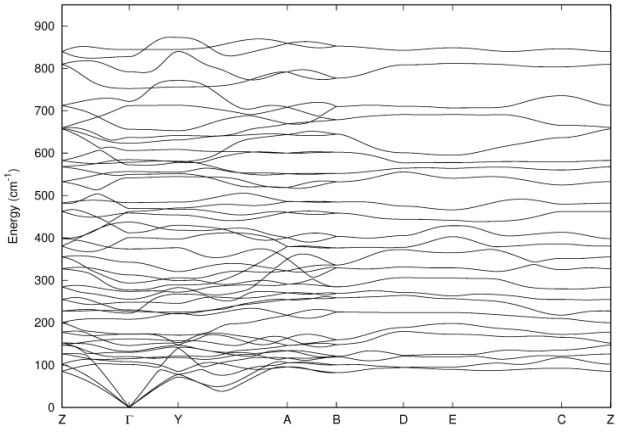

Figure S10. Phonon dispersion for β-$SrBeO_2$ along high symmetry directions in the first Brillouin zone.

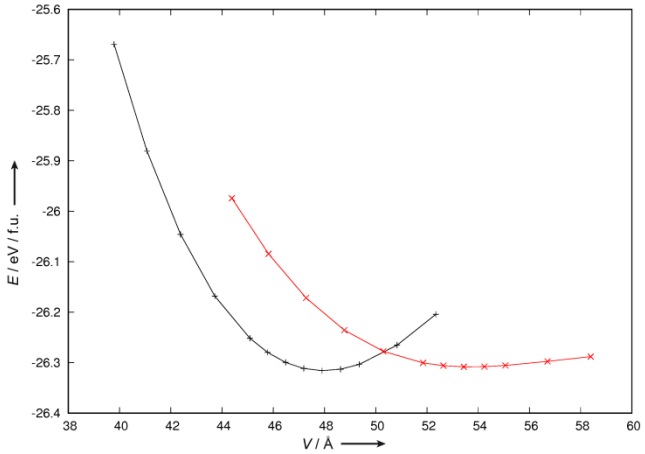

Figure S11. E–V diagram for α-$SrBeO_2$ (red line) and β-$SrBeO_2$ (black line).

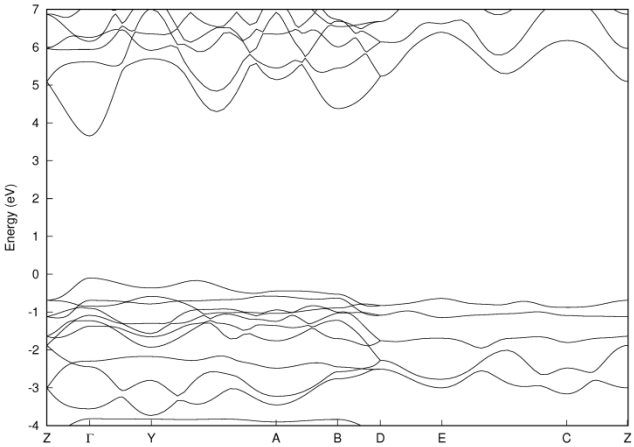

Figure S12. Band structure of α-$SrBeO_2$ along high symmetry directions in the first Brillouin zone.

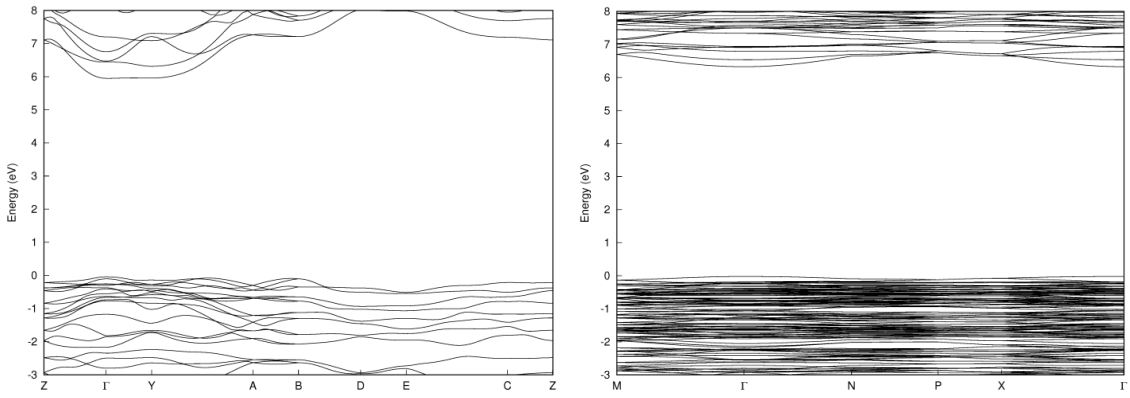

Figure S13. MBJ-corrected band structure of β-$SrBeO_2$ (left) and b) $Sr_{12}Be_{17}O_{29}$ (right) along high symmetry directions in the first Brillouin zone.

Additional luminescence data of $Sr_{12}Be_{17}O_{29}:Eu^{2+}$ and β-$SrBeO_2:Eu^{2+}$

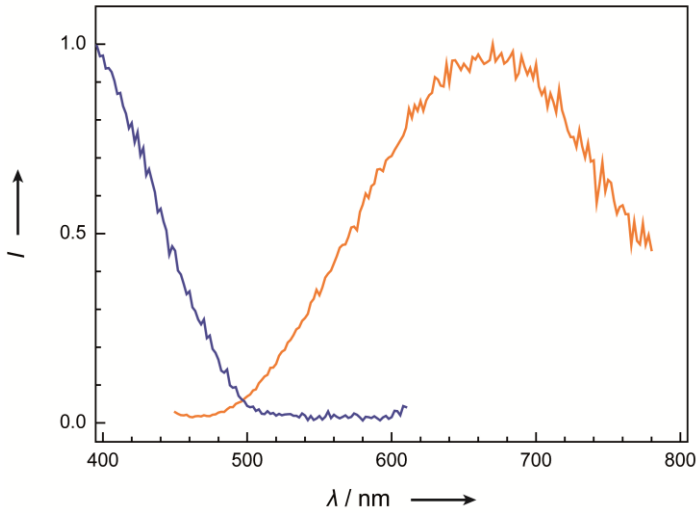

Figure S14. Excitation (blue, $\lambda_{monitor}$= 630 nm) and emission (black, λ_{exc}= 400 nm) spectra of $Sr_{12}Be_{17}O_{29}:Eu^{2+}$.

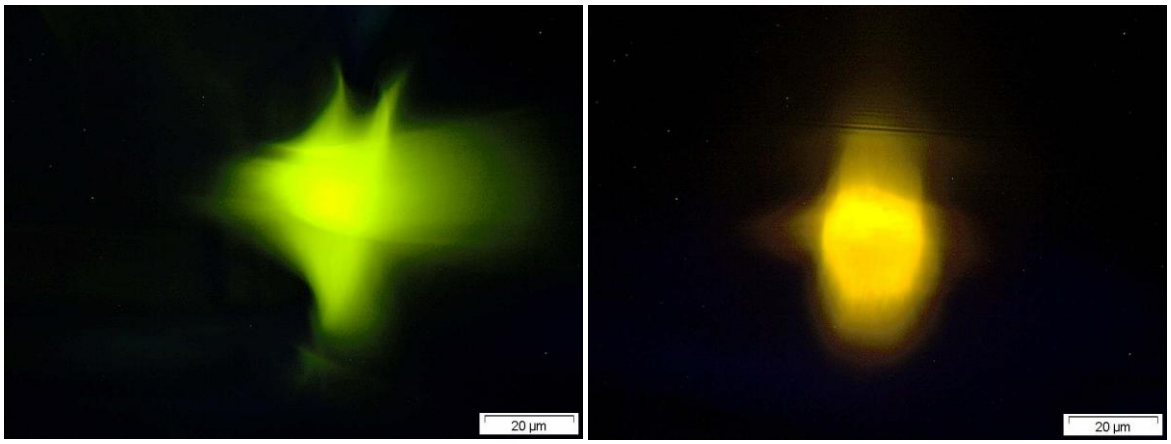

Figure S15. Luminescent crystals of β-$SrBeO_2:Eu^{2+}$ (left) and $Sr_{12}Be_{17}O_{29}:Eu^{2+}$ (right).

References

[1] Strobel, P.; de Boer, T.; Weiler, V.; Schmidt, P. J.; Moewes, A.; Schnick, W. Luminescence of an Oxonitridoberyllate: A Study of Narrow-Band Cyan Emitting $Sr[Be_6ON_4]:Eu^{2+}$. *Chem. Mater.* **2018**, *30*, 3122-3130.

[2] Harris, L. A.; Yakel, H. L. The crystal structure of $SrBe_3O_4$. *Acta Crystallogr. Sect. B* **1969**, *25*, 1647-1651.

[3] Bashir, J.; Khan, R. T. A.; Butt, N. M.; Heger, G. Thermal atomic displacement parameters of SrO. *Powder Diffr.* **2012**, *17*, 222-224.

[4] Zachariasen, W. Über die Kristallstruktur von BeO. *Norsk. Geol. Tidssk* **1925**, *8*, 189-200.

7.7 Supporting Information for Chapter 4.4

Philipp Strobel, Volker Weiler, Peter J. Schmidt, and Wolfgang Schnick, *Angew. Chem. Int. Ed.* **2018**, https://doi.org/10.1002/anie.201804721.

Synthesis

Single crystals of $AELi_2[Be_4O_6]:Eu^{2+}$ (*AE* = Sr,Ba) (1mol% Eu nominal composition) were obtained by a solid-state reaction in Ta-ampules. 1 mmole of $AECO_3$ ($SrCO_3$: Merck, 99%, 147.6 mg,; $BaCO_3$: Philips, 197.3 mg), 1.33 mmole Be_3N_2 (73.2 mg, synthesized from Be (ABCR, 99+%, 325. mesh) in a radio-frequency (rf) furnace under N_2-atmosphere at 1300 °C), 2 mmole Li_2O (Schuchardt, 98%, 59.8 mg). The reaction mixture was filled in Ta ampules and heated in 3 h to 950 °C in evacuated silica ampules. The temperature was kept for 24 h and then cooled down to 500 °C in 3 h.

Powder samples of $AELi_2[Be_4O_6]:Eu^{2+}$ (*AE* = Sr,Ba) were synthesized by heating of a stoichiometric mixture of *AE*O (SrO: Sigma Aldrich, 99.9%; BaO: Sigma Aldrich, 99.99%), Li_2O (Schuchardt, 98%), BeO (Alfa Aesar, 99.95%) and Eu_2O_3 ((ABCR, 99.99%) for 2 h to 1100 °C in Ar gas atmosphere. The starting materials were thoroughly ground in a mortar under Ar and filled in a tungsten crucible The product is obtained as colorless powder, which is stable in 0.1M HCl.

Luminescence

Luminescence investigations on single crystals of $AELi_2[Be_4O_6]:Eu^{2+}$ (*AE* = Sr,Ba) have been performed with a Horiba Fluorimax4 spectrofluorimeter system attached to an Olympus BX51 microscope via fiber optics. Photoluminescence measurements on powder samples were carried out with an in-house-built system based on a 5.300 integrating sphere and a spectrofluorimeter equipped with a 150 W Xe lamp, two 500 mm Czerny-Turner monochromators, 1,800 1/mm lattices and 250/500 nm lamps, with a spectral range from 230 to 820 nm. Low-temperature emission spectra of powder samples were recorded with an Ocean Optics HR2000 C ES spectrometer (2,048 pixels, grating UA (200-1,100 nm), slit-50) with the samples mounted in a closed-cycle He cryostat. The samples were measured on PTFE sample holders. The excitation wavelength was 410nm with a spectral width of 10 nm. The emission spectra were recorded in the wavelength range between 460nm and 820nm with a 1 nm step size. Excitation spectra were monitored at 470 nm under an excitation wavelength range from 380 to 450nm with a 2 nm step size. For photoluminescence quantum efficiency measurements a manufactured $SrSi_2O_2N_2:Eu^{2+}$ reference with internal quantum efficiency of 95% excited at 440 nm was used.

Elemental Analysis

For the determination of the chemical composition of different crystallites EDS spectroscopy and ICP-OES analysis was applied. For EDS, a Dualbeam Helios Nanolab G3 UC scanning electron microscope (SEM, FEI) with X-Max 80 SDD detector (Oxford Instruments) was used. The EDS data were collected from several particles at an accelerating voltage of 20 kV. Additionally, SEM was used to collect images of particles to investigate the morphology. Inductively coupled plasma optical emission spectrometry (ICP-OES) was conducted with a Varian Vista RL spectrometer, to determine the Sr, Li, Be and Eu ratio.

Table S2. Elemental Analysis via energy dispersive X-ray spectroscopy (EDS) of $AELi_2[Be_4O_6]:Eu^{2+}$ (1% Eu, *AE* = Sr,Ba)

		AE	**Eu**	**Li**	**Be**	**O**
$SrLi_2[Be_4O_6]:Eu^{2+}$	EDS	1	-	-	-	5
	ICP	1	<0.01	1.5	3.6	-
$BaLi_2[Be_4O_6]:Eu^{2+}$	EDS	1	-	-	-	6
	ICP	1	<0.01	1.7	3.8	-

MAPLE calculations

Table S1. Results of MAPLE calculations [kJ/mol] for $SrLi_2[Be_4O_6]$; Δ = MAPLE sum of constituting binary/ternary nitrides / MAPLE sum compound.

	$SrLi_2[Be_4O_6]$
Sr^{2+}	1594
Li^+	641
Be^{2+}	2920
O^{2-}	2445-2527
Total	29600
Δ	0.7%
Total MAPLE: $Li_2O + SrBe_3O_4 + BeO$ = 29795 kJ/mol;	

The deviation Δ = 0.7% can be explained by the change of coordination of Be. While Be is in trigonal planar coordination in $SrBe_3O_4$, it is tetrahedrally coordinated in $SrLi_2[Be_4O_6]$, leading to an increased deviation.

This can be seen when applying the MAPLE concept for $SrBe_3O_4$. The partial MAPLE value for the trigonal planar coordinated Be yields decreased values (2880 kJ/mol), when compared to tetrahedrally coordinated (O^{2-} ligands) Be (2980 kJ/mol).

NMR spectroscopy

Solid-state MAS-NMR experiments were performed at 11.74 T on a Bruker 500 Avance III FT spectrometer equipped with a commercial 4 mm triple-resonance MAS probe at a ^{6}Li frequency of 73.6 MHz ^{7}Li frequency of 194.4 MHz 7 and ^{9}Be frequency of 70.3 MHz. All experiments were performed in ZrO_2 rotors at room temperature. The chemical shift of ^{6}Li, ^{7}Li and ^{9}Be is reported using the frequency ratios published by IUPAC [δ-scale relative to 1% tetramethylsilane (TMS) in $CDCl_3$].[1]

The ^{6}Li MAS-NMR spectrum was acquired with a 90° pulse length of 2.5 µs and a recycle delay of 128000 s, the ^{7}Li MAS-NMR spectrum was acquired with a 90° pulse length of 5.0 µs and a recycle delay of 4096 s and the ^{9}Be MAS-NMR spectrum was acquired with a 90° pulse length of 2.5 µs and a recycle delay of 8192 s. The spinning frequency for all measurements was 10 kHz.

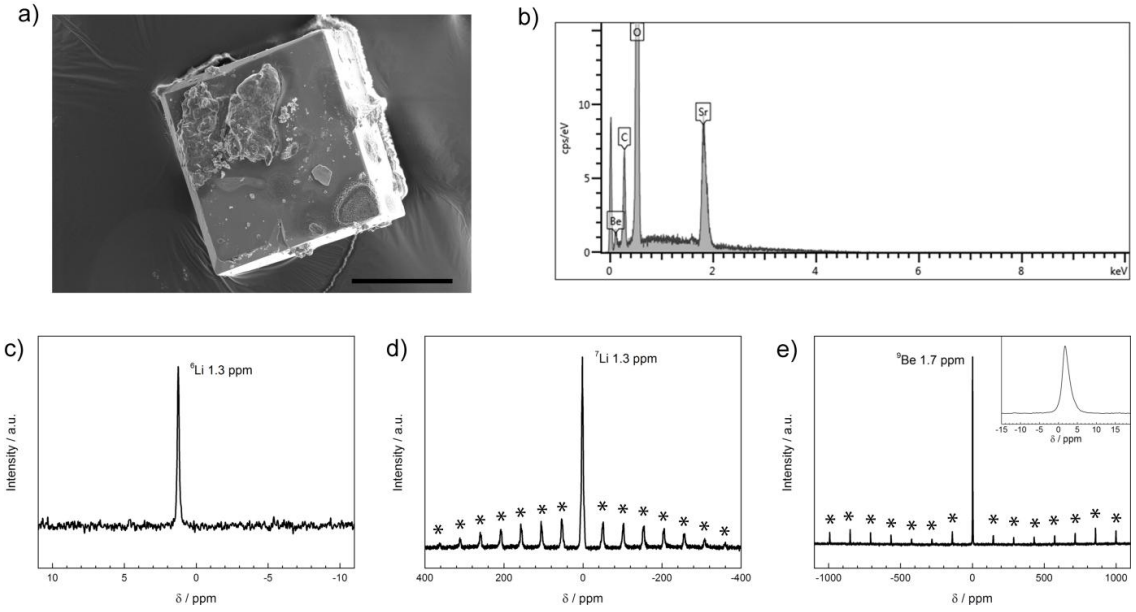

Figure S1. Morphology and composition of ultra-narrow band blue emitting $AELi_2[Be_4O_6]:Eu^{2+}$ (*AE* = Sr,Ba). a, SEM image of a SLBO single crystal. Scale bar, 100 µm. b, EDS scan of SLBO single crystal, coated with C. c, ^{6}Li solid-state MAS-NMR spectrum of BLBO (rotation frequency 10 kHz). d, ^{7}Li solid-state MAS-NMR spectrum of BLBO. Rotation side-bands are indicated by asterisks (rotation frequency 10 kHz). e, ^{9}Be solid-state MAS-NMR spectrum of BLBO. Rotation side-bands are indicated by asterisks (rotation frequency 10 kHz).

X-ray Diffraction

Crystal structure of $AELi_2[Be_4O_6]$ (*AE* = Sr,Ba) were determined by single-crystal X-ray diffraction on a Bruker D8 Venture diffractometer (Mo-Kα radiation, rotating anode generator, graphite monochromator). Blue luminescent single crystals of $AELi_2[Be_4O_6]:Eu^{2+}$ (*AE* = Sr,Ba) were placed on micromounts (MiTeGen) for measurements. Integration and multi-scan absorption correction was applied using the program APEX3.[2] The crystal structure was solved using direct methods with SHELXS.[3] The refinement of the structure was carried out with a least-squares algorithm using SHELXL.[4,5] The crystal structure was refined with the Rietveld method on the powder X-ray diffraction data. PXRD data were collected on a STOE STADI P diffractometer (Cu-$K\alpha_1$ radiation,

Ge(111) monochromator, position sensitive detector) in transmission geometry. Rietveld refinement was carried out using the TOPAS package.[6]

Further details of the crystal structure investigations can be obtained from the Fachinformationszentrum Karlsruhe, 76344 Eggenstein-Leopoldshafen, Germany (Fax, (+49)7247-808-666; email, crysdata@fiz-karlsruhe.de) upon quoting the depository numbers CSD-434376 ($BaLi_2[Be_4O_6]$) and CSD-434377 ($SrLi_2[Be_4O_6]$).

Table S3. Single crystal data for $AELi_2[Be_4O_6]$ (*AE* = Sr,Ba) [a]

	$SrLi_2[Be_4O_6]$	**$BaLi_2[Be_4O_6]$**
Formula mass [g mol^{-1}]	233.54	283.26
Crystal system / space group	Tetragonal, P4/ncc (130)	
Lattice parameters [Å]	a = 7.1659(2)	a = 7.2770(4)
	c = 8.9085(6)	c = 8.8872(5)
Cell volume [Å^3]	457.45(4)	470.62(6)
Formula units per cell Z	4	
X-ray density [g cm^{-1}]	3.391	3.998
Linear absorption coefficient [cm^{-1}]	11.730	8.385
F(000)	432	504
Crystal dimensions (mm^3)	0.246 × 0.150 × 0.059	0.08 × 0.03 × 0.02
Diffractometer	D8 Quest	
Radiation	Mo-Kα (λ = 0.71073 Å)	
Temperature [K]	297(2)	
Abs correction	Multi-scan	
θ range [°]	4.022-29.999	3.960-29.974
Measured reflns	8810	8043
Independent reflns	339 [R_{int} = 0.0365]	349 [R_{int} = 0.0347]
observed reflns	306	310
Min./max. transmission	0.466/1.000	0.837/1.000
Refined params	33	33
GOF	1.194	1.098
R indices (Fo2 ≥ 2σ(Fo2))	R1 = 0.0174, wR2 = 0.0473	R1 = 0.0121, wR2 = 0.0365
R indices (all data)	R1 = 0.0193, wR2 = 0.0487	R1 = 0.0137, wR2 = 0.0374
min./max. residual electron density (eÅ^{-3})	-0.906/0.506	-0.848/0.499

[a] The e.s.d.s are given in parentheses.

Table S4. Atomic coordinates and equivalent isotropic displacement parameters of $SrLi_2[Be_4O_6]$ and $BaLi_2[Be_4O_6]$ [a]

	Atom (*Wyck.*)	***x***	***y***	***z***	**U_{eq} (Å^2)**	***sof***
$SrLi_2[Be_4O_6]$	Sr1 (4*c*)	1/4	1/4	0.34572(3)	0.00909(17)	1
	Li1 (8*f*)	0.3697(4)	0.6303(4)	1/4	0.0122(7)	1
	Be1 (16*g*)	0.1197(3)	0.5311(3)	0.0776(2)	0.0059(3)	1
	O1 (16*g*)	0.50309(13)	0.16231(15)	0.04168(10)	0.0064(2)	1
	O2 (8*f*)	0.59096(15)	0.40904(15)	1/4	0.0088(3)	1
$BaLi_2[Be_4O_6]$	Ba1 (4*c*)	1/4	1/4	0.32551(2)	0.00909(17)	1
	Li1 (8*f*)	0.3665(4)	0.6335(4)	1/4	0.0120(7)	1
	Be1 (16*g*)	0.1207(3)	0.5337(3)	0.0766(2)	0.0066(4)	1
	O1 (16*g*)	0.50530(15)	0.15991(16)	0.04538(12)	0.0061(2)	1
	O2 (8*f*)	0.59636(15)	0.40364(15)	1/4	0.0075(3)	1

[a] The e.s.d.s are given in parentheses.

Table S5. Selected bond lengths and angles in $SrLi_2[Be_4O_6]$ and $BaLi_2[Be_4O_6]$ [a]

	$SrLi_2[Be_4O_6]$	$BaLi_2[Be_4O_6]$
Bond name	**Bond length / Å**	
Sr/Ba1-O1 (4x)	2.5945(10)	2.7749(11)
Sr/Eu1-O2 (4x)	2.8276(5)	2.8378(6)
Be1-O1 (1x)	1.607(2)	1.633(3)
Be1-O2 (1x)	1.608(2)	1.617(2)
Be1-O1 (1x)	1.646(2)	1.650(2)
Be1-O1 (1x)	1.673(2)	1.704(3)
Li1-O2 (2x)	2.017(3)	1.985(3)
Li1-O1 (2x)	2.0802(14)	2.0527(15)
Li1-O2 (1x)	2.242(4)	2.365(5)
Li1-Li1 (1x)	2.427(8)	2.399(9)
Angle name	**Angle / °**	
O1-Sr/Ba1-O1 (4x)	63.08(2)	60.27(2)
O1-Sr/Ba1-O1 (2x)	95.43(4)	90.47(4)
O1-Sr/Ba1-O2 (4x)	154.76(2)	148.68(2)
O1-Sr/Ba1-O2 (4x)	105.98(3)	102.74(3)
O2-Sr/Ba1-O2 (4x)	84.782(3)	86.794(2)
O2-Sr/Ba1-O2 (2x)	144.895(12)	152.642(9)
O2-Be1-O1	110.35(11)	107.73(12)
O2-Be1-O1	113.54(12)	114.42(13)
O1-Be1-O1	115.86(12)	117.16(12)
O2-Be1-O1	109.66(12)	109.21(14)
O1-Be1-O1	111.68(13)	113.19(15)
O1-Be1-O1	94.76(10)	94.56(10)
O2-Li1-O2	106.0(2)	105.6(2)
O2-Li1-O1 (2x)	116.69(7)	117.57(8)
O2-Li1-O1 (2x)	80.18(4)	81.10(5)
O1-Li1-O1	153.2(2)	150.5(2)
O2-Li1-O2 (2x)	126.98(10)	127.18(10)
O1-Li1-O2 (2x)	76.60(11)	75.23(12)

[a] The e.s.d.s are given in parentheses.

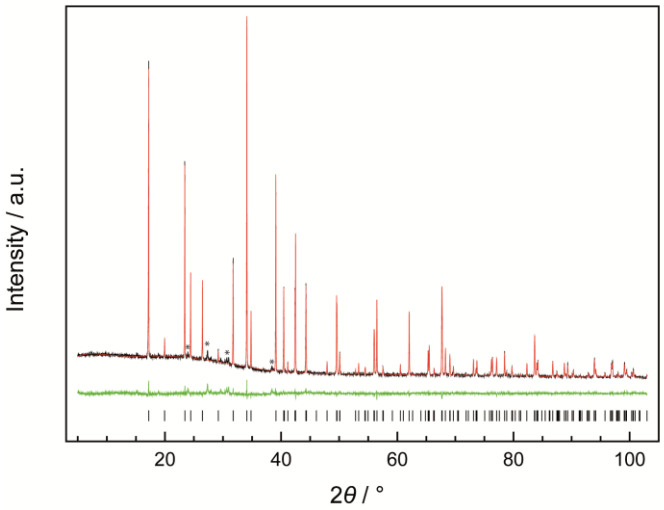

Figure S2. Crystal structure characterization of ultra-narrow band blue emitting $AELi_2[Be_4O_6]:Eu^{2+}$ (*AE* = Sr,Ba). X-ray powder diffractogram (Cu-Kα_1 radiation) of BLBO with the measured data (black line), calculated pattern based on Rietveld refinement data (red line), difference curve (green line) and tick marks (black) that give positions of Bragg reflections of BLBO; unknown side-phases are marked with asterisks.

UV/vis spectroscopy

UV/vis-reflectance data were obtained to investigate the optical band gap of $AELi_2[Be_4O_6]:Eu^{2+}$ (*AE* = Sr,Ba). Reflectance spectra of Eu^{2+}-doped and undoped powder samples were obtained with an Edinburgh Photonics FLS920-s spectrometer equipped with a 450 W Xe900 arc lamp (single photon-photomultiplier detector, Czerny-Turner monochromator with triple grating turret). The spectra were measured in the wavelength range from 230 to 780 nm (5 nm step size).

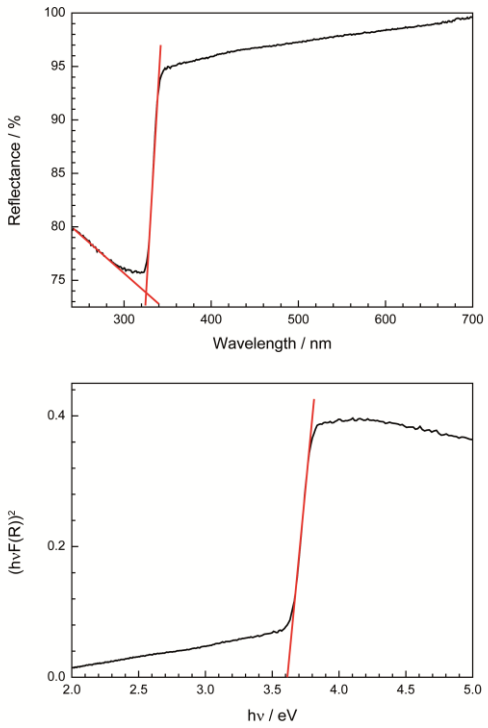

Figure S3. a) Reflectance spectrum of undoped $BaLi_2[Be_4O_6]$. b) Tauc plot (n = 1/2) for $BaLi_2[Be_4O_6]$. The band gap is estimated with both methods and is found in a range from 3.6-3.8 eV.

Reference

[1] Harris, R. K.; Becker, E. D.; Cabral de Menezes, S. M.; Goodfellow, R.; Granger, P. NMR nomenclature: nuclear spin properties and conventions for chemical shifts. IUPAC Recommendations 2001. International Union of Pure and Applied Chemistry. Physical Chemistry Division. Commission on Molecular Structure and Spectroscopy. *Magn. Reson. Chem.* **2002**, *40*, 489-505.

[2] BrukerAXS, *APEX3 v2016.5-0*: Billerica, **2016**.

[3] Sheldrick, G. M., *SHELXS-97: A program for crystal structure solution*, University of Göttingen, **1997**.

[4] Sheldrick, G. M. A short history of SHELX. *Acta Crystallogr. Sect. A* **2008**, *64*, 112-122.

[5] Sheldrick, G. M., *SHELXL-97: A program for crystal structure refinement*, University of Göttingen, **1997**.

[6] Coelho, A. A., *TOPAS-Academic*, Version 4.1: A program for Rietveld refinement: Brisbane, Australia, **2007**.

8 Publications

8.1 List of Publications Included in this Thesis

1. **Narrow-Band Green Emitting Nitridolithoalumosilicate $Ba[Li_2(Al_2Si_2)N_6]:Eu^{2+}$ with Framework Topology whj for LED/LCD-Backlighting Applications**

   Philipp Strobel, Sebastian Schmiechen, Markus Siegert, Andreas Tücks, Peter J. Schmidt, and Wolfgang Schnick
   Chem. Mater. **2015**, *27*, 6109–6115

   In this contribution, writing the main part of the manuscript, structure determination based on single-crystal and powder XRD data, topology investigations, interpretation of UV/vis and sorption measurements and image preparation were done by Sebastian Schmiechen and Philipp Strobel. Sample syntheses and synthesis optimization were done by Andreas Tücks, Sebastian Schmiechen, Markus Siegert and Philipp Strobel. Luminescence investigations and interpretation of measured values were done in the LPC Aachen, supported by Peter J. Schmidt. The research project was supervised by Wolfgang Schnick.

2. **Luminescence of the Narrow-band Red Emitting Nitridomagnesosilicate $Li_2(Ca_{1-x}Sr_x)_2[Mg_2Si_2N_6]:Eu^{2+}$ (x = 0–0.06)**

   Philipp Strobel, Volker Weiler, Cora Hecht, Peter J. Schmidt, and Wolfgang Schnick
   Chem. Mater. **2017**, *29*, 1377–1383

   For this article, writing the main part of the manuscript, syntheses and image preparation, structure solution and refinement of the nitridomagnesosilicates and UV/vis measurements were done by Philipp Strobel. Syntheses were optimized by Philipp Strobel, Cora Hecht and Volker Weiler. Luminescence investigations and interpretation of measured values were done in the LPC Aachen by Peter J. Schmidt. Supervision of the research project was carried out by Wolfgang Schnick.

3. **Designing Luminescent Materials and Band Gaps: A Soft X-ray Spectroscopy and Density Functional Theory Study of $Li_2Ca_2[Mg_2Si_2N_6]:Eu^{2+}$ and $Ba[Li_2(Al_2Si_2)N_6]:Eu^{2+}$**

   Thomas M. Tolhurst, Philipp Strobel, Peter J. Schmidt, Wolfgang Schnick, and Alexander Moewes
   J. Phys. Chem. C. **2017**, *121*, 14296–14301

   For this contribution, writing the manuscript main part, conception and performance of Soft X-ray investigations and image preparation were done by Thomas Tolhurst. Sample synthesis was performed by Philipp Strobel, supported by the LPC Aachen. Interpretation of measured values was done by Thomas Tolhurst, Philipp Strobel and Peter J. Schmidt. Supervision of the research project was carried out by Wolfgang Schnick and Alexander Moewes.

4. **Direct Measurements of Energy Levels and Correlation with Thermal Quenching Behavior in Nitride Phosphors**

   Thomas M. Tolhurst, Philipp Strobel, Peter J. Schmidt, Wolfgang Schnick, and Alexander Moewes
   Chem. Mater. **2017**, *29*, 7976–7983

   In this contribution, writing the manuscript main part and image preparation was done by Thomas Tolhurst and Philipp Strobel. Soft X-ray investigations were performed by Thomas Tolhurst. Sample synthesis was performed by Philipp Strobel. Interpretation of analysis results were done by Thomas Tolhurst, Philipp Strobel and Peter J. Schmidt. Luminescence data were provided by the LDC Aachen by Peter J. Schmidt. Supervision of the research project was carried out by Wolfgang Schnick and Alexander Moewes.

5. **$Sr[BeSi_2N_4]:Eu^{2+}/Ce^{3+}$ and $Eu[BeSi_2N_4]$: Nontypical Luminescence in Highly Condensed Nitridoberyllosilicates**

   Philipp Strobel, Volker Weiler, Peter J. Schmidt, and Wolfgang Schnick
   Chem. Eur. J. **2018**, *24*, 7243-7249

   For this article, writing the main part of the manuscript, syntheses, structure solution and refinement of the nitridoberyllosilicates, UV/vis analysis and image preparation were conducted by Philipp Strobel. Luminescence investigations and analysis of measurements were done in the LPC Aachen by Volker Weiler and Peter J. Schmidt. Supervision of the research project was carried out by Wolfgang Schnick.

6. Luminescence of an Oxonitridoberyllate: A Study of Narrow-Band Cyan Emitting $Sr[Be_6ON_4]:Eu^{2+}$

Philipp Strobel, Tristan de Boer, Volker Weiler, Peter J. Schmidt, Alexander Moewes, and Wolfgang Schnick
Chem. Mater. **2018**, *30*, 3122-3130

For this contribution, writing the main part of the manuscript, sample syntheses, structure determination based on single-crystal and powder XRD data, interpretation of UV/vis measurements, and image preparation were done by Philipp Strobel. X-ray spectroscopy investigations were done by Philipp Strobel and Tristan de Boer. DFT calculations were conducted by Tristan de Boer. Luminescence investigations and interpretation of measurement results were supported by Volker Weiler and Peter J. Schmidt in the LPC Aachen. The research project was supervised by Alexander Moewes and Wolfgang Schnick.

7. Oxoberyllates $SrBeO_2$ and $Sr_{12}Be_{17}O_{29}$ as Novel Host Materials for Eu^{2+} Luminescence

Philipp Strobel, Robin Niklaus, Peter J. Schmidt, and Wolfgang Schnick
Chem. Eur. J. **2018**, https://doi.org/10.1002/chem.201801951

For this contribution, writing the manuscript main part, sample syntheses, structure determination based on single-crystal data and luminescence analysis was performed by Philipp Strobel. DFT calculations were conducted by Robin Niklaus. Image preparation was done by Philipp Strobel and Robin Niklaus. Interpretation of measured values was done by Philipp Strobel, Robin Niklaus and Peter J. Schmidt. Supervision of the research project was carried out by Wolfgang Schnick.

8. Ultra-Narrow Band Blue Emitting Oxoberyllates $AELi_2[Be_4O_6]:Eu^{2+}$ (*AE* = Sr,Ba) Paving the Way to Efficient RGB pc-LEDs

Philipp Strobel, Christian Maak, Volker Weiler, Peter J. Schmidt, and Wolfgang Schnick
Angew. Chem. Int. Ed. **2018**, https://doi.org/10.1002/anie.201804721

For this contribution, writing the manuscript main part, sample syntheses, structure determination based on single-crystal data, elemental analysis and image preparation was performed by Philipp Strobel, supported by Christian Maak. Luminescence investigations were done at the LPC Aachen, supported by Volker Weiler and Peter Schmidt. Interpretation of measured values was done by Philipp Strobel, Volker Weiler and Peter J. Schmidt. Supervision of the research project was carried out by Wolfgang Schnick.

8.2 Patent Applications

1. **LED phosphors comprising bow tie shaped A2N6 building blocks**

   Peter. J. Schmidt, Philipp Strobel, Sebastian Schmiechen, Cora Hecht, Volker Weiler, and Wolfgang Schnick

   PCT Int. Appl. **2016**, WO 2016075021, A1

   Koninklijke Philips NV, Ludwig-Maximilians-Universität München

8.3 Other Publications

1. **Nitridomagnesosilicate $Ba[Mg_3SiN_4]:Eu^{2+}$ and Structure-Property Relations of Similar Narrow-Band Red Nitride Phosphors**

   Sebastian Schmiechen, Philipp Strobel, Cora Hecht, Thomas Reith, Markus Siegert, Peter J. Schmidt, Petra Huppertz, Detlef Wiechert, and Wolfgang Schnick

   Chem. Mater. **2015**, *27*, 1780-1785

2. **Unprecedented Deep-Red Ce^{3+} Luminescence of the Nitridolithosilicates $Li_{38.7}RE_{3.3}Ca_{5.7}[Li_2Si_{30}N_{59}]O_2F$ (*RE* = La,Ce,Y)**

   Christian Maak, Philipp Strobel, Volker Weiler, Peter J. Schmidt, and Wolfgang Schnick

   Chem. Mater., submitted, 20.06.2018

3. **$Ca[BeSi_2N_4]$: Synchrotron X-ray Diffraction Revealing Nitridoberyllosilicate Superstructure**

   Tobias Giftthaler, Philipp Strobel, Lucien Eisenburger, Oliver Oeckler, and Wolfgang Schnick

   To be published

4. **Weiße LEDs: Licht mit Spitzenleistung**

   Philipp Strobel, Dajana Durach, and Wolfgang Schnick

   GDCH-Wochenschau, **2015**

8.4 Conference Contributions

1. **To Be or not to Be (talk)**

   Philipp Strobel, and Wolfgang Schnick

   Hemdsärmelkolloquium

   08.–10.03.2018, Leipzig, Deutschland

2. **Band Gap And Electronic Structure of $Zn(Ge,Si)N_2$: Probing Defects Using XEOL (poster)**

   Tristan de Boer, Philipp Strobel, Jonas Häusler, Wolfgang Schnick, and Alexander Moewes

   ALS User Meeting

   02.–04.10.2017, Berkeley, USA

3. **Synthesis in liquid Ammonia with Lithium and Silicon (poster)**

   Alexander Beck, Philipp Strobel, and Wolfgang Schnick

   Undergraduate Research Conference on Molecular Sciences (URCUP)

   01.07.–02.07.2017, Herrsching, Deutschland

4. **Luminescence Tuning in Red Emitting $Li_2(Ca,Sr)_2[Mg_2Si_2N_6]:Eu^{2+}$ (poster)**

   Philipp Strobel, Cora Hecht, Volker Weiler, Peter J. Schmidt, and Wolfgang Schnick

   18. Vortragstagung der FG Festkörperchemie und Materialforschung

   19.09.–21.09.2016, Innsbruck, Österreich

5. **$Ba[Li_2Al_2Si_2N_6]:Eu^{2+}$: A Narrow-band Green Emitting Phosphor (talk)**

   Philipp Strobel, and Wolfgang Schnick

   2. Obergurgl-Seminar Festkörperchemie

   26.01.–29.01.2016, Obergurgl, Österreich

6. The missing nitridomagnesosilicate: $Ba[Mg_3SiN_4]:Eu^{2+}$ (talk)

Philipp Strobel, and Wolfgang Schnick

1. Obergurgl-Seminar Festkörperchemie

28.01.–31.01.2014, Obergurgl, Österreich

8.5 Depository Numbers of Single-crystal and Powder X-ray Diffraction Data

Details of crystal structure investigations (cif-file) of characterized compounds can be obtained from the Fachinformationszentrum Karlsruhe, 76344 Eggenstein-Leopoldshafen, Germany (fax: (+49)7247-808-666; e-mail: crysdata@fiz-karlsruhe.de) by quoting the corresponding depository numbers.

$Ba[Li_2(Al_2Si_2)N_6]$	CSD-429872
$Ba[(Mg_{0.2}Li_{1.8})(Al_{2.2}Si_{1.8})N_6]$	CSD-429873
$Ba[(Mg_{0.4}Li_{1.6})(Al_{2.4}Si_{1.6})N_6]$	CSD-429874
$Li_2(Ca_{1.88}Sr_{0.12})[Mg_2Si_2N_6]$	CSD-432118
$Sr[BeSi_2N_4]$	CSD-434198
$Eu[BeSi_2N_4]$	CSD-434199
$Sr[Be_6ON_4]$	CSD-434259
$Sr_{12}Be_{17}O_{29}$	CSD-434343
α-$SrBeO_2$	CSD-434344
β-$SrBeO_2$	CSD-434345
$BaLi_2[Be_4O_6]$	CSD-434376
$SrLi_2[Be_4O_6]$	CSD-434377